OAK RIDGE NATIONAL LABORATORY LIBRARIES
3 4456 0548182 2

CENTRAL RESEARCH LIBRARY
DOCUMENT COLLECTION

113

ORNL-3885
UC-80 – Reactor Technology
TID-4500 (47th ed.)

GAS-COOLED REACTOR PROGRAM

SEMIANNUAL PROGRESS REPORT

FOR PERIOD ENDING SEPTEMBER 30, 1965

CENTRAL RESEARCH LIBRARY
DOCUMENT COLLECTION
LIBRARY LOAN COPY
DO NOT TRANSFER TO ANOTHER PERSON
If you wish someone else to see this document, send in name with document and the library will arrange a loan.

OAK RIDGE NATIONAL LABORATORY
operated by
UNION CARBIDE CORPORATION
for the
U.S. ATOMIC ENERGY COMMISSION

Printed in USA. Price $7.00. Available from the Clearinghouse for Federal Scientific and Technical Information, National Bureau of Standards, U.S. Department of Commerce, Springfield, Virginia

LEGAL NOTICE

This report was prepared as an account of Government sponsored work. Neither the United States, nor the Commission, nor any person acting on behalf of the Commission:

A. Makes any warranty or representation, expressed or implied, with respect to the accuracy, completeness, or usefulness of the information contained in this report, or that the use of any information, apparatus, method, or process disclosed in this report may not infringe privately owned rights; or

B. Assumes any liabilities with respect to the use of, or for damages resulting from the use of any information, apparatus, method, or process disclosed in this report.

As used in the above, "person acting on behalf of the Commission" includes any employee or contractor of the Commission, or employee of such contractor, to the extent that such employee or contractor of the Commission, or employee of such contractor prepares, disseminates, or provides access to, any information pursuant to his employment or contract with the Commission, or his employment with such contractor.

ORNL-3885

Contract No. W-7405-eng-26

GAS-COOLED REACTOR PROGRAM SEMIANNUAL PROGRESS REPORT

For Period Ending September 30, 1965

D. B. Trauger, AGCR Program Director
G. D. Whitman, EGCR Program Director

FEBRUARY 1966

OAK RIDGE NATIONAL LABORATORY
Oak Ridge, Tennessee
operated by
UNION CARBIDE CORPORATION
for the
U.S. ATOMIC ENERGY COMMISSION

OAK RIDGE NATIONAL LABORATORY LIBRARIES
3 4456 0548182 2

The Oak Ridge National Laboratory Gas-Cooled Reactor Program acknowledges the efforts of Ann W. Savolainen and her staff in collecting, compiling, and editing the information contained in this report.

CONTENTS

Page

SUMMARY vii

PART 1. ADVANCED GAS-COOLED REACTOR PROGRAM

1. FUELED-GRAPHITE DEVELOPMENT 3

Pyrolytic-Carbon Coating Studies 3

Coating of Large Particles with Methane in 1-in.-diam Fluidized Beds 3

Coatings Deposited from Methane in a 2-in.-diam Fluidized Bed 13

Porous Coatings Deposited on Fuel Particles from Acetylene in a 1-in.-diam Fluidized Bed 14

Characterization of Porous Coatings 23

Effects of Heat Treatment on Pyrolytic Carbon 28

Phase Studies of the Pseudobinary System UC_2-ThC_2 in the Presence of Excess Graphite 33

Analysis of Thermodynamic Data for the Uranium-Carbon System 35

Uranium Monocarbide 36

Uranium Dicarbide 36

Conversion of Sol-Gel Oxide Particles to Carbides 40

Conversion of ThO_2 to ThC_2 40

Conversion of Sol-Gel UO_2 and $(Th,U)O_2$ to Carbides 42

Testing and Evaluation of Coated Fuel Particles 43

Effects of Heat Treatment on Pyrolytic-Carbon-Coated Oxide Particles 43

Preparation of Coated Fuel Particles for Irradiation Tests 50

General Evaluation of ETR X-Basket Irradiation Specimens 50

Mathematical Simulation of Coated-Particle Behavior 53

Coated-Particle-Survey Irradiation Tests 59

General Evaluation of Coated Fuel Particles 62

Evaluations of Experimental Fuel Assemblies 64

Irradiation of Experimental Fuel Assembly 14 in GCR-ORR Loop 1 64

Postirradiation Examination of Experimental Fuel Assembly 14 67

Irradiation of Experimental Fuel Assembly 15 in GCR-ORR Loop 1 73

High-Burnup Coated-Particle Experiment in ORR Position F-9 78

Compatibility of Oxide Fuel Pellets and Graphite Under Irradiation 82

Coated-Particle Irradiations in LITR 83

2. INVESTIGATIONS OF FUELED-GRAPHITE SYSTEMS 87

Instantaneous Fission-Gas Release Experiments 87

Fission-Gas Release from UO_2 87

Fission-Gas Release from Coated UO_2 and $(Th,U)C_2$ Particles 92

Fission-Product Release from High-Burnup Coated UC_2, $(Th,U)C_2$, and UO_2 Particles by Postirradiation Annealing 108

Fission-Product Transport and Deposition 112

Fission-Product Deposition in ORNL Out-of-Pile Loop 112

Packed-Bed Laminar-Flow Deposition Experiment 116

Analytical Model for Fission-Product Deposition 118

Sorption of Fission-Product Vapors on Structural Metals ... 121

Compatibility of Pyrolytic-Carbon-Coated Fuel Particles with Water Vapor 125

Recoil of Fission Products in Pyrolytic Carbon 131

Basic Considerations 132

Experimental Procedures and Results 140

Additional Findings 146

3. STUDIES FOR AVR — GERMAN PEBBLE-BED REACTOR 150

Introduction 150

Fueled-Sphere Experiments — Capsule 05-8 153

Irradiation in ORR Poolside Facility 153

Postirradiation Examination 153

Eight-Ball Capsule F1-8B-5 Experiment 159
Irradiation in ORR Core 159
Postirradiation Examination 162
AVR Prototype Sphere Experiments — Capsule O1A-8 175
Irradiation in ORR Poolside Facility 175
Postirradiation Examination 176
Fission-Gas Release from AVR Production Particles 184
Evaluation of Fueled-Graphite Spheres 186
4. INVESTIGATIONS OF MODERATOR MATERIALS 195
Thermal Conductivity of AGOT Graphite 195
Dimensional Stability of AGOT Graphite 195
Creep of Graphite Under Irradiation 198
Deposition of Carbon on ATJ Graphite 203
BeO-Graphite Compatibility 208
Failure Characteristics of EGCR-Type AGOT Graphite 210
Crack Propagation and Fracture Characteristics of EGCR-Type AGOT Graphite 211
Theoretical and Experimental Investigation of the Applicability of Weibull's Statistical Theory of Strength to EGCR-Type AGOT Graphite Fracture Data 216
Correlation of EGCR-Type AGOT Graphite Properties Data 225
Compressive Modes of Failure in EGCR-Type AGOT Graphite 229
Investigation of Multiaxial Stress States for EGCR-Type AGOT Graphite 231
5. STUDIES FOR ADVANCED SYSTEMS 236
Fuel Cycles for Fission-Product-Releasing Fuel 236
Analyses of Nozzle-to-Spherical Shell Attachments 241
6. FAST REACTOR DEVELOPMENT 244
Fuel Irradiation Tests in ORR Poolside Facility 244

PART 2. EXPERIMENTAL GAS-COOLED REACTOR PROGRAM

7. PERFORMANCE ANALYSES 253

Reactor Commissioning Program 253

Graphite—Air Oxidation Studies 253

Core Cooling Requirements and Nitrogen Purge Effectiveness for Extreme Coolant Piping Ruptures 254

Effect of Increased Oxidation Rate, Higher Initial Temperatures, and Increased Oxidation Depth on Required Air Coolant Flow 263

8. COMPONENT DEVELOPMENT AND TESTING 268

Compressor Shaft Seals 268

Control-Rod Drive Test 271

Charge-Machine Cylinder-Seal Development 273

Experimental Studies of Steam-Graphite Reactions 279

Special Fuel Assemblies for Flux Mapping 280

Analysis of Failure of 42-in. Bellows Between EGCR Containment Shell and Experimenter's Cell 281

9. IRRADIATION TESTING OF COMPONENTS AND MATERIALS 284

EGCR Prototype Fuel Tests 284

Irradiation of Capsules 03A-6 and 04-8 in ORR Poolside Facility 284

Postirradiation Examination of EGCR Prototype Fuel 284

Pressure-Vessel Surveillance Program 291

Fast Fracture Analysis of the EGCR Pressure Vessel 292

Accelerated Irradiations 293

Graphite Surveillance Program 293

SUMMARY

Part 1. Advanced Gas-Cooled Reactor Program

The major effort in the AGCR program is directed to the development and evaluation of high-temperature fuels. In particular, this involves the preparation of fuel kernels and the improved design of pyrolytic-carbon coatings for rather specific types of reactor service applications. Characterizations of particles and particle coatings, including extensive irradiation testing, constitute an important phase of the work. Closely related effort involves the study of fission-product behavior in gas-cooled reactor systems, particularly as maintenance requirements may be affected. Although helium is an inert coolant, the chemical properties of impurities that may be introduced from the graphite through steam leaks, or from other sources, are of concern. Both the coolant properties and fission-product behavior constitute areas requiring study, particularly as related to the safety of high-temperature gas-cooled reactors. Reactor physics studies have emphasized the evaluation of fuel cycles, including both thorium and plutonium utilization. This work is closely coordinated with the fuel-reprocessing development for the HTGR, which is conducted under the Thorium Utilization Program. Fuel particle studies utilize sol-gel microspheres wherever possible in order to implement more fully this promising fuel-production method.

In coated particle development, the most significant recent advancement has been the development and evaluation of coated oxide particles. The oxides offer advantages over carbides in that easier fabrication results from omission of the conversion step and from the more convenient handling of thorium. Also, it appears that some metallic fission products are retained more effectively in an oxide kernel. Coatings applied to the oxide have had lower contamination levels which, in turn, has facilitated more detailed and effective evaluation of coating properties through irradiation testing. Both the development of oxide fuels and the coating improvements have had a common objective — the reduction of coated particle

fuel fabrication costs and the tailoring of fuels for particular service requirements.

The retention of noble gases by pyrolytic-carbon-coated oxide particles has been striking. Release to birth ratios, R/B, for ^{88}Kr between 5×10^{-6} and 4×10^{-8} have been obtained in irradiation experiments carried to burnups between 12 and 28 at. % of heavy metal at temperatures up to 1600°C. Reaction between the oxide kernel and the pyrolytic-carbon coating has been remarkably low or, in many cases, unobservable. Evaluations of coating properties continue to show that a low-density, porous, inner-coating layer combined with a high-density outer coating (which serves as a pressure vessel) is a desirable combination. Recent studies have emphasized understanding of the basic properties of the coating material and the factors involved with particle geometry in order to provide an improved basis for predicting particle performance. Mathematical expressions relating these properties have shown encouraging results for particle evaluation. Such relationships may facilitate the design of particles having the necessary properties for a particular service without excessive safety factors, for example, excessive thickness represents unnecessary cost and reduces the possible fuel loading per unit of particle bed volume in the fuel element.

Fission-product behavior studies have been directed toward an understanding of mechanisms of transport. Data obtained in an out-of-pile loop show that an analogy between well-developed heat transfer theory and mass transfer is valid for fission-product transport, at least in simple geometrical channels. Extensive studies have been conducted with iodine, including adsorption and desorption mechanisms, as well as transport in the gas stream. Emphasis is now being placed on the behavior of other fission products in order to develop a more general theory.

Two in-pile loop experiments with loose coated particles in a graphite sleeve have shown particularly favorable overall performance under realistic or perhaps quite unfavorable impurity levels in the coolant. Noble gas release, R/B, values of about 3×10^{-5} for ^{88}Kr were obtained in the first irradiation of nine months duration at 1400°C with coolant oxidizing impurity levels up to several hundred parts per million. The second test,

now under way, is operating satisfactorily with lower impurity concentrations and at lower release levels; however, these two facts may not be related.

This summary highlights important work which has produced particularly significant results during this reporting period. The following pages of the summary provide additional details of this and other work in brief for the convenience of the reader. The format is directly related to that of the body of the report and thus can be followed as an elaboration of the chapter outlines.

1. Fueled-Graphite Development

Pyrolytic-Carbon Coating Studies. Both large and small fuel particles are being considered in fuel element design studies, and therefore the systematic investigation of coating techniques was extended to particles having a nominal diameter of 530 μ. Such particles have much less surface area and require much greater gas flow to maintain fluidization. The charge size and flow rate were adjusted to duplicate the surface area and bed volume of the previous study of 200-μ-diam particles, and it was determined that the higher flow rates actually smoothed the axial temperature gradient in the fluidized bed. Results from a series of coating runs at temperatures between 1300 and 2000°C indicated that at 1300°C coating efficiencies were so low that it became impractical to utilize methane as a source of hydrocarbon for coating large particles. At higher temperatures the coatings were quite similar to those deposited on smaller particles. The higher flow rates required with large particles permitted deposition of isotropic types of coatings at rates as high as 650 μ/hr, that is, much higher than with the smaller particles.

More than 100 coating runs on 200-μ-diam particles in a 2-in.-diam coating apparatus were completed as part of another such systematic study. Crystallite size and anisotropy factors for these deposits are quite consistent with results from the smaller apparatus. Measurements of all coating densities will permit complete analysis of the results.

The conditions for depositing porous coatings of the type that appear best as inner coating layers were also investigated. A study of the

effects of the exothermic pyrolysis of acetylene, which may cause a temperature rise of 200°C or more during a coating run, indicated that precise control of the temperature was impractical. The results of a series of runs confirmed that high acetylene supply rates are essential for depositing low-density coatings. Under optimum conditions, deposits having densities of 0.6 to 0.8 g/cm^3 could be formed at rates as high as 60 μ/min at coating efficiencies of 80%. In general these coatings showed large variations in thickness, but average values were reproducible. High-density coatings were deposited over the porous layers without detectable penetration of the pore structure or abrasion of the porous coatings during handling.

The accessible porosity of these coatings, as measured by mercury porosimetry, increased steadily to a maximum of approximately 65% as density decreased from 1.4 to 0.6 g/cm^3. The pore size distribution seemed to be characteristic of the coating density and independent of other conditions. Crushing tests on individual coated particles confirmed that these porous coatings are quite weak and that the crushing load increases in direct proportion to the density.

Results from a series of heat treatments of pyrolytic-carbon coatings showed that isotropic coatings remain isotropic even when heated to 2800°C, while anisotropic coatings deposited at low rates at 1300 and 1400°C become more anisotropic during heating. The density and crystallite size of coatings deposited at 1300°C increased greatly when heat treated, while those of coatings deposited at 1400°C increased slightly, and all coatings deposited at higher temperatures showed little if any change in properties.

Phase Studies and Thermodynamic Data on the UC_2-ThC_2 System. The dilatometer used in previous measurements was recalibrated. Data on additional specimens of $(Th,U)C_2$ essentially agreed with prior results, but cooling curves of ThC_2 showed a dependence on thermal history. Oxygen contamination is suspected. Published data on the high-temperature heat content of UC and UC_2 were compiled and compared with smooth curves derived from mathematical relationships. Equations that provide a smooth

fit to the data were derived and used in a computer program to obtain all thermodynamic functions.

Conversion of Sol-Gel Oxide Microspheres to Carbides. The yield was improved and the time required for conversion of ThO_2 microspheres to ThC_2 was reduced by using a single fin in the rotating crucible. Conversion was complete after 3 hr at 2150°C, and sintering of particles was minimized. Microspheres of $(Th,U)O_2$ could be completely converted under the same conditions but developed large pores near the center of each particle. When converted at 2000°C the porosity was avoided, but most of the particles then contained numerous inclusions of an unidentified phase. Sol-gel UO_2 microspheres could be completely converted after 2 hr at 2000°C or 5 hr at 1700°C but developed gross porosity. On the other hand, fused UO_2 granules could be converted without porosity, which indicates that the residual carbon in sol-gel UO_2 may produce the pores.

Testing and Evaluation of Coated Fuel Particles. Several batches of pyrolytic-carbon-coated UO_2 particles were heat treated at 1900°C for 680 hr and at 2000°C for 500 hr. Fuel migration into the coatings of all batches was slight or even undetectable, with the exception of one batch that had been coated at 1800°C over a porous inner layer. Particles in this batch developed a layer of graphite at the UO_2-carbon interface, and as much as 10 μ of fuel migration into the inner coating was observed. This phenomenon must be attributed to a slight permeability of the outer coating or to the formation of small amounts of UC_2 during deposition of the outer coating.

A previously developed mathematical model for predicting stresses and strains in pyrolytic-carbon coatings of fuel particles was used to perform calculations to investigate the effects of configuration and environment on the expected service life of typical coated particles. Failure of such particles would be expected to initiate at the inner coating surface from the combined effects of fuel-particle swelling and fission-gas pressure or to initiate at the outer surface as the result of anisotropic dimensional changes in the coating. Enriched fuel particles operated to high burnup will normally fail by the first mode, but adequate life may be assured by providing free volume within the coated

particle. On the other hand, fuels with low enrichment or high thorium content may fail by the second mode. Results also show that the release of gaseous fission products from the fuel particle has a minor effect on coating life as long as adequate free volume is provided.

In order to correlate actual performance of coated fuel particles with their behavior as predicted by the mathematical model, ten batches of UO_2 or UC_2 particles with various types of coatings were prepared and evaluated. These are being irradiated simultaneously at two or three different temperatures in a long capsule that contains 28 compartments for individual specimens. Meanwhile, a series of calculations based on the model was made to determine the conditions under which these particles might be expected to fail.

Evaluation of Experimental Fuel Assemblies. Irradiation testing of experimental fuel assembly 14 in GCR-ORR loop 1 was terminated after approximately nine months of operation and 5183 hr at power. The fuel consisted of two types of pyrolytic-carbon-coated particles: pure ThO_2 and $(Th,U)O_2$ having a thorium-to-uranium ratio of 11.9. Pellets of BeO were also included in the assembly. The objectives of the test were (1) to determine the problems associated with fuel elements containing loose particles, (2) to evaluate the performance and fission-gas retention properties of sol-gel oxide cores with pyrolytic-carbon coatings, and (3) to determine the compatibility of BeO and graphite under simulated reactor conditions. One region of the assembly was vented to the loop coolant. Periodic gas samples showed that the noble-gas fission products in the loop gas reached equilibrium and remained constant over periods of constant-temperature operation.

No fission products were found on support structures after irradiation, and the gamma scan of the element showed no unusual radioactivity distribution. Dimensional measurements revealed no changes that could be attributed to irradiation. Particles in the upper compartment, although intact, had some coating surface pits that were probably due to oxidation. Fuel particles in the lower compartment had bluish circular spots on one side and many particles were in clusters of up to ten particles held together by small amounts of reddish-brown or orange material. The BeO

specimens had not changed in appearance. Metallographic examinations are under way.

Experimental assembly 15, which is similar to assembly 14 and contains a mixed bed of pyrolytic-carbon-coated fuel particles, was inserted in ORR loop 1 July 5. This experiment will further the evaluation of loose beds of coated particles under conditions that simulate service in a TARGET reactor. An effort will be made during this experiment to characterize the radioactive species other than noble gases that are transported in the loop coolant.

High-Burnup Coated-Particle Experiment in ORR Position F-9. A capsule containing pyrolytic-carbon-coated UO_2 and UC_2 particles is being irradiated for an evaluation of fission-product retention and overall stability at burnups up to 50% heavy metal at temperatures between 1100 and 1400°C. The burnup is being limited to 10% per month, and the total irradiation time will be 225 days.

Compatibility of Oxide Fuel Pellets and Graphite Under Irradiation. Bare $(Th,U)O_2$ pellets in a graphite structure are being irradiated to study the effect of fuel pellet swelling on the graphite structure at high burnups, fuel-graphite compatibility at TARGET conditions, and fission-gas release. In future experiments a wide range of pellet densities and powers will be examined. The pellets for the first capsule (05-10) were supplied by General Atomic.

Coated Particle Irradiations in LITR. Irradiation of capsules L-CP9 and L-CP10 containing coated UC_2 particles was completed, and a similar capsule, L-CP11, was assembled for irradiation. Irradiation of capsule L-CP11 will complete the present series of LITR coated-particle irradiations.

2. Investigations of Fueled-Graphite Systems

Instantaneous Fission-Gas Release Experiments. Fission-gas release from UO_2 during irradiation does not occur by a simple diffusion and recoil process. The principal release at low temperatures (below ~600°C) is by a knock-out process rather than direct recoil. This is indicated

by the relative proportions of isotopes in the fission gas during steady-state operation, by the dependence on total surface area, and by a phase shift and hysteresis in the release during dynamic operation.

The fission-gas release at higher temperatures is controlled by a trapping process. A defect-trap model can be used to explain, at least quantitatively, all the phenomena of fission-gas release observed during in-pile experiments. Grain boundaries behave as defect traps, as predicted by the model.

The interpretation of the experimental observations is complicated because the fission gas must pass through the surface of the UO_2 specimen. Thus, surface conditions, as well as migration within the specimen body, affect fission-gas release. The model suggests that only a thin surface region is involved in the fission-gas release process at temperatures below 1500°C. However, the depth of the surface layer is yet to be determined, and indeed this depth may vary with temperature.

The mathematical model contains several unknowns — too many for evaluation by steady-state experiments — and therefore dynamic experiments are under way. No quantitative conclusions have yet been obtained from the dynamic experiments, but the oscillation method appears promising, and the qualitative results support the defect-trap model. Experiments are still in progress, and refinements are to be expected as additional data are accumulated.

Fission-gas release rates were measured during irradiation of ten capsules containing pyrolytic-carbon-coated fuel particles. Eight capsules contained particles with uranium oxide cores, and two capsules contained particles with thorium-uranium carbide cores. Fractional fission-gas release rates were in the 10^{-8} range for the triplex-coated oxide-core particles irradiated to 25.2% burnup at 1600°C. A direct relation between coating contamination was found based on alpha count and fission-gas release. Postirradiation metallographic examination revealed that particles with a porous carbon layer between the core and pyrolytic-carbon coating had little or no damage from fission fragments at the core-coating interface. The coating that consisted of an inner layer of low-density isotropic pyrolytic carbon followed by a higher density

isotropic layer also had little damage because of the formation of a gap caused by shrinkage of the inner layer.

Fission-Product Release from High-Burnup Coated UC_2, $(Th,U)C_2$, and UO_2 Particles by Postirradiation Annealing. Postirradiation annealing studies are being conducted on irradiated coated fuel particles to determine the stability of the coatings and to measure their ability to contain fission products at temperatures higher than the irradiation temperature (up to 2000°C). A comparison between $(Th,U)C_2$ triplex pyrolytic-carbon-coated particles irradiated to different burnups indicated some changes that might be attributed to burnup. The particles irradiated to 8.9% burnup had 2% coating failures during the first hour of annealing at 1700°C and at 2000°C, while the particles irradiated to 0.29% uranium burnup had no failures during 19 hr at 2000°C. Barium and strontium fission-product release was lower for the higher burnup.

Duplex-coated UO_2 particles with an outer coating density of 1.8 g/cm^3 had high rates of release of barium and strontium during annealing.

Fission-Product Transport and Deposition. Additional experimental data indicate that for simple flow geometry it will be possible to predict fission-product deposition from turbulently flowing helium reasonably well by the heat-mass analogy, provided the deposition surface acts as a perfect sink for the fission products. Additional deposition and desorption tests were run to compare silver, stainless steel, and carbon steel surfaces.

A small experimental assembly for fission-product deposition studies was constructed in which the progression of depositable fission-product species through a packed bed of spheres can be followed by gamma-ray scanning. Studies will be made of the physical and chemical conditions under which fission products deposited from a helium stream onto various surfaces will reenter the gas stream and deposit farther downstream.

Further development of an analytical model for fission-product deposition indicated that the equilibrium solution for a connecting system approaches that of a static system. This conclusion implies that by establishing the surface chemistry of fission-product mixtures through

systematic static tests, the limiting contamination levels for actual operation under flow conditions can be predicted.

Sorption of Fission-Product Vapors on Structural Metals. Much work has been done on the deposition behavior of iodine, and the elemental form has been assumed to be the depositing species. A computer program was developed recently that utilizes equilibrium constants evaluated with available thermodynamic information and calculates the fraction of iodine in the more reactive monoatomic form. The results indicate that at 500°K and an iodine pressure of 10^{-12} atm, 90% of the iodine may be in the atomic form. Fractional dissociation increases with higher temperature and lower iodine concentration. Fractional dissociation is displayed graphically versus temperature (0 to 1700°C) for iodine pressures from 1 to 10^{-12} atm.

Compatibility of Pyrolytic-Carbon-Coated Fuel Particles with Water Vapor. Data are presented for the compatibility of seven batches of pyrolytic-carbon-coated fuel particles with partial pressures of water vapor of 4.5, 45, and 567 torr at 1000°C for exposure periods of 1 to 28 hr. Reaction rates for the carbon-water vapor reaction obtained from weight changes are given along with the incidence of failure of coatings determined from acid leaching of uranium and thorium. Surface areas determined by the BET method are presented for unoxidized and oxidized fuel particles.

Recoil of Fission Products in Pyrolytic Carbon. A study of the recoil of fission products in pyrolytic carbon to determine fission-fragment distributions in pyrolytic-carbon targets after exposure to fragment beams was initiated. The experimental conditions of the target specimens simulate those in coatings on oxides. Preliminary measurements indicate a recoil range of 11.4 μ for ^{140}La in dense pyrocarbons.

3. Studies for AVR — German Pebble-Bed Reactor

The remaining work for AVR has involved irradiation testing and evaluation of coated particles and spheres. Final irradiation data and results of postirradiation examinations are presented for capsules 05-8

and F1-8B5, which contained $(Th,U)C_2$ fuel, and capsule O1A-8, which contained UC_2 fuel.

Fueled Sphere Experiments — Capsule O5-8. Capsule O5-8 contained three 6-cm-diam graphite-matrix spheres manufactured by the 3M Company and fueled with laminar-coated $(Th,U)C_2$ particles. The fuel was irradiated to about 8% burnup, and no failures were found in the particles examined from two spheres. Wedge-shaped fractures originating at the fuel-coating interfaces were found in the coatings; in some cases, they extended about one-third through the coating. Some delamination of the coatings, swelling of the fuel core, and loss in fuel crystalline detail were noted. When this capsule was disassembled, it was found that the No. 1 position sphere was broken. A preirradiation radiograph showed that the thermowell hole was probably not drilled normal to the surface of the sphere, and as a result the thermowell cracked when inserted into the hole. It is not likely, however, that this caused sufficient strain to crack the sphere.

Eight-Ball Capsule F1-8B-5 Experiment. Postirradiation examinations were completed on capsule F1-8B-5 containing eight 1 1/2-in.-diam fueled-graphite spheres irradiated to 25% heavy metal burnup, the highest burnup of any of the fueled spheres. The shrinkage of the molded spheres was predictably large, and the compression strength of those having machined shells (which do not shrink appreciably) with molded cores was poor due to lack of bonding between the cores and shells.

Four spheres were examined metallographically. The enriched-uranium laminar-coated 3M fuel particles in two of these spheres had failed extensively (100% of those examined in one sphere and 67% in the other). The failures of these 3M particles irradiated to 25% burnup are in contrast to the behavior of the 3M particles in capsule O5-8, described above, which showed no failures after 8% burnup. The laminar-coated natural uranium particles in the same sphere were the first unenriched particles yet observed to show spear-head fractures at the core-coating interfaces. The triplex-coated GA particles examined showed no failures or potential failures, and similarly the NCC duplex-coated particles showed no failures.

The fuel in the NCC particles was amorphous in appearance and showed considerable swelling.

AVR Prototype Sphere Experiments – Capsule 01A-8. The 6-cm-diam spheres contained in capsule 01A-8 were prototypes of AVR spheres manufactured by the Carbon Products Division of Union Carbide. The burnup was 8 to 10% heavy metal. Compression testing of one unirradiated and two irradiated spheres from this capsule indicated that bonding of the cores and shells was marginal, but apparently acceptable, since the central thermocouple of No. 1 sphere indicated reasonable heat transfer from core to shell during irradiation. Both unirradiated controls and irradiated particles from these spheres showed that some of the particles had inclusions in the fuel cores. The particles with inclusions had irregular surfaces at the fuel-coating interfaces that resulted in an inner coating of varying thickness that was generally thinner than the coatings of particles with no inclusions. Over 500 particles were examined from the three spheres. No failures were found. Wedge-shaped fractures at fuel-coating interfaces penetrated deeper into the coatings of the particles that had the inclusions.

Evaluation of Fueled-Graphite Spheres. Analyses of the results of all irradiation tests on 6.0-cm and 1 1/2-in.-diam spheres indicate that molded fueled-graphite spheres shrink at significantly higher rates than do spheres with fully graphitized type-ATJ-graphite unfueled shells. In spheres having such machined shells, differential shrinkage between the molded core and unfueled shell occurred in some cases. The resulting gap caused an increase in the temperature of the fueled core and a marked reduction in the crushing load of the sphere. Further development work on the properties of the fueled core are indicated if the machined shell concept is to be fully utilized. Measurements of thermal conductivity on three spheres gave values between 0.15 and 0.20 w/cm·°C at 1000°C and indicated that the conductivity decreases with increasing temperature.

4. Investigations of Moderator Materials

Thermal Conductivity of AGOT Graphite. The thermal conductivity of AGOT graphite was measured over a range of temperatures up to 900°C, and

the data were compared with results on CGB graphite. The data on AGOT will be used to evaluate results from EGCR surveillance specimens.

Dimensional Stability of AGOT Graphite. The dimensional instability of AGOT graphite, which is associated with its anisotropic thermal expansion and deformation during thermal cycling, was investigated. The plastic strain of specimens subjected to a constant tensile stress during a thermal cycle was quite close to that predicted by theoretical relationships. The measured values indicate a greater increase in plastic strain with increasing temperatures than the theoretical curve, which suggests that the plastic behavior changes with temperature.

Creep of Graphite Under Irradiation. In-pile testing of AGOT moderator graphite at temperatures of 130 to 370°C showed that irradiation-induced creep is consistent with a theoretical model and enables graphite to accommodate strains greater than 0.8% without fracturing. Special attention was required at the lower temperatures in order to distinguish the plastic deformation from differential growth, which is caused by a 10% flux gradient across the specimens.

Deposition of Carbon on ATJ Graphite. Gas mixtures containing helium, water vapor, and methane were contacted with ATJ graphite to determine the rate of carbon deposition on the graphite surface. A water vapor concentration of 110 ppm and methane concentrations of 100 to 700 ppm were employed at temperatures of 700 to 850°C. A comparison of the results with those obtained with helium-methane mixtures showed that water vapor had little effect on the decomposition rate of methane. The presence of methane was found to retard the water vapor—graphite reaction.

Studies were also made of the disproportionation of carbon monoxide on ATJ graphite. Carbon monoxide concentrations of 120 to 1500 ppm in helium were used at temperatures of 550 to 850°C. Low rates of carbon deposition were observed, with a maximum rate occurring at approximately 750°C.

BeO-Graphite Compatibility. Irradiation of the Mark II BeO-graphite compatibility test capsule is continuing. This capsule was designed to evaluate the overall feasibility of using BeO in a TARGET-type reactor as a means of increasing the conversion ratio.

Failure Characteristics of EGCR-Type AGOT Graphite. The program of tests for determining the failure characteristics of EGCR-type AGOT graphite is essentially completed. Experimental studies were made of crack propagation and multiaxial stress states. The data were correlated with the Griffith-Irwin fracture mechanics concept, which involves the principle and practice of controlling brittle fracture by limiting the stress to a value compatible with defect size.

The applicability of Weibull's statistical theory of strength to EGCR-type AGOT graphite fracture data was investigated. Weibull's theory attempts to account for variations in observed fracture strength by treating the strength as a statistical variable. The theory is complete in the sense that, given a sufficient amount of laboratory data on a particular material, the probability that a component will fail under a given set of service conditions can be calculated. In order to test Weibull's theory according to mathematically sound statistical methods, fracture data for four samples (approximately 30 specimens each) were used. Some of the statistical methods were standard, but the complete investigation depended on methods we developed recently. The study demonstrated conclusively that EGCR-type AGOT graphite fracture data are distributed according to a Weibull distribution function; however, the weakest-link hypothesis and therefore the strength-volume relationship are not valid.

Graphite exhibits considerable variability of mechanical properties even within the same block, and consequently ultimate strength values used in graphite component design could be increased safely if there were a method for determining the portions of a specific block most capable of sustaining the highest stresses without failing. In order to test this possibility, strength, hardness, and density measurements were made. The data indicate that with sufficient sample size the initial modulus of elasticity, density, and hardness all correlate fairly well with strength properties. It thus appears possible to use nondestructive means to choose the stronger components of EGCR-type AGOT graphite from a given set.

Compressive modes of failure were also investigated. Specimens cut in the parallel direction were tested, and where complete failure occurred

there was a series of jagged cracks running vertically and diagonally through the specimen; no vertical splitting occurred. These tests showed that end conditions had affected previous test results and that the end restraint had been reduced.

In most design applications, graphite is subject to triaxial stresses, and the most likely mode of failure is either cracking or spalling at a surface at which the state of stress is biaxial or almost so. In order to analyze these stresses, the behavior of graphite under multiaxial stress states and the applicability of uniaxial properties to the investigation of this behavior are being determined.

5. Studies for Advanced Systems

Fuel Cycles for Fission-Product-Releasing Fuel. The effect on high-temperature gas-cooled reactor conversion ratios of using fuel that rapidly releases the volatile fission products instead of retaining them was investigated. The reference design was the TARGET reactor. The net conversion ratio decreased at long burnup because of accumulation of slowly saturating fission products and at very short burnup because of excessive processing losses. At 50,000 Mwd/T the releasing fuel had a conversion ratio 0.07 higher than that of retaining fuel. No doubling times of less than about 21 years were found. Fuel-cycle costs for releasing fuels optimized at higher burnups than for retaining fuels. The releasing fuels gave 0.2 to 0.3 mills/kwhr(e) lower fuel costs than the retaining fuels. Further the releasing fuels always optimized with conversion ratios above 1.0, whereas the retaining fuels nearly always optimize below 1.0.

Analyses of Nozzle-to-Spherical Shell Attachments. The first phase of the experimental work on analyses of nozzles attached to spherical shells was completed. Comparisons showed that the experimental results were well approximated by theoretical analyses.

6. Fast Reactor Development

An irradiation test program was initiated in support of the development of fuel elements for the fast gas-cooled reactor. The General Atomic

fast gas-cooled reactor design was used as the first reference in the selection of test parameters. One capsule is being irradiated in the ORR poolside facility and another is being prepared for irradiation.

2. Experimental Gas-Cooled Reactor Program

7. Performance Analyses

Reactor Commissioning Program. Assistance was given to the Tennessee Valley Authority physics staff in tasks relative to final safety reviews of the EGCR and preparations for the physics commissioning experiments. A series of experiments was performed with the unfueled core, and analyses of the results are under way.

Graphite-Air Oxidation Studies. Additional investigations were completed of various situations following a rapid depressurization of the EGCR primary cooling system. A study of circumferential ruptures in the primary loops and emergency cooling loop piping and nozzles was made to determine the worst effects on the core. It was found that the emergency cooling loop, if used before the core has been cooled by some other means, may allow excessive core temperatures from uncontrolled graphite oxidation because of purge ineffectiveness or allow hot-leg temperatures above design criteria, even with no graphite oxidation heat generation, because of high core bypass flow. Main blower operation for 10 to 15 hr is sufficient for all ruptures considered except catastrophic ruptures of the hot-leg nozzles that allow flow bypass through the temperature barrier. As the bypass flow increases to a limit of about 25% of the total flow, the main blower operating time increases to about four days. The effects of increased oxidation rate, higher initial temperatures, and increased oxidation depth on air flow required to control graphite oxidation were also studied.

8. Component Development and Testing

Compressor Shaft Seals. Operation of the shaft seals of the EGCR main blowers during acceptance testing indicated serious spillover of the seal buffering water into the bearing lubrication system when the shaft was stationary and into the reactor primary coolant when the shaft

was rotating and the reactor system was either depressurized or at subatmospheric pressure. The first difficulty also occurred with the vessel cooling compressor. The spillover of the seal buffering water into the bearing lubrication system was eliminated without making any major changes to the compressors or the seal water system with the addition of a slinger ring outboard of the atmospheric seal, a "visco"-type seal, and a water leg in the seal water system. Spillover into the reactor primary coolant was eliminated with a visco-type seal that occupies the same space and has the same radial clearance to the shaft as the existing labyrinth.

Control-Rod Drive Test. An endurance test was run on the first production-model control-rod drive. The test program required that the mechanism be operated in helium through 130 full insertion-withdrawal cycles, 2000 insertion-withdrawal cycles over 4 in. of rod travel, and 1400 scram cycles. The performance of the mechanism was entirely satisfactory and in all cases met or exceeded specified design requirements.

Charge-Machine Cylinder-Seal Development. A dynamic seal is being developed for the actuating cylinders in the EGCR charge machine. Tests have indicated that the most important design parameters to be considered are lubricity of the seal mating surfaces and the compression set and stress relaxation properties of the material.

Experimental Studies of Steam-Graphite Reactions. Rates of graphite reaction and hydrogen generation resulting from exposure of EGCR core graphite to superheated steam were correlated with a modified Arrhenius-type equation that describes the reaction rate as a function of temperature and burnoff.

Special Fuel Assemblies for Flux Mapping. Assistance was given to the EGCR operating group in the design and preparation of ten special fuel assemblies to be used for flux mapping experiments.

Analysis of Failure of 42-in. Bellows Between EGCR Containment Shell and Experimenter's Cell. One 42-in.-diam stainless steel bellows at the EGCR developed several leaks, and another bellows in a similar location showed corrosive attack but had not failed. Evaluation of samples established that the failure was the result of a pitting type of attack that is

often associated with chloride ions. The chloride may have come from $CaCl_2$ in the concrete around the bellows.

9. Irradiation Testing of Components and Materials

EGCR Prototype Fuel Tests. Capsule 04-8, which contains prototype-diameter specimens of EGCR fuel and cladding supplied by the fuel-element vendor, is being irradiated. Similar capsules irradiated previously were examined. Except for capsule E-3, which showed extensive cladding deformation and two fractures, no damage was found. Capsule E-3 contained solid UO_2 fuel pellets and had been subjected to unusually high irradiation temperatures.

Pressure-Vessel Surveillance Program. Preparations for insertion of surveillance specimens in the EGCR pressure vessel are nearing completion. Trial loading of a completed surveillance string indicated the need for minor modifications to the removal cask and to the pressure-cap linkages of the strings.

A fast fracture analysis of the EGCR pressure vessel indicated that none of the postulated flaws could initiate fast ductile failure. Tensile tests of specimens irradiated in the ORR at elevated temperatures are in progress.

PART 1. ADVANCED GAS-COOLED REACTOR PROGRAM

1. FUELED-GRAPHITE DEVELOPMENT

J. H. Coobs O. Sisman
H. C. McCurdy

Pyrolytic-Carbon Coating Studies

Coating of Large Particles with Methane in 1-in.-diam Fluidized Beds (H. Beutler, R. L. Beatty)

A previous systematic investigation[1] of the effects of varying deposition conditions on the properties of pyrolytic-carbon coatings provided a basis for further coating studies and for the preparation of irradiation test specimens. The initial investigation was limited to the coating of 200-μ (nominal diameter) uranium carbide particles, but in consideration of coating economy and a potentially higher fuel-to-coating volume ratio it is also necessary to have the capability of coating larger particles. Therefore, we investigated the problems concerned with the application of pyrolytic-carbon coatings to 530-μ (nominal diameter) uranium carbide particles in a 1-in.-diam fluidized bed and the problems involved in the control of coating properties such as density, anisotropy, crystallite size, and microstructure.

In the earlier experiments the significant controllable variables were deposition temperature and the rate of supply of methane relative to charge surface area. Other variables, such as contact time and axial temperature gradients, were not considered unimportant but were held constant for each deposition temperature. However, the fluidizing gas flow requirement increases with larger particles, and thus a significant decrease in contact time is effected if the gas velocity is sufficient to expand the fluidized bed to the same height as the small-particle bed. Furthermore, the decrease in surface area relative to gas volume throughput that accompanies an increase in particle size necessitates a change in methane concentration if the methane supply rate relative to charge

[1]R. L. Beatty and F. L. Carlsen, Jr., Coatings Deposited from Methane in Fluidized Beds, pp. 3–9, GCRP Semiann. Progr. Rept. Mar. 31, 1965, USAEC Report ORNL-3807, Oak Ridge National Laboratory.

surface area is to be maintained constant. This introduces the possibility of obtaining a concentration effect superimposed on the supply rate variable.

Selection of Charge Size and Total Flow Rate. The given coater capacity (approximately 35 cm^3) limits the final volume of the charge, and the original charge volume depends, therefore, on particle size, coating thickness, and expansion of the bed due to fluidization. For example, if a 100-μ coating is applied to 200-μ particles, the volume increase is eightfold as compared with a threefold increase in charge volume if the same 100-μ coating is applied to 500-μ particles. In view of this increased weight capacity of the coater for the larger particles and the desirability of maintaining a total charge surface area comparable with that of the 25-g charges used in the earlier study, we used a standard charge of 50 g for all experiments involving the 530-μ particles.

We determined suitable fluidizing conditions experimentally by measuring the expansion of the fluidized bed at various helium flow rates ranging from 2000 to 6500 cm^3/min. The axial temperature profile and the bed height were measured simultaneously by inserting an unsheathed thermocouple probe (94% Pt–6% Rh vs 70% Pt–30% Rh) into the fluidized bed to a point near the gas inlet orifice and withdrawing it in 1/2-in. increments while the thermocouple signal was recorded. Temperature fluctuations caused by intermittent impact of hot particles on the thermocouple junction were observed during most of the immersion. The largest temperature fluctuations were noted in the lower part of the bed where, presumably, the particles were significantly hotter than the surrounding gas. As the thermocouple was raised, the fluctuations decreased until a region of uniform temperature was reached near the center of the fluidized column. Above this point the fluctuations again appeared and increased toward the top of the bed, where the particles were apparently cooler than the surrounding gas. The upper boundary of the fluidized bed was clearly defined by the sudden cessation of fluctuations in the thermocouple signal. These measurements of bed height showed that a gas flow rate of 4 liters/min was necessary with a 50-g charge of 530-μ particles in

order to duplicate the expansion of a 25-g charge of 200-μ particles with a total flow rate of 2.5 liters/min.

We should point out that this technique for measuring bed height applies only where a large axial thermal gradient exists in the coating tube, as is the case when a water-cooled gas injector is used. If the injector is not water cooled and the fluidizing chamber is essentially isothermal, the output of an immersed thermocouple will not fluctuate.

Effect of Axial Temperature Profile. The results of the measurements of axial temperature profiles are presented in Fig. 1.1. The significance of these profiles with regard to control of the deposition temperature cannot be overemphasized. In all cases the reference pyrometer reading on the reaction tube surface 2 in. above the gas inlet orifice was held constant at 1500°C. However, since most of the coating deposition occurs in the lower 2 in. of the chamber, the true deposition temperature is quite dependent on the total gas flow rate and on the volume of charge in the coater when a "gradient bed" is used. The term "gradient bed" refers to the existence of an axial temperature gradient resulting

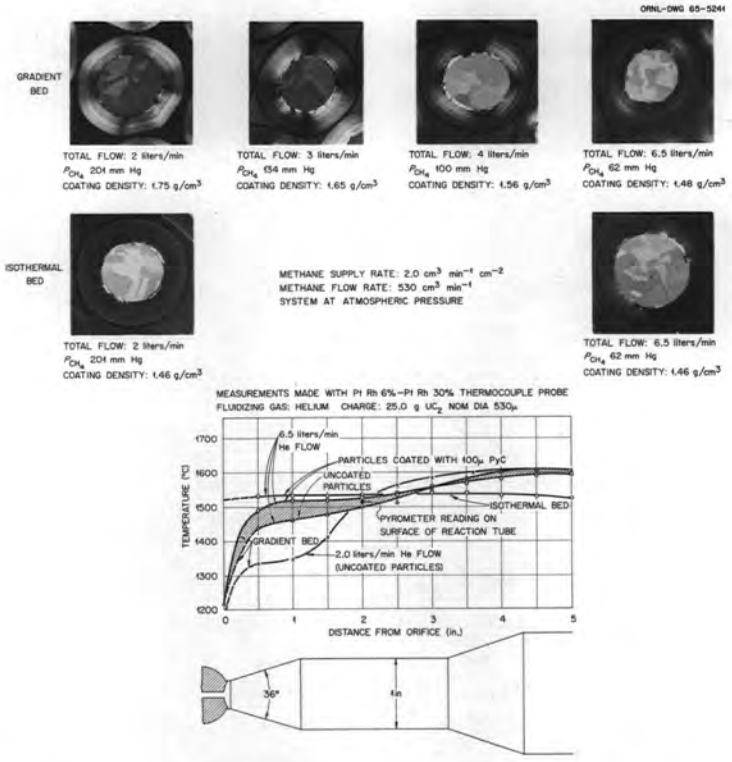

Fig. 1.1. Effect of Fluidizing Gas Flow Rate and Bed Volume on Temperature Distribution in a Fluidized Bed of UC_2 Particles.

from the use of a water-cooled gas injector. The three curves in Fig. 1.1 that represent gradient-bed profiles show that the actual coating temperature was raised approximately 100°C by increasing the gas flow rate from 2.0 to 6.5 liters/min and was further increased approximately 50°C by application of a 100-μ coating. The use of a 50-g charge rather than a 25-g charge would have an effect similar to that of applying the coating. On the other hand, in an isothermal bed, which is characterized by an uncooled graphite injector, the temperature profile does not change with increasing gas flow or with increasing charge size. Hence, only one curve is shown.

It may also be seen from Fig. 1.1 that increased bed expansion not only raises the actual coating temperature in a gradient bed but improves axial temperature uniformity as well. The point to be emphasized is that when using a fluidizing chamber in which an inherent axial temperature gradient exists, the selections of the fluidizing gas flow rate and the charge size are extremely important if the true coating temperature is to be known and controlled. Obviously temperature control can be assured only if proper calibrations are made. Failure to fully appreciate the potential error in temperature "measurement" in fluidized-bed coaters may account for many of the discrepancies in results reported by various investigators. A typical example of the dependence of coating properties on total gas flow rate (actually on deposition temperature) in a gradient bed is clearly shown by the upper series of photomicrographs in Fig. 1.1. Similarly, the lack of property dependence on flow rate when using an isothermal bed is shown by the lower two photographs.

A further complication in obtaining accurate, reproducible data on pyrolytic-carbon coatings deposited in a gradient bed is the inherent gradual temperature increase during the coating run. If this increase is not compensated for by gradually decreasing the reference temperature, a radial gradation in coating properties could result that would preclude defining coating properties as functions of any particular process variables.

It is apparent from these results that an isothermal bed should be used where possible in order to take advantage of the better temperature

definition. However, when methane is used as the carbon source, the upper temperature limit of the isothermal bed is 1600°C. Above this temperature the gas inlet orifice blocks quickly and it is necessary to use a gradient bed.

Coating Procedure and Property Measurements. After completing the study of flow rates and the effects of thermal gradients, we coated a series of 50-g charges of the 530-μ-diam UC_2 particles in a 1-in.-diam resistance-heated graphite coater. Five graphite disks, 3/16 in. in diameter, were included with each charge to provide specimens for measurement of coating properties.

Deposition temperature and methane supply rate relative to the initial surface area of the charge were the controllable variables studied. The deposition temperatures ranged from 1300 to 2000°C in increments of 100°C. From 1300 to 1600°C, inclusive, an isothermal bed having an uncooled graphite gas injector was used, while at higher temperatures a gradient bed was employed.

Coatings were deposited in runs covering a methane supply rate range from 0.06 to 6.0 $cm^3/min \cdot cm^2$ with a total gas flow rate of 4 liters/min. The surface area on which the methane supply rate was based was a value calculated from the mean particle diameter of 530 μ and a measured density of 10.7 g/cm^3. The duration of each run was adjusted to produce coatings about 70 μ thick.

Densities of the coatings deposited on the particles were measured. The technique consisted of measuring the density of the coated particles with a helium densitometer and then burning the carbon-coated UC_2 particles to U_3O_8 in oxygen while collecting the evolved CO_2 to determine the total weight of carbon present in the sample. Coating densities were then calculated based on previously determined values for the density and carbon content of the base carbide particles.

Examination of the coated-disk specimens indicated that the 3/16-in.-diam disks did not circulate properly in the fluidized bed under these conditions. In most runs the coatings on the disks were much thinner than on the particles, probably because the disks tended to float on top of the bed. Therefore, the disk specimens were not considered representative

of the particle coatings. However, anisotropy factors for the various coatings were estimated by visual analysis of the polarized light photomicrographs shown in Fig. 1.2. This method of estimating coating anisotropy was developed during an earlier study[1] in which it became apparent that the intensity of the Maltese cross shown by polarized illumination of a cross section of a spherical particle coating could be correlated with x-ray anisotropy measurements[2] if coating texture were taken into account.

Results and Discussion. The results of all experiments included in this study are presented in Table 1.1. Estimated values of apparent crystallite size are included for reference. In the previous systematic study this property was found to depend on deposition temperature and flow rate in a very predictable manner.

The coating density values listed in Table 1.1 and shown as a contour plot in Fig. 1.3 are in good general agreement with densities obtained on coatings applied to 200-μ-diam particles. The highest densities are achieved at 1300°C with a high methane supply rate and at 2000°C with an intermediate methane supply rate. A low-density region shown as a valley on the contour plot extends from the area of maximum supply rate at 1600°C to the lower supply rates at 1300°C. The occurrence of high-density regions on either side of a low-density trough suggests that two basically different deposition mechanisms are involved.

The decrease in density from intermediate to low methane supply rates at the higher temperatures is inexplicable from the standpoint of any conceivable deposition mechanism. However, we believe that this decrease in density with decreasing supply rate is a real effect and is due to the temperature gradient in the fluidized bed. As the deposition temperature is increased the zone in which most of the coating occurs moves progressively downward, while depletion of the hydrocarbon occurs at progressively lower levels in the bed as the methane supply rate is decreased. Thus, as the methane supply rate is decreased at constant temperature

---

[2]F. L. Carlsen, Jr., Examination of Pyrolytic-Carbon Coatings Using X-Ray Diffraction Techniques, pp. 6–16, GCRP Semiann. Progr. Rept. Sept. 30, 1964, USAEC Report ORNL-3731, Oak Ridge National Laboratory.

PHOTO 80758

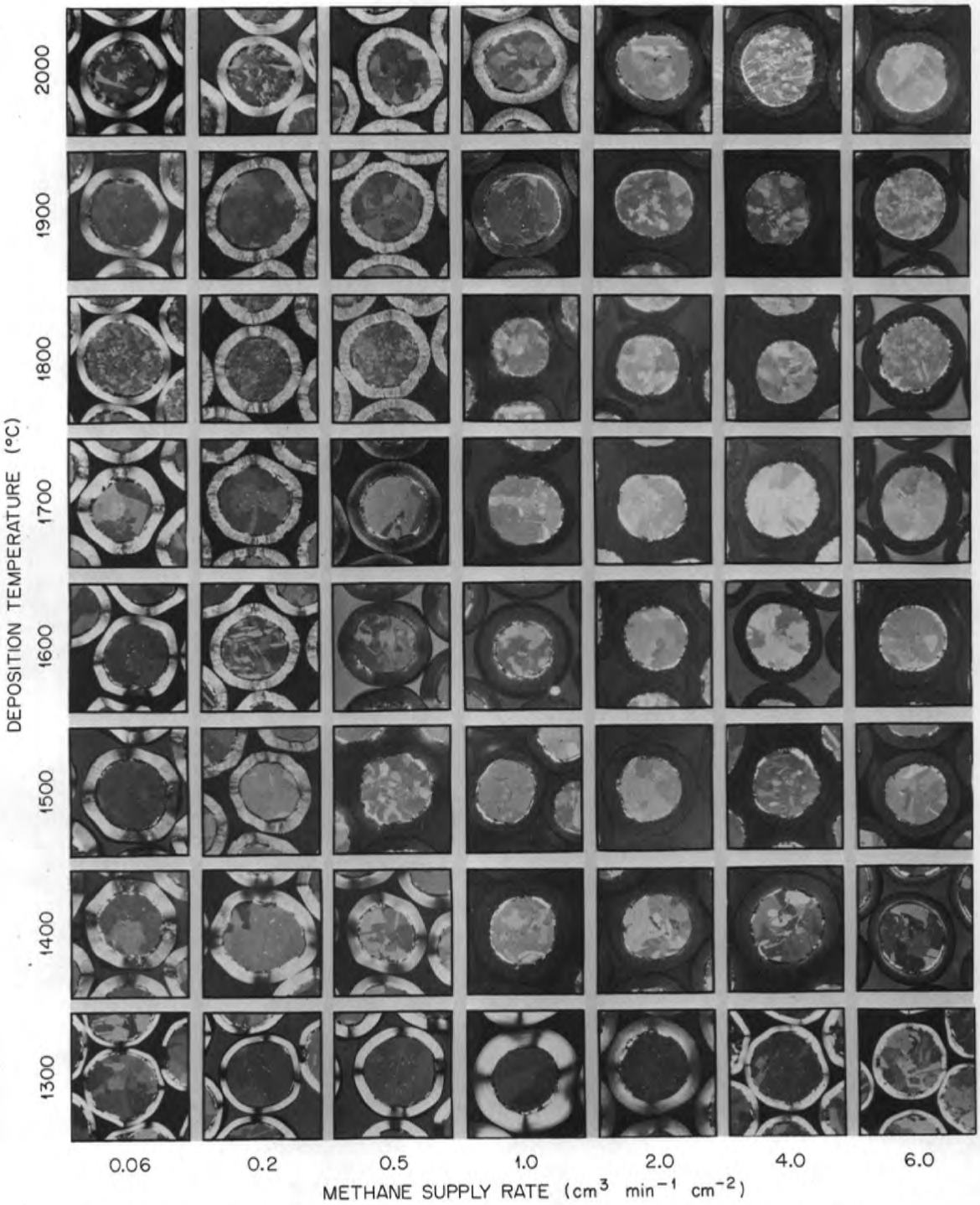

Fig. 1.2. Effect of Deposition Conditions on Microstructure of Pyrolytic-Carbon Coatings Applied to 530-μ-diam UC_2 Particles. As polished; polarized light.

Table 1.1. Deposition Conditions and Properties of Pyrolytic-Carbon Coatings Applied to 530-μ-diam Uranium Carbide Particles

Deposition Temperature (°C)	Run	Methane Partial Pressure[a] (torr)	Methane Supply Rate ($cm^3/min \cdot cm^2$)	Average Deposition Rate (μ/hr)	Deposition Efficiency (%)	Coating Density[b] (g/cm^3)	Apparent Crystallite Size[c] (A)	Anisotropy Factor,[d] σ_{oz}/σ_{ox}
1300	G13-7	6	0.06	1.7	19.4	1.62	35	3.0
	-1	20	0.2	5.0	17.1	1.54	35	3.0
	-2	50	0.5	13.4	21.6	1.86	35	3.0
	-3	101	1.0	23.0	25.5	1.87	35	2.0
	-4	201	2.0	47.1	23.7	2.02	30	1.5
	-5	402	4.0	45	8.7	2.26	30	1.5
	-6	604	6.0	61.2	6.0	2.26	30	1.5
1400	G14-7	6	0.06	4.6	60.1	1.59	45	2.0
	-1	20	0.2	15.7	62.6	1.69	40	2.5
	-2	50	0.5	27.6	(e)	1.56	35	2.0
	-3	101	1.0	71.9	54.7	1.49	35	1.0
	-4	201	2.0	117	46.0	1.66	30	1.0
	-5	402	4.0	214	44.8	1.61	30	1.0
	-6	604	6.0	263	35.3	1.81	30	1.0
1500	G15-7	6	0.06	5.3	76.7	1.76	70	1.8
	-1	23	0.2	20	69	1.73	60	1.5
	-2	50	0.5	48.3	73	1.74	55	1.2
	-3	101	1.0	100	68	1.65	50	1.0
	-4	203	2.0	190	70	1.46	40	1.0
	-5	402	4.0	359	(e)	1.55	35	1.0
	-6	610	6.0	440	58	1.65	35	1.0
1600	G16-7	6	0.06	5.2	73.8	1.90	90	1.8
	-1	20	0.2	18.2	78.5	1.84	85	1.5
	-2	50	0.5	51.5	79.6	1.60	80	1.2
	-3	101	1.0	97.1	76.7	1.67	65	1.0
	-4	201	2.0	230	77.4	1.53	55	1.0
	-5	402	4.0	442	69.8	1.40	45	1.0
	-6	604	6.0	615	63.9	1.50	40	1.0
1700	W17-7	6	0.06	5.3	84.5	1.93	110	1.8
	-1	20	0.2	20.5	87.3	1.93	110	1.5
	-2	50	0.5	48.4	83.3	1.80	100	1.2
	-3	101	1.0	103	88.0	1.73	95	1.0
	-4	201	2.0	227	72.1	1.65	70	1.0
	-5	402	4.0	431	74.3	1.49	60	1.0
	-6	604	6.0	626	76.5	1.50	50	1.0
1800	W18-7	6	0.06	4.3	68.0	1.96	130	2.0
	-1	20	0.2	17.3	91.2	1.88	120	1.8
	-2	50	0.5	44.4	88.5	1.87	110	1.4
	-3	101	1.0	98.6	88.4	1.82	100	1.1
	-4	201	2.0	191	85.7	1.80	90	1.0
	-5	402	4.0	440	88.1	1.67	80	1.0
	-6	604	6.0	662	80.0	1.60	70	1.0
1900	W19-7	6	0.06	3.8	64.7	1.96	140	2.5
	-1	20	0.2	16.6	92.8	2.02	130	1.8
	-2	50	0.5	43.3	90.0	2.08	120	1.4
	-3	101	1.0	91.9	88.0	1.85	110	1.1
	-4	201	2.0	182	85.0	1.78	100	1.0
	-5	402	4.0	393	86.5	1.72	90	1.0
	-6	604	6.0	668	88.3	1.69	80	1.0
2000	W20-7	6	0.06	4.2	61.2	2.01	150	3.0
	-1	20	0.2	17.3	73.6	1.99	140	2.0
	-2	50	0.5	38.3	80.0	2.08	130	1.4
	-3	101	1.0	86.9	89.7	2.16	120	1.2
	-4	201	2.0	186	82.7	1.91	110	1.0
	-5	402	4.0	366	73.8	1.79	100	1.0
	-6	604	6.0	611	77.9	1.91	90	1.0

[a]System at atmospheric pressure.

[b]Determined by helium densitometer burnoff method on particles.

[c]Estimated from results of a previous study.

[d]Estimated from visual analysis of photomicrographs of Fig. 1.2.

[e]Not determined.

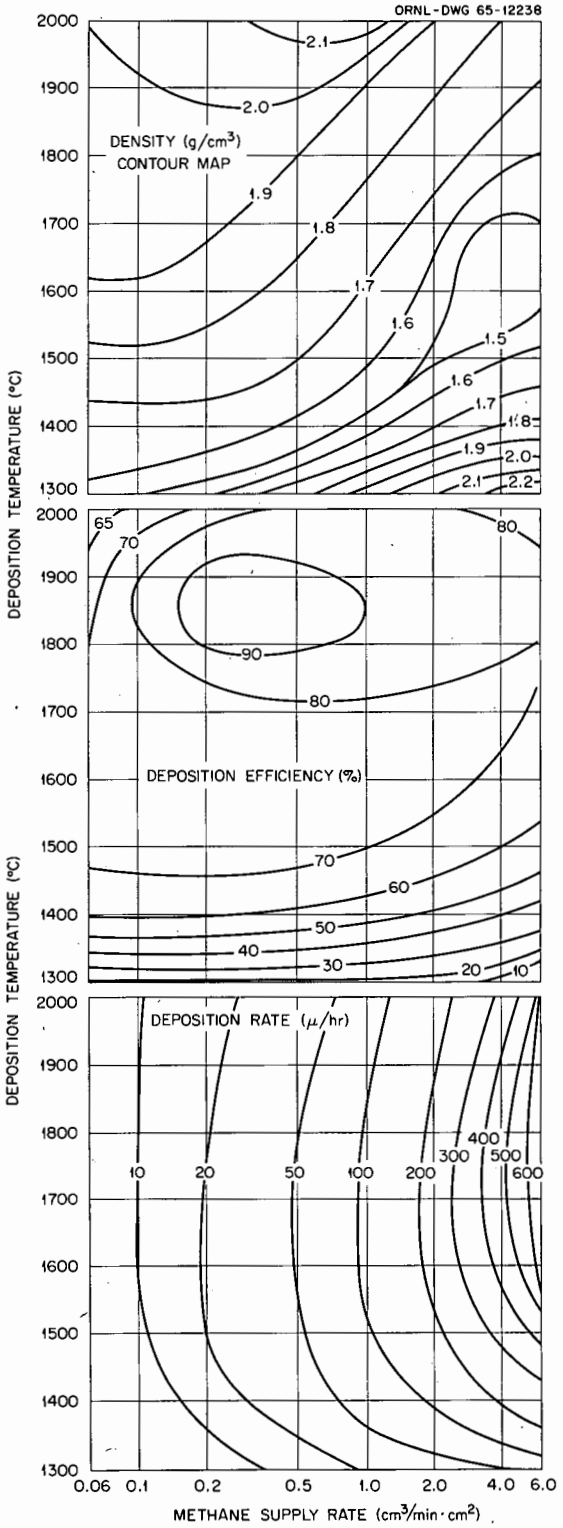

Fig. 1.3. Effect of Methane Flow Rate and Deposition Temperature on Deposition Rate and Efficiency and on Density of Pyrolytic-Carbon Coatings Deposited on 530-μ-diam UC_2 Particles in a Fluidized Bed.

in a gradient bed, the actual temperature at which most of the coating occurs is reduced.

The deposition efficiencies listed in Table 1.1 and shown as a contour plot in Fig. 1.3 are calculated values representing the percentage of the total carbon supplied that is deposited on the particles. The decrease in efficiency with decreasing deposition temperature below 1600°C is caused by a reduction in the fraction of the methane that decomposes in the fluidized bed and a corresponding increase in the amount of methane that decomposes above the bed and forms soot that coats the upper part of the reaction tube and the exhaust filter. Thus a high deposition efficiency is desirable not only from the standpoint of efficiently utilizing the hydrocarbon supplied but also from the standpoint of system maintenance.

In this series of coating runs we encountered difficulty in applying coatings at 1300°C. While efficiencies of about 30% can be obtained at 1300°C with 200-μ particles, the increased gas velocity required to fluidize the 530-μ particles apparently decreased the contact time sufficiently to cause a drastic reduction in coating efficiency. Deposition efficiencies of less than 10% were obtained at high methane supply rates, and it was impractical even to do experimental work because the reaction tube became blocked with soot above the fluidized bed. It should be noted that the highest efficiency is obtained between 1800 and 1900°C. The decrease in efficiency at 2000°C is due to a greater amount of deposit formed on the walls of the reaction tube immediately above the gas inlet orifice.

The deposition rates listed in Table 1.1 and shown as a contour plot in Fig. 1.3 represent linear coating buildup rates, which are strong functions of the methane supply rate. However, for any given methane supply rate the deposition rate decreases with decreasing temperature below 1600°C, because of reduced efficiency, and decreases with increasing temperature above 1700°C, primarily because of higher coating densities.

From the results of this series of coating runs, we conclude that it is possible to deposit the same types of coatings on 530-μ particles as can be applied to 200-μ particles. However, coating temperatures below 1400°C are not practical for the large particles if methane is used as

the source of carbon. A greater fluidizing gas flow rate is required for the larger particles, but this has the advantage of making it possible to coat the large particles at a much higher rate than small particles. On the other hand, the choice of coating properties available with very high deposition rates is limited.

Coatings Deposited from Methane in a 2-in.-diam Fluidized Bed (D. M. Hewette, R. L. Beatty)

The specimen preparation phase of a systematic study of the effect of deposition conditions on the properties of coatings applied in a 2-in.-diam coater was completed. More than 100 coating experiments were performed to cover a temperature range of 1300 to 2000°C and a specific methane supply rate range of 0.1 to 3.57 $cm^3/min \cdot cm^2$. All experiments were performed in a 2-in.-diam graphite resistance-heated coating chamber with a 36° cone angle. A graphite injector was used at temperatures between 1300 and 1500°C, while a water-cooled injector was used at temperatures between 1500 and 2000°C. Thus there was an overlap at 1500°C in experiments carried out with the two types of injectors. The coating temperature was measured on the outside of the reaction tube with an optical pyrometer and correlated with temperatures measured on top of the bed fluidized with helium only.

A fluidizing gas flow rate of 10 liters/min was selected for a 100-g charge of 200-μ-diam spheroidal bed-melted UC_2 particles. This was four times the flow rate used for fluidization of 25-g charges of similar particles in the 1-in.-diam coater and was consistent with the fourfold increase in charge size and coating chamber cross-sectional area.

Our measurements of coating properties are still in progress, but preliminary results show consistent trends. The results of measurements of apparent crystallite size and anisotropy factor are compared in Table 1.2 with data obtained from 1-in.-diam coaters. Apparent crystallite sizes for coatings deposited in the 2-in.-diam coater showed excellent agreement with values obtained from smaller coaters and justified cessation of crystallite size determinations on a routine basis in subsequent experiments. Anisotropy factors were determined by a technique

Table 1.2. Apparent Crystallite Sizes and Anisotropy Factors for Disk Samples Coated in 2-in.-diam Coater

Run	Deposition Temperature (°C)	Flow Rate ($cm^3/min \cdot cm^2$)	Apparent Crystallite Size (A)		Anisotropy Factor,[a] σ_{oz}/σ_{ox}	
			2-in. Coater	1-in. Coater	2-in. Coater	1-in. Coater
NL-2	1700	2.0	67	70		
-3	1400	2.0	40	(b)		
-6	2000	2.0	115	110		
-13	2000	0.13	150	(b)	2.8	3.0
-14	1600	1.7	50	54		
-17	1700	0.13	88	105		
-20	1700	0.08	100	110	1.8	1.7
-21	1600	1.0	62	60		
-23	1700	3.57	65	(b)		
-24	1500	3.57	40	(b)		
-25	1500	1.7	33	40		
-27	1700	3.57	62	(b)		
-28	1700	2.0	77	70		
-30	1700	0.13	90	105		
-32	1700	0.05	113	115	2.4	1.8

[a]Measured only for those coatings that showed marked anisotropy by metallographic examination.

[b]Not determined.

previously described,[2] but only coatings for which metallographic examination indicated marked anisotropy were considered. The anisotropy factors determined for three batches agree with values obtained in similar runs in the small coaters.

The effect of temperature on coating densities obtained at a specific methane flow rate of 2 $cm^3/min \cdot cm^2$ is shown in Fig. 1.4. Densities achieved at the lower and higher temperatures were high, while a minimum density of 1.48 g/cm^3 was found at 1600°C. The same trend was observed with the small coaters under similar conditions.

Porous Coatings Deposited on Fuel Particles from Acetylene in a 1-in.-diam Fluidized Bed (H. Beutler, R. L. Beatty)

Pyrolytic-carbon-coated particles with three-layer coatings, including a porous inner layer deposited from acetylene, have shown remarkably

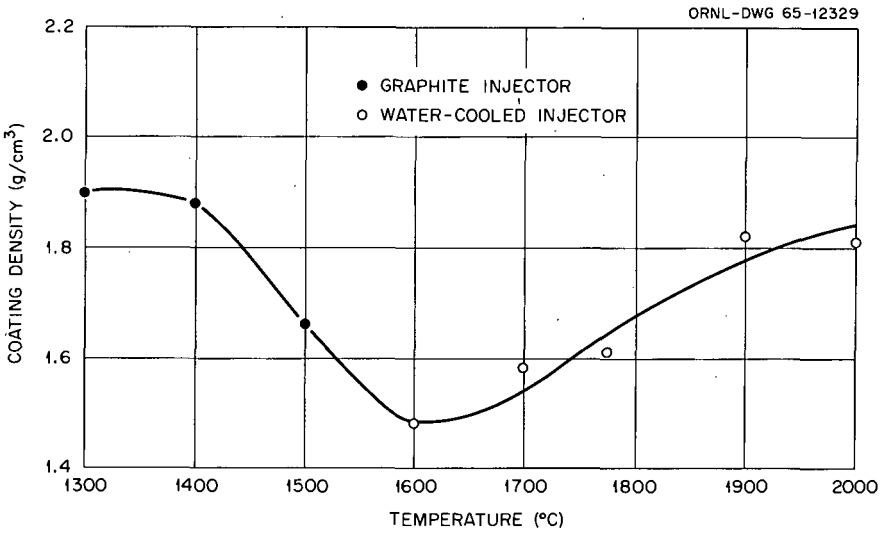

Fig. 1.4. Effect of Deposition Temperature on Density of Coatings Deposited in a 2-in.-diam Coater at a Methane Supply Rate of 2 $cm^3/min \cdot cm^2$.

good irradiation behavior.[3] The porous inner layer accommodates swelling of the fuel and provides volume for storage of gaseous fission products, and it thereby limits the internal mechanical stressing of the outer coating. At the same time, it protects the outer layer from fission fragment recoil damage. The desired properties of the inner layer are, therefore, a high degree of porosity and low mechanical strength. We have investigated the conditions for depositing such porous layers on microspheres of various sizes (150, 250, and 460 μ) in a 1-in.-diam fluidized bed.

Equipment and Procedure. All coating experiments were carried out in a graphite resistance-heated fluidizing furnace, the design of which is described elsewhere.[4] Because of the short coating times involved, it was essential to adjust the acetylene-helium mixture before the coating operation and to introduce the mixture rapidly. A gas feeding system

---

[3]General Atomic Division, General Dynamics Corporation, Graphite-Matrix Fuels Development for the AVR, USAEC Report GA-4695, October 1963.

[4]R. L. Beatty and E. S. Bomar, Particle Coating Studies, pp. 182–185, Development of Fueled Graphite Containing Pyrolytic-Carbon-Coated Carbide Particles for Nonpurged, Gas-Cooled Reactor Systems, compiled by F. L. Carlsen, Jr., E. S. Bomar, and W. O. Harms, Nucl. Sci. Eng., 20(2): 180–200 (October 1964).

enabled preadjustment of the fluidizing mixture and automatic changeover and timing of the coating process. The commercial grade acetylene used was dried before passing into the coater.

Temperature was controlled by means of an optical pyrometer viewing the surface of the reaction tube at a distance of 2.1 in. from the orifice. As a standard procedure, fuel particles were introduced into the preheated furnace and fluidized with helium until equilibrium temperature was reached. The exothermic pyrolysis of acetylene always caused a considerable temperature rise during the coating operation. However, in view of the large thermal inertia of the furnace compared with the short coating times involved (0.5 to 5 min), it was not considered possible to achieve constant temperature conditions during the run. Once the coating run was started no adjustments in power were made. Deposition temperatures reported here refer to equilibrium temperatures at the beginning of the experiment.

Temperature Changes in the Fluidized Bed. We performed a series of experiments to measure the temperature changes in the fluidized bed due to the exothermic pyrolysis of acetylene. The conditions and results of these runs are given in Table 1.3. Since the temperature rise observed on the surface of the reaction tube is not indicative of the actual conditions inside the fluidized bed, two thermocouples (90% Pt–10% Rh vs Pt) were inserted into the reaction tube to measure temperatures in the fluidized bed and immediately above it. A third thermocouple (Chromel-P vs Alumel) was positioned at the surface of the reaction tube at the point where the coating temperature is normally measured optically. The positions of these thermocouples are shown in Fig. 1.5. Their outputs were recorded by three independent recording instruments. The recorder chart tracings from run GLP-22, shown in Fig. 1.5, are typical for the series.

These results show that the temperature rise in the fluidized bed due to the pyrolysis of acetylene is significant and depends on acetylene concentration, deposition temperature, and coating time. The most significant temperature rise occurs within 15 sec after the introduction of acetylene. After 30 sec the rate of temperature increase is constant until the end of the experiment. In experiment GLP-20, in which a 50-g

Table 1.3. Conditions and Results of Experiments for Determining the Temperature Change of the Fluidized Bed During the Deposition of Porous Coatings

	Experiment					
	GLP-20	GLP-21	GLP-22	GLP-24	GLP-25	GLP-26
Coating conditions						
Charge, g	50[a]	50[a]	50[a]	25[b]	50[a]	50[a]
Acetylene flow rate, cm^3/min	4000	4000	6000	2500	4000	4000
Acetylene partial pressure, torr	760	760	510	760	760	760
Coating time, min	3	1	3	3	2	0.3
Coating thickness, μ	120	57	37	22	120	(c)
Coating density, g/cm^3	0.63	0.61	1.84	0.68	0.48	(c)
Deposition efficiency, %	82	72	42	68	76	(c)
Temperature measurements[d]						
Equilibrium temperature (°C) prior to coating at position						
A	970	970	960	960	950	1150
B	980	980	970	970	975	1180
C	1000	1000	1000	1000	1000	1200
Maximum temperature change (°C) during coating process at position						
A	225	180	145	130	200	215
B	190	135	140	120	195	50
C	70	30	50	45	−55	(c)
Initial temperature rise[e] (°C/sec) at start of coating run at position						
A	8.7	7.3	6.5	4.7	10.0	11.7
B	3.7	3.3	5.3	3.2	4.5	2.3
Initial temperature rise ratio of A/B	2.3	2.2	1.2	1.5	2.2	5.0

[a]Sol-gel ThO_2 particles, 400-μ nominal diameter.

[b]Sol-gel ThO_2 particles, 200-μ nominal diameter.

[c]Not determined.

[d]Position: A — Thermocouple in fluidized bed; 1 in. above orifice
B — Thermocouple above fluidized bed; 3 in. above orifice
C — Thermocouple on outer surface of reaction tube

[e]Determined between 0 and 15 sec running time.

charge of 460-μ-diam ThO_2 microspheres was coated, the thermocouple immersed in the fluidized bed indicated an overall temperature rise of 225°C after a 3-min coating time, in contrast to an increase of 190°C immediately above the bed. The temperature rise measured on the surface of the reaction tube was only 70°C, however. For comparison, in a 25-g charge of 200-μ-diam ThO_2 particles (see experiment GLP-24) coated at the same temperature but at a lower flow rate, the maximum temperature rise obtained inside the fluidized bed was 130°C and, above the fluidized bed, 120°C. In both cases the linear temperature rise in a 3-min run was approximately 18°C/min·liter.

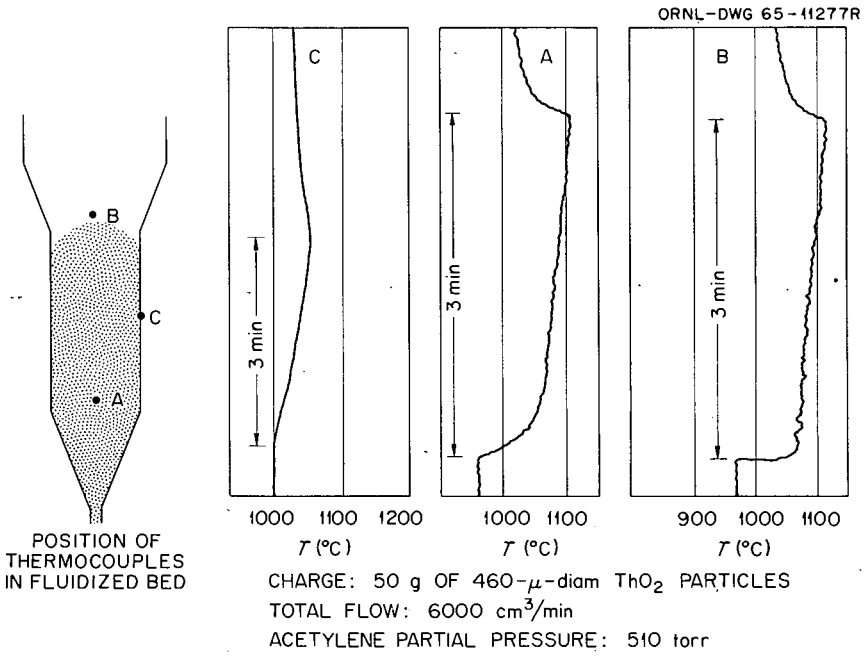

Fig. 1.5. Chart Tracings of Thermocouple Output Readings During Experiment GLP-22 Showing Temperature Rise in Fluidized Bed Due to Decomposition of Acetylene.

The comparative rates of temperature increase of the thermocouple immersed in the fluidized bed and the one positioned above the bed were found to be measures of coating efficiency. The very rapid temperature rise above the bed during run GLP-22 (shown in Fig. 1.5) indicates that a significant portion of the acetylene was decomposing above the bed and hence was not available for coating. In a highly efficient run the temperature above the bed should not rise faster than the temperature of the bed itself and may, in fact, rise much more slowly.

Because of the short duration of these coating experiments, it was impractical with the given furnace characteristics to maintain a constant temperature inside the fluidized bed. This was demonstrated by experiment GLP-25, in which the furnace power was switched off at the start of the coating run. The temperature rise inside the reaction tube was virtually the same as it would have been without the power shut off during the 2-min coating run.

Effect of Coating Conditions on Coating Density, Deposition Efficiency, and Deposition Rate. We investigated the effect of deposition

temperature on coating properties at three different acetylene partial pressures (490, 610, and 760 torr) with a charge of 50 g of 460-μ-diam ThO_2 particles fluidized at a total gas flow of 4 liters/min. Experimental conditions and results are summarized in Table 1.4.

The effects of deposition temperature on density and efficiency are shown in Fig. 1.6. At an acetylene partial pressure of 760 torr the density change due to temperature is insignificant between 950 and 1150°C, but at an acetylene partial pressure of 490 torr the effect of temperature is marked. At each temperature studied an increase in coating density with decreasing acetylene concentration is evident.

The deposition efficiency increases with increasing temperature to a maximum of about 80% for a given acetylene supply rate and is independent of acetylene partial pressure. However, while maximum efficiency is reached at approximately 1000°C with an acetylene partial pressure of 760

Table 1.4. Conditions and Results of Experimental Application of Porous Carbon Layers on Sol-Gel 460-μ-diam ThO_2 Microspheres by the Decomposition of Acetylene

Run	Coating Application Temperature (°C)	Acetylene Supply Rate ($cm^3/min \cdot cm^2$)	Acetylene Partial Pressure[a] (torr)	Average Deposition Rate (μ/min)	Coating Thickness[b] (μ)	Coating Density[c] (g/cm^3)	Deposition Efficiency (%)
GLP-5	910	6.2	760	59	59	0.48	57
-4	940	6.2	760	56	110	0.56	67
-1	970	6.2	760	56	110	0.58	81
-2	1000	6.2	760	55	83	0.60	76
-3	1030	6.2	760	52	100	0.63	82
-6	1100	6.2	760	60	90	0.60	83
-7	1150	6.2	760	63	94	0.54	80
-8	1250	6.2	760		Blockage occurred		
-38	900	5.0	610		No coating		
-40	950	5.0	610	27	53	0.82	53
-34	1000	5.0	610	37	75	0.75	67
-35	1050	5.0	610	37	75	0.77	75
-32	1100	5.0	610	40	79	0.77	84
-36	1150	5.0	610	40	80	0.80	86
-33	1200	5.0	610	37	74	0.86	85
-39	1250	5.0	610	37	73	0.90	88
-31	900	4.0	490		No coating		
-11	1000	4.0	490	12	37	1.40	51
-29	1050	4.0	490	16	47	1.20	57
-18	1100	4.0	490	26	77	1.11	75
-30	1150	4.0	490	22	65	1.16	84
-28	1200	4.0	490	21	63	1.24	85

[a]System at atmospheric pressure.

[b]Obtained from random scanning of radiographs.

[c]Density calculated from weight increase and measurement from radiograph.

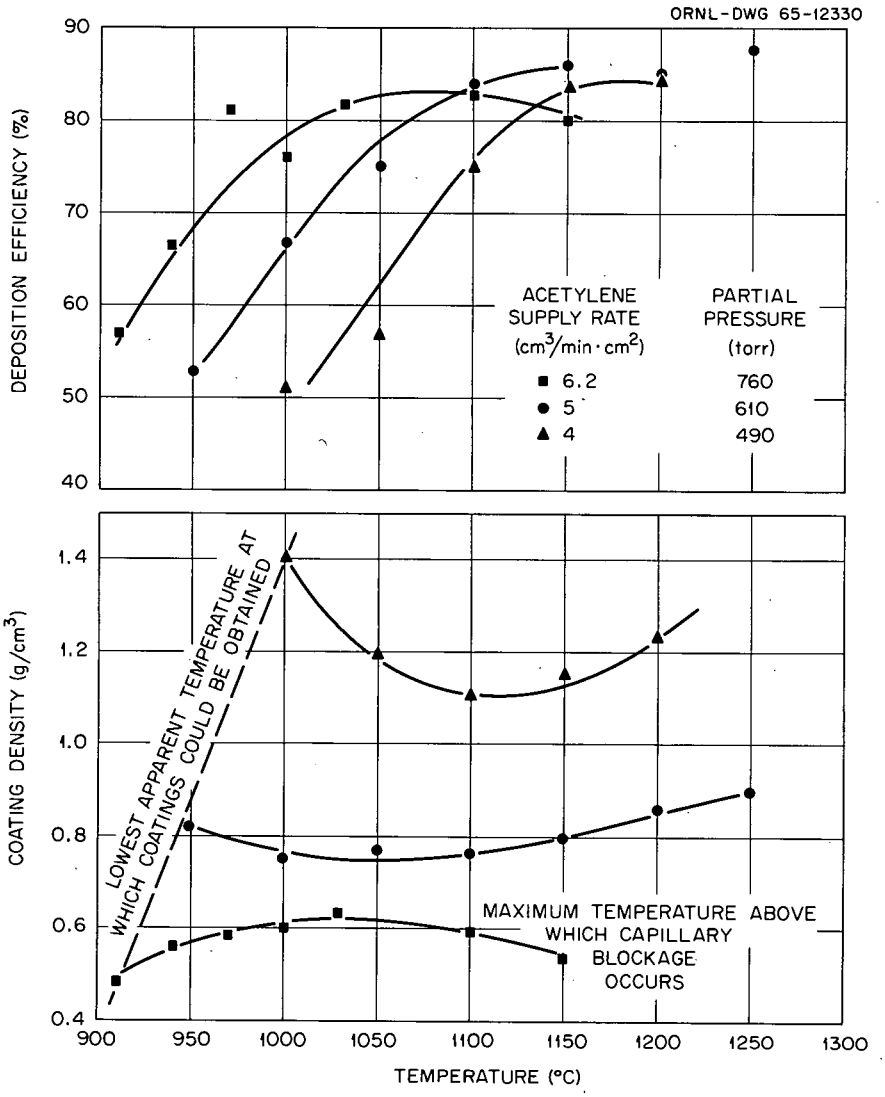

Fig. 1.6. Effects of Temperature and Acetylene Supply Rate on Density and Efficiency of Porous Coating Deposition on 460-μ-diam ThO_2 Particles.

torr, a partial pressure of 490 torr gives maximum efficiency at 1150°C. This apparent temperature displacement in the efficiency maximum is probably due to the error in temperature determination caused by neglecting the temperature rise inside the fluidized bed. A deposition efficiency of 50% was found to be the lower limit for practical coating application. Soot buildup in the reaction tube caused frequent blockage at low efficiencies, and coatings were inconsistent in shape and texture.

From the results of these experiments it can be concluded that high acetylene supply rates are essential for low-density coatings. The maximum supply rate is, of course, limited by the fluidizing requirements and is mainly a function of the particle size. With 220-μ-diam particles the maximum supply rate obtainable at an acetylene pressure of 760 torr is 3.7 $cm^3/min \cdot cm^2$, and for 180-μ-diam particles a rate of 2.5 $cm^3/min \cdot cm^2$ yields equivalent bed expansion. However, in a series of experiments the densities of coatings on smaller particles were lower than would be predicted if supply rate alone were controlling because of the increased contact time at the lower total flow rate. Thus, within the range of experimental conditions studied the coating density decreased with increasing acetylene supply rate and with increasing contact time, with the contact time being inversely proportional to the total flow for a given bed volume. The dependence of coating density on the ratio of total flow rate to acetylene supply rate is shown graphically in Fig. 1.7.

The variation of coating density with acetylene supply rate and deposition temperature follows the same trend as for coatings derived from

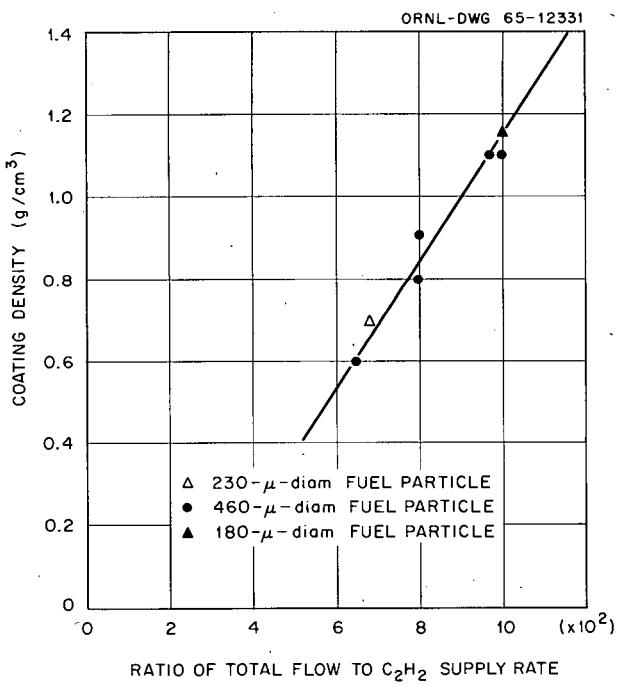

Fig. 1.7. Ratio of Total Fluidizing Gas Flow Rate to Acetylene Supply Rate Versus Coating Density.

methane at high supply rates in the temperature range 1400 to 1800°C.[1,5] If consideration is given to the differences in carbon content and thermal stability of the two gases, it is probable that the deposition mechanism is similar to that described by Bokros.[5] High supply rates of hydrocarbon are required to encourage the gas-phase condensation of soot particles, while long contact times increase the chance of agglomeration and incorporation of soot particles into the coating. Preheating shifts the decomposition region toward the orifice; this increases the concentration of soot particles in the base of the fluidized bed and results in an apparent increase in contact time.

Thickness Control and Utilization of Porous Coatings. Porous coatings deposited from acetylene have exhibited larger variations in coating thickness within a given batch than are normally obtained with deposits formed from methane in the same coater. The coating thicknesses on individual particles from the same coating run may vary by nearly a factor of 2 without relation to the fuel particle or total particle diameter, which indicates that the variation is not caused by segregation of different-sized particles in the fluidized bed. Furthermore, the variations in coating thickness were found to increase with increasing coating thickness; from this we conclude that such variations are not caused by the transient conditions during the initial stages of the coating process.

Repeated runs have now shown that the thickness distributions of coatings deposited under identical conditions are similar and therefore controllable. This reproducibility of coating thickness was demonstrated in eight successive coating runs carried out under identical conditions, as given in Table 1.5. Although the variations in thickness and density of the porous coatings were considerably greater than variations in methane-derived coatings, the control limits are acceptable for practical application.

The use of coated particles with porous carbon layers requires that one or more dense carbon layers be deposited over the porous coating.

---

[5]J. C. Bokros, The Structure of Pyrolytic Carbon Deposited in a Fluidized Bed, p. 14, USAEC Report GA-5163, General Atomic Division, General Dynamics Corporation, July 1, 1964.

Table 1.5. Variation in Average Coating Thickness, Density, and Deposition Efficiency for Acetylene-Derived Coatings on ThO_2 Particles

Charge: 25 g of 220-μ-diam ThO_2 particles
Coating application temperature: 1070°C
Total acetylene flow: 2.5 liters/min
Acetylene partial pressure: 760 torr
Coating time: 55 sec
Average deposition rate: 34 μ/min

Run		Average Coating Thickness (μ)	Coating Density, Calculated (g/cm^3)	Deposition Efficiency (%)
GLP-50		31	0.60	66
-51		25	0.75	70
-52		30	0.60	65
-53		30	0.65	67
-54		33	0.55	69
-55		33	0.55	67
-56		31	0.60	67
-57		34	0.70	80
	Mean	31	0.73	
	Standard deviation	2.6	0.07	
	Mean deviation	1.9	0.06	

We applied such outer coatings by charging the particles into a preheated coater and saw no indication that this thermal shock or abrasion during fluidization damaged the porous layer. Metallographic examinations of coated particles with inner porous carbon layers and outer layers deposited from methane at high rates (~150 μ/hr) or low rates (9 μ/hr) showed no penetration of pyrolytic carbon into the pores of the inner layer; instead they revealed distinct transitions between the layers.

Characterization of Porous Coatings (H. Beutler, R. L. Beatty)

In order to characterize the porous coatings deposited from acetylene, we studied the following properties: (1) density, (2) pore size distribution, (3) microstructure, and (4) crushing strength.

Density. Because of the open porosity of porous coatings, densities calculated from helium-pycnometer measurements or direct measurements obtained by a sink-float technique are not applicable. The densities of porous coatings are therefore calculated from the carbon-to-particle weight ratios and the coating-to-core volume ratios. Since a coating weight determination from the charge recovery weight is affected by possible losses of particles during the coating process or during the discharge operation, the coating-to-core weight ratio was obtained by removal of coatings by oxidation of about 3 g of coated particles in an alumina crucible at 900°C in air for 5 hr. To obtain the average coating-to-core volume ratio, we measured 50 particles randomly selected from a microradiograph. The accuracy of this technique depends to a large degree on the validity of the 50-particle sample for measuring the particle and coating dimensions. To minimize the error, sol-gel ThO_2 microspheres of a narrow size range and a high degree of sphericity were used. The variation in density resulting from such sampling errors was studied on a batch having a wide variation in coating thickness (65 to 130 μ). The coating densities calculated from ten independent measurements of a 50-particle sample ranged from 0.634 to 0.696 g/cm^3, with a mean of 0.661 g/cm^3 and a standard deviation of 0.016.

In cases of high-density coatings of uniform thickness, good agreement was found with results from helium-pycnometer determinations. The accuracy of density determinations made with this technique on low-density coatings is, however, expected to be lower due to the inherent variation in coating thickness.

Porosity and Pore-Size Distribution. The pore-size distributions of a series of porous coatings deposited on large (460-μ) and small (220-μ) sol-gel ThO_2 microspheres were determined by mercury porosimetry. Similar pore-size distributions were obtained from coatings of similar density that were independent of particle size, coating thickness, and coating conditions. However, a marked effect of coating density on pore-size distribution was noted. A comparison of pore-size distribution patterns from porous coatings of different densities (0.55, 0.95, and 1.35 g/cm^3) is shown in Fig. 1.8. An increase in pore size with decreasing density is evident.

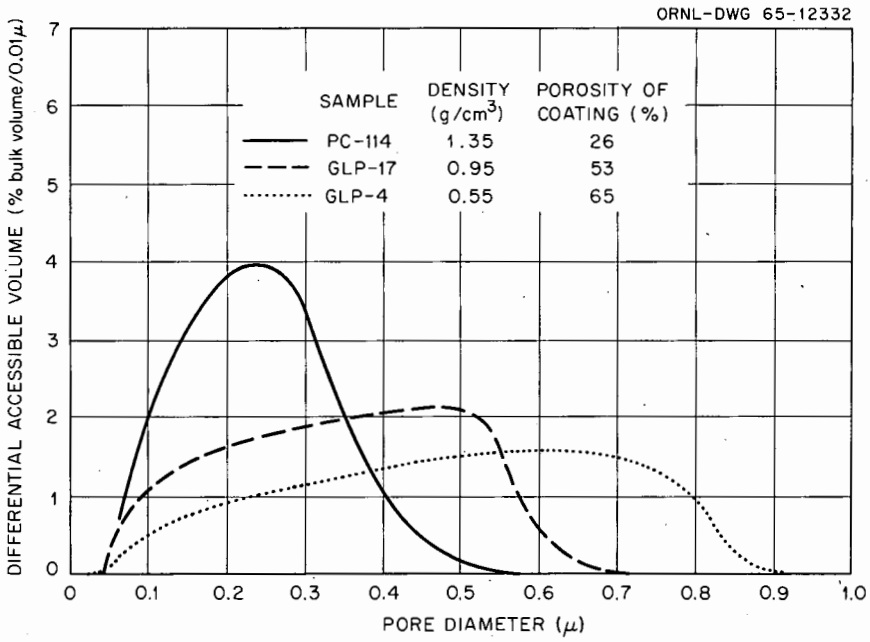

Fig. 1.8. Comparison of Pore Size Distribution Pattern of Porous Coatings of Different Density.

The total accessible porosity of porous coatings was also determined from mercury porosimetry data. In the density range 0.6 to 1.4 g/cm^3, we observed a linear increase in accessible porosity with decreasing density that was independent of coating conditions, as shown in Fig. 1.9. At densities below 0.6 g/cm^3 the porosity appears to be constant. It is suspected that coatings with densities less than 0.6 g/cm^3 are too weak to sustain the mechanical stress inherent to porosimetry measurements.

Microstructure. Microscopic examinations were made to evaluate the structure of porous coating layers. Standard techniques[6] were used for the preparation of specimens, but it was evident that the epoxy resin normally used for mounting particles penetrated into the outer shell of the porous coating and gave the impression of a difference in structure. We also noted that the depth of penetration of mounting resin varied among individual particles; however, it was not established whether this was

[6]C. K. H. DuBose and R. J. Gray, Metallography of Pyrolytic Carbon Coated and Uncoated Uranium Carbide Spheres, USAEC Report ORNL-TM-91, Oak Ridge National Laboratory, Mar. 21, 1962.

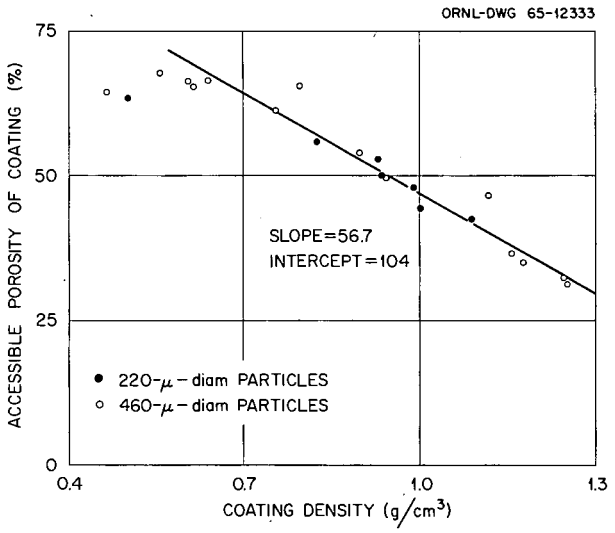

Fig. 1.9. Accessible Mercury Porosity of Low-Density Coatings Versus Coating Density. Data obtained from deposition of porous carbon layers from acetylene on sol-gel ThO_2 microspheres.

due to differences in porosity or to differences of accessibility of the pores on the surface.

Porous coatings of different densities are compared in Fig. 1.10. The previously discussed increase in pore size with decreasing density is clearly evident in the structure of these coatings.

Crushing Strength. Crushing strengths were determined on selected batches of porous coatings on both small (200-μ) and large (460-μ) sol-gel ThO_2 particles. The average crushing load of each batch plotted versus the calculated density yielded a wide scatter band of the data. Since the batches examined varied extensively in average coating thickness, the crushing strength expressed in terms of unit coating thickness was then plotted versus the calculated coating density. The scatter was significantly reduced, as shown in Fig. 1.11, and an increase in crushing strength with increasing density was evident.

The results also showed that the crushing strengths of coatings with densities above 1.5 g/cm^3 that were deposited from acetylene in the temperature range 1000 to 1300°C were significantly higher than those of coatings derived from methane.

PHOTO 81749

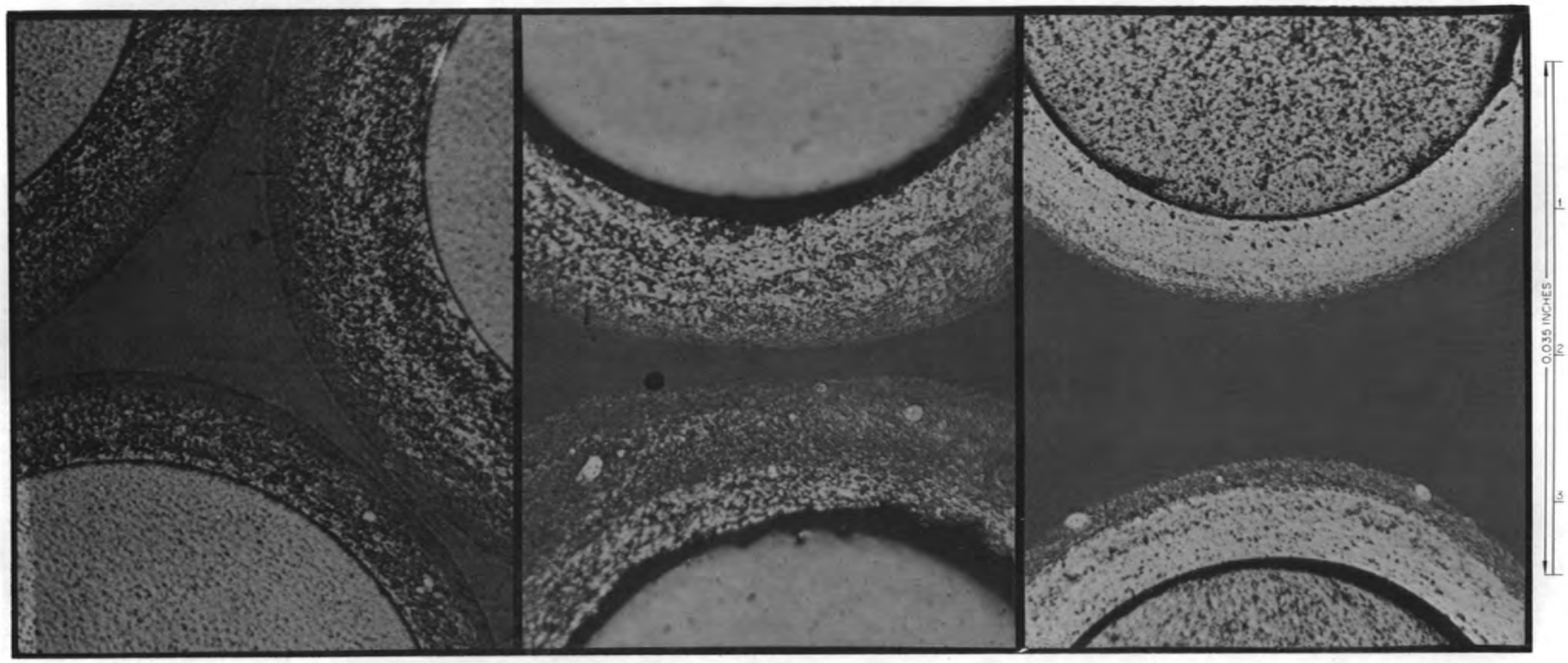

PC 98-4 DENSITY 0.81 g/cm^3 PC 92-3 DENSITY 1.0 g/cm^3 PC 91-3 DENSITY 1.37 g/cm^3

Fig. 1.10. Comparison of Photomicrographs of Porous Coatings of Different Density. As polished.

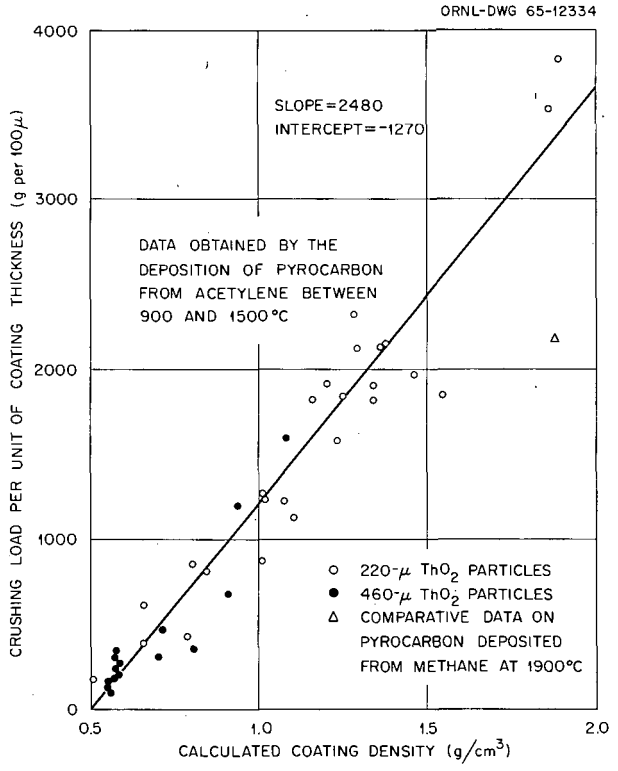

Fig. 1.11. Relationship of Crushing Load Per Unit of Coating Thickness to the Coating Density.

Effects of Heat Treatment on Pyrolytic Carbon (F. L. Carlsen, Jr.)

A series of heat treatments was conducted on pyrolytic-carbon coatings to study the effects on measurable properties. These coatings were stripped from carbon disks that were coated along with particles in a fluidized bed at temperatures from 1300 to 2000°C. Deposition conditions used in preparing the samples are given in Table 1.6. Most of the samples were coated at 1300 and 1400°C; they had small crystallites and a wide range of densities.

The samples were heated in graphite holders in a resistance-heated vacuum furnace for 2 hr at temperatures of 1800, 2000, 2100, 2200, 2400, 2600, and 2800°C. Densities were measured on the disk coatings by the sink-float method, and apparent crystallite sizes and Bacon anisotropy factors were measured by x-ray technique. Dimensions of the samples were also measured, but the poor precision of the technique plus warpage of the specimens made the results unsatisfactory.

Table 1.6. Effect of 2-hr Heat Treatment at 2800°C on the Density and Crystallite Size of Pyrolytic-Carbon Coatings

Coating Run	Coating Application Temperature (°C)	Methane Partial Pressure (torr)	Methane Flow Rate ($cm^3/min \cdot cm^2$)	Average Deposition Rate (μ/hr)	Density of Disk Coating			Apparent Crystallite Size (A), L_c	
					As Deposited (g/cm^3)	After 2 hr at 2800°C (g/cm^3)	Increase in Density (%)	As Deposited	After 2 hr at 2800°C
222	1300	16	0.053	2.3	1.41	1.60	13.0	37	105
247	1300	60	0.20	10	1.60	2.18	36.0	33	>1000
209	1300	80	0.27	10	1.78	2.22	25.0	34	>1000
217	1300	760	2.5	82	2.06	2.18	5.8	38	200
229	1300	760	2.5	87	2.06	2.16	4.9	38	200
329	1300	760	3.6	110	2.03	2.14	5.4	45	210
180	1400	45	0.15	13	1.70	2.16	27.0	65[a]	420
245	1400	55	0.17	14	1.37	1.55	13.0	35	80
135	1400	85	0.17[b]	16	1.44	1.57	9.0	42	110
327	1400	38	0.18	13	1.47	1.57	6.8	45	90
204	1400	333	0.83[b]	83	1.53	1.60	5.0	40	110
197	1400	760	2.9[b]	200	1.76	1.90	7.9	55[a]	160
326	1600	760	3.6	350	1.51	1.53	1.0	60	90
NL-2	1700	425	2.0	200	1.47	1.60	8.8	67	80
354	1800	380	2.0	190	1.59	1.62	2.0	80	105
357	2000	29	0.15	10	2.04	2.05	0.0	160	180
338	2000	380	1.7	170	1.81	1.83	1.0	115	120
351	2000	380	2.0	190	1.78	1.83	3.0	120	120
352	2000	380	2.0	190	1.82	1.79	0.0	125	130

[a]After 2 hr at 2100°C.

[b]Estimated values.

The as-deposited and final values of density and crystallite size are also given in Table 1.6. These results show a wide variation in behavior, with the coatings deposited at 1300°C showing the greatest changes. The effect of heat treatment temperature on density is shown in Fig. 1.12 for the coatings deposited at 1300 and 1400°C. The crystallite size in coatings deposited at these two temperatures also increased greatly during the heat treatments. The effects of temperature on the crystallite

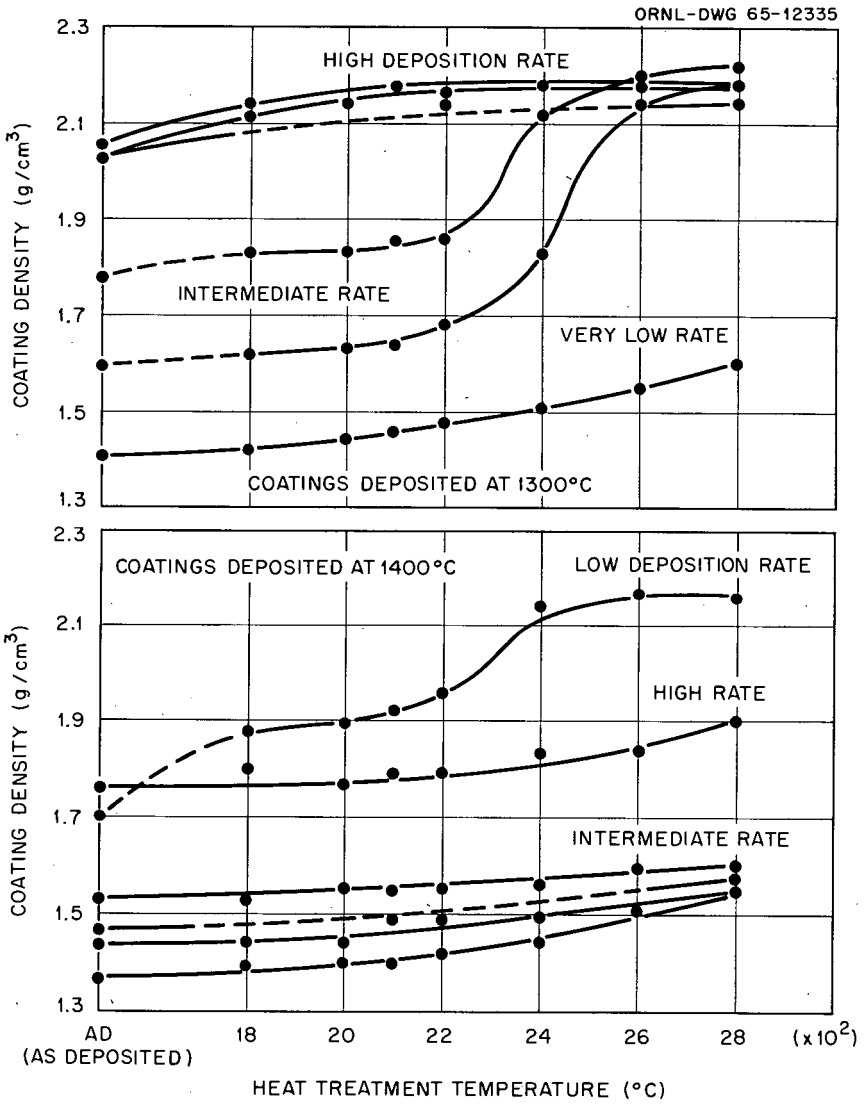

Fig. 1.12. Effect of Heat Treatment on the Density of Pyroltyic-Carbon Coatings Deposited at 1300 and 1400°C.

sizes in coatings deposited at 1300 and 1400°C are shown in Figs. 1.13 and 1.14, respectively.

The anisotropy factors of most of the disk coatings were measured after the 2100°C and subsequent heat treatments, with results as given in Table 1.7. Note that many of the coatings changed only slightly.

The results from this heat treatment study may be summarized as follows:

1. Coatings deposited at high methane flow rates at temperatures from 1300 to 2000°C that are isotropic when deposited remain isotropic even after heat treatment at 2800°C.

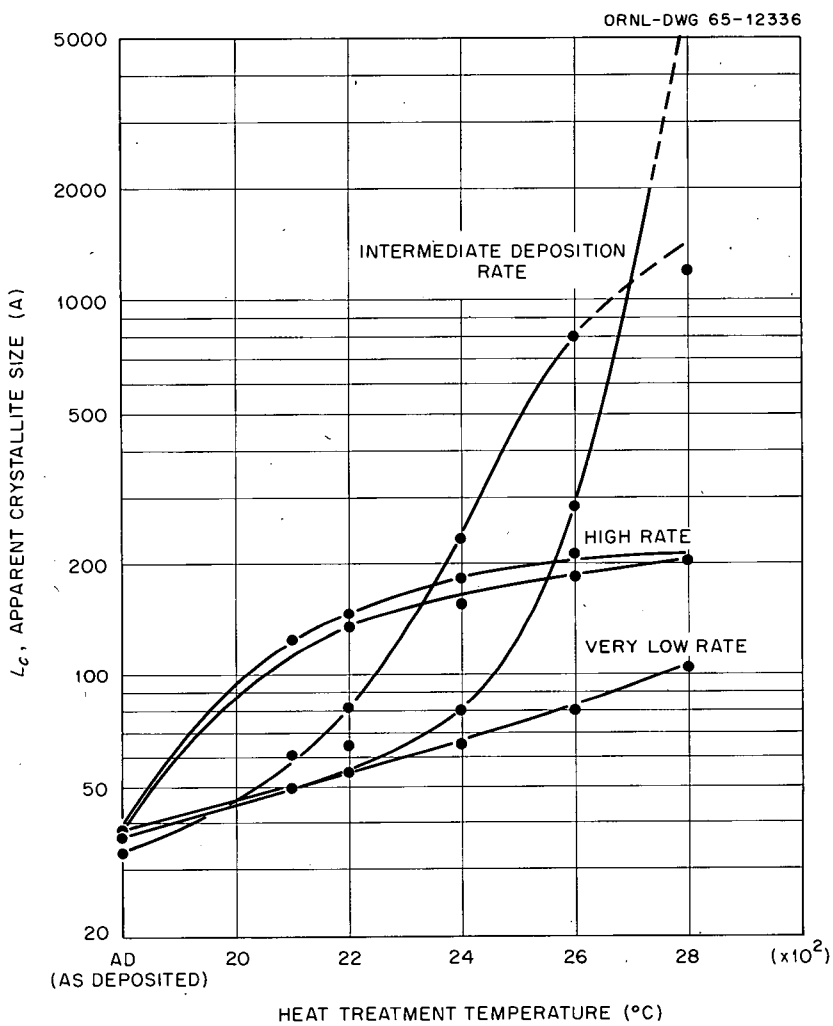

Fig. 1.13. Effect of Heat Treatment on Crystallite Size in Pyrolytic-Carbon Coatings Deposited at 1300°C.

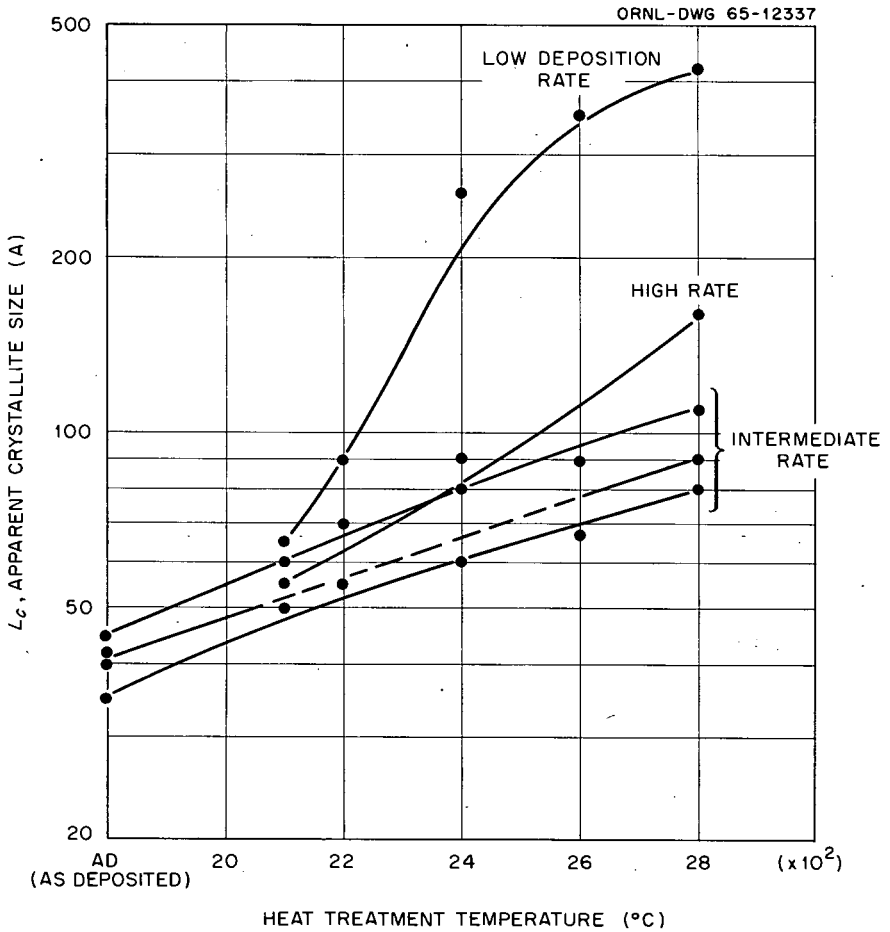

Fig. 1.14. Effect of Heat Treatment on Crystallite Size in Pyrolytic-Carbon Coatings Deposited at 1400°C.

2. Coatings deposited at 1300 and 1400°C that are highly anisotropic become more anisotropic during heating.

3. Density changes depend on the deposition conditions. With one exception (a sample deposited at a very low rate), all coatings deposited at 1300°C had densities of 2.14 g/cm^3 or greater after heat treatment. The densities of coatings deposited at 1400°C, on the other hand, increased much less, except for one deposited at a low rate. Coatings deposited at higher temperatures showed very little change in density.

4. The crystallite sizes of coatings deposited at 1300°C increased by factors of 3 to more than 30, while coatings deposited at 1400°C showed much less increase. All coatings deposited at higher temperatures (≥1600°C) showed little if any change in crystallite size.

Table 1.7. Effects of Heat Treatment on the Anisotropy Factor of Pyrolytic-Carbon Coatings

Coating Run	Anisotropy Factor (σ_{OZ}/σ_{OX}) After Indicated Heat Treatment for 2 hr					
	As Deposited	2100°C	2200°C	2400°C	2600°C	2800°C
222	1.8	(a)	1.9	(a)	1.5	(a)
247	3.8	5.8	6.3	6.5	36.0	46.0
209	3.3	5.1	8.8	24.0	39.0	73.0
217	1.3	1.4	1.4	(a)	1.4	(a)
229	1.3	1.3	1.4	(a)	1.3	(a)
180	2.9	3.9	4.1	7.5	5.8	8.7
245	2.4	2.3	(a)	2.8	4.5	3.2
135	2.8	3.0	2.5	2.2	2.5	(a)
204	1.0	1.0	1.0	1.0	1.0	(a)
197	1.0	1.0	1.0	1.0	1.0	(a)

[a]Not determined.

Phase Studies of the Pseudobinary System UC_2-ThC_2 in the Presence of Excess Graphite

J. L. Cook O. B. Cavin J. M. Leitnaker

Experimental results obtained from the study of the system UC_2-ThC_2 plus graphite during the past year were published.[7] Included in the publication are (1) thermal expansion measurements across the range from 40 to 1000°C and (2) two proposed phase diagrams that summarize results obtained by dilatometry, long-term annealing studies using x-ray and metallographic examination, and time-temperature thermal cycles. A summary of phase diagram information is presented in Fig. 1.15.

The physical behavior of UC_2-ThC_2 alloys was described within the limits of present equipment. However, several additional experiments were run in an attempt to clarify some of the uncertainties. Pertinent

[7]J. L. Cook, Studies of the Thorium-Uranium Dicarbide Pseudobinary System in the Presence of Excess Graphite, USAEC Report ORNL-TM-1188, Oak Ridge National Laboratory, September 1965.

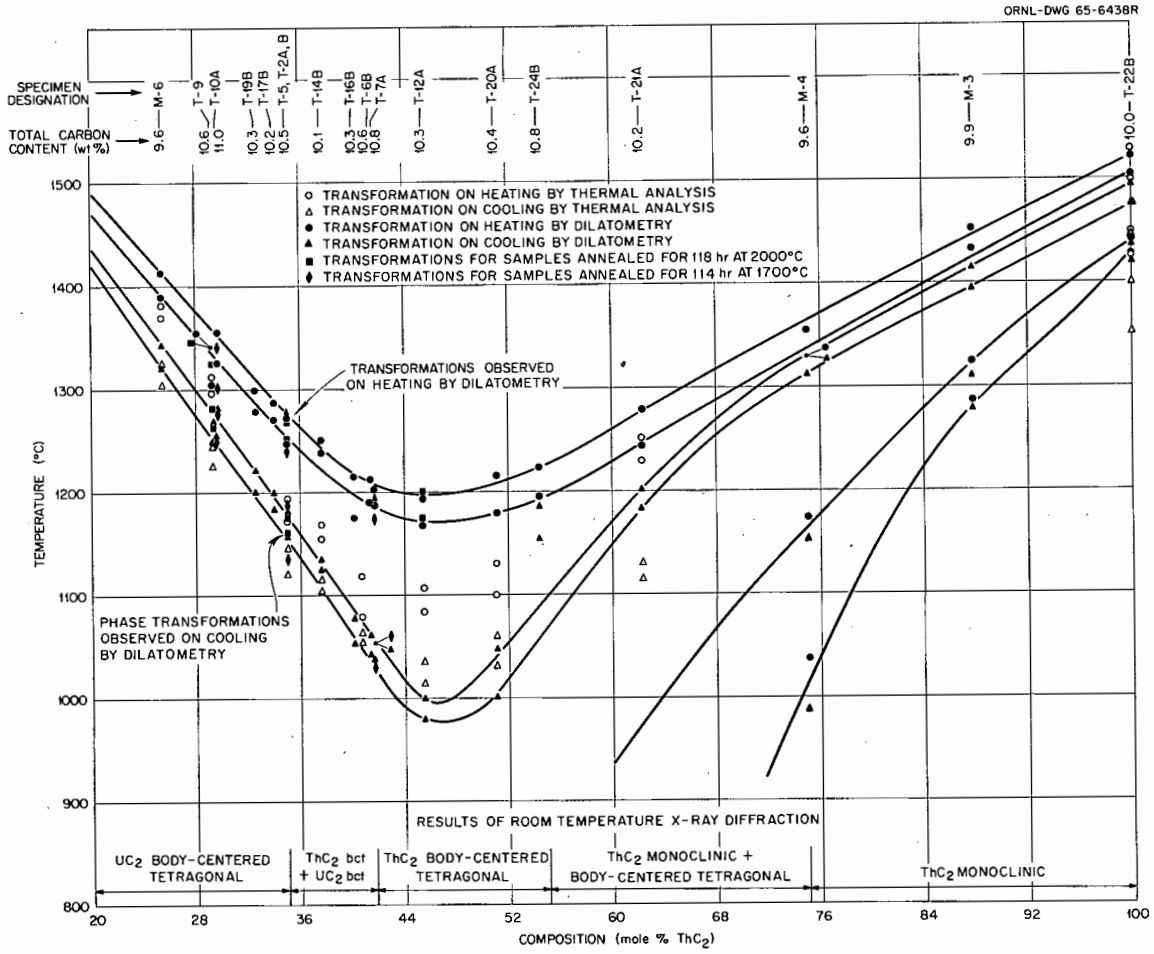

Fig. 1.15. Results of Room-Temperature X-Ray Diffraction Studies of the UC_2-ThC_2 Pseudobinary System in the Presence of Excess Graphite.

dilatometer data for three tests of ThC_2-UC_2 alloys plus data on two different samples of iron are given in Table 1.8.

One sample, T6B, had been measured previously by Cook.[7] Agreement was excellent (i.e., within the stated mean deviation) at the initial break temperature on heating; the temperature difference was about 10° smaller in this experiment than in the data originally reported. The data for the other samples lay, within experimental error, on the smooth curve drawn by Cook. Sample T6B was examined over a period of two weeks in the dilatometer in an attempt to see whether the transitions were a function of previous history. Within the limits of the apparatus, the results were negative.

Table 1.8. Phase Changes Observed by Dilatometry

Sample	Number of Runs	Temperatures[a] (°C)			
		T_{LH}	T_{UH}	T_{UC}	T_{LC}
T6B, UC_2–41.4 mole % ThC_2	13	1193 ± 3.4[b]	1204 ± 3.2	1059 ± 1.6	1051 ± 1.9
T8B, UC_2–40.7 mole % ThC_2	6	1193	1206	1063	1052
T21B, UC_2–62.3 mole % ThC_2	7	1261	1282	1206	1184
"Armco" iron	4	890	923	875	856
"Pure" iron	1	915	935	903	890

[a] T_{LH} is the lower temperature at which a change in slope in the length versus time plot occurred on heating, and T_{UH} is the upper temperature. The difference between the two is the temperature range over which a transition took place. T_{UC} and T_{LC} are comparable numbers for cooling.

[b] The error quoted is the mean deviation from the average temperature.

The data for iron should indicate a measure of the reliability of the dilatometer. The α-γ transition on heating should occur between 910 and 915°C, depending on the heating rate. On cooling it should take place between 910 and 905°C. Since iron has a deleterious effect on 90% Pt–10% Rh vs Pt thermocouples, the "pure" iron sample was wrapped in 0.004-in.-thick platinum foil (around the circumference but not top or bottom) to protect the thermocouple, and a new thermocouple was used.

Oxygen contamination is suspected as the cause for the changes in the thermal behavior of the mixed carbide samples. Cooling curves of ThC_2 across the two known transition temperatures were observed to show a dependence on previous thermal history. Samples that had been melted or heated for long periods above 2000°C showed much more pronounced breaks than samples that were cooled without either prior treatment and "aged" at room temperature (in vacuum of 10^{-3} torr) for a month.

Analysis of Thermodynamic Data for Uranium-Carbon System

J. M. Leitnaker T. G. Godfrey

Thermodynamic data needed on nuclear ceramics are becoming available. The uranium-carbon system is being studied, in particular, but much of the information has not been examined critically or tabulated in useful form. A continuing program is therefore under way to correlate and tabulate such data.

Uranium Monocarbide

The high-temperature heat content data of Herrington and Vozzella (as reported by DeCrescente and Miller)[8] and of Levinson[9] (corrected to $H_T^\circ - H_{298}^\circ$, where T is in °K) agree quite well in their region of overlap. Between 298 and 2014°K (25 and 1741°C), the combined data yield the equation

$$H_T^\circ - H_{298}^\circ = 14.94T + (2.090 \times 10^{-4})\, T^2 + \frac{2.626 \times 10^5}{T} - 5.353 \times 10^3 \quad (1)$$

Above 2014°K the data are best described by a straight line. A cubic equation of the form

$$H_T^\circ - H_{298}^\circ = aT + bT^2 + cT^3 + \frac{d}{T} + e \quad (2)$$

did not fit the data as well at high temperatures, and an extrapolation of Eq. (1) would appear to yield high results. Moreover, the fit of Eq. (2) with the low-temperature heat capacity data of Westrum, Suits, and Lonsdale[10] and of Andon and his co-workers[11] was not as good as with Eq. (1) for which a smooth fit was obtained. Thermal data for UC above 298.15°K (25°C) are listed in Table 1.9.

Uranium Dicarbide

The high-temperature heat content data of Levinson[12] cannot be treated adequately with Eq. (1) because a smooth juncture with the

---

[8]M. A. DeCrescente and A. D. Miller, High Temperature Properties of Uranium Carbide, pp. 342–357 in Carbides in Nuclear Energy, MacMillan, London, 1964.

[9]L. S. Levinson, High Temperature Heat Content of Uranium Carbides, pp. 429–434 in Carbides in Nuclear Energy, MacMillan, London, 1964.

[10]E. F. Westrum, Jr., E. Suits, and H. K. Lonsdale, Advances in Thermophysical Properties at Extreme Temperatures and Pressures, Third Symposium on Thermophysical Properties, Purdue University, 1965.

[11]R. J. L. Andon, J. F. Counsell, J. F. Martin, and H. J. Hedger, Faraday Soc. Trans., 60: 1030 (1964).

[12]L. S. Levinson, J. Chem. Phys., 38: 2105 (1963).

Table 1.9. Thermodynamic Functions for UC

Temperature (°K)	Specific Heat, C_p (cal/deg·mole)	Heat Content, $H_T^\circ - H_{298}^\circ$ (cal/mole)	Entropy, S_T° (cal/deg·mole)	Heat of Formation, $(F_T^\circ - H_{298}^\circ)/T$ (cal/deg·mole)
298.15	12.1100	0	14.2800	-14.2800
300.00	12.1471	22.44	14.3550	-14.2802
350.00	12.9420	651.15	16.2918	-14.4314
400.00	13.4653	1,312.18	18.0564	-14.7759
450.00	13.8307	1,995.08	19.6646	-15.2311
500.00	14.0979	2,693.62	21.1364	-15.7491
550.00	14.3011	3,403.82	22.4900	-16.3012
600.00	14.4607	4,123.01	23.7414	-16.8698
650.00	14.5895	4,849.38	24.9042	-17.4436
700.00	14.6960	5,581.59	25.9894	-18.0157
750.00	14.7860	6,318.70	27.0065	-18.5815
800.00	14.8634	7,059.98	27.9633	-19.1383
850.00	14.9311	7,804.88	28.8664	-19.6842
900.00	14.9913	8,552.97	29.7216	-20.2183
950.00	15.0454	9,303.91	30.5336	-20.7400
1000.00	15.0947	10,057.43	31.3066	-21.2492
1050.00	15.1400	10,813.31	32.0442	-21.7458
1100.00	15.1821	11,571.37	32.7495	-22.2301
1150.00	15.2214	12,331.47	33.4252	-22.7022
1200.00	15.2585	13,093.48	34.0738	-23.1626
1250.00	15.2937	13,857.29	34.6974	-23.6116
1300.00	15.3273	14,622.82	35.2979	-24.0496
1350.00	15.3595	15,389.99	35.8770	-24.4770
1400.00	15.3905	16,158.75	36.4361	-24.8942
1450.00	15.4205	16,929.03	36.9767	-25.3016
1500.00	15.4496	17,700.78	37.5000	-25.6995
1550.00	15.4779	18,473.97	38.0071	-26.0884
1600.00	15.5055	19,248.55	38.4989	-26.4686
1650.00	15.5325	20,024.51	38.9764	-26.8404
1700.00	15.5590	20,801.79	39.4405	-27.2042
1750.00	15.5850	21,580.40	39.8919	-27.5603
1800.00	15.6106	22,360.29	40.3313	-27.9089
1850.00	15.6358	23,141.45	40.7594	-28.2505
1900.00	15.6607	23,923.86	41.1767	-28.5852
1950.00	15.6853	24,707.52	41.5838	-28.9133
2000.00	15.7096	25,492.39	41.9812	-29.2350
2014.03	15.7164	25,712.89	42.0911	-29.3242
2050.00	20.2282	26,440.44	42.4492	-29.5514
2100.00	20.2282	27,451.85	42.9366	-29.8643
2150.00	20.2282	28,463.26	43.4126	-30.1739
2200.00	20.2282	29,474.67	43.8776	-30.4800
2250.00	20.2282	30,486.08	44.3322	-30.7828
2300.00	20.2282	31,497.50	44.7768	-31.0822
2350.00	20.2282	32,508.91	45.2118	-31.3783
2400.00	20.2282	33,520.32	45.6377	-31.6709
2450.00	20.2282	34,531.73	46.0548	-31.9602
2500.00	20.2282	35,543.14	46.4635	-32.2462
2550.00	20.2282	36,554.55	46.8640	-32.5289
2660.00	20.2282	37,565.96	47.2568	-32.8084
2650.00	20.2282	38,577.37	47.6421	-33.0846
2700.00	20.2282	39,588.79	48.0203	-33.3577
2750.00	20.2282	40,600.20	48.3914	-33.6277

available low-temperature data is not obtained.[10,11,13] The most reasonable treatment of the data is believed to be

$$H_T^\circ - H_{298}^\circ = 16.65T + 2.022 \times 10^{-3}T^2 + \frac{3.073 \times 10^5}{T} - 6.175 \times 10^3 \qquad (3)$$

for 298 to 1630°K (25 to 1357°C),

$$H_T^\circ - H_{298}^\circ = 29.54T - 2.162 \times 10^4 \qquad (4)$$

for 1630 to 2060°K (1357 to 1787°C), and

$$H_T^\circ - H_{298}^\circ = 29.43T - 1.872 \times 10^4 \qquad (5)$$

for 2060 to 2483°K (1787 to 2210°C). Thermal data for the dicarbide above 298.15°K (25°C) are given in Table 1.10. The assumption that the composition of the dicarbide was $UC_{1.86}$ necessitated a small adjustment in the low-temperature data. The two points at 300 and 350°K (27 and 77°C) from Westrum's data (suitably adjusted) were used to help smooth the juncture of the high-temperature data to the heat capacity curve at 298.15°K (25°C).

The justification for this admittedly unusual procedure is threefold. First, although Levinson's data seem excessively high for the dicarbide, his results were reasonable for the monocarbide and he obtained good agreement with the only other investigators, Herrington and Vozzella.[8] Second, photomicrographs of UC_2 cooled from above the cubic-tetragonal transformation (1780°C) show precipitates of UC wholly contained within the UC_2 matrix grains. This argues that UC precipitates below the cubic-tetragonal transformation with a resulting heat effect. Third, the thermal data thus obtained yield reasonable results when combined with other thermodynamic data for the system.

---

[13] J. D. Farr, W. G. Witteman, P. L. Stone, and E. F. Westrum, Jr., Advances in Thermophysical Properties at Extreme Temperatures and Pressures, Third Symposium on Thermophysical Properties, Purdue University, 1965.

Table 1.10. Thermodynamic Functions for UC_2

Temperature (°K)	Specific Heat, C_p (cal/deg·mole)	Heat Content, $H_T^\circ - H_{298}^\circ$ (cal/mole)	Entropy, S_T° (cal/deg·mole)	Heat of Formation, $(F_T^\circ - H_{298}^\circ)/T$ (cal/deg·mole)
298.15	14.4000	0	16.2700	-16.2700
300.00	14.4500	26.69	16.3592	-16.2703
350.00	15.5580	778.63	18.6753	-16.4506
400.00	16.3482	1,577.26	20.8070	-16.8638
450.00	16.9535	2,410.40	22.7689	-17.4124
500.00	17.4440	3,270.72	24.5813	-18.0398
550.00	17.8596	4,153.56	26.2638	-18.7119
600.00	18.2240	5,055.83	27.8338	-19.4074
650.00	18.5525	5,975.36	29.3056	-20.1128
700.00	18.8549	6,910.64	30.6917	-20.8194
750.00	19.1379	7,860.53	32.0023	-21.5216
800.00	19.4063	8,824.19	33.2461	-22.2159
850.00	19.6633	9,800.98	34.4304	-22.8998
900.00	19.9115	10,790.38	35.5613	-23.5720
950.00	20.1526	11,792.01	36.6444	-24.2318
1000.00	20.3880	12,805.54	37.6841	-24.8785
1050.00	20.6188	13,830.73	38.6844	-25.5123
1100.00	20.8458	14,867.36	39.6489	-26.1331
1150.00	21.0696	15,915.25	40.5804	-26.7411
1200.00	21.2907	16,974.27	41.4818	-27.3366
1250.00	21.5097	18,044.29	42.3554	-27.9200
1300.00	21.7267	19,125.21	43.2033	-28.4916
1350.00	21.9422	20,216.94	44.0273	-29.0518
1400.00	22.1562	21,319.40	44.8291	-29.6010
1450.00	22.3690	22,432.54	45.6104	-30.1396
1500.00	22.5808	23,556.29	46.3723	-30.6681
1550.00	22.7917	24,690.60	47.1161	-31.1867
1600.00	23.0018	25,835.44	47.8431	-31.6959
1630.72	23.1305	26,543.98	48.2817	-32.0042
1650.00	29.5361	27,113.51	48.6289	-32.1965
1700.00	29.5361	28,590.31	49.5106	-32.6928
1750.00	29.5361	30,067.12	50.3668	-33.1856
1800.00	29.5361	31,543.93	51.1989	-33.6745
1850.00	29.5361	33,020.73	52.0081	-34.1591
1900.00	29.5361	34,497.54	52.7958	-34.6392
1950.00	29.5361	35,974.34	53.5630	-35.1146
2000.00	29.5361	37,451.15	54.3108	-35.5852
2050.00	29.5361	38,927.95	55.0401	-36.0509
2060.00	29.5361	39,223.31	55.1839	-36.1434
2100.00	29.4343	43,089.56	57.0552	-36.5364
2150.00	29.4343	44,561.27	57.7478	-37.0216
2200.00	29.4343	46,032.99	58.4245	-37.5004
2250.00	29.4343	47,504.70	59.0860	-37.9728
2300.00	29.4343	48,976.42	59.7329	-38.4388
2350.00	29.4343	50,448.13	60.3659	-38.8986
2400.00	29.4343	51,919.85	60.9856	-39.3523
2450.00	29.4343	53,391.56	61.5925	-39.8000
2500.00	29.4343	54,863.28	62.1872	-40.2419
2550.00	29.4343	56,334.99	62.7701	-40.6779
2600.00	29.4343	57,806.71	63.3416	-41.1083
2650.00	29.4343	59,278.42	63.9023	-41.5331
2700.00	29.4343	60,750.14	64.4525	-41.9524
2750.00	29.4343	62,221.85	64.9926	-42.3664

Conversion of Sol-Gel Oxide Particles to Carbides

R. L. Hamner

Studies of the conversion of dense sol-gel ThO_2 microspheres to dense ThC_2 microspheres continued.[14] Additional studies were made of the conversion of sol-gel UO_2 and $(Th,U)O_2$ to the carbides.

Conversion of ThO_2 to ThC_2

The materials used in these studies were dense sol-gel microspheres 300 to 400 μ in diameter and carbon in the form of lampblack pretreated in vacuum at 10^{-4} torr for 2 hr at 2200°C. A 1:1 carbon-to-thoria weight ratio was used in most of the experiments. Conversion was accomplished in a cylindrical, horizontally disposed graphite crucible, 5 in. long and 2 1/4 in. in inside diameter, rotating at approximately 44 rpm in a flowing atmosphere of approximately 3 ft^3/hr of argon. Emphasis was placed on optimizing the process with respect to time and temperature and on minimizing reaction bonding and sintering. We found these variables and problems to be closely related to crucible design.

The three crucible designs used are shown in Fig. 1.16. In the smooth-walled crucible (crucible 1) the thoria particles became segregated during rotation, and there was relatively poor and nonuniform carbon-to-thoria contact. This not only inhibited complete conversion but the constant close contact of the particles with each other was conducive to sintering. In the multifinned crucible (crucible 2) which was designed to redisperse the particles and carbon during rotation, the time required for complete conversion was shortened; for example, conversion required 3 hr as compared with 5 to 6 hr in the smooth-walled crucible at 2150°C. However, in this configuration the charge was merely transferred from one fin to another during rotation and about half of the particles became entrained by the fins, where they sintered and bonded. This effect was eliminated by using a single fin in the crucible (crucible 3), which

[14] R. L. Hamner and E. S. Bomar, Conversion of Sol-Gel Microspheres from ThO_2 to ThC_2, pp. 24–27, GCRP Semiann. Progr. Rept. Mar. 31, 1965, USAEC Report ORNL-3807, Oak Ridge National Laboratory.

ORNL-DWG 65-4800

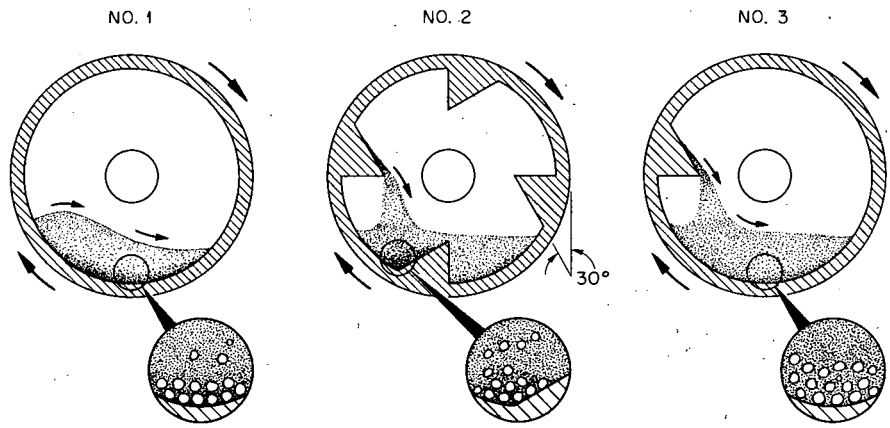

Fig. 1.16. Designs of Crucibles for Preparing $(Th,U)C_2$ Microspheres.

redispersed the charge very satisfactorily without bonding or sintering. The uniform carbon-to-thoria contact in crucible 3 is clearly indicated by the product shown in Fig. 1.17; the unconverted regions are at the centers of the particles, and all particles show approximately the same degree of conversion, as they should if the conversion proceeds uniformly during tumbling.

With crucible 3 and the weight ratio and operating conditions given above, we determined the time required for complete conversion at three temperatures, as follows:

Temperature (°C)	Time for Complete Conversion (hr)
2050	>5
2150	3
2200	2

We further sought to simplify the process by reducing the quantity of carbon used, since a carbon-to-thoria weight ratio of only 0.18 to 1 is needed for complete conversion. Results indicated, however, that the carbon-to-thoria weight ratio should be at least 0.5 to 1 to assure sufficient contact for conversion during tumbling and to inhibit sintering.

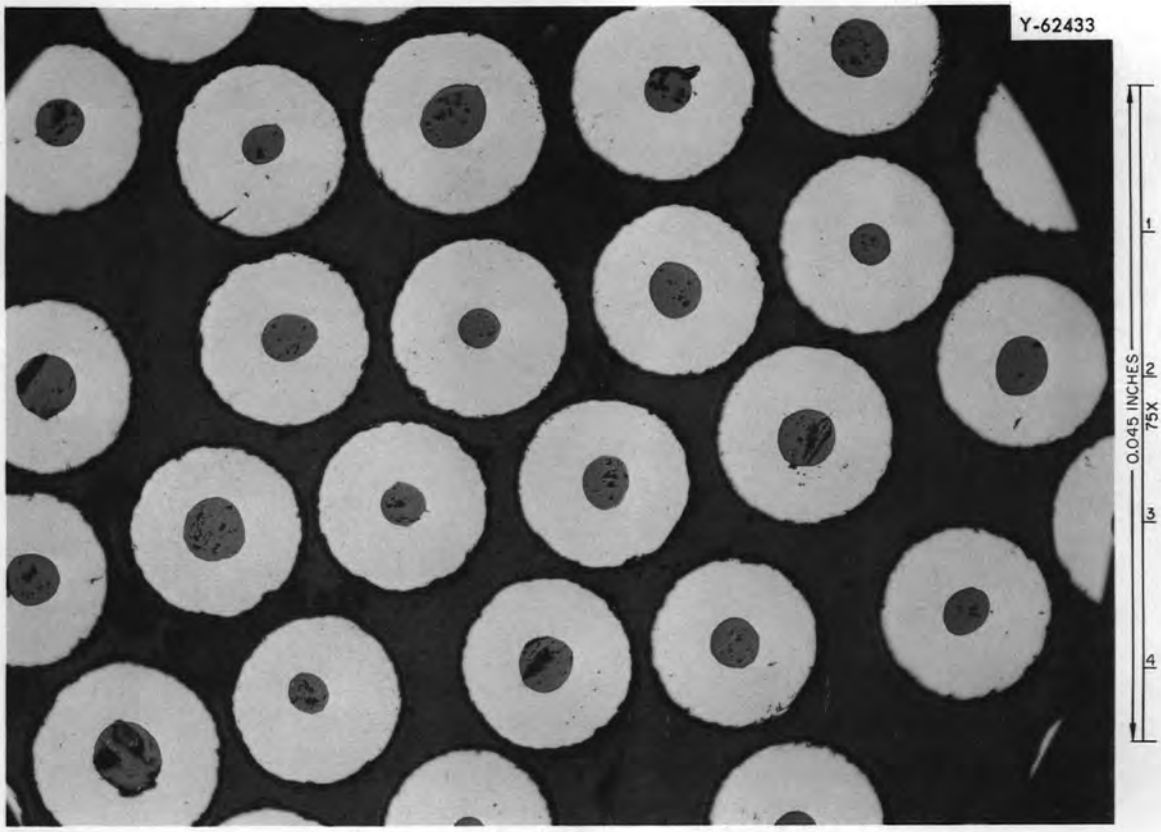

Fig. 1.17. Microstructure of 300- to 400-μ ThO_2 Particles Partially Converted to ThC_2 by Heating with Lampblack for 2 hr at 2150°C in a Rotating Crucible Having One Fin. The white phase is ThC_2, the gray phase is ThO_2, and the black spots are metallographic flaws. As polished. 75×

Conversion of Sol-Gel UO_2 and $(Th,U)O_2$ to Carbides

Conversions of 177- to 250-μ sol-gel (Th–20% U)O_2 microspheres and 100- to 150-μ sol-gel UO_2 microspheres to carbides were made in essentially the same environment as that described for the thoria conversions. The $(Th,U)O_2$ particles were completely converted by heating with lampblack at 2150°C for 2 hr. They retained their sphericity after this treatment but developed large holes near the center of most particles. These pores were eliminated when the conversion temperature was reduced to 2000°C, but most of the particles then contained numerous small isolated spots of material that has not been identified.

Temperatures for the conversion of the sol-gel UO_2 particles ranged from 1700 to 2000°C. Complete conversion was obtained according to metallography after heating for 2 hr at 2000°C or 4 hr at 1900°C, but it was not complete after 3 hr at 1800°C or after 5 hr at 1700°C. Gross porosity was observed in most of the completely converted particles regardless of the conversion temperature. The number and size of these pores decreased with decreasing temperature. Chemical analysis indicated that the oxide particles contained 0.6 wt % (~12 mole %) carbon, half of which should be removed as carbon monoxide during the conversion; this could account for appreciable porosity. For example, wide variations in density and porosity were reported by Kelly and his co-workers[15] in ThC_2 and $(Th,U)C_2$ particles prepared by a sol-gel process in which the carbon for the reaction was incorporated into the particles before heating. To confirm the effect of carbon in the oxide particles, we studied the conversion of fused UO_2 granules averaging 300 to 400 μ in diameter and containing only 60 ppm C. These particles were fully converted to carbide with little or no porosity after heating under the same conditions as the sol-gel UO_2 particles.

Testing and Evaluation of Coated Fuel Particles

Effects of Heat Treatment on Pyrolytic-Carbon-Coated Oxide Particles (R. L. Hamner, R. L. Beatty, H. Beutler)

Studies of the effects of isothermal heat treatment on pyrolytic-carbon-coated UO_2 and ThO_2 particles were continued.[16] The coated fuel particles used in the present studies were fully dense sol-gel ThO_2 microspheres and 85 to 90% dense conventionally prepared spheroidal UO_2 particles, both of which were 150 to 250 μ in diameter. The coating conditions and coating thicknesses of the batches tested are given in Table 1.11.

---

[15] J. L. Kelly, A. T. Kleinsteuber, S. D. Clinton, and O. C. Dean, Ind. Eng. Chem., Process Design Develop., 4: 212 (April 1965).

[16] R. L. Hamner, R. L. Beatty, and J. L. Cook, Effects of Heat Treatment on Pyrolytic-Carbon-Coated Oxide Particles, pp. 12–20, GCRP Semiann. Progr. Rept. Mar. 31, 1965, USAEC Report ORNL-3807, Oak Ridge National Laboratory.

Table 1.11. Conditions for Deposition of Pyrolytic-Carbon Coatings on Particles Used for Heat Treatments and Irradiation Experiments

Batch	Core Particle	Coating Layer	Coating Gas	Hydrocarbon Flow Rate ($cm^3/min \cdot cm^2$)	Application Temperature (°C)	Average Deposition Rate (μ/hr)	Coating Thickness (μ)	Coating Density[a] (g/cm^3)
OR-67	ThO_2 (b)		CH_4	1.33	1400	43.0	110–130	1.56
OR-85	ThO_2 (b)		CH_4	1.33	1400	21.0	40–45	(c)
OR-114	ThO_2 (b)		CH_4	(d)	1400	42.0	250–300	1.50
OR-339	UO_2	Inner	CH_4	3.57	1300	111.0	50	2.03
		Outer	CH_4	0.10	2000	9.1	73	2.03
OR-341	UO_2	Inner	CH_4	0.18	1400	13.1	49	1.47
		Outer	CH_4	0.10	2000	8.9	71	2.03
OR-342	UO_2	Inner	CH_4	0.18	1400	13.1	49	1.47
		Outer	CH_4	1.74	2000	203.0	67	1.75
OR-343	UO_2	Inner	CH_4	3.57	1600	346.0	52	1.51
		Outer	CH_4	1.74	2000	191.0	63	1.79
OR-344	UO_2	Inner	CH_4	3.57	1600	346.0	52	1.51
		Outer	CH_4	0.10	2000	8.1	63	2.00
OR-348	UO_2	Inner	C_2H_2	2.54	1030	960.0	36	0.93
		Outer	CH_4	2.90	1300	106.0	88	2.01
OR-349	UO_2	Inner	CH_4	3.57	1300	100.0	45	2.05
		Outer	CH_4	1.95	2000	200.0	74	1.81
OR-354	UO_2	Inner	C_2H_2	2.47	1030	990.0	41	0.83
		Outer	CH_4	1.95	1800	189.0	85	1.59
OR-352	UC_2	Inner	C_2H_2	2.45	1030	805.0	37	1.00
		Outer	CH_4	1.95	2000	186.0	79	1.82
OR-357	UC_2	Inner	C_2H_2	2.55	1030	850.0	35	1.09
		Outer	CH_4	0.15	2000	10.2	85	2.04
HB-23	UO_2 (b)	Inner	C_2H_2	2.3	1020	540.0	49	1.1
		Inter-mediate	CH_4	1.20	1320	56.0	20	(c)
		Outer	CH_4	0.05	1900	8.0	60	2.03[e]

[a]Determined by sink-float method on disk coatings when possible.

[b]Sol-gel microspheres.

[c]Not determined.

[d]Varied widely during coating run because of excessive thickness of coating.

[e]Composite density of all three layers.

The conditions of heat treatment are summarized below:

Heat Treatment Conditions at a Pressure of 10^{-5} torr

Temperature (°C)	Time (hr)	Batches Heat Treated
1900	168	OR-326
1900	680	OR-348, -354
2000	100	OR-67, -85, -114
2000	500	OR-339, -341, -342, -343, -344, -348, -349, -354

Under these conditions of heat treatment, rupture of the coating and subsequent reaction between the particle and coating occurred in only one batch of coated particles, OR-85. According to macroexamination and radiography, these particles had thin coatings (40 to 45 μ), but only a few particles (<0.1%) failed after 100 hr at 2000°C.

Fuel migration into the coatings of all batches of the coated UO_2 particles was very slight. The microradiograph shown in Fig. 1.18 of batch OR-343 after heating for 500 hr at 2000°C is typical. Only the coated ThO_2 particles developed a gap between particle and coating that could be detected by microradiography; this was accompanied by high-density material in the gap, as observed previously.[16] This high-density material was observed during metallographic examination to be present as transparent or translucent crystals. Electron microprobe analyses showed

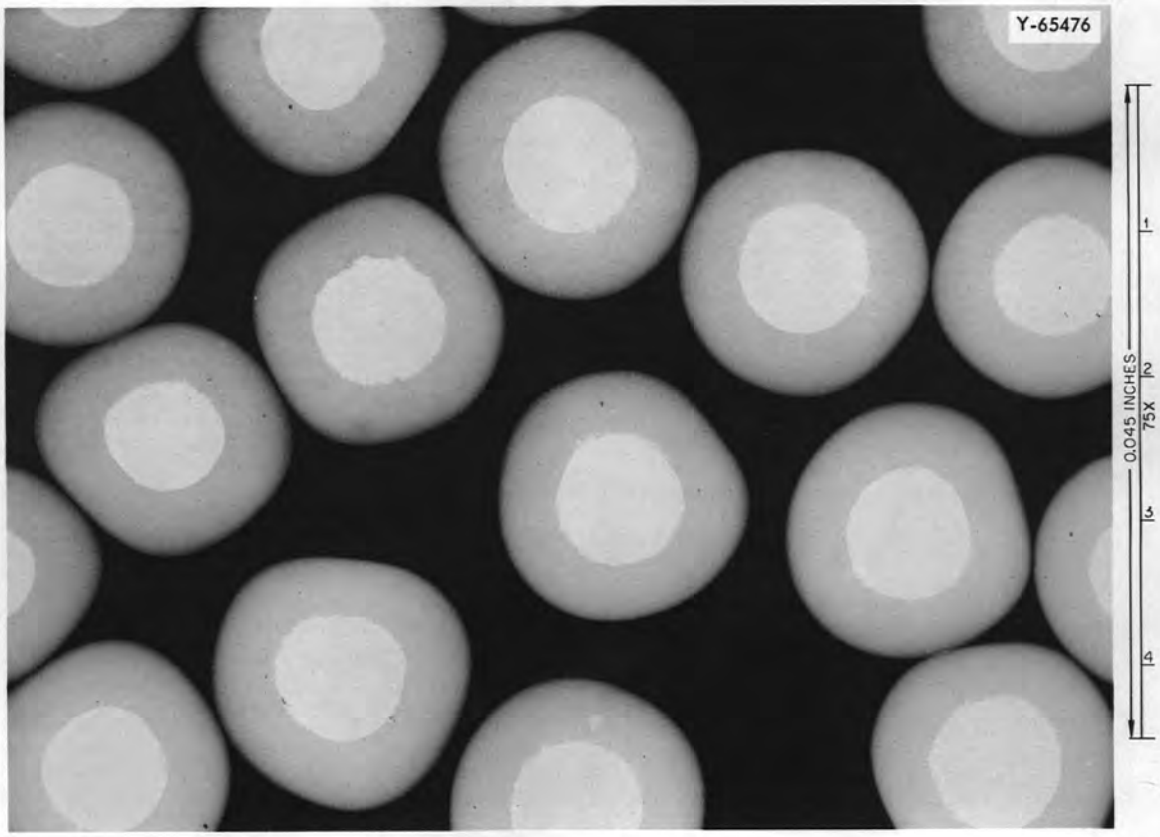

Fig. 1.18. Microradiograph of Pyrolytic-Carbon-Coated UO_2 Particles (Batch OR-343) After Heat Treatment at 2000°C for 500 hr at 10^{-5} torr. 75×

this material to be composed only of thorium and oxygen, and we therefore concluded that it was ThO_2.

Metallographic examination indicated that the only effect of the heat treatments on most of the batches was gap formation between the fuel particles and coatings; the gap was very small in the coated UO_2 particles but sufficient to require impregnation of the particles for polishing. Except for batch OR-354, the results of heat treatments on coated UO_2 particles are typified by the appearance of batch OR-343 in Fig. 1.19. Two small high-density particles are present in the gap, but no other change is evident.

Examination of batch OR-354 after heating at 1900°C for 168 hr disclosed a third phase, which was more prominent after 680 hr at 1900°C.

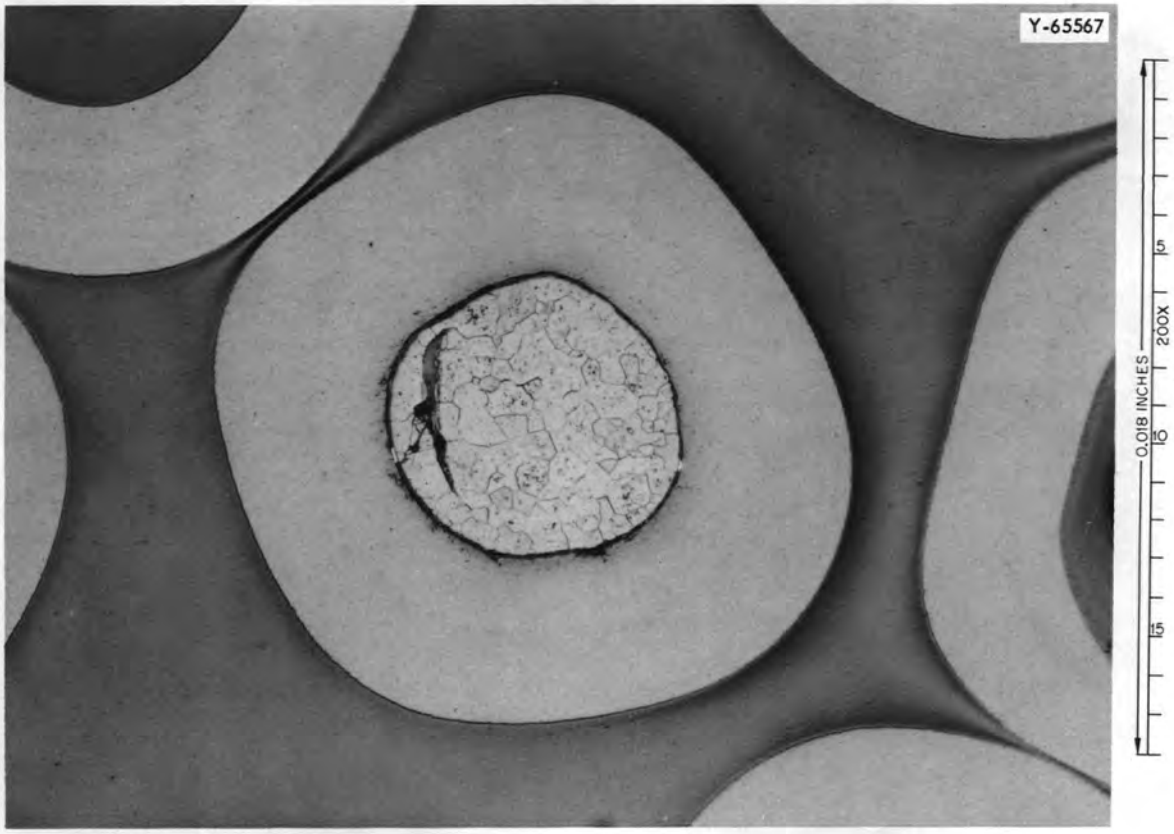

Fig. 1.19. Microstructure of Typical Pyrolytic-Carbon-Coated UO_2 Particle (Batch OR-343) After Heat Treatment for 500 hr at 2000°C and 10^{-5} torr. Etchant: 70 H_2O, 20 H_2O_2, 10 H_2SO_4. 200×

Only a minute quantity of this material was noted in batch OR-348, which also had a porous inner layer. The major difference between these two batches was the lower density and higher deposition temperature of the outer layer on batch OR-354. None of this third-phase material was observed after heat treatment in other batches that had higher density coatings.

This third phase is shown in Fig. 1.20 as gray areas surrounding a UO_2 particle, and it also appears in a crack that extends into the UO_2 particle. The dark zone adjacent to the third-phase material is apparently the uranium that diffused into the porous inner coating. The graphitic material was also present in batch OR-354 after heat treatment for 500 hr at 2000°C. However, after this heat treatment more of the graphite was present and was distributed as larger discontinuous grains, as shown in Fig. 1.21.

Electron diffraction patterns showed this third phase to be graphite without a particularly high degree of preferred orientation. Some opaque particles were also observed in electron micrographs of flake specimens scraped from the UO_2 particles; these were not identifiable by electron diffraction but were similar to particles that have been observed in the diffusion zones of uranium carbide—pyrolytic-carbon couples.[17]

The mechanism for formation of the graphite layer has not been explained; the only source of carbon was the coating, since the UO_2 particles contained only 20 ppm C prior to coating. However, the fact that it was found only in this batch (in a significant quantity), which had a porous inner layer and a relatively low-density outer coating, suggests that carbon monoxide could have diffused slowly through the coating and allowed conversion to proceed. This still would not explain why the final product of reaction under the conditions of heat treatment was graphite rather than uranium carbide.

---

[17] J. O. Stiegler and R. B. Evans III, Actinide-Enhanced Structural Improvements in Pyrolytic Carbon, Metals and Ceramics Div. Ann. Progr. Rept. June 30, 1965, USAEC Report ORNL-3870, Oak Ridge National Laboratory, in press.

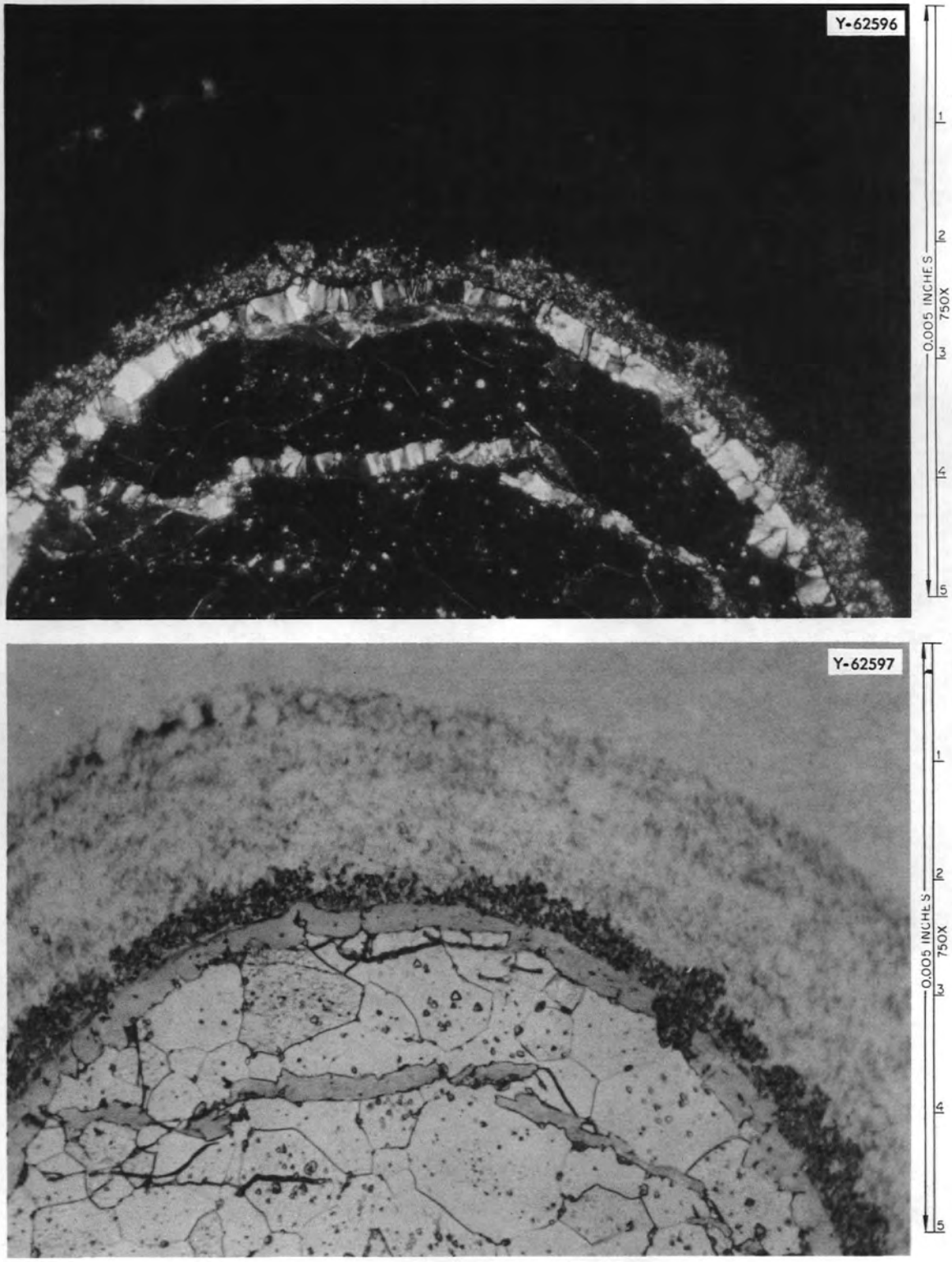

Fig. 1.20. Polished Section of Pyrolytic-Carbon-Coated UO_2 Particles (Batch OR-354) After Heat Treatment for 680 hr at 1900°C and 10^{-5} torr. The dark gray phase at the edge of the UO_2 particles and in the crevice extending into the UO_2 particle is graphite. Etchant: 70 H_2O, 20 H_2O_2, 10 H_2SO_4. 750×

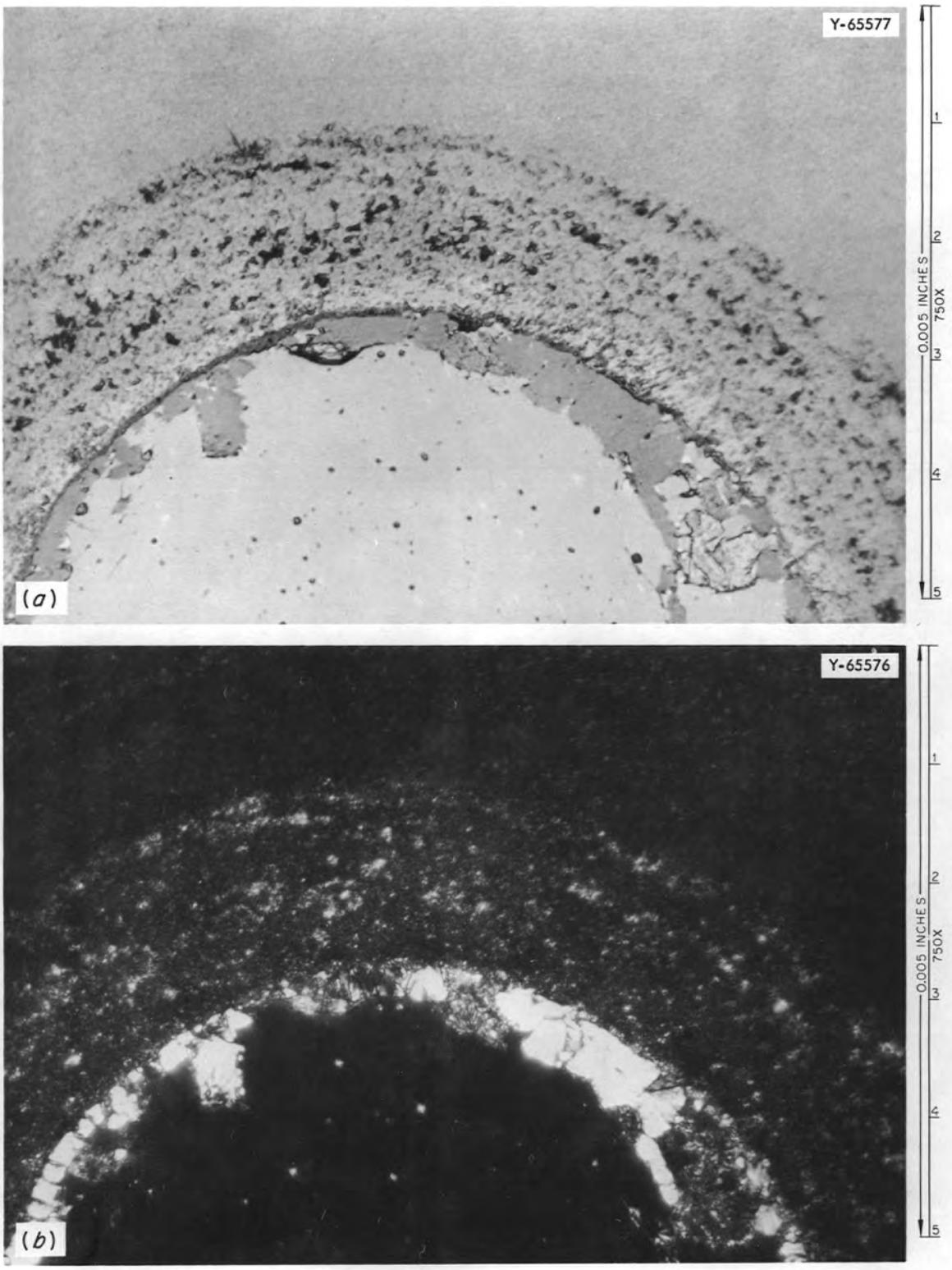

Fig. 1.21. Microstructure of Pyrolytic-Carbon-Coated UO_2 Particles (Batch OR-354) After Heat Treatment at 2000°C for 500 hr at 10^{-5} torr. The dark gray phase in (a) and the bright phase in (b) at the fuel particle-coating interface is graphite. (a) Bright field. (b) Polarized light. As polished. 750×

The crushing strengths of the particles were generally reduced by heat treatment. The greatest reduction was observed with batch OR-67, for which the average crushing load was reduced 57% after 100 hr at 2000°C. This severe effect was due to lack of support for the coating by the oxide particle as a result of gap formation between particle and coating. Two batches of coated UO_2 particles having high-density inner coatings showed slight increases (~5%) in crushing strength after 500 hr at 2000°C. The crushing strengths of all other batches of coated UO_2 were reduced by 6 to 33% without any correlation with the structure or density of the coatings.

Preparation of Coated Fuel Particles for Irradiation Tests
(R. L. Beatty, H. Beutler, D. M. Hewette)

The two-layer coated UO_2 and UC_2 particles designated OR in Table 1.11 of the preceding section will be used for an X-basket irradiation experiment in the ETR. The experiment is designed to test the Scott-Prados model for coated-particle behavior, as explained in a later section. The microstructures of this group of ten lots of coated particles are shown in Fig. 1.22, along with pertinent data on deposition conditions, coating densities, and anisotropy factors. The correlation between the anisotropy factor and the appearance under polarized light should be noted.

The coated sol-gel UO_2 particles designated batch HB-23 in Table 1.11 of the preceding section were prepared for use in a high-burnup irradiation experiment. Table 1.11 gives the deposition conditions for each layer of the three-layer coatings, which were specially designed to withstand high fuel burnup at high temperature.

Evaluation of ETR X-Basket Irradiation Specimens (J. H. Coobs)

The results of routine and special characterization studies on the group of coated fuel particles prepared for the ETR X-basket irradiation experiment mentioned above are given in Table 1.12. Included are results of a special crushing test to determine discontinuities between coating layers and results of activation analysis of the solution obtained in leaching the particles the second time to remove surface contamination.

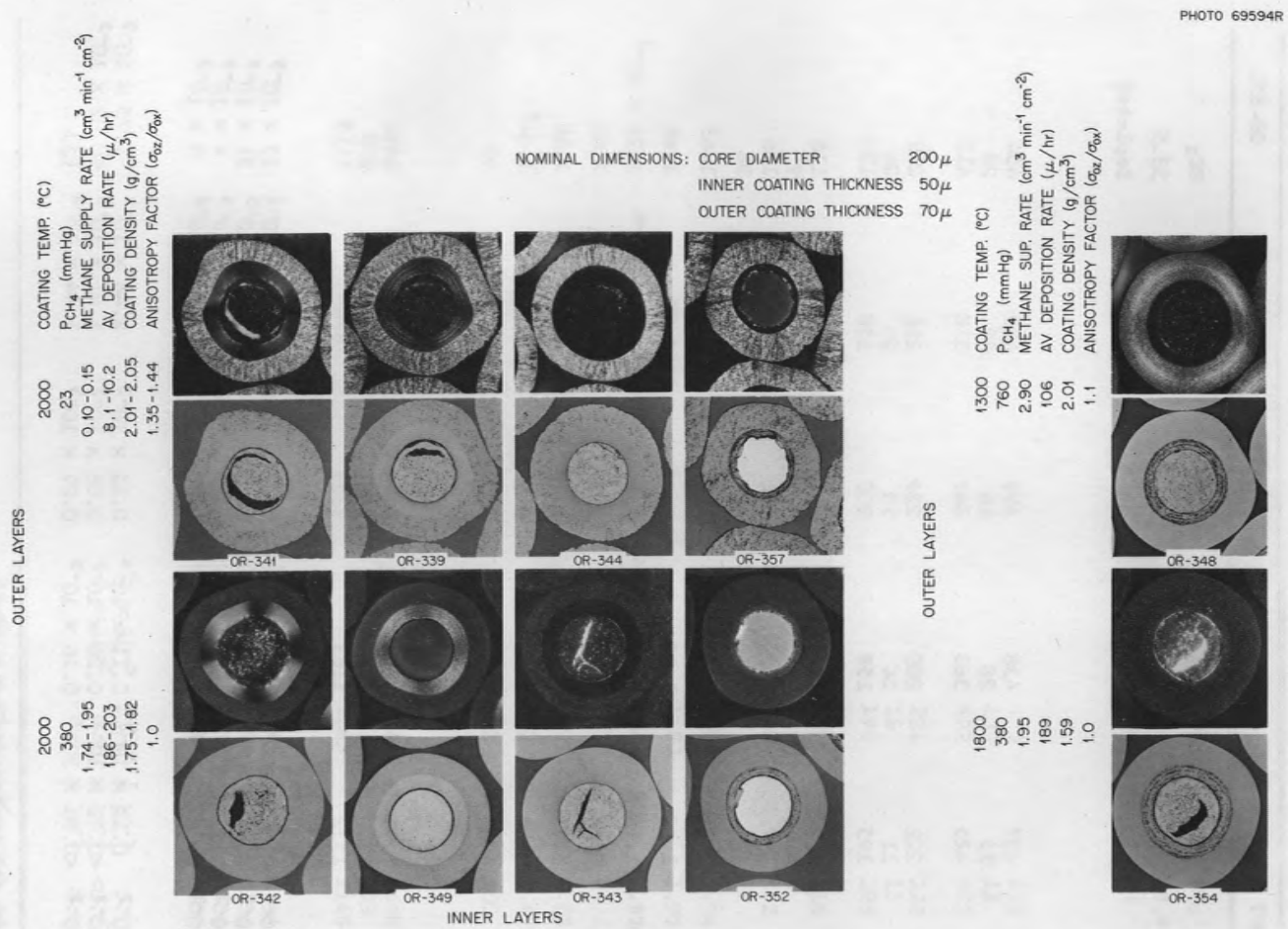

FUEL PARTICLE	UO_2	UO_2	UO_2	UC_2	UO_2
COATING TEMP. (°C)	1400	1300	1600	1030	1030
$P_{HYDROCARBON}$ (mmHg)	38 (CH_4)	760 (CH_4)	760 (CH_4)	760 (C_2H_2)	760 (C_2H_2)
HYDROCARBON SUP. RATE ($cm^3\ min^{-1}\ cm^{-2}$)	0.18	3.57	3.57	2.50	2.50
AV DEPOSITION RATE (μ/hr)	13	105	346	1020-805	960-1000
COATING DENSITY (g/cm^3)	1.47	2.04	1.51	0.94-1.00	0.83-0.93
ANISOTROPY FACTOR (σ_{0z}/σ_{0x})	1.45	1.34	1.0	1.0	1.0

Fig. 1.22. Irradiation Test Specimens Prepared with Different Combinations of Two-Layer Coatings.

Table 1.12. Results of Characterization of Pyrolytic-Carbon-Coated UO_2 Particles for X-Basket Irradiation Experiment

	Batch Designation											
	OR-338	OR-339	OR-341	OR-342	OR-343	OR-344	OR-348	OR-349	OR-352	OR-354	OR-357	OR-351
Fuel material	UO_2	UO_2	UO_2	UO_2	UO_2	UO_2	UO_2	UO_2	UC_2	UO_2	UC_2	UC_2
Uranium content, wt %	35.8	30.0	33.9	38.5	39.6	35.4	32.1	36.1	37.4	37.0	30.9	38.5
^{235}U enrichment, at. %	Depleted	93	93	93	93	93	93	93	93	93	93	Depleted
Particle dimensions,[a] μ												
Total diameter												
Average	464	475	455	446	448	450	467	457	438	477	428	454
Standard deviation	21	13	12	19	14	10	16	13	28	16	28	28
Minimum	432	455	435	412	427	423	423	425	363	442	378	412
Fuel particle diameter												
Average	226	221	222	219	223	218	218	222	208	229	216	219
Standard deviation	19	16	13	19	12	12	18	11	24	13	25	26
Minimum	195	196	198	186	198	193	193	195	158	200	178	170
Coating thickness												
Average	119	127	116	114	112	116	124	117	114	124	106	118
Standard deviation	4	5	4	4	4	5	6	4	7	9	8	7
Minimum	111	118	112	105	106	109	113	108	102	104	92	106
Average inner coating thickness,[b]	52	50	49	49	52	52	36	45	37	42	35	36
Pour density, g/cm³	1.51	1.76	1.74	1.64	1.60	1.75	1.79	1.66	1.58	1.47	1.76	1.63
Tapped density, g/cm³	1.56	1.80	1.77	1.65	1.63	1.76	1.81	1.68	1.62	1.47	1.77	1.66
Average coated particle weight, g	1.23×10^{-4}	1.44×10^{-4}	1.32×10^{-4}	1.16×10^{-4}	1.19×10^{-4}	1.34×10^{-4}	1.43×10^{-4}	1.58×10^{-4}	1.07×10^{-4}	1.28×10^{-4}	1.02×10^{-4}	1.25×10^{-4}
Density of coated particle,[c] g/cm³	2.53	2.77	2.74	2.59	2.59	2.78	2.79	2.64	2.53	2.32	2.73	2.60
Coating density,[d] g/cm³	1.66	1.99	1.78	1.55	1.60	1.84	1.95	1.73	1.75	1.48	1.98	1.68
Inner coating density,[e] g/cm³	1.36[d]	2.03	1.47	1.47	1.51	1.51	0.93[f]	2.05	1.00[f]	0.83[f]	1.09[f]	1.04[f]
Particles with discontinuity at interface,[g] %	0	100	100	100	0	92	0	40	40	60	80	50
Crushing load,[h] g												
Average	1878	1511	1458	2156	1606	1297	1894	1999	1494	1639	1055	1432
Standard deviation	167	157	153	594	290	191	240	234	174	186	134	199
Minimum	1494	1183	1148	1282	1120	946	1496	1532	1163	1329	874	1115
Surface contamination, % of total U												
As coated	14×10^{-3}	0.10×10^{-3}	0.06×10^{-3}	$<0.01 \times 10^{-3}$	0.09×10^{-3}	0.22×10^{-3}	$<0.01 \times 10^{-3}$	0.02×10^{-3}	8.35×10^{-3}	1.10×10^{-3}	9.16×10^{-3}	13×10^{-3}
After first leach	24×10^{-3}	0.03×10^{-3}	0.04×10^{-3}	$<0.01 \times 10^{-3}$	0.14×10^{-3}	0.26×10^{-3}	$<0.01 \times 10^{-3}$	0.01×10^{-3}	8.91×10^{-3}	1.42×10^{-3}	9.81×10^{-3}	31×10^{-3}
After first leach and thermal cycle	$<1 \times 10^{-3}$	0.08×10^{-3}	0.04×10^{-3}	0.02×10^{-3}	0.26×10^{-3}	0.27×10^{-3}	0.14×10^{-3}	0.12×10^{-3}	10.96×10^{-3}	4.32×10^{-3}	8.86×10^{-3}	4×10^{-3}
After thermal cycle and second leach	1×10^{-3}	0.06×10^{-3}	0.05×10^{-3}	0.03×10^{-3}	0.16×10^{-3}	0.24×10^{-3}	0.09×10^{-3}	0.08×10^{-3}	11.00×10^{-3}	4.07×10^{-3}	10.39×10^{-3}	3×10^{-3}
Fuel removal, % of total U												
First leach	$<0.03 \times 10^{-3}$	13.48×10^{-3}	0.19×10^{-3}	10.45×10^{-3}	0.57×10^{-3}	0.48×10^{-3}	1.61×10^{-3}	0.12×10^{-3}	0.11×10^{-3}	0.12×10^{-3}	2.46×10^{-3}	1.75×10^{-3}
Second leach	$<0.02 \times 10^{-3}$	0.10×10^{-3}	$<0.01 \times 10^{-3}$	$<0.01 \times 10^{-3}$	0.05×10^{-3}	$<0.01 \times 10^{-3}$	$<0.01 \times 10^{-3}$	$<0.01 \times 10^{-3}$	0.20×10^{-3}	0.08×10^{-3}	1.21×10^{-3}	$<0.02 \times 10^{-3}$
Second leach measured by activation analysis[i]	(j)	0.12×10^{-3}	0.03×10^{-3}	0.02×10^{-3}	0.03×10^{-3}	0.01×10^{-3}	$<0.01 \times 10^{-3}$	$<0.01 \times 10^{-3}$	0.16×10^{-3}	0.07×10^{-3}	1.44×10^{-3}	(j)

[a]Measured on 25 randomly selected particles from a microradiograph of a riffled sample.

[b]Measured by random scanning of a microradiograph.

[c]Measured with helium pycnometer.

[d]Calculated from the pycnometer density of the coated particles and the amount of carbon collected when particles were oxidized.

[e]Average of two measurements on each specimen; sink-float technique used; except where noted.

[f]Calculated from mercury porosimeter and carbon analysis data.

[g]Determined by cracking coated particles between anvils of a micrometer; percentages given represent the fraction of particles that exhibited clean separation between layers.

[h]Twenty-five particles were crushed from each lot.

[i]Measured by activation analysis of a portion of leach solution.

[j]Not measured.

Mathematical Simulation of Coated-Particle Behavior (J. W. Prados, J. L. Scott)

We developed a mathematical model for predicting stresses and strains in pyrolytic-carbon coatings surrounding fuel microspheres under irradiation. The stresses arise from differential thermal expansion of the fuel particle against the coating, fuel swelling, fission-gas release, damage from recoils, and anisotropic dimensional changes in pyrolytic carbon resulting from thermal expansion and fast-neutron damage. With this model we can evaluate the relative merits of low- or high-density fuel particles, single- or multilayer coatings, and high or low values for coating thickness, density, and strength. Although lack of precise knowledge of the properties of the pyrolytic-carbon coatings and their behavior under irradiation requires that results calculated from the model be interpreted with caution, the results do furnish valuable insight into the relationships between a coated particle's configuration and environment in determining its service life and thus provide a rational basis for the planning and interpretation of irradiation tests. Details of the mathematical development and a computer program, STRETCH, for performing the necessary calculations were discussed in an earlier report.[18]

We performed a series of calculations using the model to determine the effects of coated-particle dimensions and properties on expected life under irradiation. Geometric parameters and irradiation conditions investigated were typical of coated particles of interest in current reactor technology[19–22] and are summarized in Table 1.13. The basic coating configuration investigated is shown in Fig. 1.23. The pyrolytic-carbon coating is formed in two layers that consist of an impervious outer layer to provide primary fission-product containment and a low-density inner layer.

---

[18]J. W. Prados and J. L. Scott, Analysis of Stress and Strain in Spherical Shells of Pyrolytic Carbon, USAEC Report ORNL-3553, Oak Ridge National Laboratory, June 1964.

[19]E. S. Bomar and R. J. Gray, Thorium-Uranium Carbides for Coated-Particle Graphite Fuels, pp. 703–728 in Proceedings of a Symposium on Compounds of Interest in Nuclear Reactor Technology, Boulder, Colorado, Nuclear Metallurgy, Vol. X, Am. Inst. Mining Met. Engrs., 1964.

[20]R. W. Dayton, J. H. Oxley, and C. W. Townley, Ceramic Coated-Particle Nuclear Fuels, J. Nucl. Mater., 11: 1–31 (January 1964).

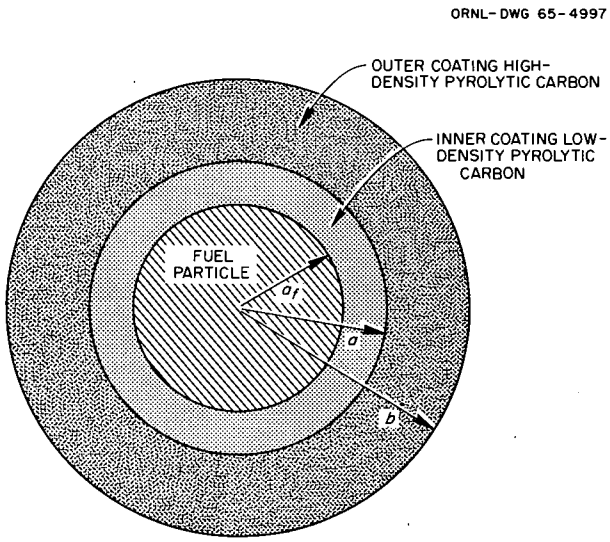

Fig. 1.23. Model of Fuel Particle with Two-Layer Coating.

It is expected that the inner layer will densify under irradiation and thus provide free volume to accommodate gaseous fission products released from the fuel, as well as swelling of the fuel particle itself. The metallographic appearance of particle coatings after irradiation suggests that such densification does occur.

Coating failure is assumed to occur when the tangential tensile stress at any point in the outer coating layer exceeds a preselected value (chosen in this study as 30,000 psi). The model predicts that two modes of failure can occur: (1) failure initiated at the inner surface of the outer coating, resulting from a combination of fuel-particle swelling, fission-gas pressure, and shrinkage of the outer coating due to fast-neutron damage, and (2) failure initiated at the outer coating surface resulting from anisotropic dimensional changes (also due to fast-neutron damage)

---

[21] W. V. Goeddel, Development and Utilization of Pyrolytic-Carbon-Coated Fuel for the High-Temperature Gas-Cooled Reactor, Nucl. Sci. Eng., 20: 201–218 (October 1964).

[22] J. B. Sayers, K. S. B. Rose, J. H. Coobs, G. P. Hauser, and C. Vivante, The Irradiation Behavior of Coated-Particle Fuels, pp. 912–962 in Proceedings of a Symposium on Carbides in Nuclear Energy, Harwell, England, November 5–7, 1963, MacMillan, London, 1964.

Table 1.13. Dimensions and Test Conditions Employed in Coated-Particle Simulation Calculations

Test Conditions	Limits and Dimensions
Ratios of inner to outer radius of outer coating layer, a/b	0.5, 0.6, 0.667, 0.75, 0.86
Ratio of fuel radius to inner radius of outer coating, a_f/a	0.667
Ratios of free volume provided by inner coating to fuel volume, F_V	0.475, 0.95, 1.425, 1.90
Anisotropies of outer coating	1.0, 1.5, 2.0, 3.0
Fuel material	UC_2
Irradiation temperatures, °C	800, 1400
Fraction of fission gas released, f	0.01, 1.0
Neutron dose, neutrons/cm^2	0 to 2×10^{22}

in the pyrolytic-carbon structure. The first mode is observed with highly enriched fuel particles operating to high burnups or, with isotropic coatings, in particles of low uranium enrichment or high thorium content where large fast-neutron doses (and hence extensive coating shrinkage) may occur without significant burnup of fuel. The second mode is restricted to anisotropic outer coatings and fuel compositions favoring the high-dose low-burnup condition just referred to. By performing calculations with our model for a given coated-particle configuration with varying degrees of fuel enrichment and varying ratios of fast- to thermal-neutron dose, it is possible to define a "failure locus" or curve for the given configuration. Such a curve relates values of fast-neutron dose and burnup below which a specified tensile stress in the coating will not be exceeded. Coated-particle failure would not be expected so long as the design burnup and accumulated fast-neutron dose were held below the limits specified by the failure locus.

Typical failure loci for coated-particle configurations listed in Table 1.13 are shown in Figs. 1.24 through 1.27. In Figs. 1.24 and 1.25 the parametric curves show the effect of varying the ratio of free volume

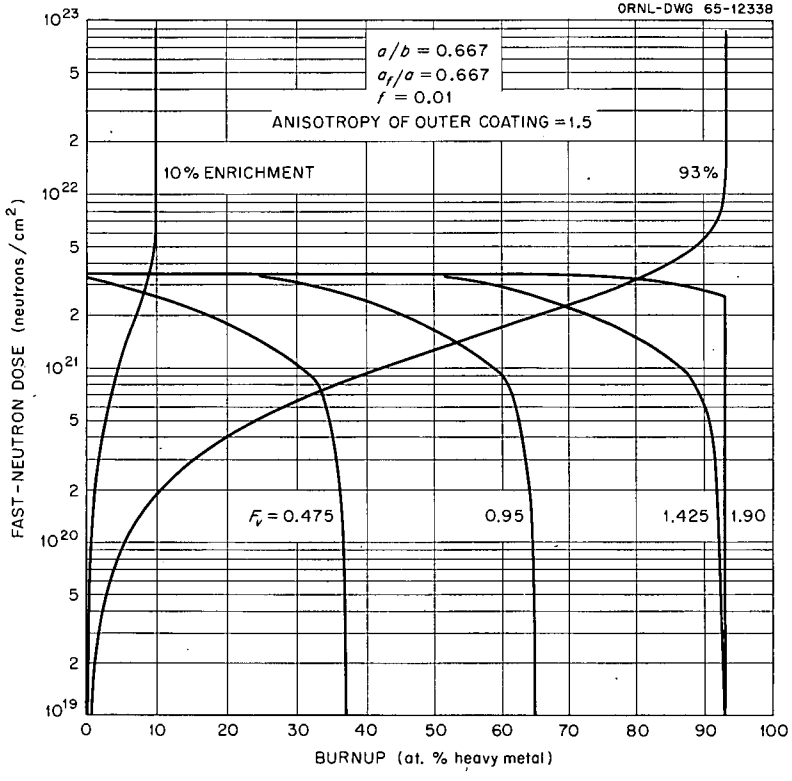

Fig. 1.24. Failure Loci for Coated Particles with Various Values of Fractional Free Volume, F_V, and Fractional Fission-Gas Release, f, of 0.01.

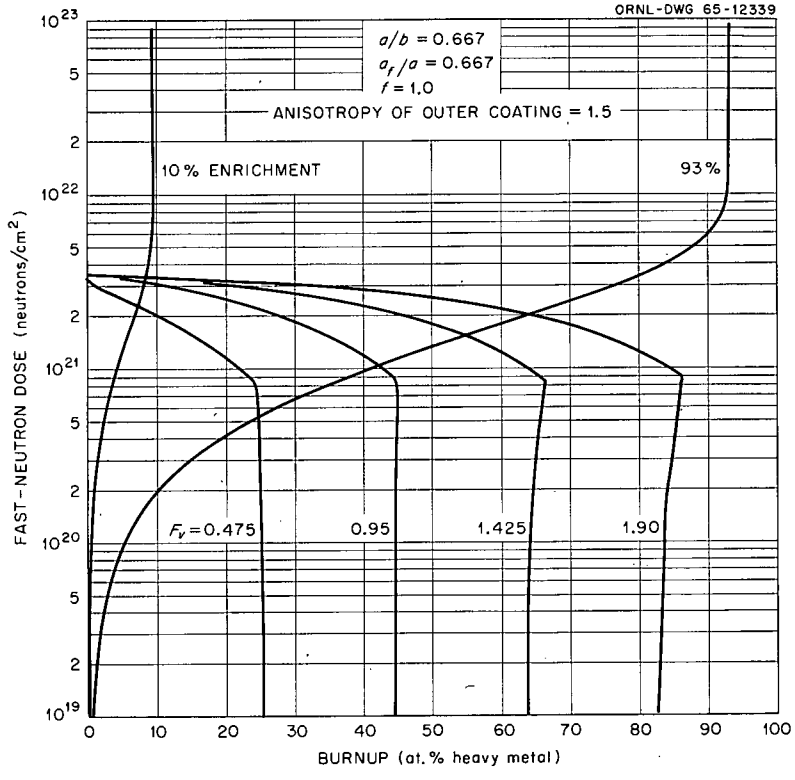

Fig. 1.25. Failure Loci for Coated Particles with Various Values of Fractional Free Volume, F_V, and Fractional Fission-Gas Release of 1.0.

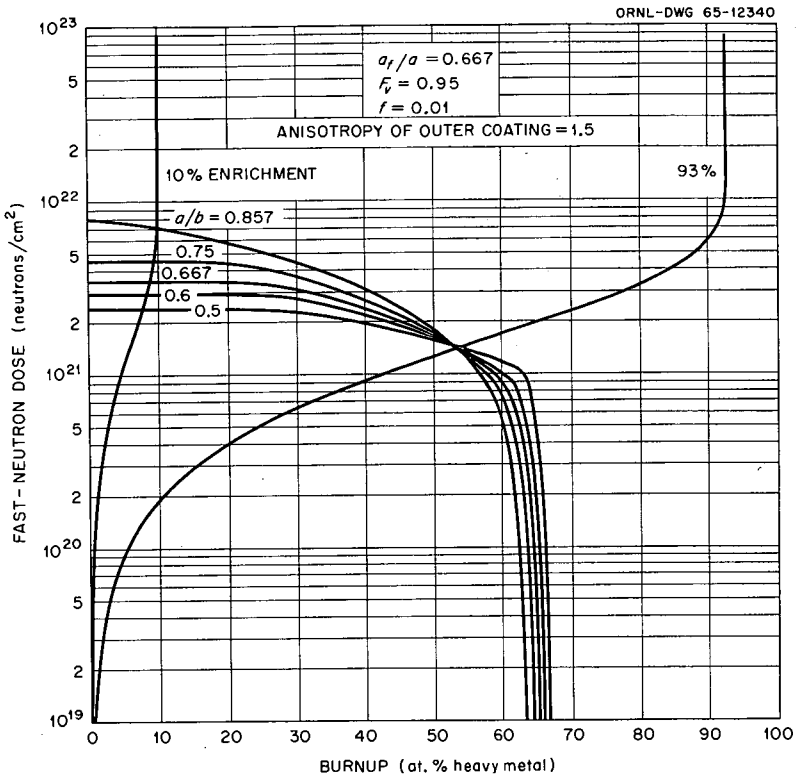

Fig. 1.26. Failure Loci for Coated Particles with Various Thicknesses of Outer Coating and Fractional Fission-Gas Release of 0.01.

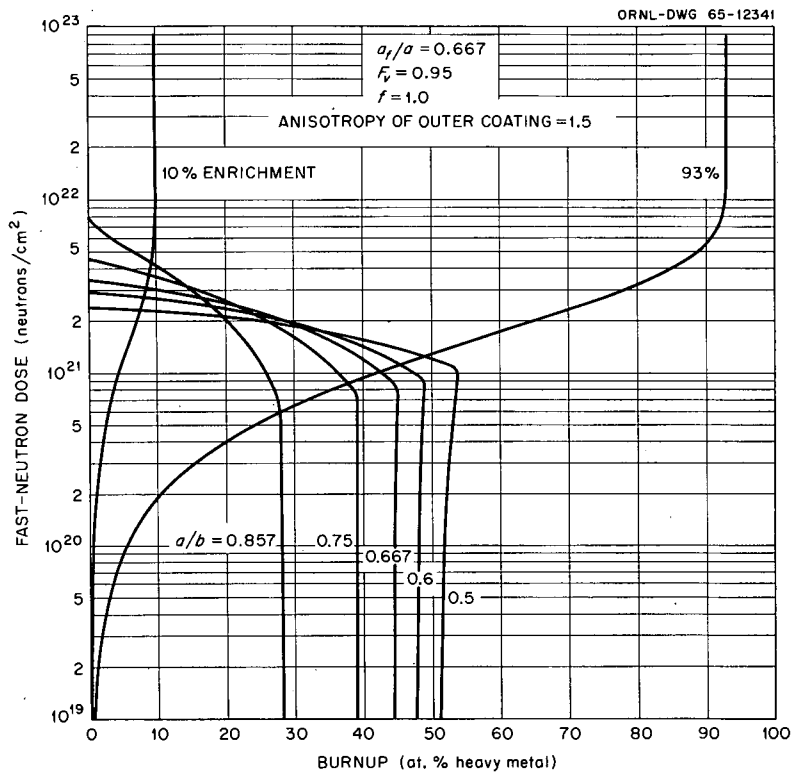

Fig. 1.27. Failure Loci for Coated Particles with Various Thicknesses of Outer Coating and Fractional Fission-Gas Release of 1.0.

to fuel volume on expected coated-particle life, with all other properties held constant. The two figures are for 1 and 100% fission-gas release from the fuel, respectively. Similar curves in Figs. 1.26 and 1.27 show the effect of varying the outer coating thickness (represented as the ratio of inner to outer radius of the coating). On each plot, the relations between fast-neutron dose and burnup are shown for UC_2 particles with 10 and 93% ^{235}U enrichment (and a fast- to thermal-neutron flux ratio of unity). These curves permit estimates of the actual dose and burnup at failure for such fuels and provide a rough indication of values for fuels of intermediate enrichment. Note that all coated-particle dimensions are expressed as ratios and that the results should apply to particles of different sizes so long as the dimensional ratios are unchanged.

Based on the results of these calculations, we arrive at the following predictions regarding the effect of configuration and environment on the expected service life of a coated fuel particle.

1. From Figs. 1.24 and 1.25, it may be seen that the most important single factor in promoting coating longevity is the provision of adequate free volume for accommodation of fuel particle swelling and fission gas. A reasonable value for this free volume would be 2% of the fuel particle volume per atom percent burnup desired in the fuel. Free volume may be provided by use of a low-density fuel particle, by the use of a porous inner coating that densifies readily when subjected to fission recoil bombardment, by manufacturing techniques that actually provide empty space between fuel and coating, or by a combination of these.

2. Primary containment of fission products should be provided by an outer coating whose inner surface is protected against fission recoils. The thickness of this coating should be such that the ratio of inner-to-outer diameters is approximately 2/3. Figure 1.27 shows that thicker coatings do not provide an appreciable increase in strength and may be more subject to failure from anisotropic dimensional change.

3. Comparison of Figs. 1.24 and 1.25 with Figs. 1.26 and 1.27 indicates that the release of gaseous fission products from the fuel has a secondary effect on coating life, except for thin coatings ($a/b > 0.667$). In general, the maximum burnup attainable is reduced by about 10% in going

from 1 to 100% fission-gas release, and this effect could be easily counteracted by provision of additional free volume. Hence, the use of a low-density fuel particle to help provide this free volume should have no adverse effect on coated-particle life.

4. Two distinct modes of coating failure may occur: (1) failure initiated at the inner-coating surface as a result of a combination of fuel particle swelling, fission-gas pressure, and outer coating shrinkage, and (2) failure initiated at the outer coating surface as a result of anisotropic thermal expansion and fast-neutron damage to the pyrolytic-carbon structure. The transition from one mode to another is shown by sudden changes in slope of the failure loci. We should point out that even isotropic coatings are subject to failure from fast-neutron damage if sufficient shrinkage occurs.

When failure occurs by the first mode, the maximum fuel burnup attained depends primarily on the free volume provided and the degree of fuel swelling, and only weakly on other coated-particle properties.

The predictions can be employed to arrive at a satisfactory coated-particle configuration with a minimum of information on the properties of the particle and coating materials. Accurate economic optimization of coated-particle design must await critical comparison of the mathematical model predictions with the results of controlled experimental tests and the development of any necessary corrections.

Coated-Particle-Survey Irradiation Tests (J. L. Scott, J. W. Prados)

We designed and built an irradiation capsule to provide a relatively simple and low-cost method of evaluating the integrity of a large number of batches of pyrolytic-carbon-coated fuel particles simultaneously. The capsule is 36 in. long, has an outside diameter of 1 1/8 in., and contains 28 compartments for individual batches of coated particles. The capsule is divided into three sections: the central section, which will operate at a centerline temperature of 1400°C, and the two end sections, which will operate at a centerline temperature of 400°C.

For economy, no instrumentation was provided; however, we incorporated fusible alloys within individual bottles to measure the maximum

temperatures. A schematic diagram of the capsule is shown in Fig. 1.28. The capsule is designed for irradiation in the ETR or MTR X-basket facilities. An individual bottle for containing coated particles is shown in Fig. 1.29.

The first capsule in the series, designated ORNL-43-89, is presently being irradiated to test coating variables such as coating temperature, density, and anisotropy. The data will also serve to reduce uncertainties in the Scott-Prados model of coated-particle behavior, which was discussed in the preceding section. The capsule contains ten different experimental batches of particles coated at ORNL plus two control batches (see Tables 1.11 and 1.12 for descriptions). All fuel cores are approximately 200 μ in diameter, and the duplex experimental coatings consist of approximately 50-μ-thick inner layers and 70-μ-thick outer layers.

With the mathematical model described in the preceding section for simulating the behavior of coated particles under irradiation, we performed a series of calculations to determine the conditions under which failure might be expected to occur for these coated particles. It was postulated in the calculations that the inner layer of the two-layer coating would undergo densification during irradiation to provide a free volume to accommodate fuel swelling and released fission gas. Two alternate assumptions regarding this densification were considered: (1) that the inner layer would attain theoretical density (2.26 g/cm^3), and (2) that the inner layer would attain an average density halfway between its initial density and the theoretical value.

Particle batch designations and significant properties are listed in Table 1.14, together with calculated failure conditions (burnup and

ORNL-DWG 65-2802

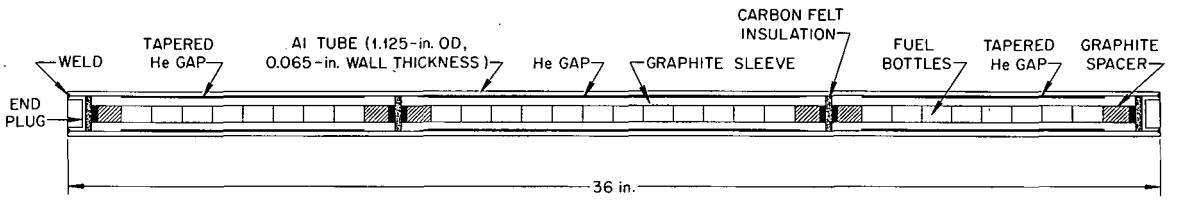

Fig. 1.28. Capsule for Irradiation of Coated Particles in ETR and MTR X-Basket Facilities.

Table 1.14. Properties and Predicted Burnup and Fast-Neutron Dose at Failure for Coated Particles in X-Basket Irradiation Experiment

Coated Particle Batch Designation	Anisotropy Factor	Effective Porosity of Inner Coating Layer	Approximate Thickness of Inner Coating Layer (μ)	Estimated Burnup at Failure (at. % U)		Estimated Fast-Neutron Dose at Failure (neutrons/cm^2)	
				100% Densification of Inner Layer	50% Densification of Inner Layer	100% Densification of Inner Layer	50% Densification of Inner Layer
						$\times 10^{20}$	$\times 10^{20}$
OR-339	1.4	0.2	50	39	28	9.1	6.1
OR-344	1.4	0.4	50	55	39	14.9	9.2
OR-341	1.4	0.5	50	61	44	18.0	10.6
OR-357	1.4	0.5	40	54	38	14.4	8.7
OR-348	1.1	0.6	40	59	42	16.7	10.0
OR-349	1.0	0.2	40	32	24	7.0	4.9
OR-343	1.0	0.4	50	56	38	15.6	8.6
OR-342	1.0	0.5	50	65	43	20.0	10.2
OR-352	1.0	0.6	40	62	40	18.1	9.3
OR-354	1.0	0.6	40	62	40	18.1	9.3

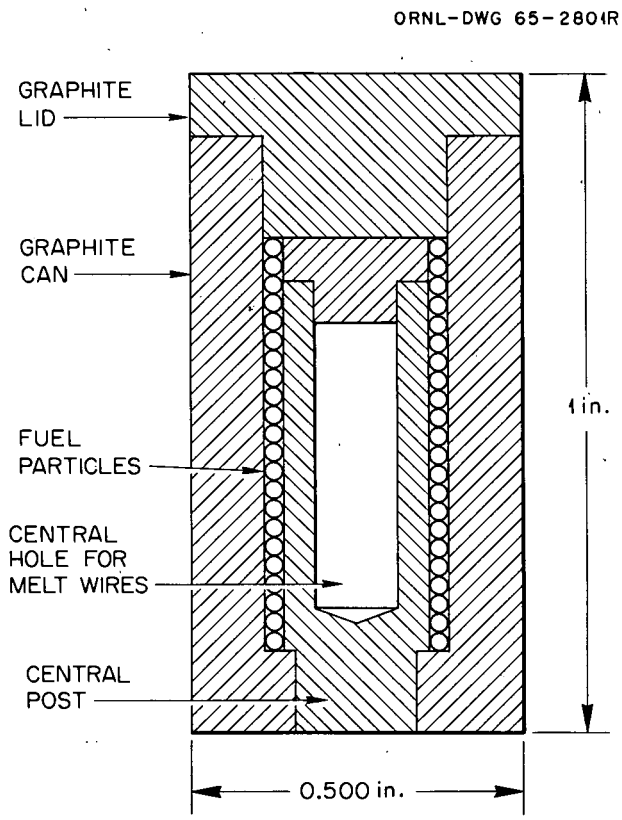

Fig. 1.29. Fuel Bottle for Containing Coated Particles During Irradiation.

fast-neutron dose) under the assumptions of both 50 and 100% densification of the inner coating layer. It was assumed that the ratio of fast- to thermal-neutron flux at the experiment locations was unity and that failure would occur when the tensile stress in the coating exceeded 30,000 psi. The fuel particle assumed in all calculations was a 220-μ-diam UO_2 microsphere with 90% theoretical density and 93% enrichment of the uranium in ^{235}U; the overall coated-particle diameter was taken as 460 μ.

General Evaluation of Coated Fuel Particles (J. H. Coobs)

Results from routine characterization studies on pyrolytic-carbon-coated fuel particles received from the Carbon Products Division of Union Carbide Corporation (NCC) and the General Atomic Division of the General Dynamics Corporation are presented in Table 1.15. Many of these batches

Table 1.15. Results of Characterization of Pyrolytic-Carbon-Coated Fuel Particles

	Batch Designation													
	NCC-220	NCC-222	NCC-OR-6F	NCC-OR-7F	NCC-OR-10F	NCC-OR-11F	GA-320	GA-321-1	GA-321-2	GA-322	GA-323	GA-324	OR-337	HB-23
Fuel material	UC_2	$(Th,U)C_2$	ThO_2	ThO_2	$(Th,U)O_2$	$(Th,U)O_2$	UC_2	$(Th,U)C_2$	$(Th,U)C_2$	UC_2	$(Th,U)O_2$	ThO_2	UO_2	UO_2
Uranium content, wt %	(a)	5.55			2.6	3.2	20.4	18.4	17.2	64.6	4.5		30.6	17.8
Thorium content, wt %		25.4	40.0	38.9	32.2	36.2		17.6	17.2		53.9	48.4		
Thorium-to-uranium ratio		4.93[b]			12.4	11.3		0.96	1.0		12.0			
Enrichment in ^{235}U, at. %	93	93			93	93	93	93	93	Normal	93		93	93
Particle dimensions,[c] μ														
Total diameter														
Average	411	437	411	421	445	472	379	395	375	579	542	412	481	407
Standard deviation	16	52	26	31	29	48	25	30	25	45	23	11	13	14
Minimum	364	341	371	370	403	408	353	351	334	524	504	393	464	385
Core diameter														
Average	199	214	216	219	216	247	125	195	181	382	343	233	222	148
Standard deviation	24	37	30	27	34	62	9	24	20	38	23	9	15	12
Minimum	154	148	166	171	146	138	111	154	156	338	318	220	193	126
Coating thickness														
Average	106	112	98	100	114	112	127	100	97	99	100	89	129	129
Standard deviation	13	13	2	7	8	10	11	7	5	7	6	3	5	7
Minimum	72	86	93	91	108	103	112	89	89	87	93	81	123	118
Pour density, g/cm^3	(a)	1.66	1.81	1.74	1.73	1.85	1.20	1.68	(a)	2.70	2.26	1.96	1.65	1.52
Tapped density, g/cm^3	(a)	1.72	1.82	1.78	1.76	1.87	1.21	1.71	(a)	2.74	2.29	1.98	1.68	1.54
Average coated particle weight, g	(a)	1.15×10^{-4}	1.19×10^{-4}	1.22×10^{-4}	1.42×10^{-4}	1.71×10^{-4}	0.51×10^{-4}	0.86×10^{-4}	(a)	4.23×10^{-4}	3.19×10^{-4}	1.14×10^{-4}	1.43×10^{-4}	0.82×10^{-4}
Density of coated particle,[d] g/cm^3	(a)	2.67	3.04	3.03	2.90	3.10	(a)	(a)	(a)	(a)	3.77	3.25	2.66	2.43
Coating density,[e] g/cm^3	(a)	1.93	1.92	1.93	1.99	2.01	(a)	(a)	(a)	(a)	1.66	1.75	1.89	2.03
Coating structure	Duplex	Duplex	Duplex	Duplex	Duplex	Duplex	Biso[f]	Biso[f]	Biso[f]	Biso[f]	Biso[f]	Biso[f]	Duplex	Triplex
Crushing load,[g] g														
Average	(a)	1780	1250	1580	1420	1610	1550	1610	(a)	(a)	1370	1300	1410	1210
Standard deviation	(a)	600	137	164	132	191	337	248	(a)	(a)	117	95	221	160
Minimum	(a)	840	1020	1250	1200	1350	1100	1080	(a)	(a)	1130	1100	1050	900
Surface contamination, % of total U														
As received	(a)	8.7×10^{-3}	8×10^{-3} (h)	5×10^{-3} (h)	13.6×10^{-3}	10.0×10^{-3}	0.08×10^{-3}	3.1×10^{-3}	(a)	4.1×10^{-3}	1.7×10^{-3}	(a)	0.12×10^{-3}	0.16×10^{-3}
After first leach	(a)	9.8×10^{-3}	8×10^{-3} (h)	5×10^{-3} (h)	15.2×10^{-3}	7.2×10^{-3}	0.08×10^{-3}	3.8×10^{-3}	(a)	2.9×10^{-3}	1.6×10^{-3}	(a)	0.12×10^{-3}	0.16×10^{-3}
After first leach and thermal cycle	(a)	14.1×10^{-3}	(a)	(a)	(a)	(a)	(a)	(a)	(a)	(a)	5.4×10^{-3}	(a)	0.14×10^{-3}	0.17×10^{-3}
After thermal cycle and second leach	(a)	11.9×10^{-3}	(a)	(a)	(a)	(a)	(a)	(a)	(a)	(a)	4.7×10^{-3}	(a)	0.13×10^{-3}	0.13×10^{-3}
Fuel removal, % of total U														
First leach	(a)	2.3×10^{-3}	$<1.4 \times 10^{-3}$ (h)	$<1.7 \times 10^{-3}$ (h)	12.9×10^{-3}	80.0×10^{-3}	0.15×10^{-3}	0.06×10^{-3}	(a)	2.1×10^{-3}	$<0.1 \times 10^{-3}$	(a)	3.51×10^{-3}	$<0.01 \times 10^{-3}$
Second leach	(a)	0.5×10^{-3}	(a)	(a)	(a)	(a)	(a)	(a)	(a)	(a)	$<0.1 \times 10^{-3}$	(a)	0.04×10^{-3}	$<0.02 \times 10^{-3}$

[a] Not measured.

[b] Ratio of thorium to ^{235}U.

[c] Measured on 25 randomly selected particles from a microradiograph of a riffled sample.

[d] Measured with helium pycnometer.

[e] Measured by oxidizing coated particles and calculating from the pycnometer density of the coated particles.

[f] Two-layer coating composed of a porous buffer layer and an outer layer of isotropic pyrolytic carbon.

[g] Based on crushing of 25 coated particles.

[h] As percent of total thorium.

of particles have been used in irradiation experiments and are mentioned in other sections of this report. The batches designated NCC-OR-6F to NCC-OR-11F consist of sol-gel microspheres coated by the Carbon Products Division under special contract with Oak Ridge National Laboratory. Two of these contain enriched uranium, but these have not yet been designated for testing under irradiation.

Evaluation of Experimental Fuel Assemblies

Irradiation of Experimental Fuel Assembly 14 in GCR-ORR Loop 1
(I. T. Dudley, A. W. Longest, J. A. Conlin)

Irradiation testing of experimental fuel assembly 14 in GCR-ORR loop 1 was terminated on May 2, 1965 after approximately 9 months of operation and 5183 hr at power. The objectives of the test were (1) to determine the problems associated with fuel elements containing loose coated particles, (2) to evaluate the performance and fission-gas retention properties of sol-gel oxide cores with pyrolytic-carbon coatings, and (3) to determine the compatibility of BeO and graphite under simulated reactor conditions.[23] In addition, radiation-induced shrinkage of the graphite parts supporting the fuel particles and deposition of fission products in the graphite structure will receive particular attention during postirradiation examination, since this was a long-term test with an estimated fast-neutron exposure of 9×10^{20} neutrons/cm^2 ($E > 0.18$ Mev).

The fuel used in this experiment consisted of a mixture of two batches of pyrolytic-carbon-coated particles fabricated at ORNL by the sol-gel technique and designated OR-205 and OR-206. The fuel particles of batch OR-205 (16.5 wt % of mixture) were pure ThO_2 and those of batch OR-206 were $(Th,U)O_2$ having a thorium-to-uranium ratio of 11.9. The experimental assembly, described previously,[23] contained loose particles in two regions. The bulk of the fuel was contained in the upper region in an annulus between an ATJ graphite sleeve and a central rod of the same material. Five

[23] J. L. Scott, C. Michelson, and E. A. Franco-Ferreira, Preparation of Fueled-Graphite Irradiation Specimens, pp. 53–56, GCRP Semiann. Progr. Rept. Sept. 30, 1964, USAEC Report ORNL-3731, Oak Ridge National Laboratory.

BeO pellets were inserted in a longitudinal hole in the lower half of the central rod. The upper fueled region was vented to the loop coolant and was instrumented with thermocouples in the central rod, in the graphite sleeve, and on the stainless steel support tube. The lower fueled region consisted of beds of loose particles in longitudinal holes of a solid graphite rod contained in a sealed uninstrumented stainless steel capsule. The upper region was intended to operate at a maximum central fuel temperature of 2500°F (1371°C), and the lower region was designed for a fuel temperature of 1200 to 1300°F (649 to 704°C).

Operating experience during approximately 80% of the irradiation was discussed previously.[24,25] The temperatures in the upper vented fuel region were maintained within the following limits throughout the irradiation:

Central	2350–2500°F (1288–1371°C)
Graphite sleeve	1800–1950°F (982–1066°C)
Support tube	1100–1350°F (593–732°C)

These temperatures were maintained, despite the loss of power resulting from fuel burnup, by the addition of neon to the loop coolant to lower its thermal conductivity. The final coolant composition was 30% neon and 70% helium. Fuel burnup of the $(Th,U)O_2$ particles in the upper region was estimated to be 2.7 at. % heavy metal (44 at. % ^{235}U depletion from fission plus ^{236}U formation).

Gas samples were taken periodically from the loop coolant stream and analyzed for contaminants and noble-gas fission products. It was found that the noble-gas fission products in the loop gas reached equilibrium levels and remained constant over periods of constant temperature operation. From these equilibrium activities the escape rate from the fuel element and the ratio of release rate to birth rate (R/B) were determined. Table 1.16 gives a history of the fission-gas release, in terms of R/B, for the $(Th,U)O_2$ particles in the vented region of the assembly.

---

[24] I. T. Dudley and A. W. Longest, Irradiations in GCR-ORR Loop No. 1, pp. 73–78, GCRP Semiann. Progr. Rept. Sept. 30, 1964, USAEC Report ORNL-3731, Oak Ridge National Laboratory.

[25] I. T. Dudley, A. W. Longest, and J. A. Conlin, Irradiations in GCR-ORR Loop No. 1, pp. 47–49, GCRP Semiann. Progr. Rept. Mar. 31, 1965, USAEC Report ORNL-3807, Oak Ridge National Laboratory

Table 1.16. Fission-Gas Release Data for GCR-ORR Loop 1 Irradiated Fuel Element 14

Date	Estimated Fuel Burnup (% heavy metal)	^{235}U Consumed (%)	Central Temperature		Ratio of Release to Birth Rate, R/B				
			°F	°C	^{85m}Kr	^{87}Kr	^{88}Kr	^{133}Xe	^{135}Xe
					$\times 10^{-5}$	$\times 10^{-5}$	$\times 10^{-5}$	$\times 10^{-5}$	$\times 10^{-6}$
8-7-64	0.1	1.7	2190	1198	0.43	0.27	0.59		1.0
9-20-64	0.66	11	2350-2400	1288-1316	1.2	0.58	1.5	0.54	2.0
11-15-64	1.35	23	2450-2500	1343-1371	2.0	0.99	2.8		3.1
1-10-65	2.0	33	2450-2500	1343-1371	2.6	1.2	3.4	1.0	3.6
4-20-65	2.7	44	2450-2500	1343-1371	3.2	1.6	4.2	1.3	4.0

Another factor of importance in the operation of experimental assembly 14 was the relatively high concentrations of CO and CO_2 in the loop coolant. The loop was not equipped with a cleanup system at this time, and the only means of controlling the buildup of these contaminants was to replace the coolant about once every 3 or 4 weeks. The maximum and average concentrations of the contaminants during operation of the element are listed in Table 1.17.

Table 1.17. Contaminants in ORR-GCR Loop 1 Coolant Gas During Irradiation of Element 14

Contaminant	Concentration (ppm by volume)	
	Maximum	Average[a]
N_2 + CO	239	73
CO_2	325	48
O_2	15	1.5
H_2	516	171
H_2O	71	9
CH_4	36	8

[a]Arithmetic average for 81 samples analyzed.

Postirradiation Examination of Experimental Fuel Assembly 14
(M. F. Osborne, E. L. Long, Jr., J. G. Morgan)

Immediately after experimental assembly 14 was removed from the reactor, samples of the surface contamination (smears) were collected from three areas of the experiment support structure that had been exposed to the recirculating helium coolant. Analyses of the smears revealed only ^{198}Au in addition to the components of stainless steel. Apparently the thin gold plating applied to the inner surface of the upper fuel compartment tube vaporized during irradiation and migrated through the nickel filter to the loop coolant. The absence of fission products in the smears probably indicates that the pyrolytic-carbon coatings on the fuel particles were effective, although the sleeve and filter may have removed many species.

The gamma scan of the fuel element (Fig. 1.30) showed no unusual radioactivity distribution, except for the small increase in radioactivity near the bottom end of the upper compartment, which may have been the result of fuel compaction during irradiation. Subsequent examination showed the top of the fuel to be about 1/2 in. below the top of the compartment. The general radioactivity levels were consistent with the much greater fuel loading in the upper compartment.

The external appearance of the fuel element was normal, and dimensional measurements revealed no appreciable distortions in the stainless

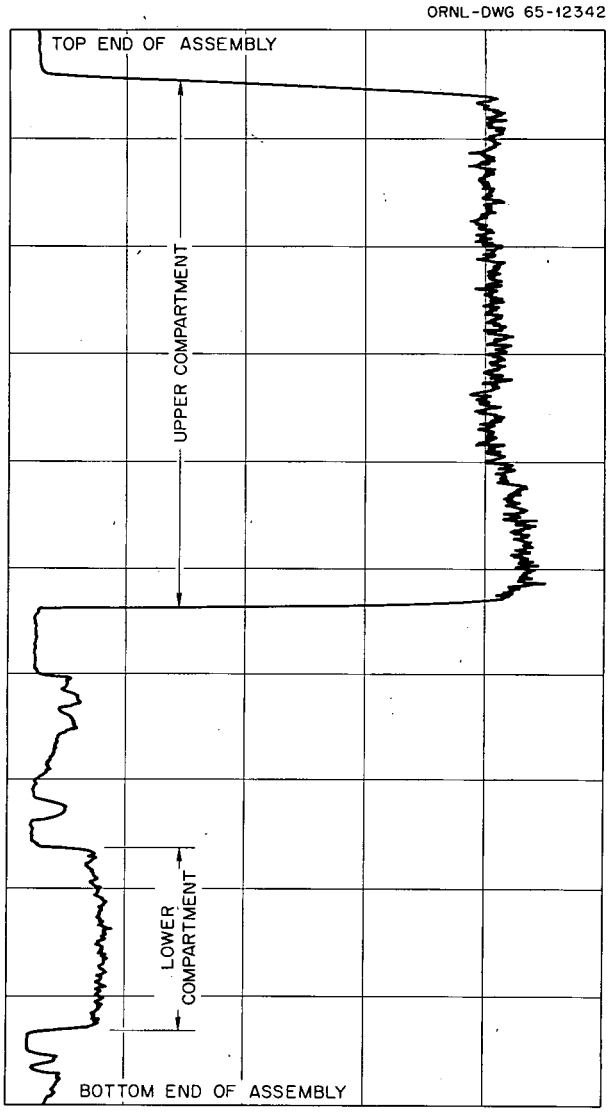

Fig. 1.30. Gamma Scan of Irradiated Experimental Fuel Assembly 14.

steel containment tubes. The lower fuel compartment was drilled for fission-gas collection, but no fission gas was detected.

When the upper compartment was disassembled, evidence of mild oxidation was found on the fuel particles, on the graphite containers, and possibly on one thermocouple. As shown in Fig. 1.31, only the stainless steel-sheathed thermocouple, which had been coated with tungsten, appeared to have reacted with its environment.

The central graphite tube that contained the molybdenum thermowell was attacked near the top end plug, as shown in Fig. 1.32. Dimensional measurements of the upper capsule, which are summarized in Table 1.18, showed a diameter decrease of about 0.010 in. (~4%) in this groove and smaller diameter decreases throughout the length of the tube. All measurements on the graphite holder of the lower capsule were within fabrication dimensions.

Fig. 1.31. Central Thermowell (Molybdenum Plated with Tungsten) and Four Stainless Steel-Sheathed Thermocouples After Irradiation in Experimental Fuel Assembly 14. Only the sheathed thermocouple plated with tungsten shows a surface reaction. 3×

Table 1.18. Dimensions of Upper Capsule Graphite Parts in Experimental Fuel Assembly 14

Axial Position	Sleeve Diameter[a] (in.)			Change in Sleeve Diameter (%)
	At 0°	At 90°	Average	
Top end	0.9290	0.9279	0.9285	0
1 in.	0.9285	0.9276	0.9281	-0.043
2 in.	0.9281	0.9276	0.9279	-0.065
3 in.	0.9279	0.9270	0.9275	-0.108
4 in.	0.9278	0.9275	0.9277	-0.086
5 in.	0.9277	0.9275	0.9276	-0.097
6 in.	0.9276	0.9270	0.9273	-0.129
Bottom end	0.9276	0.9280	0.9278	-0.075

Radial Position	Sleeve Length[b] (in.)	Change in Sleeve Length (%)
0°	6.488	-0.185
90°	6.490	-0.154
180°	6.489	-0.170
270°	6.486	-0.216

Radial Position	Center Rod Diameter[c] (in.)			Change in Center Rod Diameter (%)
	At 0°	At 90°	Average	
Top end	0.2496	0.2495	0.2496	+0.04
3/4 in. (min)	0.2421		0.2421	-3.05
1 in.	0.2466	0.2466	0.2466	-1.18
2 in.	0.2474	0.2470	0.2472	-0.93
3 in.	0.2472	0.2470	0.2471	-0.97
4 in.	0.2470	0.2468	0.2469	-1.05
5 in.	0.2465	0.2466	0.2466	-1.18
6 in.	0.2478	0.2476	0.2477	-0.73
Bottom end	0.2485	0.2485	0.2485	-0.40

[a]Preirradiation: 0.9285 ± 0.0005 in.

[b]Preirradiation: 6.500 ± 0.005 in.

[c]Preirradiation: 0.2495 ± 0.0005 in.

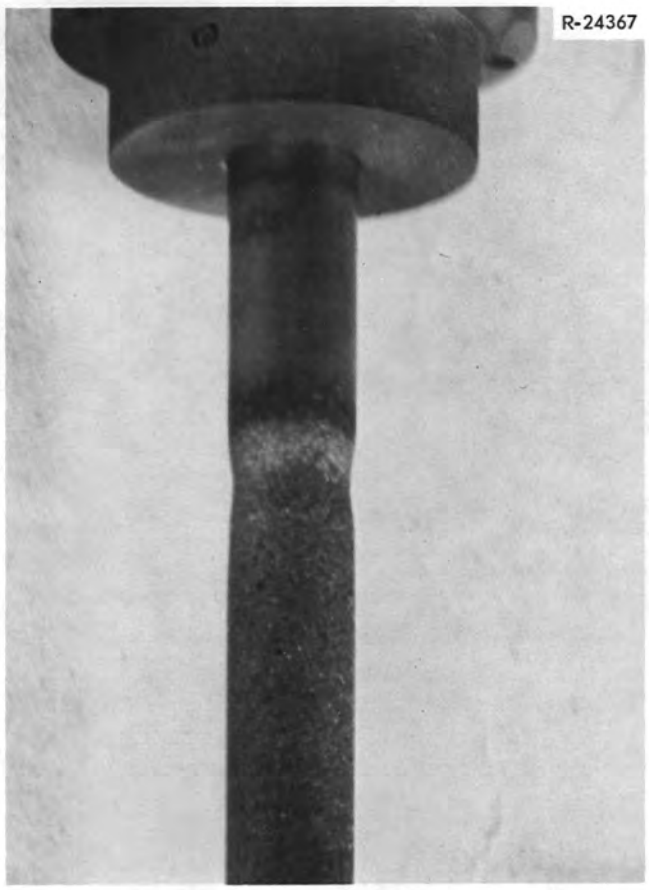

Fig. 1.32. Graphite Tube That Contained Thermowell in Experimental Fuel Assembly 14. Note the shallow circumferential groove about 1/2 in. below the top end plug, which apparently was caused by oxidation. 2.6×

Based on gamma-scan measurements, the area of maximum attack of the upper capsule coincided with the top surface of the fuel bed. Slight roughening of the outer surface of the graphite sleeve indicated some oxidation, but the dimensional changes were small (Table 1.18). The measured decrease in the length of this sleeve was nominally 0.012 in. (~0.2%). No significant shrinkage that could be attributed to radiation damage was detected.

The fuel particles from each compartment were inspected at magnifications up to 30×. Many small pits were present in the coatings of the particles from the upper compartment (Fig. 1.33), but no broken coatings were found. In addition, the surface appearance of the particles was somewhat different after irradiation.

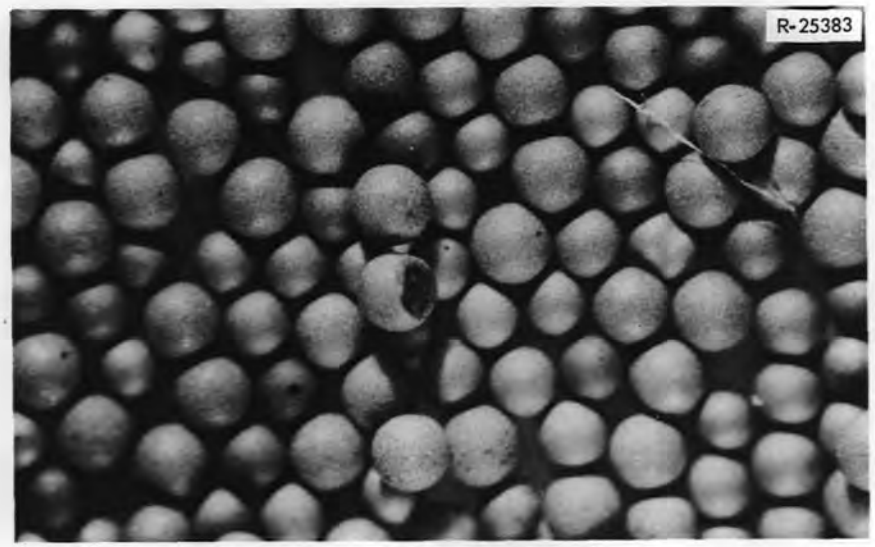

Fig. 1.33. Representative Fuel Particles from the Upper Compartment of Experimental Fuel Assembly 14. Note the small pits in the surfaces of some particles; these were apparently caused by oxidation. 20×

The fuel particles from the lower compartment, which are shown in Fig. 1.34, exhibited two unusual features: (1) many particles had bluish circular spots on one side and (2) many were in clusters of up to ten particles apparently held together by small amounts of reddish-brown or orange material. However, only one broken particle was found in this group. These striking anomalies were recorded by color photography.

Visual inspection, weighing, and measuring of the cylindrical BeO specimens in the central graphite tube in the upper compartment revealed no significant changes.

Inspection of the inner surface of the upper stainless steel containment vessel revealed a very thin, dark deposit, but efforts to collect a sample of this deposit were unsuccessful. Very little evidence of the original gold plating could be seen.

Five radial samples of the graphite sleeve from the upper compartment were collected for fission-product investigation, and samples of the stainless steel tube and nickel filter will be analyzed for both fast- and

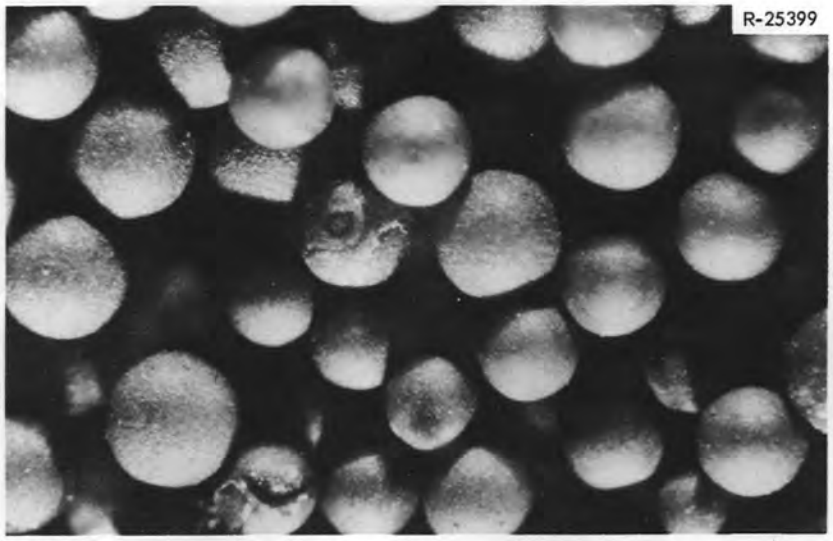

Fig. 1.34. Representative Fuel Particles from the Lower Compartment of Experimental Fuel Assembly 14. Note spots and foreign material on the surface of some particles. 30×

thermal-neutron flux determinations. These data and the results of metallographic examinations of thermocouples, fuel particles, and BeO specimens will be reported later.

Irradiation of Experimental Fuel Assembly 15 in GCR-ORR Loop 1
(I. T. Dudley, A. W. Longest, J. A. Conlin)

Experimental assembly 15, which contains a mixed bed of pyrolytic-carbon-coated fuel particles, was inserted in ORR loop 1 July 5. This experimental assembly is similar to assembly 14 and is shown in Fig. 1.35. The experiment is intended to further the evaluation of loose beds of coated particles under conditions that more realistically simulate service in a TARGET reactor than conditions attainable in a capsule.

The upper region, which is vented to the loop, contains a loose mixed bed of three types of coated particles in two size ranges, similar to a fuel arrangement proposed for TARGET. Physical separation of different size particles has been suggested as an initial step in the chemical reprocessing of spent fuel. One object of loop 1 experiment 15 is to determine whether segregation occurs during irradiation.

Both carbide and oxide particles were used. The carbide fuel particles were manufactured by General Atomic; the oxide particles are ORNL

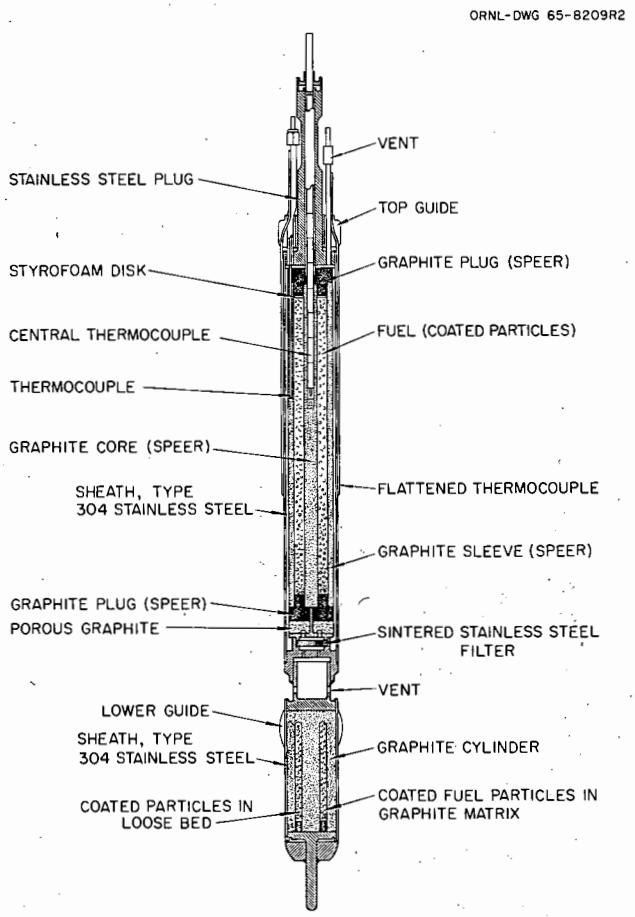

Fig. 1.35. Experimental Fuel Assembly 15 for Irradiation in GCR-ORR Loop 1.

sol-gel particles. All particles were coated by General Atomic and loaded into the graphite containers by General Atomic personnel with techniques developed by them to insure good mixing in the initial loading. A small Styrofoam disk that weighed approximately 0.1 g was placed on top of the fuel in the upper capsule. This disk maintained a slight pressure on the fuel particles to prevent agitation and segregation of the particles prior to installation in the loop. The Styrofoam disk is assumed to have vaporized when the temperature reached 1200°F (649°C).

The lower (static) region contains a graphite cylinder that has two holes loaded with coated fuel particles, instead of five holes, as in experimental assembly 14. One hole is loaded with a mixture of loose

particles, and the other contains particles bonded in a fuel-graphite matrix. This arrangement will subject bonded matrix and loose particle fuels to similar service conditions, and in the postirradiation examination we will look for evidence of differences in behavior. The graphite cylinder loaded with fuel was supplied by General Atomic. Tables 1.19 and 1.20 summarize the data on the loadings for the vented and sealed regions.

The upper region is vented to the loop coolant stream both at the top and bottom (the upper region of element 14 was vented at the bottom only) to insure some positive gas flow past the graphite sleeve. The upper end is vented through two screened 1/8-in.-OD tubes and the lower end through a porous stainless steel disk. The lower capsule is completely sealed.

To provide a more realistic chemical composition of the gas for the vented element, a bypass cleanup system was added to the loop to remove the H_2O, H_2, CO, and CO_2 impurities from the helium coolant. The concentration of impurities in the coolant will be maintained at much lower levels during experiment 15 than prevailed during experiment 14, and the

Table 1.19. Data on Fuel Particles in Upper Vented Region of Experimental Fuel Assembly 15

Total fuel volume: 33.9 cm^3
Mixed-bed fuel density: 0.059 g of ^{235}U per cm^3

Particle lot			
GA designation	3031-31E	3031-34E	3031-35D
ORNL designation	GA-321-2	GA-323	GA-324
Type of fuel particle	$(Th,U)C_2$	$(Th,U)O_2$	ThO_2
Weight of coated particles, g	6.30	25.00	38.66
Weight of uranium, g	1.08	1.08	
Weight of thorium, g	1.12	13.60	19.02
Weight of ^{235}U, g	1.00	1.00	
Particle nominal dimensions, μ			
Core diameter	181	343	233
Coating thickness	97	100	89
Particle diameter	375	542	412

Table 1.20. Data on Fuel Particles in Lower Sealed Region of Experimental Fuel Assembly 15

	Bonded Particles		Loose Particles	
Particle lot				
GA designation	3031-31E	3031-32N	3031-31E	3031-32N
ORNL designation	GA-321-2	GA-322	GA-321-2	GA-322
Type of fuel particle	$(Th,U)C_2$	UC_2	$(Th,U)C_2$	UC_2
Weight of coated particles, g	0.430	5.510	0.430	4.708
Weight of thorium, g	0.077		0.077	
Weight of uranium, g	0.074	3.59	0.074	3.06
Weight of ^{235}U, g	0.068	0.025	0.068	0.022
Particle dimensions, μ				
Core diameter	181	382	181	382
Coating thickness	97	99	97	99
Particle diameter	375	579	375	579

effect on corrosion of coated particles and structural graphite will be observed.

The cleanup system consists of a heated copper oxide bed for the oxidation of H_2 and CO, a water-cooled heat exchanger, a molecular sieve to absorb H_2O and CO_2, and a flowmeter. The gas cleanup system has operated satisfactorily, except for a short period when a buildup of CO_2 concentration was noted. Regeneration of the molecular sieve restored its effectiveness, and the CO_2 concentration immediately dropped. All contaminants are normally less than 5 ppm each, except N_2 + CO, which varies between 5 and 20 ppm.

The linear heat generation rate (fission and gamma) is approximately 24,800 Btu/hr·ft for the upper capsule and approximately 9,400 Btu/hr·ft for the lower capsule. The combined fission heat is approximately 3.4 kw. Operating conditions for this experiment are similar to those of experiment 14. The center of the fuel in the upper capsule is at 2550°F (~1400°C), the graphite sleeve is at about 1800°F (982°C), and the stainless steel cladding at about 800°F (427°C). Control of the fuel temperature is achieved by varying the helium coolant temperature. The helium coolant flow is approximately 280 lb/hr at 290 to 300 psia.

Samples for fission-gas release studies were taken frequently following startup, and thereafter they have been taken two or three times a week. Early fractional fission-gas release rates (R/B) are

^{85m}Kr	2.0×10^{-6}
^{87}Kr	0.8×10^{-6}
^{88}Kr	2.1×10^{-6}
^{133}Xe	1.0×10^{-6}
^{135}Xe	0.7×10^{-6}

These values were calculated from equilibrium fission-gas levels in the loop coolant corrected for the calculated holdup time in the cleanup system, with no correction for the burnup of the ^{135}Xe within the fuel.

During this experiment, a limited effort will be made to characterize the radioactive species, other than noble gases, that are transported in the loop coolant. A May-pack sampler has been installed for this purpose. This device, which was originally developed for characterizing iodine aerosols in nuclear safety experiments, consists of several filtering media in series: silver-plated copper screens, a membrane filter, charcoal-impregnated filter paper, and activated charcoal. A sample of loop coolant will be taken from a point near the blower discharge, passed through the May pack at a flow rate up to 1 lb/hr, and returned to the loop by way of the cleanup system. For the initial sample a major fraction of the loop coolant will be passed through the sampler, since it is expected that the activity levels in the coolant will be quite low and a principal question is whether enough activity can be collected to permit analysis. If sufficient activity is present, the distribution among the constituents of the May pack will be determined for radioiodine and other radioactive elements.

The irradiation experiment is presently scheduled to run through ORR cycle 64, which ends February 2, 1966. Estimated ^{235}U consumption and heavy-metal burnup at that date are as follows:

Upper capsule	
^{235}U consumed,* %	26.7
Heavy-metal burnup, %	
Particles in lot 3031-31E	10.25
Particles in lot 3031-34E	1.54
Particles in lot 3031-35D	0.0

*Includes fissions plus neutron capture.

Lower capsule	
^{235}U consumed,* %	21.0
Heavy-metal burnup, %	
Particles in lot 3031-31E	8.0
Particles in lot 3031-32N	0.13

High-Burnup Coated-Particle Experiment in ORR Position F-9

A. W. Longest J. A. Conlin
V. A. DeCarlo

The high-burnup coated-particle irradiation experiment is oriented toward the TARGET reactor fuel-cycle program and is designed to irradiate coated-particle fuels to burnups considerably higher than those achieved previously. The objective of this test is to evaluate the fission-product retention and overall stability of coated-particle fuels at burnups of up to 50% heavy metal and at temperatures between 1100 and 1400°C.

The experiment is designed to permit high burnup rates, but not to exceed a rate equal to 10% heavy metal per month and to sustain a fuel-particle surface temperature of 1400°C for as long a period as practical, despite fuel depletion. The capsule design is basically the same as that reported earlier,[26] with one major exception. Instead of one batch of particles containing 0.2 g of fully enriched uranium it was decided to irradiate two 0.1-g batches simultaneously. A cross section of the fuel capsule showing the two batches of particles, each supported as a separate monolayer in the central graphite holder, is shown in Fig. 1.36.

The fuel particles are pyrolytic-carbon-coated UO_2 and UC_2 particles from batches HB-23 (see Tables 1.11 and 1.15) and GA-320 (see Table 1.15), respectively. The HB-23 particles were loaded to a higher density than was expected, and it was necessary to dilute these with a small amount of depleted-UC_2 coated particles from batch OR-42 to obtain the design weight of ^{235}U. The HB-23 and OR-42 particles were loaded into the upper

*Includes fissions plus neutron capture.

[26]A. W. Longest and J. A. Conlin, High-Burnup Coated-Particle Irradiation in ORR Position F-9, pp. 53–56, GCRP Semiann. Progr. Rept. Mar. 31, 1965, USAEC Report ORNL-3807, Oak Ridge National Laboratory.

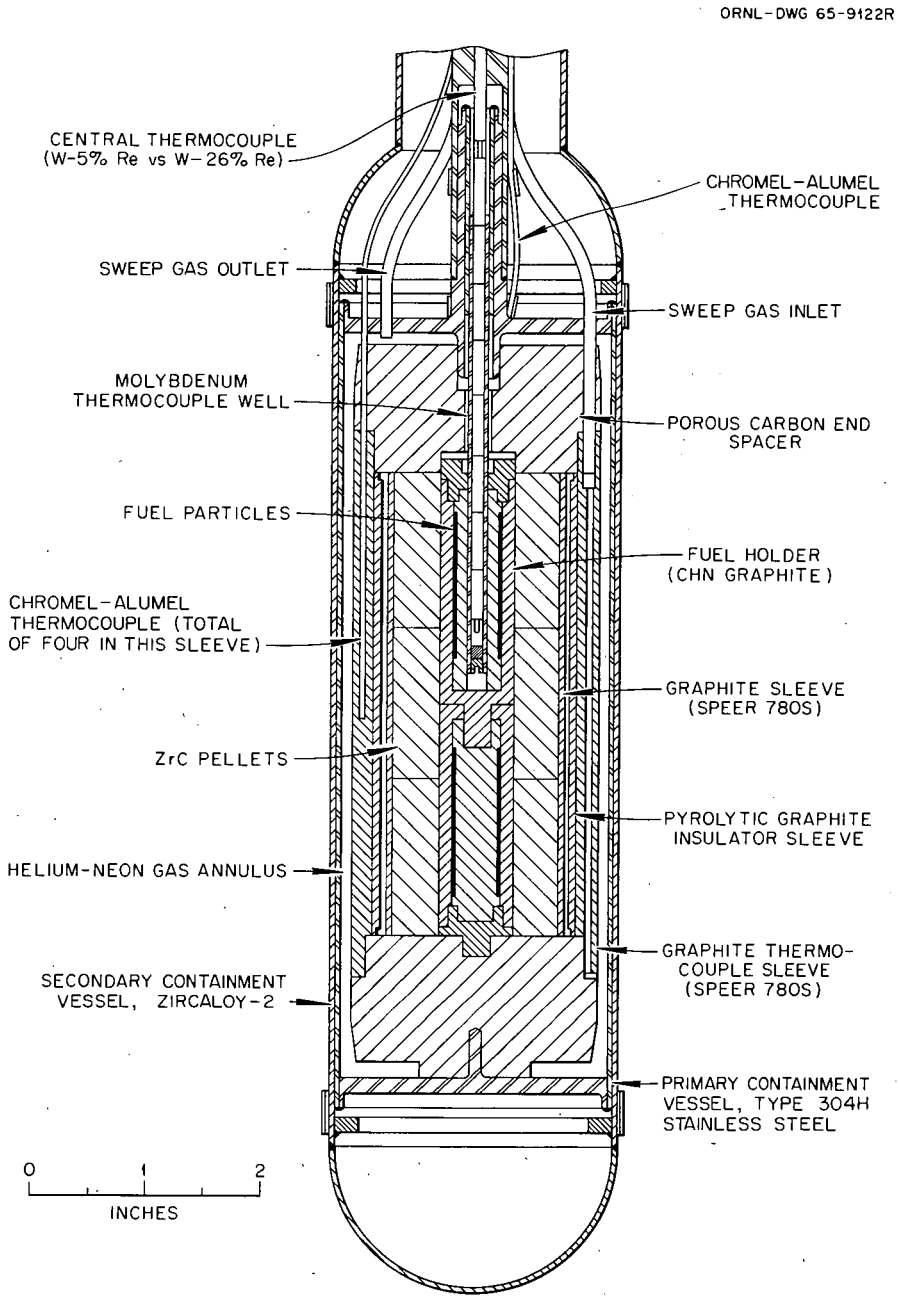

Fig. 1.36. Cross Section of Fuel Capsule for High-Burnup Experiment.

fuel compartment of the capsule and received the usual leach treatment to remove surface contamination. The GA-320 particles were loaded into the lower compartment and received no leach treatment.

The experimental assembly was installed in the ORR F-9 facility, and irradiation started on July 14, 1965. To limit the fuel burnup rate to 10% heavy metal per month, the assembly was operated at 2 1/2 in. from full insertion until August 9, 1 1/2 in. until August 19, and fully inserted thereafter. Full insertion places the center of the fuel capsule approximately 3/8 in. above the centerline of the reactor core.

The capsule temperature was about 500°F (222°C) below that predicted by the design calculations, and for this reason it was necessary to use neon as the sweep gas initially instead of a mixture of helium and neon as planned. Uncertainties in the design calculations to which the capsule temperature is sensitive were the gamma heat generation (about two-thirds of the total heat generation initially), the thermal conductivities of the insulating components, and the emissivities of surfaces.

With neon as the sweep gas the measured fuel temperature was maintained between 2325°F (1274°C) and 2400°F (1316°C) until a reactor shutdown on August 22. At this time the fuel temperature was 2380°F (1304°C). When the assembly was reinserted into the core on August 30 following the startup of reactor cycle 62, the fuel temperature reached only 2190°F (1199°C). This drop of 190°F (88°C) was attributed to changes in the core loading. On August 31 the measured fuel temperature was increased to the present operating limits of 2450 to 2500°F (1343 to 1371°C) by changing the neon sweep gas to a mixture of argon and helium. It should be noted that the lower batch of particles is uninstrumented and may, because of flux gradients in the reactor, be at a slightly higher temperature than measured in the upper region. For this reason the measured temperature has been kept slightly below the 1400°C design temperature. The sweep gas that flows continuously through the graphite structure of the capsule is sampled periodically, and the release rates of the noble-gas fission products are determined. Table 1.21 gives the release rate to birth rate (R/B) data for the five isotopes counted. The birth rates used in this ratio included the contributions from both batches of fuel

Table 1.21. Fission-Gas Release from the High-Burnup Experimental Assembly

Sample	Date	Fuel Temperature °F	Fuel Temperature °C	Estimated Burnup (% heavy metal)	Ratio of Release Rate to Birth Rate, R/B ^{85m}Kr	^{87}Kr	^{88}Kr	^{133}Xe	^{135}Xe
					$\times 10^{-6}$	$\times 10^{-6}$	$\times 10^{-6}$	$\times 10^{-6}$	$\times 10^{-6}$
F9-1-1	7-16-65	2340	1282			1.46	2.85		
-2	7-19-65	2345	1285	2.0	1.6	0.62	0.88	0.72	0.18
-3	7-21-65	2360	1293		2.1	0.83	1.2	0.81	0.21
-4	7-23-65	2355	1291		1.6	0.69	0.94	0.76	0.17
-5	7-26-65	Reactor shut down — activity too low to count							
-6	7-29-65	2325	1274		1.6	0.58	0.99	0.60	0.11
-7	8-5-65	2354	1290	6.0	1.6	0.58	1.2	0.77	0.14
-8	8-12-65	2400	1316	8.0	2.8	1.0	2.8	1.4	0.35
-9	8-18-65	2410	1321	10.0	4.9	2.0	5.7	3.0	0.81
-10	8-31-65[a]	2190	1199	11.0	27.1	31.6	0.42		
-11	9-7-65	2480	1360		217.0			93.3	57.4
-12	9-9-65	2450	1343	13.8	156.0			61.0	17.2
-13	9-10-65	2475	1357					117.0	
-14	9-15-65	Argon activity interferred with counting							
-15	9-15-65	Argon activity interferred with counting							
-16	9-16-65[b]	2145	1174	15.8	85.8	27.5	92.1	45.5	
-17	9-20-65[b]	2150	1177	17.0	79.5	27.3	81.0	47.0	1.1
-18	9-22-65	2500	1371	17.5	10.3			250.0	4.7

[a]Sample taken just prior to changing from neon sweep gas to a mixture of argon and helium.

[b]Sweep gas changed to neon temporarily to determine effect of temperature on release.

and were not corrected for relatively small flux changes and fuel burnup. When argon was added to the sweep gas, ^{87}Kr and ^{88}Kr release could not be determined because of the waiting time required for the argon activity to decay before counting the samples. Because of a noticeable increase in release rate, neon was used temporarily on September 15 as the sweep gas to verify the results (again counting all five isotopes) and to determine the effect of temperature on release rate.

The accumulated irradiation time as of September 20 was approximately 56 days, which gave an estimated heavy-metal burnup of 17.5% for the particles in the lower fuel compartment and 16% for the particles in the upper compartment. The total irradiation time required for 50% heavy-metal burnup is 225 days.

Compatibility of Oxide Fuel Pellets and Graphite Under Irradiation

C. L. Segaser J. A. Conlin

The irradiation experiment for determining the compatibility of oxide fuel and graphite, described previously,[27] is intended to evaluate a TARGET reactor fuel concept in which the fuel element consists of bare $(Th,U)O_2$ pellets in a graphite structure. The irradiation capsule was designed to provide information on the effect of fuel pellet swelling on the graphite structure at high burnups with a wide range of pellet density and power, fuel-graphite compatibility at TARGET conditions, and fission-gas release.

Fuel pellets for the first capsule, which is designated 05-10, were supplied by General Atomic, and the container is made from the same type of graphite as is proposed for the TARGET reference design. The capsule was installed in the ORR during the August 1965 shutdown.

After some preliminary checks at reduced temperatures to insure that the purge gas purification and CO addition systems were functioning, the

[27]C. L. Segaser and J. A. Conlin, Compatibility of Oxide Fuel Pellets and Graphite Under Irradiation, pp. 49–53, GCRP Semiann. Progr. Rept. Mar. 31, 1965, ORNL-3807, Oak Ridge National Laboratory.

central fuel temperature was brought to the desired value of 3000°F (1650°C) on September 3. Operation appeared to be satisfactory; however, fission-gas activity was detected in the shielded valve box, which serves as secondary containment for this and other experimental equipment. It was determined that a leak existed in the primary containment system of capsule 05-10, and it was therefore returned to low-power operation by retracting it from the ORR pool face. The rate of fission-gas release from the fuel appeared to be high, as was expected, but the operating period was too brief for measurements to be made. The leak has been located and an attempt will be made to repair it at the next ORR shutdown so that the experiment may continue.

Coated-Particle Irradiations in LITR

I. K. Namba F. R. McQuilkin

Irradiation of two miniature fueled capsules, L-CP9 and L-CP10, which were previously discussed,[28] was completed, and the capsules were removed from the reactor for postirradiation examination. Summaries of design and operating conditions for these capsules are given in Tables 1.22 and 1.23.

Capsule L-CP11 is being assembled, and insertion in the reactor is scheduled for October 7, 1965. This experiment will conclude the present series of LITR coated-particle irradiations. A summary of the design and planned operating conditions for capsule L-CP11 is given in Table 1.24.

---

[28] I. K. Namba and F. R. McQuilkin, Coated-Particle Irradiations in LITR, pp. 73–76, GCRP Semiann. Progr. Rept. Sept. 30, 1964, USAEC Report ORNL-3731, Oak Ridge National Laboratory.

Table 1.22. Summary of Design and Operating Conditions for Four-Compartment Capsule L-CP9

LITR core position: C-42
Insertion date: July 28, 1964
Removal date: July 13, 1965

Compartment	a	b	c	d
Fuel data				
Fuel material	UC_2	UC_2	UC_2	UC_2
Lot No.	OR-59	OR-53	OR-56	NCC-207
Uranium content, wt %	54.8	40.6	43.5	44.3
Enrichment, at. %	93.0	93.0	93.0	93.0
Average coated particle diameter,[a] μ	439	571	512	422
Average coating thickness,[a] μ	91	156	127	101
Density, g/cm³				
Design	2.80	1.80	1.80	2.00
Actual	1.85	1.59	1.67	1.90
Total number of particles	2450	1690	2070	3860
Weight of coated particles, g	0.3773	0.4234	0.3967	0.4166
Weight of uranium, g	0.2068	0.1720	0.1724	0.1846
Weight of ^{235}U, g	0.1932	0.1600	0.1603	0.1717
Fuel can data				
Material	ATJ graphite	ATJ graphite	ATJ graphite	ATJ graphite
Outside diameter, in.	0.265	0.2635	0.2635	0.265
Inside diameter, in.	0.216	0.214	0.214	0.215
Length, in.	0.751	0.751	0.749	0.751
Central rod outside diameter, in.	0.160	0.133	0.1455	0.1535
Insulator material	Carbon 60	Carbon 60	Carbon 60	Carbon 60
Power data (calculated)				
Effective thermal-neutron flux, neutrons/cm²·sec	1.45×10^{13}	1.51×10^{13}	1.52×10^{13}	1.49×10^{13}
Self-shielding factor	0.77	0.81	0.82	0.80
Heat rate, Btu/hr	407	352	357	374
Power density, kw/cm³ of loose particles	0.59	0.39	0.44	0.50
Burnup (est.), at. % of heavy metal	20.2	21.0	21.1	20.7
Operational data				
Temperatures, °F (°C)				
Fuel center[b]				
Startup[c]	1630 (888)			1970 (1077)
Maximum	1790 (977)			1980 (1082)
Minimum	1260[d] (682)			1810 (988)
Inconel cladding[b]				
Startup[c]	820 (438)	950 (510)	1280 (693)	1070 (577)
Maximum	925 (496)	1060 (571)	1350 (732)	1250 (677)
Minimum	785 (418)	938 (503)	1242 (672)	1030 (554)
Cooling air at inlet	220 (104)			
Cooling air at outlet	600 (333)			
Thermal barrier gas	Argon	Argon	Argon	Argon
Thermal barrier gas gap, in.	0.0075	0.008	0.008	0.0075
Drawings				
Assembly	E-10332 R 001			
Details	E-10332 R 003			
Fuel can detail	D-10332 R 002, Rev. 2			

[a]Measurements made on randomly selected particles from a microradiograph of a 0.5-g riffled sample.

[b]Fuel central thermocouple (a and d compartments) is type 304 stainless steel-sheathed BeO-insulated W-5% Re vs W-26% Re thermocouple wires bared and threaded through a two-hole BeO insulator (for details see Dwg. E-10332 R 002, Rev. 2); fuel-holder surface thermocouple (a, b, c, and d compartments) is type 304 stainless steel-sheathed MgO-insulated Chromel-P vs Alumel (see Dwg. E-10332 R 003).

[c]Indicated temperatures after apparent equilibrium conditions were first achieved.

[d]Minimum indicated temperature occurred 10-15-64 and thermocouple failed.

Table 1.23. Summary of Design and Operating Conditions for Four-Compartment Capsule L-CP10

LITR core position: C-46
Insertion date: January 26, 1965
Removal date: August 24, 1965

Compartment	a	b	c	d
Fuel data				
Fuel material	UC_2	UC_2	UC_2	UC_2
Lot No.	OR-141	OR-127, -46[a]	OR-138, -46[a]	NCC-216
Uranium content, wt %	37.0	32.8	32.8	40.5
Enrichment, at. %	93	93	93	93
Average coated particle diameter,[b] μ	370	411	400	390
Average coating thickness,[b] μ	97	116	107	93
Density, g/cm³				
Design	2.0	1.6	1.80	2.00
Actual	1.72	1.41	1.58	1.80
Total number of particles	3800	3050, 545	3550	3620
Weight of coated particles, g	0.4134	0.3721, 0.0597	0.3880, 0.0437	0.3545
Weight of uranium, g	0.1530	0.1220, 0.0222	0.1273, 0.0163	0.1436
Weight of ^{235}U, g	0.1423	0.1135	0.1184	0.1335
Fuel can data				
Material	ATJ graphite	ATJ graphite	ATJ graphite	ATJ graphite
Outside diameter, in.	0.255	0.253	0.249	0.256
Inside diameter, in.	0.205	0.204	0.199	0.207
Length, in.	0.749	0.746	0.746	0.746
Central rod outside diameter, in.	0.131	0.1175	0.118	0.150
Insulator material	Carbon 60	Carbon 60	Carbon 60	Carbon 60
Power data (calculated)				
Effective thermal-neutron flux, neutrons/cm²·sec	1.37×10^{13}	1.41×10^{13}	1.40×10^{13}	1.385×10^{13}
Self-shielding factor	0.84	0.86	0.86	0.85
Heat rate, Btu/hr	287	239	244	273
Power density, kw/cm³ of loose particles	0.35	0.26	0.29	0.40
Burnup (est.), at. % of heavy metal	12.2	12.5	12.4	12.3
Operational data				
Temperatures, °F (°C)				
Fuel center[c]				
Startup[d]	1600 (871)			1920 (1049)
Maximum	1600 (871)			1920 (1049)
Minimum	1510 (721)			1830 (999)
Inconel cladding[c]				
Startup[d]	760 (404)	1020 (549)	1275 (690)	1150 (621)
Maximum	860 (460)	1070 (577)	1300 (704)	1260 (682)
Minimum	760 (404)	1020 (549)	1275 (690)	1150 (621)
Cooling air at inlet	300 (149)			
Cooling air at outlet	690 (366)			
Thermal barrier gas	Argon	Argon	Argon	Argon
Thermal barrier gas gap, in.	0.014	0.015	0.016	0.013
Irradiation time normalized to 3 Mw, days	190	190	190	190
Drawings				
Assembly	E-10343 R 001			
Details, fuel can	E-10343 R 002			
Details, thermocouples	E-10343 R 003			

[a]Depleted UC_2 coated particles (OR-46) were mixed with the coated fuel particles to adjust the loading densities to achieve a more uniform heat generation rate.

[b]Measurements made on randomly selected particles from a microradiograph of a 0.5-g riffled sample.

[c]Fuel central thermocouple (a and d compartments) is type 304 stainless steel-sheathed BeO-insulated W-5% Re vs W-26% Re thermocouple wires bared and threaded through a two-hole BeO insulator (for details see Dwg. E-10343 R 002); fuel-holder surface thermocouple (a, b, c, and d compartments) is type 304 stainless steel-sheathed MgO-insulated Chromel-P vs Alumel (see Dwg. E-10343 R 003).

[d]Indicated temperatures after apparent equilibrium conditions were first achieved.

Table 1.24. Summary of Design and Planned Operating Conditions for Four-Compartment Capsule L-CP11

LITR core position: C-42
Scheduled insertion date: October 7, 1965
Estimated removal date based on scheduled burnup: March 1, 1966

Compartment	a	b	c	d
Fuel data				
Fuel material	UC_2	UC_2	UC_2	UC_2
Lot No.	OR-341, OR-42[a]	OR-342	OR-343	OR-344
Uranium content, wt %	33.9	38.5	39.6	35.4
Enrichment, at. %	93.0	93.0	93.0	93.0
Average coated particle diameter,[b] μ	455	446	448	450
Average coating thickness,[b] μ	116	114	112	116
Density, g/cm³				
Design	1.66	1.55	1.53	1.65
Actual	1.67	1.57	1.56	1.72
Total number of particles	5150	4350	3620	3760
Weight of coated particles, g	0.6800, 0.0366	0.5044	0.4313	0.5037
Weight of uranium, g	0.2305, 0.0130	0.1942	0.1708	0.1783
Weight of ^{235}U, g	0.2144	0.1806	0.1588	0.1658
Fuel can data				
Material	ATJ graphite	ATJ graphite	ATJ graphite	ATJ graphite
Outside diameter, in.	0.268	0.246	0.222	0.242
Inside diameter, in.	0.234	0.212	0.187	0.208
Length, in.	0.751	0.746	0.752	0.748
Central rod outside diameter, in.	0.110	0.105	0.079	0.112
Insulator material	Carbon 60	Carbon 60	Carbon 60	Carbon 60
Power data (calculated)				
Effective thermal-neutron flux, neutrons/cm²·sec	1.49×10^{13}	1.51×10^{13}	1.52×10^{13}	1.54×10^{13}
Self-shielding factor	0.80	0.81	0.82	0.83
Heat rate, Btu/hr	466	396	347	360
Power density, kw/cm³ of loose particles	0.33	0.36	0.37	0.36
Burnup (est.), at. % of heavy metal	10	10	10	10
Operational data				
Temperatures, °F (°C)				
Fuel center[c] (design)	2500 (1371)			2500 (1371)
Inconel cladding[c] (design)	900 (482)	1000 (538)	1100 (593)	1100 (593)
Thermal barrier gas	Argon	Argon	Argon	Argon
Thermal barrier gas gap, in.	0.012	0.023	0.035	0.025
Required irradiation time normalized to 3 Mw for scheduled burnup, days	144	144	140	139
Drawings				
Assembly	E-10387 R 001			
Details, fuel can	E-10387 R 002			
Details, thermocouples	E-10387 R 003			

[a]Depleted UC_2 coated particles (OR-42) were mixed with the coated fuel particles to adjust the loading densities to achieve a more uniform heat generation rate.

[b]Measurements made on randomly selected particles from a microradiograph of a 0.5-g riffled sample.

[c]Fuel central thermocouple (a and d compartments) is tantalum-tipped (tipped portion coated with 0.010-in. tungsten) type 304 stainless steel-sheathed MgO-insulated W-5% Re vs W-26% Re (for details see Dwg. E-10387-R-002); fuel-holder surface thermocouple (a, b, c, and d compartments) is type 304 stainless steel-sheathed MgO-insulated Chromel-P vs Alumel (see Dwg. E-10387 R 003).

2. INVESTIGATIONS OF FUELED-GRAPHITE SYSTEMS

O. Sisman H. W. Savage
G. M. Watson

Instantaneous Fission-Gas Release Experiments

R. M. Carroll P. E. Reagan
T. W. Fulton J. W. Gooch
J. G. Morgan E. L. Long, Jr.

Fission-Gas Release from UO_2

During the period of this report the irradiation facility for fission-gas release was used to test specimens of coated particles. The work on the UO_2 program therefore consisted of evaluating data gathered during previous periods. The basic studies of fission-gas release from UO_2 have now been shifted to the Fuels and Materials Program and subsequent progress reports on this work will be found in "Fuels and Materials Development Program Quarterly Progress Report," as well as in this report. It seems proper now to give a summary of the information obtained to date from these experiments and to evaluate the most recent data.

Background. We irradiated a series of thin-disk specimens of UO_2 in the Oak Ridge Research Reactor to obtain data for the development of a model for fission-gas release. In these experiments the specimens could be irradiated at various flux levels and at independently controlled temperatures. Fission gas was removed by a sweep gas, and the release rate from the UO_2 specimen was determined by sampling the sweep system.[1] In order to simplify the problem as much as possible, we used high-purity single crystals of UO_2.

The results of these experiments show that both burnup and fissioning rate have a large effect on the rate of steady-state fractional release of fission gas during irradiation. These and other observations could not be explained by a diffusion-controlled mechanism, and a defect-trap model was postulated.[2]

---

[1]R. M. Carroll and P. E. Reagan, Techniques for In-Pile Measurements of Fission-Gas Release, Nucl. Sci. Eng., 21(2): 141–146 (1965).

Very simply, we assume for the defect-trap model that the rate-controlling process for fission-gas release in the temperature-dependent region is the probability of being trapped and the probability of being released from traps. The traps are of three kinds: (1) intrinsic traps, which are voids, grain boundaries, or other flaws in the material, (2) point defects, which are formed in the wake of a fission fragment, and (3) clustered point defects. The point defects are mobile; they are created and destroyed by fission; and they are annealed by heat. They reach an equilibrium number at a given temperature and fission rate. The intrinsic traps are not mobile at temperatures below 1500°C and act as permanent traps for any gas that diffuses into them. This conclusion was confirmed by experiments with fine-grained UO_2.[3]

When a fission fragment penetrates the specimen surface, UO_2 molecules are knocked out of the surface and any fission gas in this region is also ejected. This knock-out release accounts for most of the fission gas released at temperatures under about 700°C. We have shown that the knock-out process affects the surface of a specimen, but only to a depth of about 10 A.[4]

A simplified mathematical expression was derived for steady-state mother-daughter migration based on the defect-trap model.[5] The mathematical model contains several unknown constants — too many for evaluation by steady-state experiments. We therefore changed to a dynamic experiment to gain the extra degree of freedom necessary to make this evaluation.

---

[2]R. M. Carroll and O. Sisman, In-Pile Fission-Gas Release from Single-Crystal UO_2, Nucl. Sci. Eng., 21(2): 147–158 (1965).

[3]R. M. Carroll and O. Sisman, In-Pile Fission-Gas Release from Fine-Grain UO_2, Accepted for Publication by the J. Nucl. Mater., December 1964.

[4]R. M. Carroll, Fission-Gas Release During Fissioning in UO_2, paper presented at June 1965 Symposium on Fission-Gas Release at ANS Annual Meeting, Gatlinburg, Tennessee; for summary see Trans. Am. Nucl. Soc., 8(1): 22 (1965).

[5]R. M. Carroll, R. B. Perez, and O. Sisman, Release of Fission-Gas During Fissioning of UO_2, J. Am. Ceram. Soc., 48(2): 55–59 (1965).

Dynamic Experiments. Extensive modifications of the experiment controls were required to allow a precise oscillation about a selected steady-state condition. The fission rate is oscillated by moving the specimen in or out of the neutron flux. We can program the flux level and the amplitude, frequency, and wave shape of the flux oscillation. The neutron flux does not vary linearly with distance, and we had expected that an eccentric motion of the specimen would be necessary to obtain a sinusoidal oscillation of flux. However, because the movement of the specimen is very slight, the change of flux is proportional to the movement, and a sinusoidal oscillation of the specimen produces a sinusoidal oscillation of neutron flux. We determine the wave shape of the flux oscillation by using a sweep gas containing 1% argon and continuously measuring the neutron activation of the argon.[6]

The specimen temperature is oscillated by a controlled cooling air flow over the specimen capsule. The specimen temperature is measured by thermocouples connected into a feedback system to automatically control the air cooling to produce a desired temperature. Thus the temperature can be programmed to oscillate about a given value with a selected amplitude, frequency, and wave shape.

The fission-gas release from the specimen during oscillations is measured by continuous gamma-ray analysis of the flowing sweep gas. The gamma-ray spectrometer is programmed to measure the time-dependent variation of a given isotope of the fission gas (usually ^{88}Kr). The delay time required for the fission gas to flow out of the reactor is determined by using sweep gas that contains argon and measuring the time lapse between position oscillations and argon activity oscillations. A precise record of the time-temperature or time-flux values is kept with a digital recording-clock voltmeter. The fission-gas release rate measurements are thus synchronized with the temperature or flux oscillations of the specimen.

Flux Oscillations. We demonstrated in the steady-state experiments that the fission-gas release below 600°C is independent of temperature

---

[6]R. M. Carroll, Argon Activation Measures Irradiation Flux Continuously, Nucleonics, 20(2): 42 (February 1962).

and directly proportional to fission rate, and we showed that this low-temperature release occurs by knock out rather than direct recoil.[2,4] Further confirmation of this theory is found in the results of oscillating the neutron flux while holding the specimen at a constant temperature of 575°C. The data of Fig. 2.1 show that the ^{88}Kr release is proportional to the fission rate but that gas-release oscillations are not instantaneous with fission-rate oscillations. Gas release by recoil would be instantaneous, while knock-out release would depend on the concentration of fission gas at the surface of the specimen as well as the fission rate. Thus this phase shift supports the contention that the low-temperature release occurs predominately by a knock-out process.

The X marks on the time-flux plot of Fig. 2.1 show when samples of fission gas were taken for a quantitative analysis. The amount of ^{88}Kr

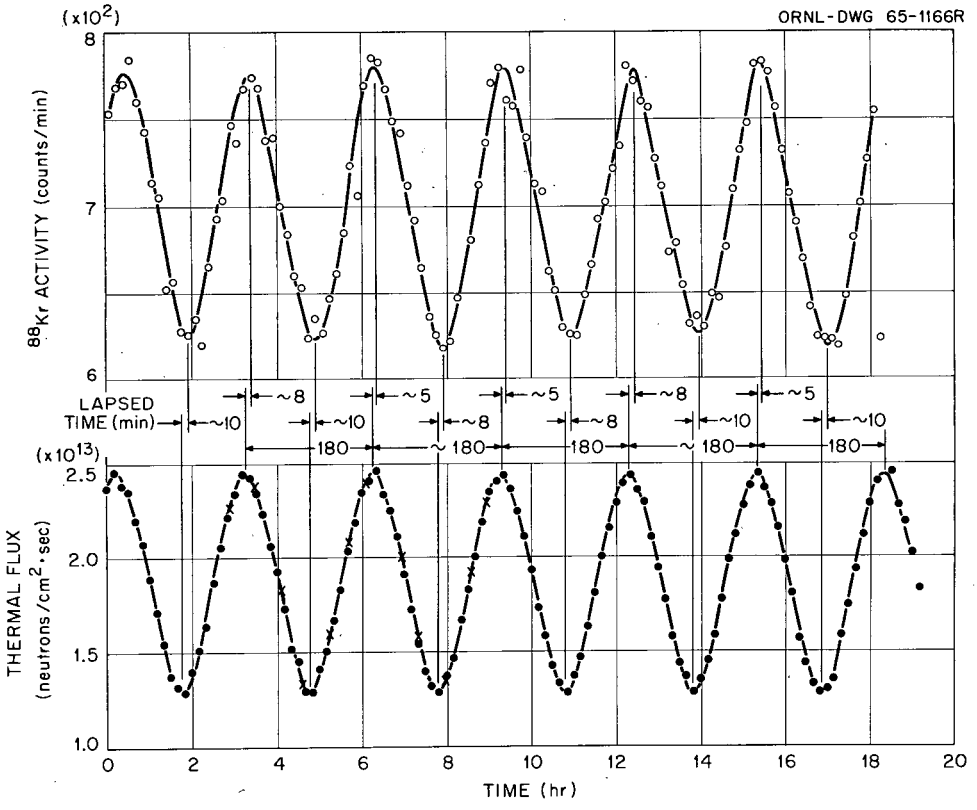

Fig. 2.1. Plots of Time Versus Flux and Time Versus Gas Release for a UO_2 Single Crystal (C1-13-9-29) Exposed to a 3-hr Flux Cycle at 575°C. X on time versus flux plot indicates when fission-gas sample was removed for analysis.

released during flux oscillation is shown in Fig. 2.2. The striking feature of Fig. 2.2 is that the amount of ^{88}Kr released during the oscillation was greater when the flux was decreasing than when the flux was increasing. The data form a sort of hysteresis curve (Fig. 2.2), which also may be explained on the basis of gas released by a knock-out process. Our reasoning is that the amount of knock out is the product of the surface concentration of fission gas and the recoil rate. Naturally, the production of the fission gas is proportional to the fission rate, and a greater concentration exists on the specimen surface after the specimen has passed through the high-flux region. This concentration is depleted while passing through the low-flux region and, for a given neutron flux, less fission gas is knocked out when the flux is increasing from a minimum value than when the flux is decreasing from a maximum value. Direct recoil release would yield the same amount of ^{88}Kr for the same neutron flux regardless of the past history of the specimen.

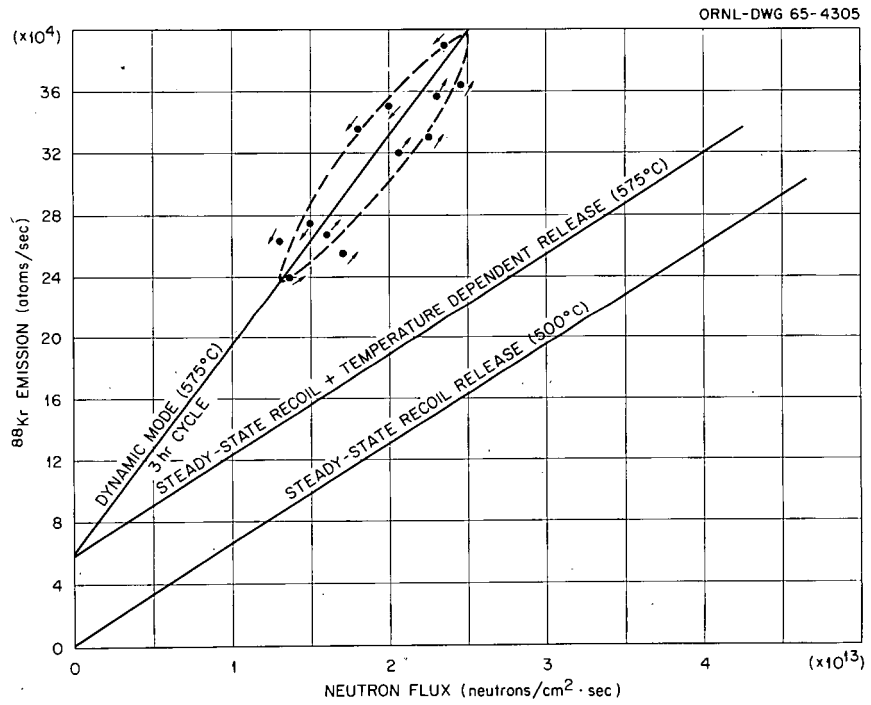

Fig. 2.2. Release of ^{88}Kr During Exposure of a UO_2 Single Crystal to 3-hr Flux Cycles.

Another factor evident in Fig. 2.2 is that the release during the dynamic operation is much greater than the release during steady-state operation; about 2.5 times greater. However, some of the release during dynamic operation is caused by the temperature-dependent contribution. If the temperature-dependent contribution is subtracted, the release rate during oscillation is still double the steady-state release rate for the same flux.

We think the larger release rate during the oscillation of flux occurs because the trap population is oscillating. The number of traps is greatest just after the neutron flux is maximum. As the flux decreases, the annealing rate of the traps exceeds the production rate and the trap population declines. Fission gas escaping the traps can migrate to the UO_2 surface and be available for knock out. When the flux is increasing, the trap population exceeds the annealing rate and the trap population increases. The increasing trap population is, however, offset by the increasing production rate of the fission gas, and the amount of fission gas arriving at the specimen surface will not be greatly different from that arriving during steady-state operation.

The specimens used to obtain these data were polished single crystals of UO_2. However, the surface of any specimen is a grain boundary and, by our model, this is a deep trap for fission gas. Thus this cyclic point-defect annealing delivers additional gas in surges to the specimen surface where it is trapped. The maximum rate of delivery occurs during the flux decrease and therefore accounts for some of the observed hysteresis. The net effect, however, is to increase the total amount of fission gas at the specimen surface available for knock out as compared with that available during steady-state operation. Thus the data of Figs. 2.1 and 2.2 support the defect-trap model.

Fission-Gas Release from Coated UO_2 and $(Th,U)C_2$ Particles

The use of fuel particles coated with pyrolytic carbon in several high-temperature gas-cooled reactors is contemplated. Tests were conducted to see how well the coated fuel particles retain fission gas and what damage is done to the particles during irradiation at high temperature. Most of the tests described here involved ORNL-developed coated

UO_2 particles. We are now at a stage of development where we have demonstrated that dense oxide cores have several distinct advantages over carbide cores both in ease of fabrication and behavior during irradiation. We have also demonstrated that we can apply several kinds of coatings, at reasonable cost, that show little damage up to 25 at. % burnup of heavy metal. We feel that the future of pyrolytic-carbon-coated fuel particles lies with the oxide cores and either a two-layer coating in which the inner layer shrinks (e.g., our batch OR-343 particles) or one that has a porous inner layer (e.g., our batch OR-348 particles).

During this reporting period we measured the fission-gas release during irradiation from ten capsules containing pyrolytic-carbon-coated particles. These particles were irradiated in the A9, B9, and C1 facilities in the ORR at 1300 to 1600°C. Preliminary data from four of the experiments (A9-1, A9-2, B9-25, and C1-15) were reported previously.[7] Eight capsules contained pyrolytic-carbon-coated UO_2 particles and two capsules contained pyrolytic-carbon-coated $(Th,U)C_2$ particles. Descriptions of the particles and the irradiation test data, including fractional fission-gas release, are given in Table 2.1.

Capsule A9-1, which contained pyrolytic-carbon-coated UO_2 particles from batch OR-201, was irradiated to 1.8 at. % uranium burnup at 630°C and then the temperature was increased to 930°C and an additional 1.9 at. % burnup was attained. The total burnup was 3.7 at. %.

No failed particles were found in 120 examined metallographically. Wedge-shaped fractures were observed that originated at the coating-fuel interface and extended into the inner coating to about half the thickness. It was interesting to note that the gap present at the fuel-coating interface prior to irradiation was no longer present after irradiation. There was no evidence of a reaction product at the fuel-coating interface. Typical particles are shown both before and after irradiation in Fig. 2.3.

Capsule A9-2 contained pyrolytic-carbon-coated UO_2 particles from batch OR-298 and was irradiated at 1400°C to 27.9 at. % uranium burnup.

---

[7]P. E. Reagan et al., Fission-Gas Release from Coated Particles, pp. 87–101, GCRP Semiann. Progr. Rept. Mar. 31, 1965, USAEC Report ORNL-3807, Oak Ridge National Laboratory.

Table 2.1. Data on Fission-Gas Release from Pyrolytic-Carbon-Coated Fuel Particles During Irradiation

Capsule Designation	Fuel Batch	Type of Coating	Type of Fuel	Burnup (at. % heavy metal)	Irradiation Temperature (°C)	Average Fractional Fission-Gas Release Rates, R/B				
						^{85m}Kr	^{88}Kr	^{87}Kr	^{133}Xe	^{135}Xe
A9-1	OR-201	Isotropic and granular pyrolytic carbon	UO_2	3.7	930	3.3×10^{-7}	3.0×10^{-7}	2.4×10^{-7}	(a)	(a)
A9-2	OR-298	Gap plus anisotropic and granular pyrolytic carbon	UO_2	27.9	1400	9.3×10^{-7}[b] 85.1×10^{-7}[c]	7.0×10^{-7}[b] 49.6×10^{-7}[c]	5.7×10^{-7}[b] 33.6×10^{-7}[c]	11.7×10^{-7}[b] (a)	6.5×10^{-7}[b] (a)
A9-3	GA-315	Porous carbon plus isotropic pyrolytic carbon	UO_2	6.1[d]	1500	4.24×10^{-6}[b] 2.5×10^{-4}[e]	3.33×10^{-6}[b] 2.2×10^{-4}[e]	2.50×10^{-6}[b] 1.8×10^{-4}[e]	3.59×10^{-6}[b] 5.4×10^{-4}[e]	2.52×10^{-6}[b] 4.2×10^{-4}[e]
B9-25	GA-315	Porous carbon plus isotropic pyrolytic carbon	UO_2	9.1	1200–1400	2.94×10^{-4}[f]	2.66×10^{-4}[f]	2.30×10^{-4}[f]	7.04×10^{-4}[f]	3.89×10^{-4}[f]
B9-26	OR-354	Porous carbon plus isotropic pyrolytic carbon	UO_2	12.1	1350	4.68×10^{-6}	4.21×10^{-6}	3.90×10^{-6}	3.7×10^{-6}	1.68×10^{-6}
B9-27	OR-348	Porous carbon plus dense isotropic pyrolytic carbon	UO_2	9.4	1500	1.55×10^{-6}	1.31×10^{-6}	1.22×10^{-6}	0.98×10^{-6}	0.57×10^{-6}
B9-28[g]	NCC-222 (AVR)	Laminar and granular pyrolytic carbon	$(Th,U)C_2$	1.2[d]	1300	6.66×10^{-6}	5.49×10^{-6}	4.37×10^{-6}	5.17×10^{-6}	2.4×10^{-6}
C1-15	GA-314	Porous carbon plus laminar and granular pyrolytic carbon	$(Th,U)C_2$	8.7	1400	4.15×10^{-5}	3.45×10^{-5}	2.98×10^{-5}	2.74×10^{-5}	1.17×10^{-5}
C1-16	OR-343	Low-density plus high-density isotropic pyrolytic carbon	UO_2	11.9 2.8	1400 1500 1400[h]	1.11×10^{-7} 1.88×10^{-7} 1.12×10^{-7}	0.83×10^{-7} 1.37×10^{-7} 0.88×10^{-7}	0.60×10^{-7} 1.14×10^{-7} 0.66×10^{-7}	0.93×10^{-7} 1.67×10^{-7} (a)	0.41×10^{-7} 0.73×10^{-7} (a)
C1-17	HB-23	Porous carbon plus isotropic and granular pyrolytic carbon	UO_2	25.2	1600	6.20×10^{-8}	4.27×10^{-8}	3.95×10^{-8}	7.62×10^{-8}	5.4×10^{-8}

[a] Data not available.
[b] Before bursts of fission gas.
[c] After bursts of fission gas at 26% burnup.
[d] Irradiation continuing.
[e] After thermal cycling.
[f] After bursts of fission gas.
[g] See Chapter 3 for discussion.
[h] After 2.8% burnup at 1500°C.

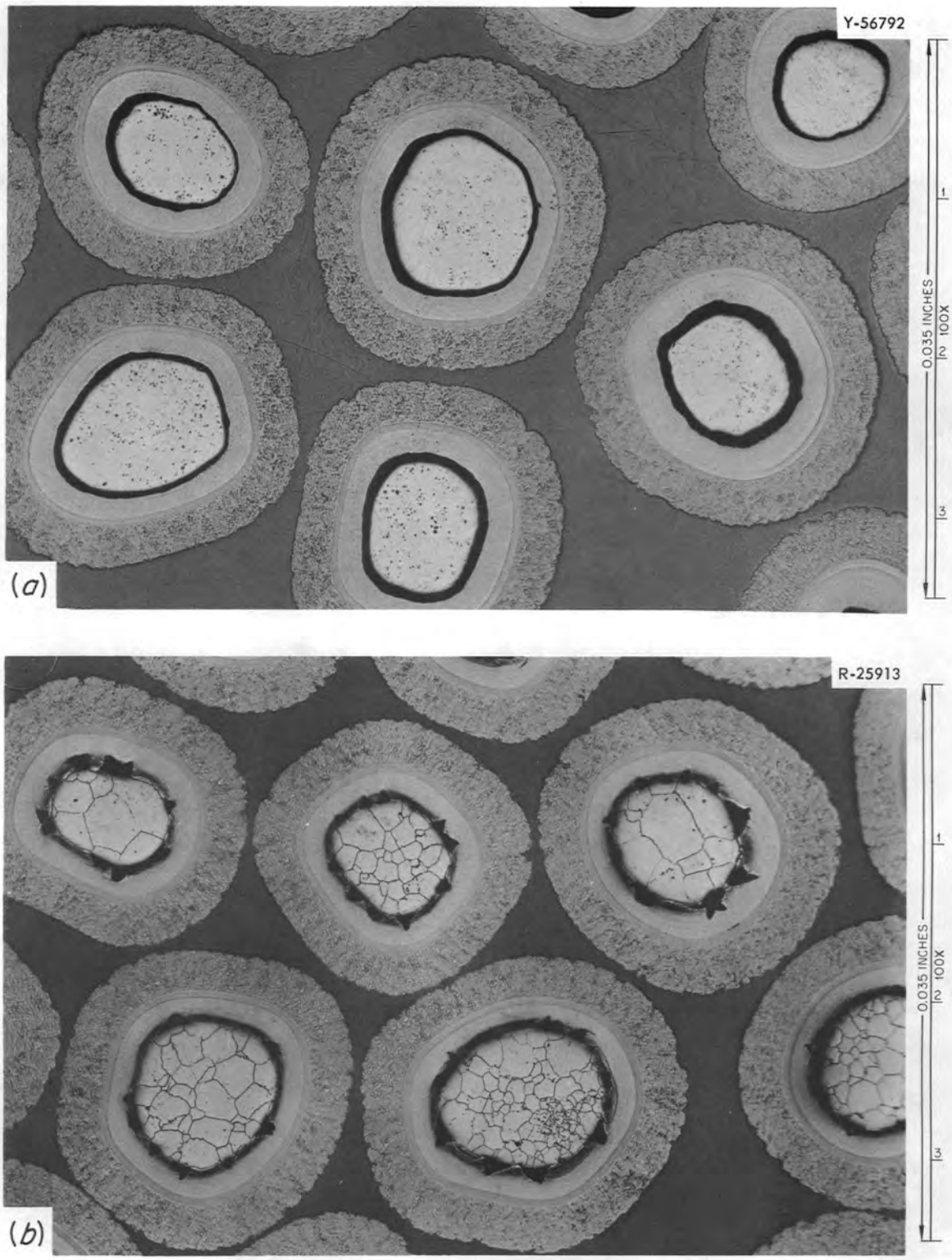

Fig. 2.3. Pyrolytic-Carbon-Coated UO_2 Particles from Batch OR-201. (a) Unirradiated. (b) Irradiated to 3.7 at. % burnup at 630 and 930°C in capsule A9-1. Etched. 100×

The coatings on these particles had an anisotropic inner layer and a granular outer layer. As shown in Fig. 2.4a, these particles had a gap between the oxide core and the inner pyrolytic-carbon layer. After the particles were irradiated to a little more than 26 at. % burnup, a few bursts of fission gas were released and the fractional release increased by about a factor of 7. The fractional fission-gas releases before and after the bursts are given in Table 2.1.

Metallographic examination of 92 particles from capsule A9-2 revealed no failed particles. The inner layers of these duplex-coated particles had undergone severe delamination, but the outer coatings were intact. There was no evidence of a reaction product at the fuel-coating interface, even though portions of the delaminated layers of the inner coatings were in intimate contact with the fuel. Examination of the UO_2 revealed the presence of small metallic inclusions in the grain boundaries. Electron microscope studies of UO_2 dispersions in stainless steel fuel plates have revealed similar metallic inclusions to be a high molybdenum-uranium alloy.[8] In addition to the collection of fission-gas bubbles at the grain boundaries, a large variation in grain size was observed, as shown in Fig. 2.4.

Capsule B9-25, which contained pyrolytic-carbon-coated UO_2 particles from batch GA-315, was irradiated to a total of 9.1 at. % uranium burnup. The particles were at 1400°C to 4 at. % burnup. After 4 at. % burnup, bursts of fission gas were released, and we reduced the temperature to 1200°C in an effort to reduce the exit helium activity. A check on the abnormal pressure at the helium inlet revealed that a small leak had developed in the in-pile helium line and that air was leaking into the capsule.

Postirradiation examination of capsule B9-25 showed that about 10% of the particles were badly oxidized and some were broken up enough to separate the core from the coating. Oxidized and broken coatings are shown in Fig. 2.5. The rest of the particles looked sound. Metallographic examination disclosed no failures or indications of potential

---

[8]Personal communication with A. E. Richt, ORNL.

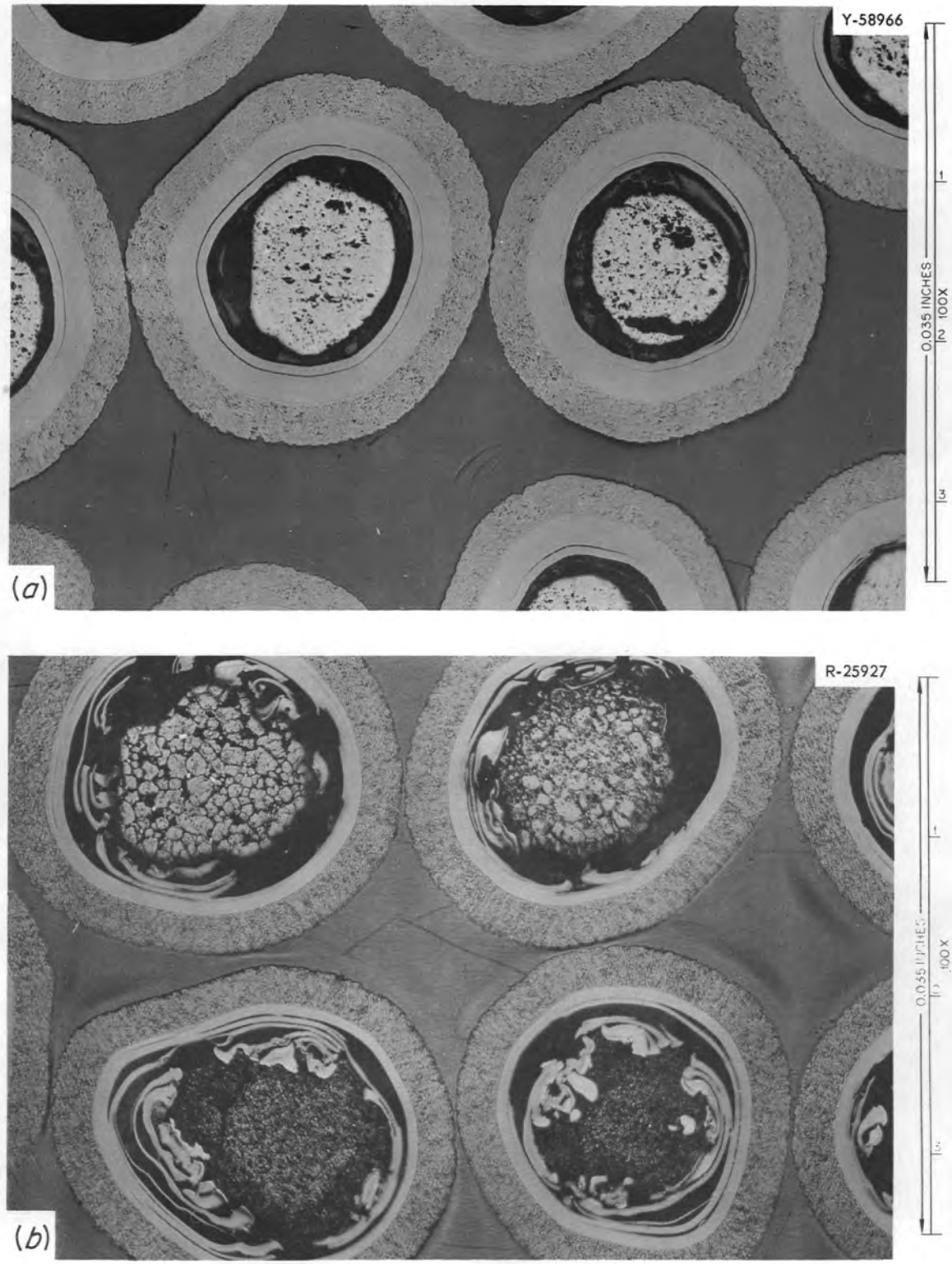

Fig. 2.4. Pyrolytic-Carbon-Coated UO_2 Particles from Batch OR-298. (a) Unirradiated. As polished. (b) Irradiated to 27.9 at. % burnup at 1400°C in capsule A9-2. Etched. 100×

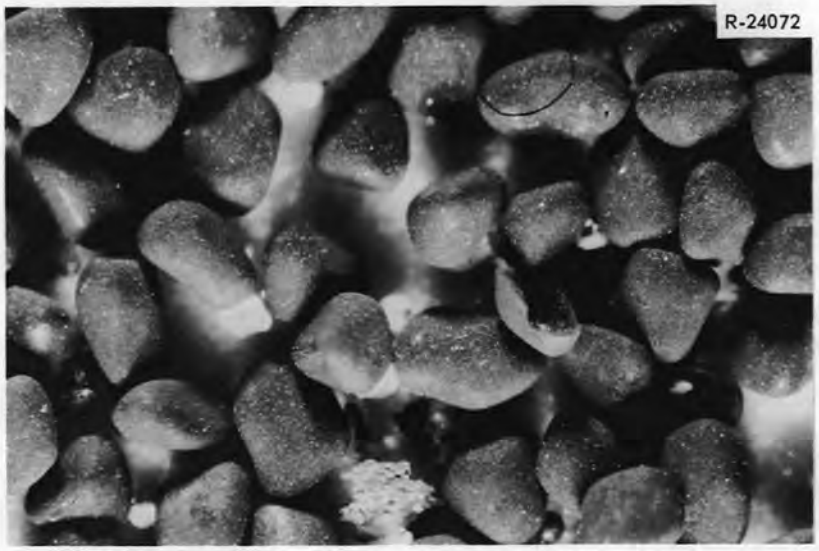

Fig. 2.5. Broken and Oxidized Coatings on Pyrolytic-Carbon-Coated UO_2 Particles (Batch GA-315) from Capsule B9-25. 30×

failures as a result of irradiation damage. As shown in Fig. 2.6, the UO_2 core was much more dense in the irradiated particles than in the unirradiated, and a gap was formed at the core-coating interface as a result of the densification.

Irradiation of capsule A9-3, which also contained pyrolytic-carbon-coated UO_2 particles from batch GA-315, is now in process. The particles were irradiated to 6.1 at. % uranium burnup at 1500°C, and then they were temperature cycled by changing the capsule position and thus changing the neutron flux. The particle temperature was cycled between 1000 and 1500°C at the rate of two cycles per day. On the third day of cycling, bursts of fission gas began. The cycling test is still going on and the average fractional fission-gas release data taken before and after the bursts of gas are listed in Table 2.1.

Capsule B9-26, which contained pyrolytic-carbon-coated UO_2 particles from batch OR-354, was irradiated to 12.1 at. % uranium burnup at 1350°C. Voids in the unirradiated oxide cores, as shown in Fig. 2.7a, seem to be typical for this batch. There was no detectable increase in fission-gas release throughout the test.

Examination of a sample of coated particles from capsule B9-26 revealed that only minor microstructural changes had occurred as a result

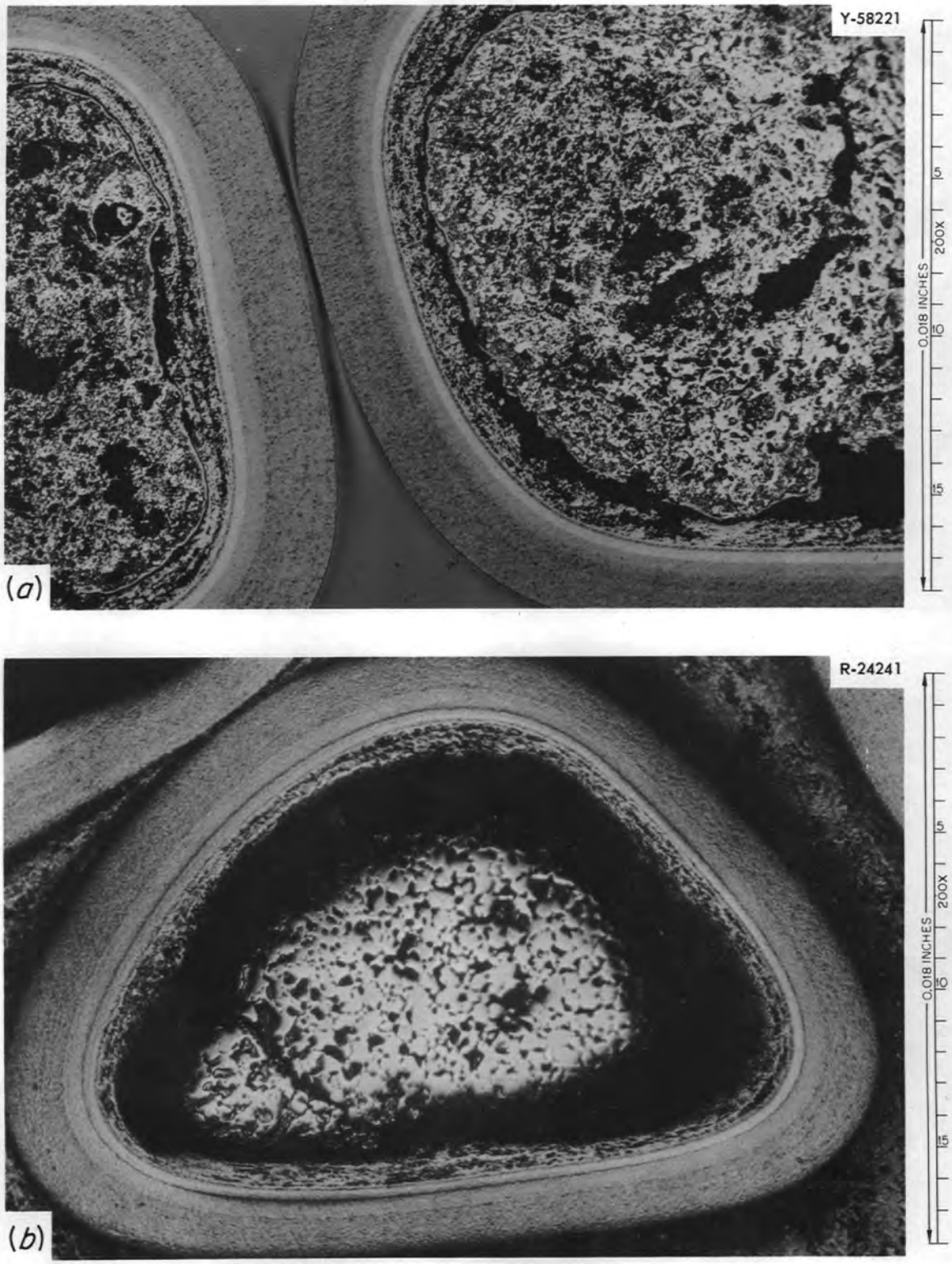

Fig. 2.6. Pyrolytic-Carbon-Coated UO_2 Particles from Batch GA-315. (a) Unirradiated. (b) Irradiated to 9.1 at. % burnup at 1200 and 1400°C in capsule B9-25. 200×

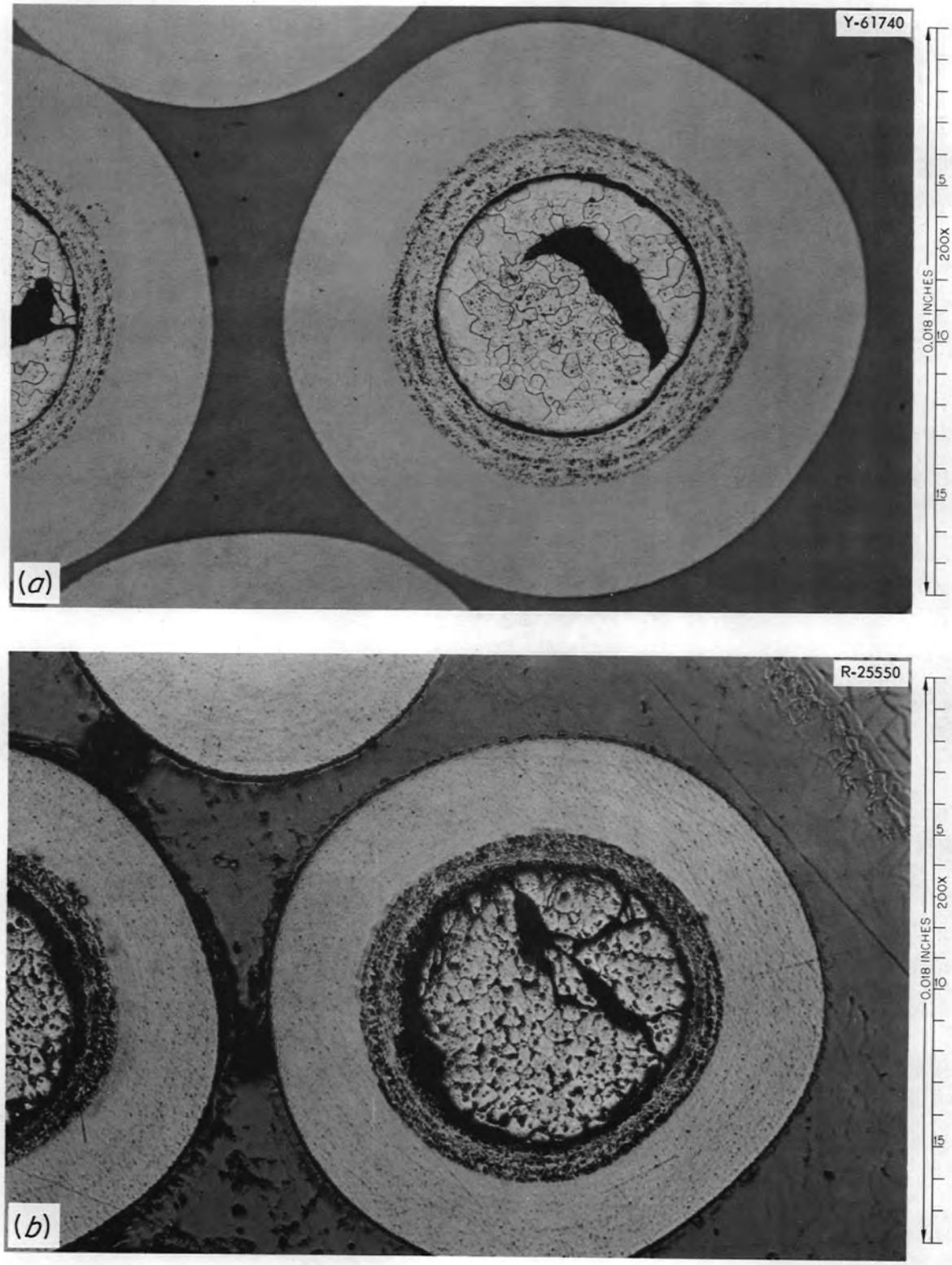

Fig. 2.7. Pyrolytic-Carbon-Coated UO_2 Particles from Batch OR-354. (a) Unirradiated. (b) Irradiated to 12.1 at. % burnup at 1350°C in capsule B9-26. Etched. 200×

of the irradiation test. No failures or evidence of potential failures were noted in the 97 particles examined. The only changes observed were an apparent densification of the inner coating and the presence of fission-gas bubbles and small metallic inclusions in the grain boundaries of the UO_2. Typical particles are shown before and after irradiation in Fig. 2.7.

Capsule B9-27, which contained pyrolytic-carbon-coated UO_2 particles from batch OR-348, was irradiated to 9.4 at. % uranium burnup at 1500°C. Unlike the OR-354 particles irradiated at 1350°C, the fission-gas release was very low (1.5×10^{-8} for ^{88}Kr) at the beginning of the test but increased continuously. The fractional fission-gas release data given in Table 2.1 are averages for the last week of irradiation.

Metallographic examination of 118 particles from capsule B9-27 revealed no failures or evidence of potential failures. Only minor microstructural changes were noted. Metallic inclusions were present in the grain boundaries of the UO_2, and the grain boundaries appeared to contain a continuous nonmetallic second phase. Spectrographic analysis of unirradiated, uncoated UO_2 particles from the same batch showed the major impurities to be calcium (220 ppm) and tungsten (580 ppm). No discernable changes were noted in the coatings, although a continuous gap approximately 5 μ wide had formed at the fuel-coating interface. Typical coated particles from this capsule are shown in Fig. 2.8. The gap at the fuel-coating interface is exaggerated because of relief polishing.

Capsule C1-16, which contained pyrolytic-carbon-coated UO_2 particles from batch OR-343 was irradiated to a total of 14.7 at. % uranium burnup. The first 11.9 at. % burnup was at 1400°C, and then the temperature was increased to 1500°C for another 2.8 at. % burnup. As shown in Table 2.1, the fractional fission-gas release approximately doubled when the temperature was increased from 1400 to 1500°C. At the end of the irradiation the temperature was lowered to 1400°C, and the release rates given in Table 2.1 were obtained.

No failed particles were found in the 123 examined metallographically. In about 20% of the particles, short fractures were noted in the coatings that originated at the fuel-coating interface. The fractures tended to spiral into the coatings. One of the more severely fractured coatings is

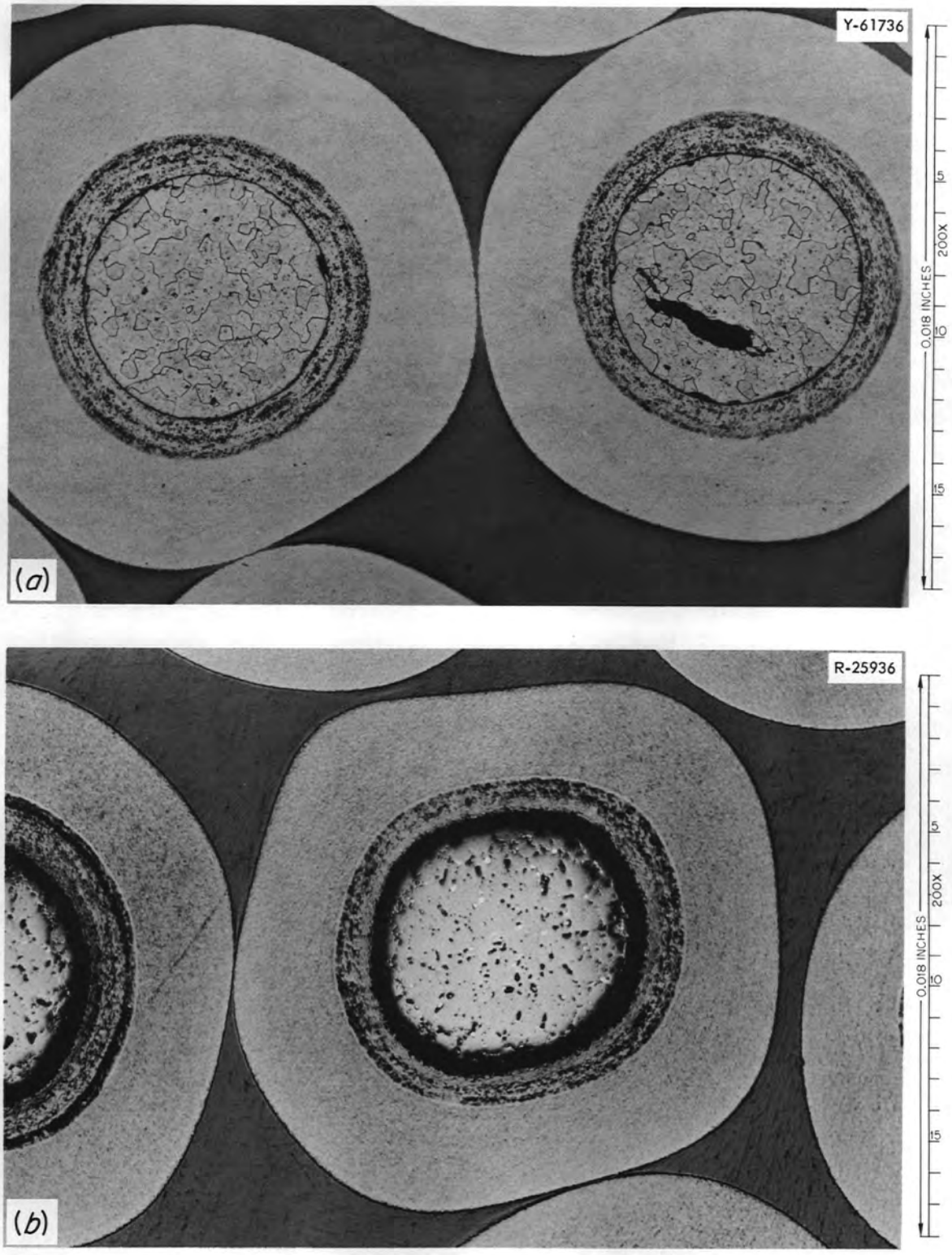

Fig. 2.8. Pyrolytic-Carbon-Coated UO_2 Particles from Batch OR-348. (a) Unirradiated. (b) Irradiated to 9.4 at. % burnup at 1500°C in capsule B9-27. Etched. 200×

shown in Fig. 2.9. Close examination of the unirradiated control particles disclosed microscopic fractures in some that originated at the fuel-coating interface and spiraled into the coating, as shown in the same figure. Thus, it appears that densification of the coatings during irradiation caused the fractures to enlarge and perhaps to propagate. There was no evidence of a reaction product at the fuel-coating interface. Except for a slight loss in crystalline detail and grain-boundary integrity in the UO_2, no other microstructural changes were noted in the particles.

Capsule C1-17, which contained pyrolytic-carbon-coated UO_2 particles from batch HB-23, was irradiated to 25.2 at. % uranium burnup at 1600°C. This is the highest irradiation temperature that coated particles have reached in the A9, B9, or C1 facilities. The fission-gas release rates were extremely low and increased less than a factor of 2 during the entire test. The fractional release values given in Table 2.1 are averages for the last week of the test.

Metallographic examination of 122 particles from capsule C1-17 disclosed no failures or evidence of potential failures. An apparent densification of the porous inner layer was the only microstructural change noted in coatings after irradiation. These particles are shown before and after irradiation in Fig. 2.10. The grain size of the sol-gel oxide is normally too small to be resolved with the light microscope. It was noted, however, that grains could be resolved in the peripheral regions of some of the UO_2 particles. Grain colonies could be seen across the entire fuel particle after irradiation.

Capsule C1-15, which contained pyrolytic-carbon-coated $(Th,U)C_2$ particles from batch GA-314, was irradiated to 8.7 at. % heavy-metal burnup at 1400°C. Because of the thorium-to-uranium ratio of 2 to 1, it required almost 2000 hr to reach this burnup. The fission-gas release rates remained about constant during the irradiation. The average fractional releases are given in Table 2.1 and are for the entire irradiation period. No failed particles were found in the 83 examined. There was no evidence of damage to the coatings. The $(Th,U)C_2$ cores contained numerous fine pores; no crystalline detail could be resolved by etching. Typical unirradiated and irradiated particles are shown in Fig. 2.11.

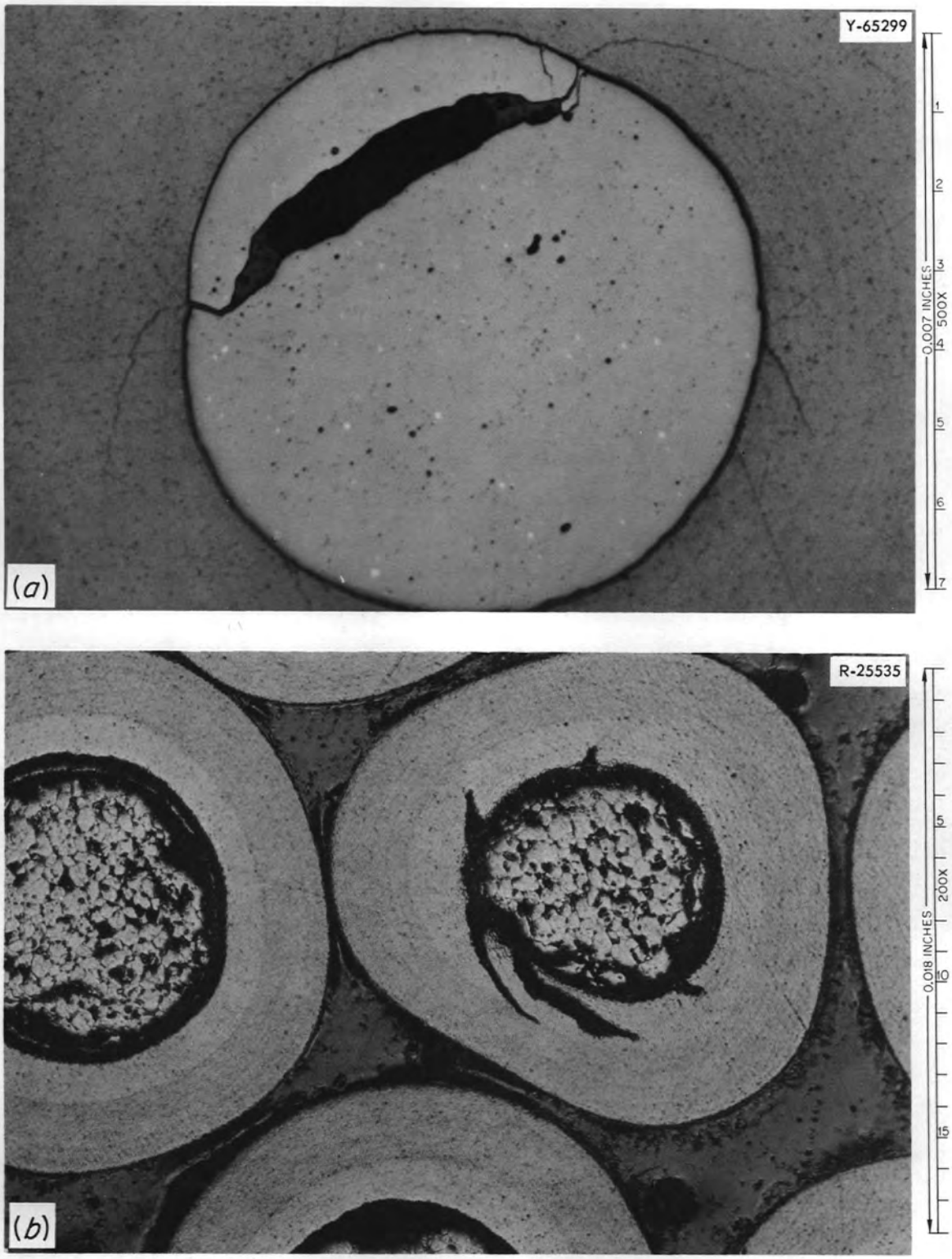

Fig. 2.9. Typical Pyrolytic-Carbon-Coated UO_2 Particles from Batch OR-343 Irradiated in Capsule C1-16. (a) Unirradiated. Note the fine fractures in the coating that originate at the fuel-coating interface. As polished. 500× (b) Irradiated. The particle on the left is typical; whereas, the severely fractured coating is atypical. Etched. 200×

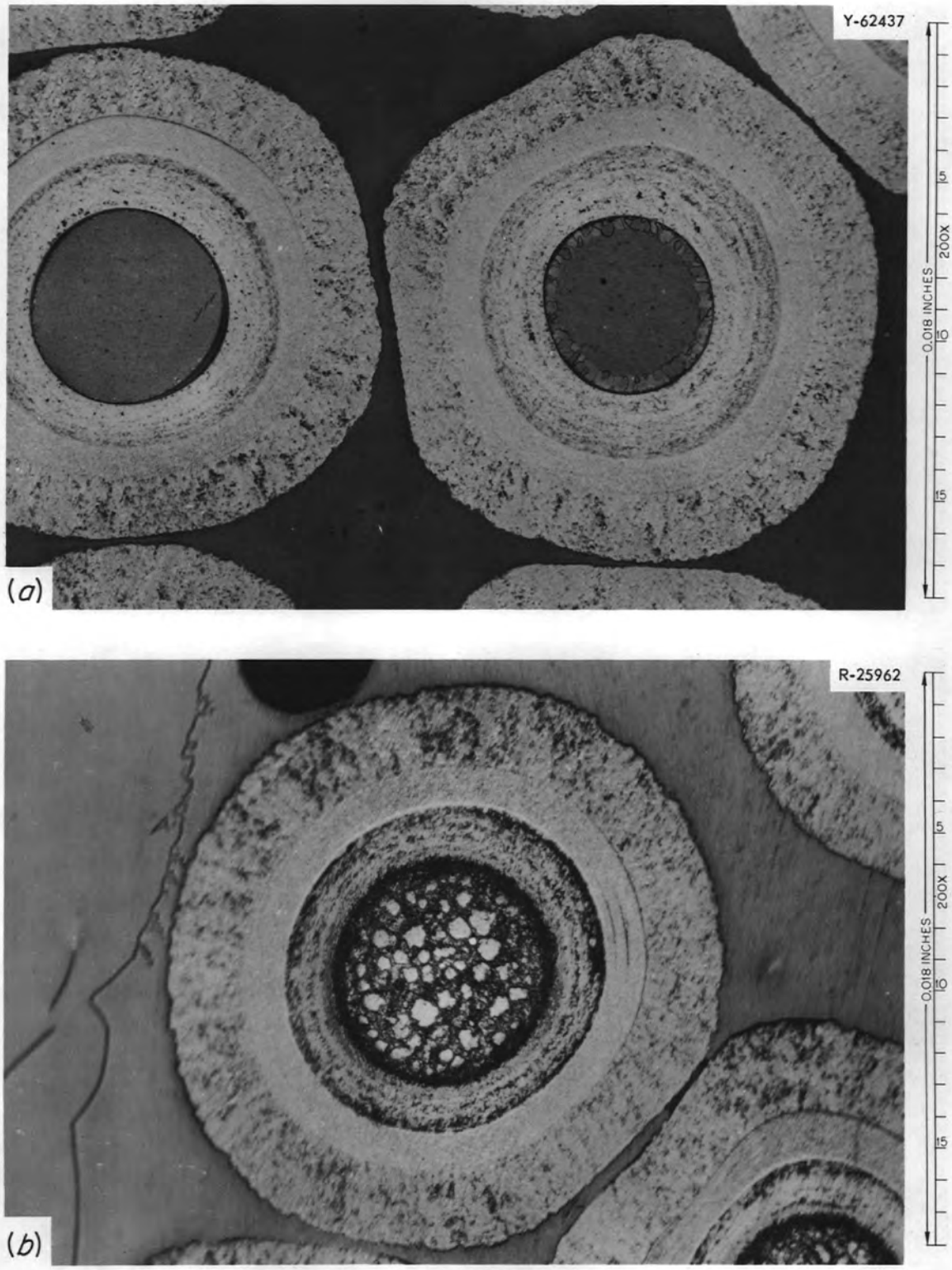

Fig. 2.10. Pyrolytic-Carbon-Coated UO_2 Particles from Batch HB-23. (a) Unirradiated. (b) Irradiated to 25.2 at. % burnup at 1600°C in capsule C1-17. Etched. 200×

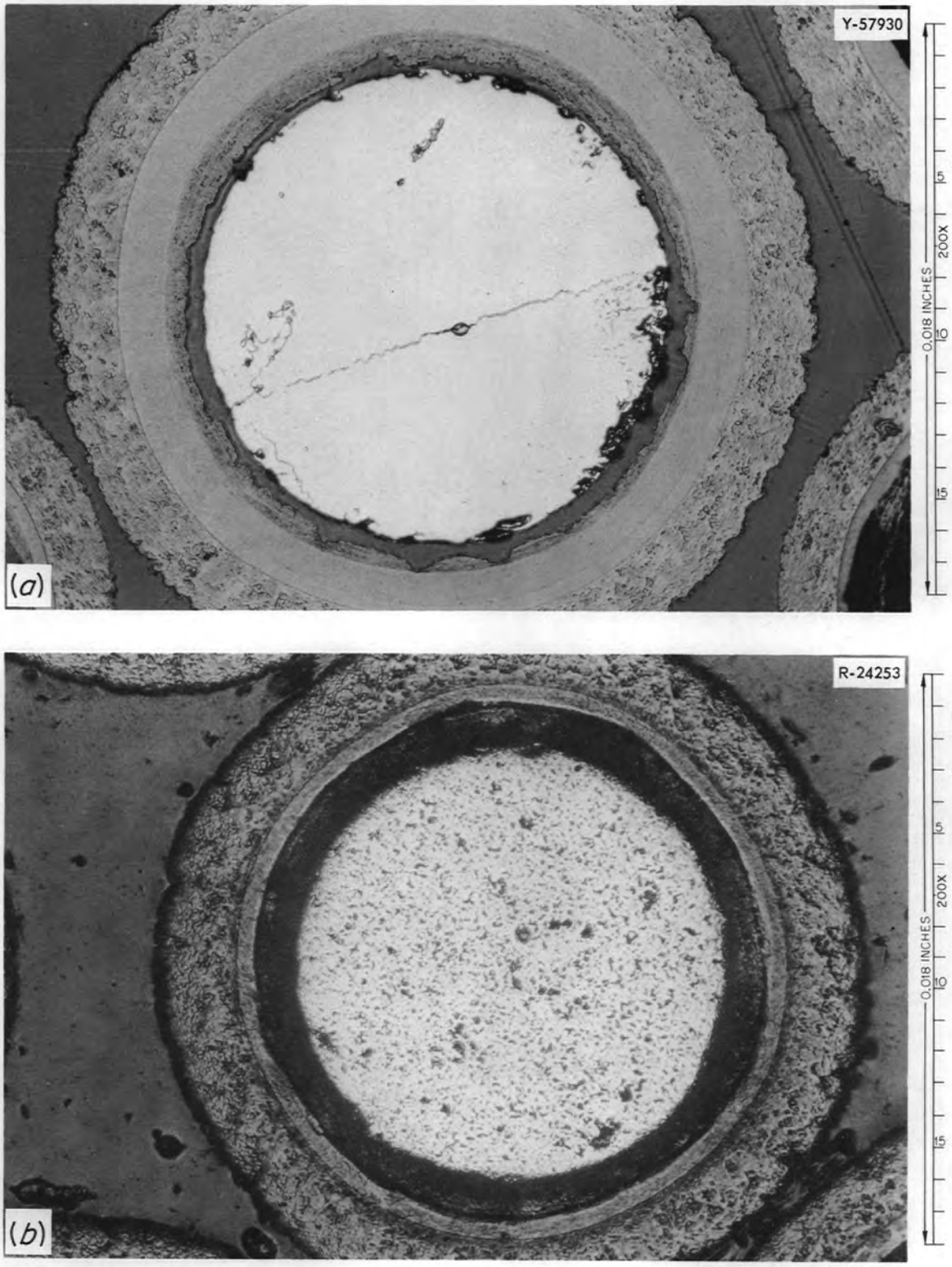

Fig. 2.11. Pyrolytic-Carbon-Coated $(Th,U)C_2$ Particles from Batch GA-314. (a) Unirradiated. (b) Irradiated to 8.7 at. % burnup at 1400°C in capsule C-15. 200×

Conclusions. We determined the fuel contamination at or near the surface of the pyrolytic-carbon coatings by alpha counts of each batch of particles before irradiation, and we observed that a correlation could be made between the degree of contamination and the fission-gas release from particles with unbroken coatings (see Fig. 2.12). Because of rather large inaccuracies in the values for the surface contamination, this correlation is only qualitative, but there is a clear indication that the particles with low contamination had low fission-gas release. This leads us to the

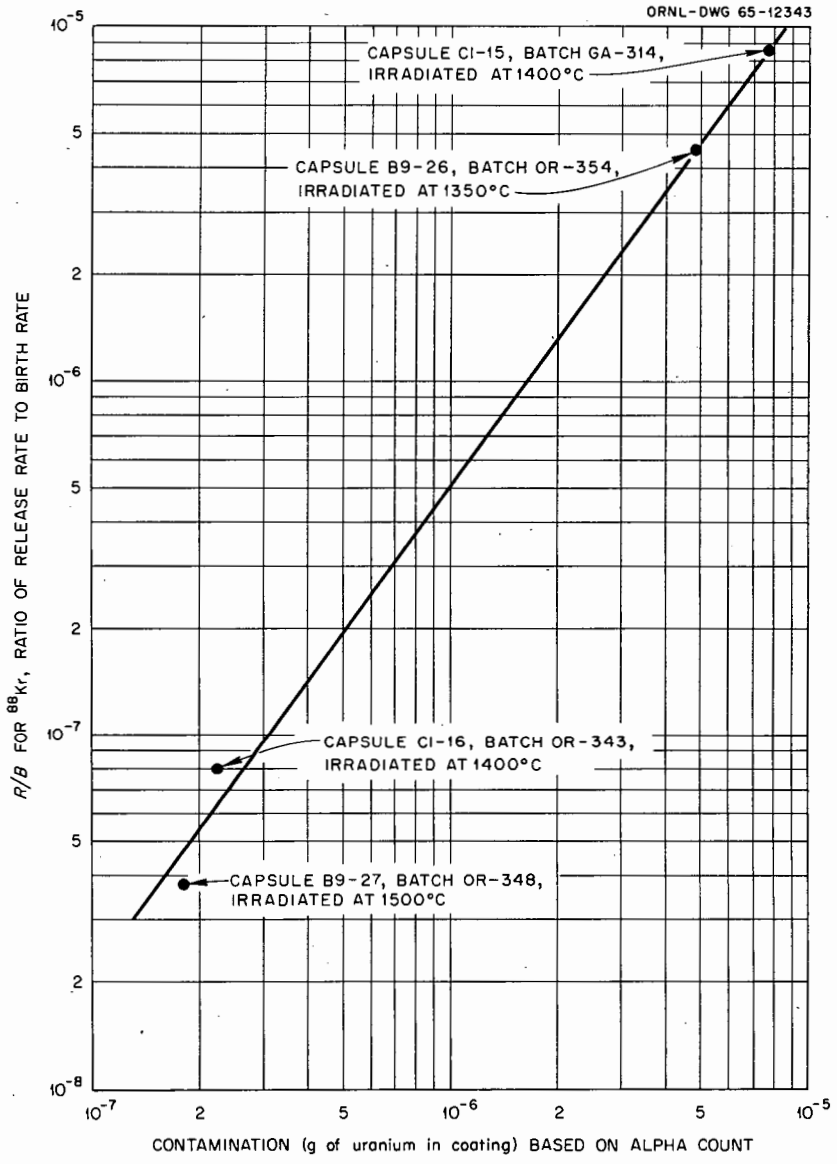

Fig. 2.12. Relationship Between Fission-Gas Release and Coating-Surface Contamination.

conclusion that the fission-gas release from unbroken particles is from contamination in the coating (at least up to 1400°C) and does not come from the fuel core.

In these experiments radiation damage to the pyrolytic-carbon coatings is primarily from fission fragments and originates at the core-coating interface. This can be alleviated by providing a sacrificial layer, a porous carbon layer, or a gap at the core-coating interface. For obvious reasons the sacrificial layer is least desirable because part of the coating is destroyed. The porous layer works very well, but it is not easy to put on and is not strong.

One of our most successful experiments was that in which particles from batch OR-343 were irradiated in capsule C1-16. These particles (UO_2 cores) were coated with a layer of low-density isotropic, pyrolytic carbon and then a high-density layer. During irradiation at high temperature the inner (low-density) layer shrank and provided the gap that appears to be necessary for good performance. These coatings are easy to apply and therefore cheap.

We now have had experience with a good number of UO_2 coated particles, and we conclude that they are superior to the UC_2 particles for the following reasons: (1) the oxide does not flow at high burnup and expand into voids or cracks as the carbide does, and thus a gap can be maintained between the core and the coating with the oxide but not with the carbide; (2) the oxide does not diffuse into the pyrolytic-carbon coatings, even at high temperatures (1800 to 2000°C); (3) uranium contamination in the coating can be kept to a much lower level during fabrication of oxide cores; and (4) the oxide is not reactive and therefore much easier to handle during fabrication of the coated particle.

Fission-Product Release from High-Burnup Coated UC_2, $(Th,U)C_2$, and UO_2 Particles by Postirradiation Annealing

M. T. Morgan R. L. Towns
J. G. Morgan

We are studying the effects of postirradiation annealing on irradiated coated fuel particles to determine the stability of the coatings

at temperatures higher than those of the irradiation and to measure their ability to contain fission products. The particles so far have been UC_2, $(Th,U)C_2$, or UO_2 with duplex or triplex pyrolytic-carbon coatings. These particles are heated to temperatures up to 2000°C, and furnace components are periodically removed for analysis to determine fission-product release as a function of time and temperature.[9] The results of several annealing experiments were reported previously,[10] and the results of anneals of particles from capsules C1-15 (batch GA-314) and C1-16 (batch OR-343) are discussed here.

The C1-15 (GA-314) particles were $(Th,U)C_2$ with triplex pyrolytic-carbon coatings and were the same as those from capsule B9-21 that were previously annealed, except that the C1-15 particles were irradiated to 8.9 at. % uranium burnup, while the B9-21 particles were irradiated to 0.29 at. % burnup. Krypton-85 release indicated failure of one particle out of 40 at 1700°C and one at 2000°C. Both failures occurred during the initial hour at the respective temperatures. The fission-product release rates averaged over 6 hr of annealing following an initial 1-hr heating period at each temperature are compared in Table 2.2 with those of three other experiments previously discussed.[10] Graphs of the accumulated release fractions of ^{140}Ba and ^{89}Sr versus time for various temperatures are given in Figs. 2.13, 2.14, and 2.15.

The higher burnup of the C1-15 (GA-314) particles apparently increased the retention of barium and strontium. This effect can be seen at all three annealing temperatures. The cerium release rate was low at 1370 and 1700°C, but it approached that of barium and strontium at 2000°C. The B9-20 particles showed a low release rate for ^{144}Ce, which may be due to the UO_2 cores.

The C1-16 (OR-343) UO_2 particles had duplex pyrolytic-carbon coatings. No coating failures were indicated during annealing. The analytical

---

[9]M. T. Morgan et al., Fission-Gas Release from High-Burnup Coated Particles, pp. 149–152, GCRP Semiann. Progr. Rept. Sept. 30, 1963, USAEC Report ORNL-3523, Oak Ridge National Laboratory.

[10]M. T. Morgan et al., Fission-Product Release from High-Burnup Coated Particles by Postirradiation Annealing, pp. 101–106, GCRP Semiann. Progr. Rept. Mar. 31, 1965, USAEC Report ORNL-3807, Oak Ridge National Laboratory.

Table 2.2. Fission-Product Release Rates from Pyrolytic-Carbon-Coated Fuel Particles During Postirradiation Annealing

Annealing Temperature (°C)	Sample Designation	Type of Fuel	Fission-Product Release Rates (%/hr)			
			^{140}Ba	^{89}Sr	^{144}Ce	^{137}Cs
1370	B9-17	UC_2	0.6	0.3	0.06	≤0.004
	B9-20	UO_2	0.1	0.3	≤0.003	≤0.03
	B9-21	$(Th,U)C_2$	0.1	0.2	≤0.01	0.01
	C1-15	$(Th,U)C_2$	0.1	0.04	0.04	0.02
1700	B9-17	UC_2	2.0	3.0	≤6.0	0.03
	B9-20	UO_2	0.8	0.6	≤0.002	≤0.1
	B9-21	$(Th,U)C_2$	0.6	2.0	0.04	0.02
	C1-15	$(Th,U)C_2$	0.5	0.4	0.3	0.08
2000	B9-17	UC_2	≤40	≤40	≤40	10
	B9-20	UO_2	2	2	0.03	≤0.2
	B9-21	$(Th,U)C_2$	6	7	5	0.3
	C1-15	$(Th,U)C_2$	3	5	3	6

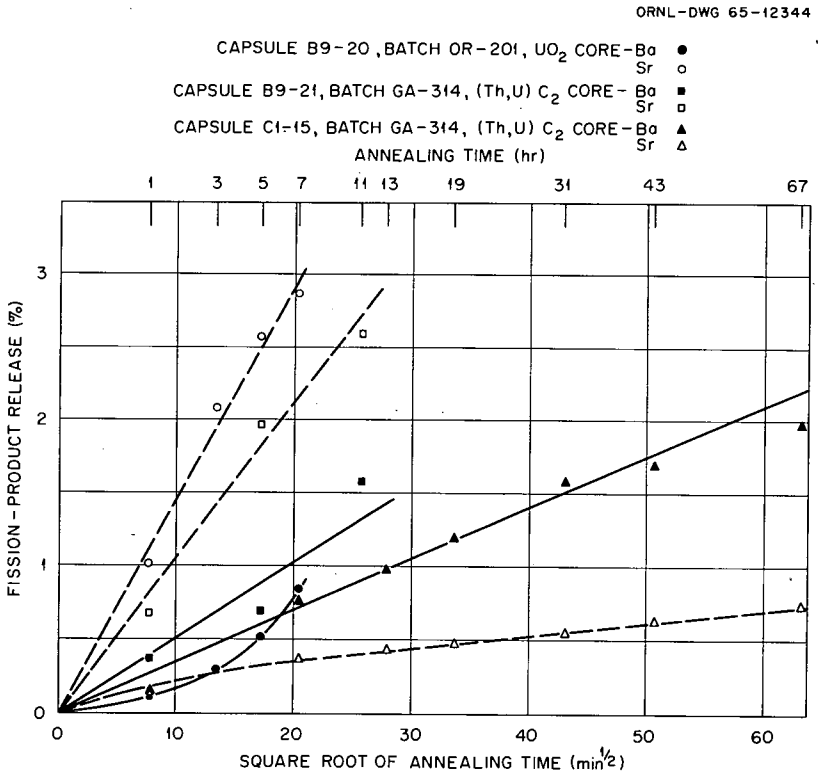

Fig. 2.13. Accumulated Fission-Product Release of Particles from Capsules B9-20, B9-21, and C1-15 During Postirradiation Annealing at 1700°C.

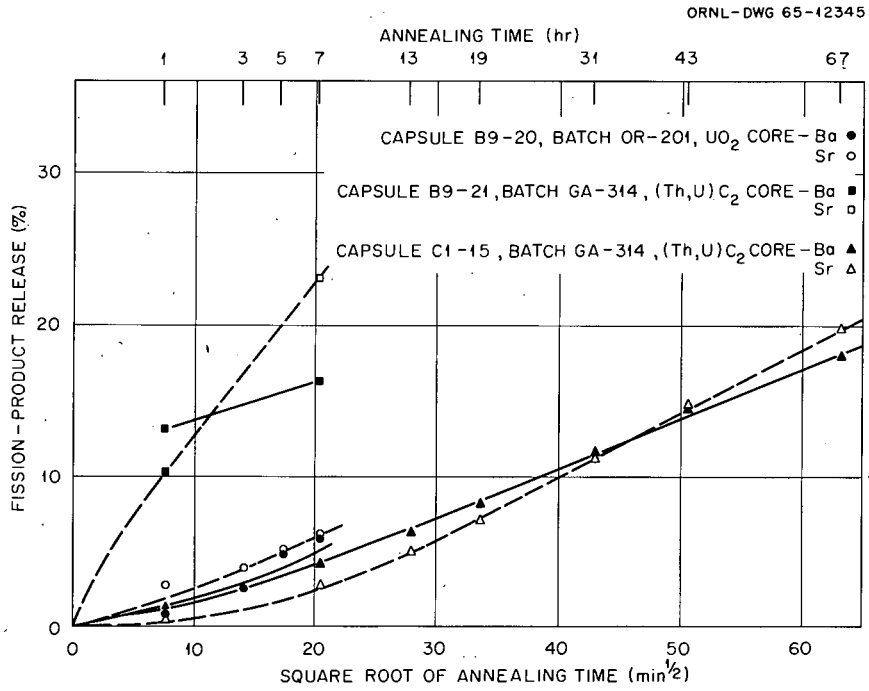

Fig. 2.14. Accumulated Fission-Product Release of Particles from Capsules B9-20, B9-21, and C1-15 During Postirradiation Annealing at 1700°C.

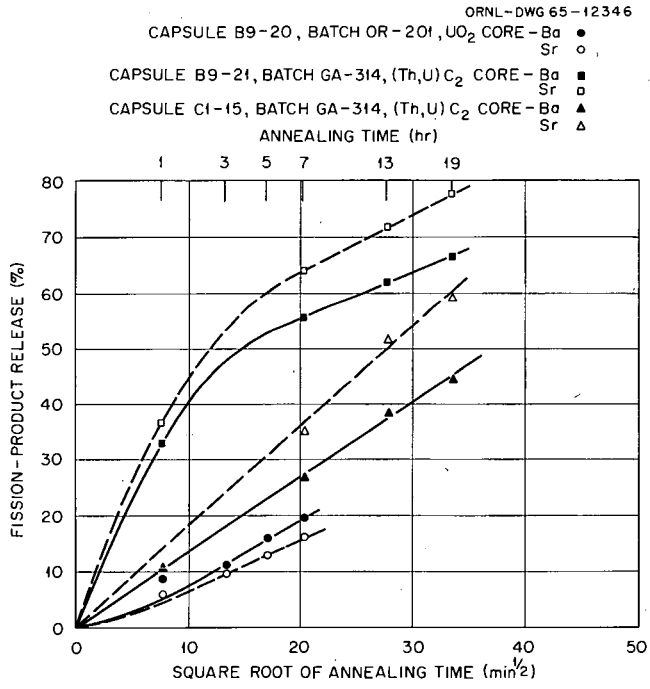

Fig. 2.15. Accumulated Fission-Product Release of Particles from Capsules B9-20, B9-21, and C1-15 During Postirradiation Annealing at 2000°C.

data are incomplete on the fission products, but preliminary calculations show high release rates for barium and strontium at 1500, 1700, and 2000°C. These particles, which were irradiated to 14.7 at. % burnup, had outer coating densities of about 1.8 g/cm^3; particles previously tested had coating densities of around 2.0 g/cm^3.

We are preparing for an irradiation experiment in which particles with different structural characteristics will be irradiated in the same capsule to gain more accurate information on the effect of coating density, anisotropy, and crystallite size on fission-product release and to compare UO_2 cores with UC_2 cores. This capsule will be inserted in the A-9 facility of the ORR about October 17. We plan to irradiate these particles to a burnup of about 10 at. % of the uranium at a temperature of 1400°C.

Fission-Product Transport and Deposition

F. H. Neill

Fission-Product Deposition in ORNL Out-of-Pile Loop (D. L. Gray, F. H. Neill)

Tests are continuing in a study of iodine deposition on small-diameter silver wires mounted perpendicular to a turbulently flowing helium stream.[11] In one series of tests in which a silver-plated tube was used, the iodine deposition on the tube and on the wires was predicted from a heat-mass analogy and compared with the experimental results. The comparison is shown in graphical form in Fig. 2.16. The predicted activity was within 13% of the actual deposition on the wires and within 35% of the actual deposition on the tube wall. Based on these results, we anticipate that for simple flow geometries it will be possible to predict fission-product deposition reasonably well by the heat-mass analogy provided the deposition surface acts as a perfect sink (negligible desorption and reflection) for the fission products.

---

[11]D. L. Gray, Fission-Product Deposition in ORNL Out-of-Pile Loop, pp. 106–111, GCRP Semiann. Progr. Rept. Mar. 31, 1965, USAEC Report ORNL-3807, Oak Ridge National Laboratory.

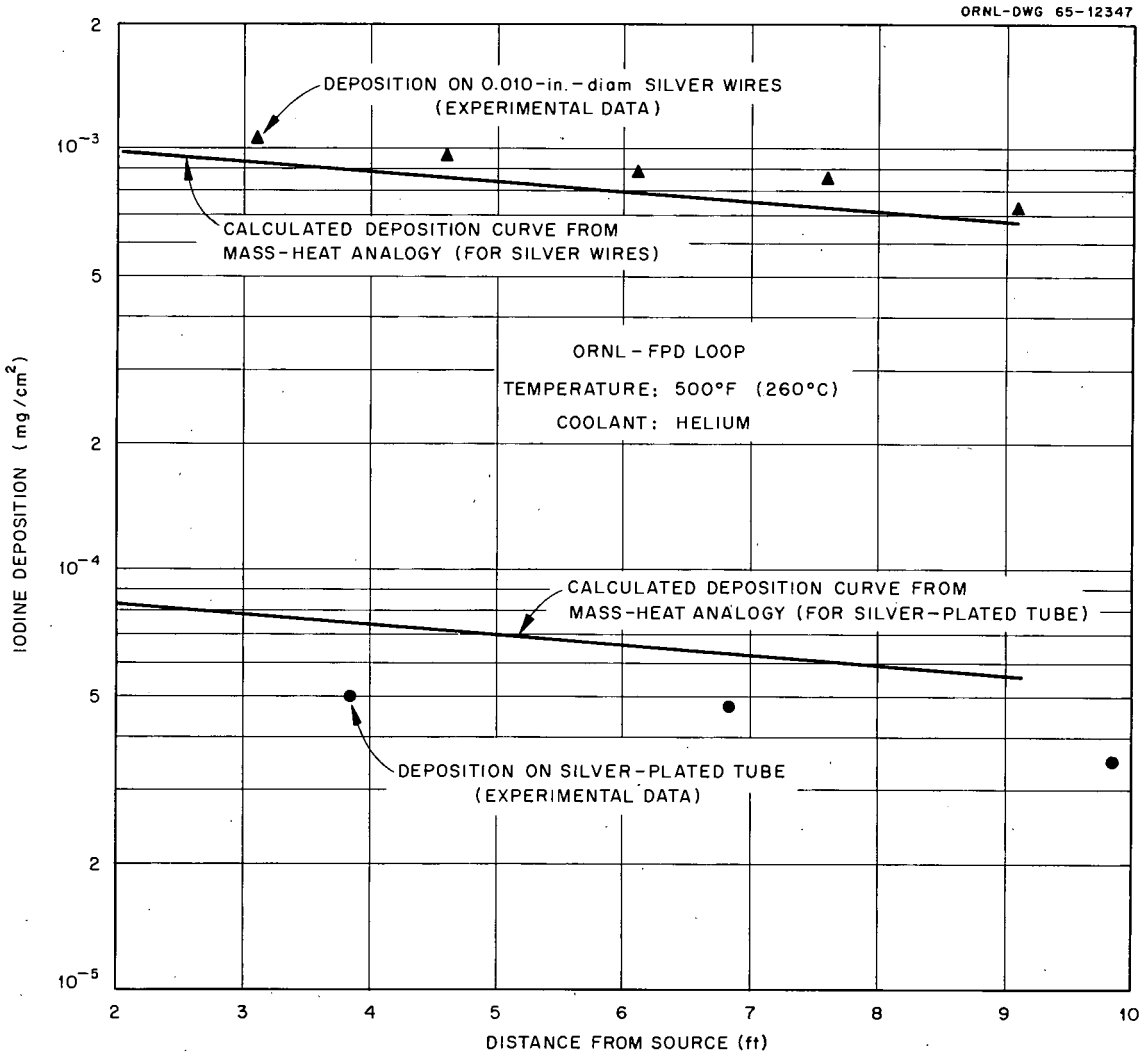

Fig. 2.16. Comparison of Analytical Results with Experimental Data for Iodine Deposition on Silver Wires and Tubing Walls from a Flowing Helium Stream.

The results of this experiment suggest the use of silver wires as a simple means of determining average gas-stream concentrations for metallic fission products. For this application, the activity on the wires could be measured at the termination of a test; then, by knowing the flow conditions of the system, the mass transfer coefficient could be readily determined. The average gas-phase concentration of the fission product adjacent to the silver wire could then be estimated.

In order to examine the difference in iodine deposition on stainless steel and carbon steel surfaces compared with silver surfaces under identical flow and surface-temperature conditions, we ran a series of tests in which 0.010-in.-diam stainless steel and carbon steel wires were mounted adjacent to similar-diameter silver wires. The wires, in groups of three, were mounted in a turbulently flowing helium stream perpendicular to the direction of flow. Stable iodine tagged with the ^{131}I isotope was injected into the helium upstream of the test section at iodine-injection rates that varied from 0.013 to 0.212 mg/min. The ratio of the deposition on the center one-third of each length of silver wire was compared with that on a similar area of an adjacent carbon steel or stainless steel wire. The results of the experiment are shown in Fig. 2.17. We believe the increase in the silver-to-metal ratio with increased deposition shown

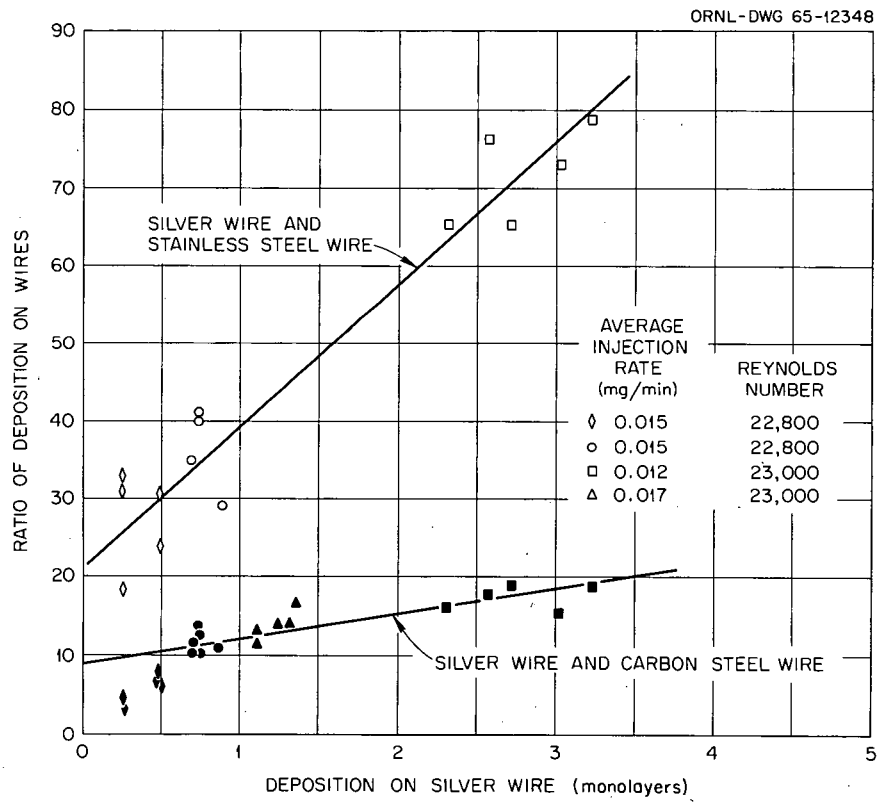

Fig. 2.17. Comparison of Iodine Deposition on a Stainless Steel Surface and a Carbon Steel Surface with Iodine Deposition on a Silver Surface at Various Levels of Surface Concentration.

in the graph results from the lower surface saturation level of the stainless steel and carbon steel as compared with the silver surface saturation level.

We conducted a third series of tests in which 1-in.-diam tubes were inserted into the test section of the loop immediately downstream of the source injector in order to investigate desorption of iodine from various metal surfaces. Iodine tagged with radioactive tracer ^{131}I was injected into the helium stream and permitted to deposit on the test surfaces. The surface activity was monitored as a function of time after injection. Figure 2.18 shows the desorption of iodine from two silver-plated surfaces and two carbon steel surfaces, each at two levels of surface concentrations, and from two stainless steel surfaces, each at one level of surface concentration. At the termination of iodine injection, the helium flow and the surface temperature were maintained constant during the monitoring period, except at one given time during each test when the loop helium inventory was dumped and the loop refilled with fresh helium to assure that no iodine remained in the gas phase. No change in the surface deposition level was noted during any of the purge operations. As an

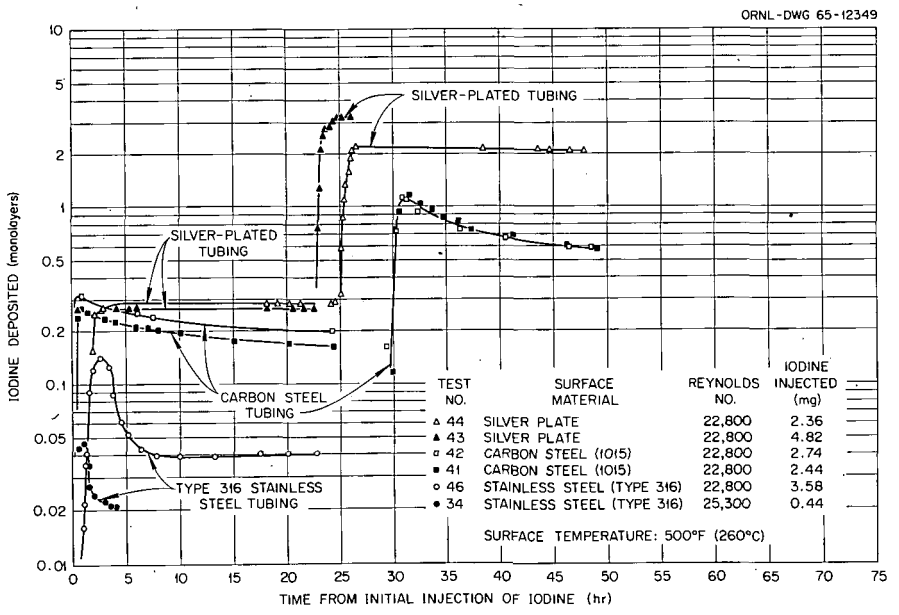

Fig. 2.18. Comparison of Iodine Desorption from Stainless Steel, Carbon Steel, and Silver-Plated Surfaces.

added precaution, a silver wool filter was installed in the loop immediately downstream of the test section to prevent recirculation of the gas-phase iodine. Results from the silver-plated tubes show that no desorption occurred at a surface temperature of 500°F (260°C). After equilibrium was achieved, the surface temperature was raised in 25° increments up to 600°F (316°C). No desorption of iodine occurred due to the increase in surface temperature. The deposited iodine on the carbon steel surfaces after desorption was 62 and 61%, respectively, of the initial levels for the lower surface concentration, and it was 53% of the initial value for the higher level of surface concentration. The deposited iodine on the stainless steel surface after desorption was 28% of the initial value at the higher surface concentration and 44% of the initial level at the lower surface concentration. In three other tests with stainless steel surfaces (not shown on the graph), the levels of deposition were 20, 23, and 29% of the initial value for an initial surface concentration in the range of 0.03 to 0.10 monolayers of iodine.

In a fourth series of experiments, iodine was deposited from a flowing helium stream on a roughened carbon steel surface, and the results were compared with deposition on an "as-received" carbon steel surface. For the conditions under which the tests were conducted [surface temperature, 500°F (260°C); Reynolds number, 25,000; average roughness, 75 ppm], no noticeable difference was detected.

Packed-Bed Laminar-Flow Deposition Experiment (D. L. Gray, D. M. Eissenberg)

A small experimental assembly for fission-product deposition studies was constructed in which the progression of depositable fission-product species through a packed bed of spheres can be followed by gamma-ray scanning. The purpose of the experiment is to determine the physical and chemical conditions under which fission products deposited from a helium stream onto various surfaces under the environmental conditions of a gas-cooled reactor primary system will reenter the gas stream and deposit farther downstream. The equipment, shown in Fig. 2.19, consists of a once-through flow system that includes a helium supply, a preheater, a simulated fission-product source, a packed-bed deposition tube, and a

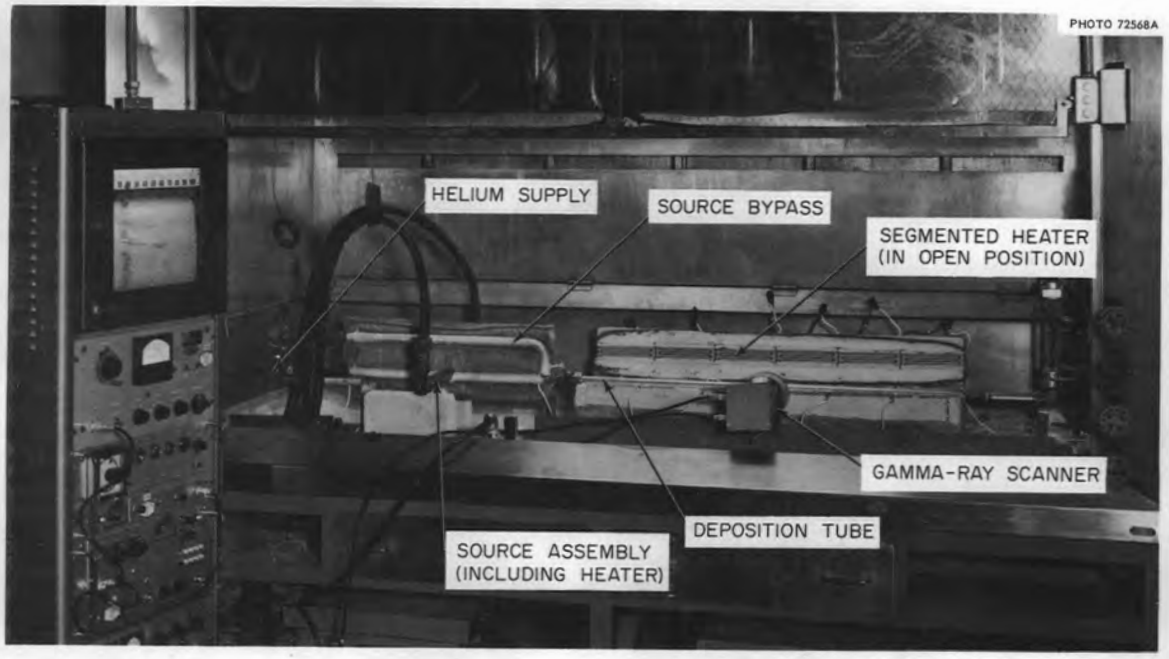

Fig. 2.19. Packed-Bed Test Facility for Fission-Product Transport and Deposition Experiments.

gamma-ray scanner. A close view of the source assembly is shown in Fig. 2.20.

The source and deposition tube can be operated at various temperatures of interest up to a source temperature of 2000°F (1093°C) and a bed temperature of 1800°F (982°C). The source is encapsulated in 1/8-in.-diam graphite rods, which are inserted into the center of the hollow injection rod. When the graphite rod is heated, the fission products are released to the gas stream by diffusion through the graphite rod. The packed bed consists of a 3-ft length of 1-in.-diam, 0.035-in.wall stainless steel tubing, which has been packed with 3/16-in.-diam stainless steel balls for the first series of tests. Electrical heaters provide individual temperature control over each section of the deposition tube.

The experimental procedure will consist of generating fission-product elements containing trace radioactive isotopes, either singly or in combination, and carrying them in the helium stream into the deposition section. The changing deposition patterns in the packed bed will be followed by scanning while temperature and helium gas velocities in the bed are

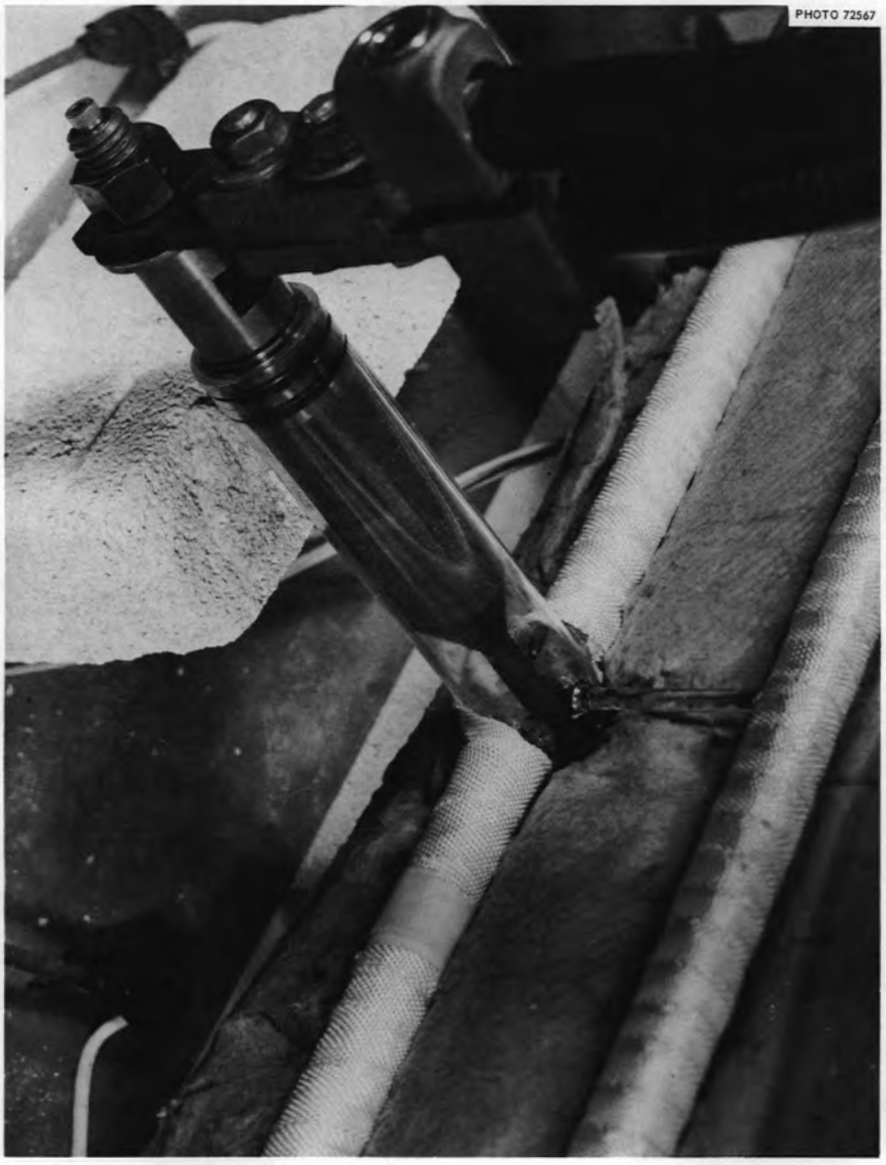

Fig. 2.20. Source Tube of Packed-Bed Test Facility. Source is inserted inside hollow graphite rod.

varied. The effect of pretreatment of the bed with stable isotopes of the same or different fission-product elements or with special additives will also be followed by determining their effects on the deposition pattern in the packed bed.

Analytical Model for Fission-Product Deposition (T. S. Kress)

In previous reports, a fission-product deposition model was developed from mass balances of fission products leaving the gas stream, adsorbing

on surfaces, and desorbing back into the stream. The adsorption rate was determined as the number of fission-product molecules colliding with the surface reduced by a factor σ, defined as the fraction of those colliding that become adsorbed. Subsequently, σ was allowed to decrease from an initial value σ_0 proportionally as the surface concentration M approaches a maximum M_s. Therefore

$$\sigma = \sigma_0 \left(1 - \frac{M}{M_s}\right) .$$

The same mass balance procedure as that used previously[12] then resulted in the following equations:*

$$\frac{\partial \overline{N}_*}{\partial t_*} + \frac{U_*}{D_*}\frac{\partial \overline{N}_*}{\partial x_*} + \left\{ \lambda_* + \frac{4h_*}{D_*} - \frac{4h_*^2}{D_*\left[h_* + \sigma_0 K r_*\left(1 - \frac{M}{M_{s*}}\right)\right]} \right\} \overline{N}_* - \left\{ \frac{4h_*\theta_*}{D_*\left[h_* + \sigma_0 K r_*\left(1 - \frac{M_*}{M_{s*}}\right)\right]} \right\} M_* = 0 , \quad (1)$$

and

$$\frac{\partial M_*}{\partial t_*} + \left\{ \theta_* + \lambda_* - \frac{\theta_*\sigma_0 K r_*\left(1 - \frac{M_*}{M_{s*}}\right)}{\left[h_* + \sigma_0 K r_*\left(1 - \frac{M_*}{M_{s*}}\right)\right]} \right\} M_* - \left\{ \frac{h_*\sigma_0 K r_*\left(1 - \frac{M_*}{M_{s*}}\right)}{\left[h_* + \sigma_0 K r_*\left(1 - \frac{M_*}{M_{s*}}\right)\right]} \right\} \overline{N}_* = 0 . \quad (2)$$

---

*For nomenclature definitions see ref. 12, pp. 116–117.

[12] T. S. Kress, Analytical Model for Fission-Product Deposition, pp. 111–117, GCRP Semiann. Progr. Rept. Mar. 31, 1965, USAEC Report ORNL-3807, Oak Ridge National Laboratory.

For these equations the following dimensionless quantities have been defined:

$$x_* = x/D \qquad t_* = t(\tau_w g_c/\mu)$$

$$D_* = D\sqrt{\tau_w g_c/\rho}/\nu \qquad \theta_* = \theta/(\tau_w g_c/\mu)$$

$$U_* = \overline{U}_x/\sqrt{\tau_w g_c/\rho} \qquad \lambda_* = \lambda/(\tau_w g_c/\mu)$$

$$\overline{N}_* = \overline{N}/\overline{N}_0 \qquad h_* = h/\sqrt{\tau_w g_c/\rho}$$

$$M_* = M\sqrt{\tau_w g_c/\rho}/\overline{N}_0\nu \qquad Kr_* = \sqrt{RTg_c/2\pi m}/\sqrt{\tau_w g_c/\rho}$$

$$M_{s*} = M\sqrt{\tau_w g_c/\rho}/\overline{N}_0\nu$$

The equilibrium solution to Eqs. (1) and (2) for nonradioactive species ($\lambda = 0$) is

$$\frac{1 - \dfrac{M_*}{M_{s*}}}{M_{s*}} = \frac{\theta_*}{\sigma_0 Kr_*} \quad . \tag{3}$$

Equation 3 is Langmuir's adsorption isotherm. This result indicates that the equilibrium solution for a convecting system approaches that of a static system. This conclusion is of particular interest to reactor designers who may be concerned with the contamination resulting from long-lived fission products and long-term reactor operation. It implies that by establishing the surface chemistry of fission-product mixtures through systematic static tests, the limiting contamination levels for actual operation under flow conditions can be predicted.

For low surface coverage, $M_*/M_{s*} \ll 1$, Eqs. (1) and (2) reduce to the set previously reported.[12] If the further limiting conditions λ and θ negligible are met, the solution to Eqs. (1) and (2) is

$$M_* = \frac{\sigma_0 Kr_* h_*}{h_* + \sigma_0 Kr_*} \exp\left(-4h_*\sqrt{C_f}\,\frac{\sigma_0 Kr_*}{h_* + \sigma_0 Kr_*}\right) t_* \ ,$$

or if, as is often the case, $\sigma_0 Kr_* >> h_*$,

$$M_* \cong h_* \exp\left(-4h_* \sqrt{C_f}\, x_*\right) t_* , \qquad (4)$$

where C_f is the Blasius friction coefficient. Equation (4) is a direct application of the heat-mass analogy. With it, one can predict low-level deposition, as shown in Fig. 2.21 for deposition of ^{127}I on a silver-plated surface.

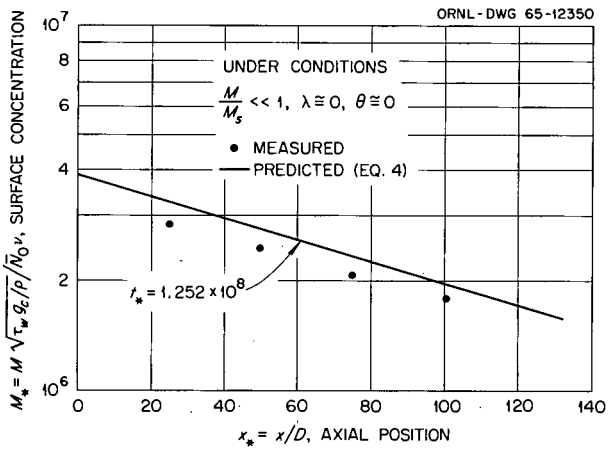

Fig. 2.21. Comparison of Analytical Results with Experimental Data for Iodine Deposition from a Flowing Helium Stream to Tubing Wall.

Sorption of Fission-Product Vapors on Structural Metals

W. E. Browning, Jr. M. E. Davis

A considerable amount of work has been done in this program on the deposition behavior of iodine, and the elemental form has been assumed to be the depositing species. Elemental iodine in the gaseous state is usually thought of as the diatomic molecule I_2. This diatomic molecule dissociates into iodine atoms, and the degree of dissociation varies directly with temperature and inversely with the gaseous iodine concentration. A computer program has been developed that utilizes equilibrium constants evaluated with available thermodynamic information to calculate the fraction of iodine in the atomic form.

Monoatomic iodine is more reactive than the diatomic molecule, both in the gas phase and on surfaces. The deposition behavior of iodine is therefore influenced by the extent of dissociation of I_2. Thermodynamic information on this dissociation is available in the literature.[13] A tabulation or plot of the fractional dissociation of molecular iodine, however, has been available only for a range of conditions that fall mostly outside those of interest in the fission-product deposition studies.[14]

The chemical equation for the dissociation of iodine is

$$\frac{1}{2} I_2 \rightleftharpoons I , \tag{1}$$

and the equilibrium constant is represented by

$$K_p = \frac{P_I}{P_{I_2}^{1/2}} , \tag{2}$$

where the P's are the respective partial pressures at equilibrium. Since each molecule of I_2 on dissociation yields 2 atoms of iodine, the fraction of iodine dissociated, F, is given by

$$F = \frac{P_I}{2P_0} , \tag{3}$$

where P_0 is a hypothetical initial pressure of all iodine in the system, taken as I_2. Two cases are of particular interest. In one P_{I_2} is held constant, for instance, by an elemental iodine source that maintains a constant iodine vapor pressure. In the other, a quantity of iodine insufficient to saturate the available volume is vaporized and comes to dissociation equilibrium.

---

[13] JANAF Interim Thermochemical Tables, Volume 3, Joint Army-Navy-Air Force Thermochemical Panel and Dow Chemical Co., 1960.

[14] R. F. Rolsten, Iodide Metals and Metal Iodides, p. 17, Wiley, 1961.

In the first case P_{I_2} is constant and can be controlled by the temperature of an iodine source. Hence

$$P_I = K_p P_{I_2}^{1/2} .$$

For this case

$$P_0 = P_{I_2} + \frac{1}{2} P_I ,$$

so

$$F = \frac{P_I}{2P_{I_2} + P_I} . \tag{4}$$

This can be expressed in terms of K_p and P_{I_2} as

$$F_1 = \frac{KP_{I_2}^{1/2}}{2P_{I_2} + KP_{I_2}^{1/2}} . \tag{5}$$

Values for F_1 are plotted versus temperature in Fig. 2.22 for I_2 pressures of 1 to 10^{-12} atm.

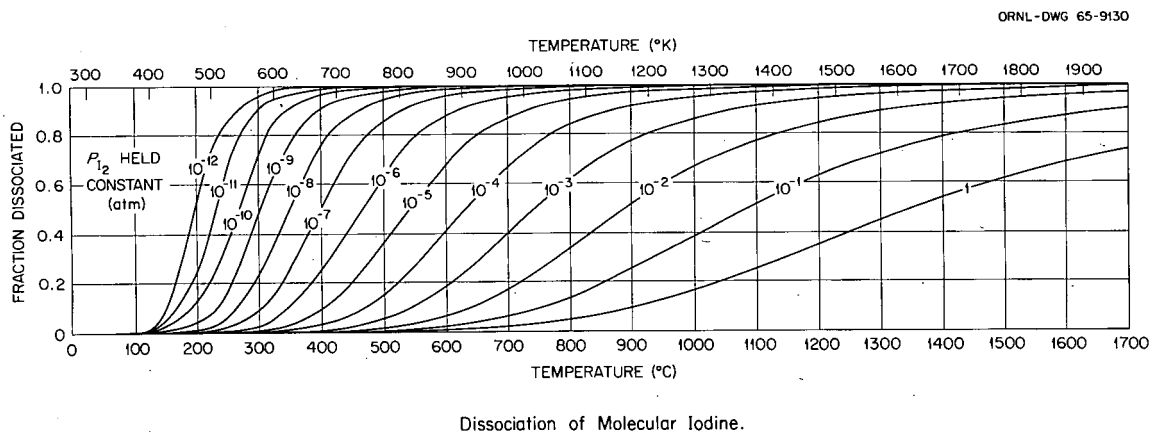

Dissociation of Molecular Iodine.

Fig. 2.22. Fractional Dissociation of I_2 Where I_2 Pressure is Maintained by Elemental Iodine Source.

In the second case, P_{I_2}, the equilibrium I_2 partial pressure, does not remain constant but is lowered from the initial value because of the dissociation of I_2 into atoms. Thus

$$P_{I_2} = P_0 - \frac{1}{2} P_I$$

and

$$K_p = \frac{P_I}{\left(P_0 - \frac{1}{2} P_I\right)^{1/2}} . \tag{6}$$

Solving this equation for P_I gives

$$P_I = -\frac{1}{4} K_p^2 + \frac{1}{2}\left[\left(\frac{K_p^2}{2}\right)^2 + 4K_p^2 P_0\right]^{1/2} . \tag{7}$$

With this expression the fraction of iodine dissociated becomes

$$F_2 = -\frac{1}{2}\frac{K_p^2}{4P_0} + \left[\frac{1}{4}\left(\frac{K_p^2}{4P_0}\right)^2 + \frac{K_p^2}{4P_0}\right]^{1/2} . \tag{8}$$

Values for F_2 are plotted versus temperature in Fig. 2.23 for initial I_2 pressures of 1 to 10^{-12} atm.

As one would expect, for a given temperature, F_2 is higher than F_1. This is because less total iodine is in the system under the conditions

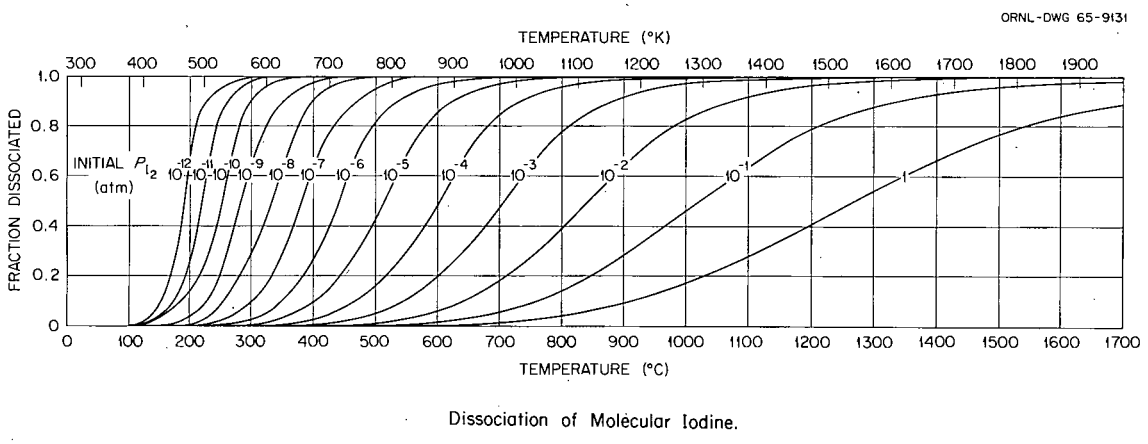

Dissociation of Molecular Iodine.

Fig. 2.23. Fractional Dissociation of I_2 Where Source of Elemental Iodine is Not Available to Maintain I_2 Pressure.

associated with F_2, and dissociation of I_2 varies inversely with the iodine concentration. Thus at 500°K (227°C, 440°F) and for iodine partial pressures of 10^{-12} atm, $F_2 = 0.896$ and $F_1 = 0.735$. Most significant is the fact that at the low iodine concentrations expected in nuclear reactor release situations, a relatively large fraction of the iodine will be in the monoatomic form. Also at these low concentrations the fraction dissociated increases sharply with temperature in a fairly low-temperature region.

Atomic iodine is more reactive than I_2, but for recombination of iodine atoms to form I_2, a third body is necessary to carry away the energy of combination.[15] At low iodine concentrations, recombination of atoms thus may require a finite time. Any process that increased the concentration of iodine atoms, such as desorption from heated surfaces, would contribute to the presence of this reactive iodine fraction, and these atoms would not necessarily be rapidly consumed by recombination. The presence of this active fraction would influence the iodine behavior observed experimentally. The data presented in Figs. 2.22 and 2.23 show that the presence of monoatomic iodine is justified on a thermodynamic basis under conditions expected in a gas-cooled reactor. With this knowledge we are closer to the description of mechanisms that explain experimentally observed iodine behavior.

Compatibility of Pyrolytic-Carbon-Coated Fuel Particles with Water Vapor

C. M. Blood L. G. Overholser

Experimental results obtained by exposure of unsupported pyrolytic-carbon-coated $(Th,U)C_2$ and UC_2 particles to water vapor were reported earlier.[16] Fuel particles examined in these studies had various types

---

[15] S. W. Benson, The Foundations of Chemical Kinetics, pp. 309–316, McGraw-Hill, 1960.

[16] C. M. Blood and L. G. Overholser, Compatibility of Pyrolytic-Carbon-Coated Fuel Particles with Water Vapor, pp. 140–142, GCRP Semiann. Progr. Rept. Mar. 31, 1965, USAEC Report ORNL-3807, Oak Ridge National Laboratory.

of pyrolytic-carbon coatings and were exposed to several different partial pressures of water vapor at 1000°C. Reaction rates of the coatings were determined from weight losses, and the incidence of failure was obtained from the quantities of uranium and thorium removed by acid leaching following the exposure to water vapor. These studies were continued with the same batches of fuel particles and the same experimental techniques as those used in the earlier studies. Surface area measurements were made of some lots of fuel particles before and after exposure to steam. The effect of changes in the supporting media for the fuel particles during reaction with water vapor was also examined. Table 2.3 gives relevant information concerning the various batches of particles examined, including surface area data not previously given.

Results obtained from the more recent runs, along with data reported previously,[16] are listed in Table 2.4. It is evident that the apparent order of the carbon-steam reaction with respect to partial pressure of steam is quite variable for the various batches of particles examined. As a result, it is not possible to extrapolate reaction rates to partial pressures either within or outside the range of steam pressures studied. The reaction rates do increase with increasing partial pressures in all

Table 2.3. Composition of Pyrolytic-Carbon-Coated Fuel Particles

Particle Designation	Uranium Content[a] (wt %)	Thorium Content[a] (wt %)	Pyrolytic-Carbon Coating (wt %)	Surface Area		Roughness Factor
				Geometric (m^2/g)	BET[b] (m^2/g)	
Laminar I	26.5		70.9			
Laminar III	31.6		65.2	0.0064	0.032	5.0
Granular IV	6.85	34.9	53.9	0.0025	0.028	11
Isotropic V	7.58	38.7	49.0	0.0029	0.024	8.3
Isotropic VI	1.58	30.0	65.2	0.0029	0.028	9.7
Isotropic VII	4.07	20.1	73.3	0.0030	0.062	20
NCC-217[c]	38.2		57.9	0.0037	0.16	43

[a]Analytical data from ORNL.

[b]Obtained with nitrogen.

[c]Duplex coatings.

Table 2.4. Summary of Results of Exposure of Pyrolytic-Carbon-Coated Fuel Particles to Water Vapor at 1000°C (~1-g Sample)

Water-Vapor Partial Pressure (torr)	Particle Designation	Exposure Time (hr)	Weight Loss Before Leaching (mg)	Coating Oxidized (%)	Reaction Rate[a] (mg/g·hr)	Uranium Leached (%)	Thorium Leached (%)	BET Surface Area[b] (m^2/g)	Roughness Factor
4.6	Laminar III	28	121	18.3	6.5	0.014		3.1	480
	Granular IV	28	24.1	4.4	1.6	0.013	0.017	0.25	100
	Isotropic V	28	30.3	6.1	2.2	0.021	0.026	0.24	80
	Isotropic VI	28	6.7	1.0	0.36	0.10	0.012	0.04	12
	Isotropic VI	76	12.7	1.9	0.26	0.028	0.017	(c)	(c)
	Isotropic VII	28	11.3	1.5	0.56	0.056	0.032	(c)	(c)
	Isotropic VII	24	16.3	2.2	0.91	0.013	0.043	(c)	(c)
	Isotropic VII	24[d]	16.0	2.2	0.90	0.014	0.064	0.92	310
	Isotropic VII	76	32.9	4.4	0.58	0.087	0.085	(c)	(c)
	NCC-217	24	25.8	4.4	1.8	0.76		(c)	(c)
	NCC-217	24[d]	22.0	3.8	1.5	0.013		0.31	85
	NCC-217	76	54.9	9.3	1.2	0.033		(c)	(c)
45	Laminar I	4.5	57.7	8.1	18	0.050		0.05	10
	Laminar III	1	18.9	2.9	29	(c)		(c)	(c)
	Laminar III	4.5[d]	68.3	9.6	23	0.52		4.7	740
	Laminar III	5.7	103	16.0	28	0.11		4.1	640
	Granular IV	4.5	13.8	2.5	5.6	0.18	0.008	0.30	120
	Isotropic V	4.5	18.7	3.8	8.3	0.37	0.035	0.15	50
	Isotropic VI	4.7	13.2	1.9	4.0	0.57	0.021	0.04	15
	Isotropic VII	4.5	9.1	1.2	2.7	0.54	0.006	0.16	50
	Isotropic VII	4.5[d]	14.3	1.9	4.3	0.012	0.014	(c)	(c)
	NCC-217	2[d]	13.4	2.3	11.4	0.15		(c)	(c)
	NCC-217	4.5[d]	23.1	3.9	8.7	0.05		0.34	90

Table 2.4 (Continued)

Water-Vapor Partial Pressure (torr)	Particle Designation	Exposure Time (hr)	Weight Loss Before Leaching (mg)	Coating Oxidized (%)	Reaction Rate[a] (mg/g·hr)	Uranium Leached (%)	Thorium Leached (%)	BET Surface Area[b] (m^2/g)	Roughness Factor
45	NCC-217	4.5[d]	24.7	4.2	9.3	0.16		(c)	(c)
	NCC-217	17.5[d]	77.4	13.3	7.6	0.31		(c)	(c)
567	Laminar I	1	111	15.6	156	5.0		0.89	180
	Laminar III	1	225	31.9	319	15.7		(c)	(c)
	Laminar III	1[d]	117	17.9	179	4.1		(c)	(c)
	Laminar III	2	208	30.8	154	17.7		3.8	600
	Granular IV	1	101	18.6	186	1.21	1.13	0.25	100
	Isotropic V	1	68.9	13.7	137	7.2	5.7	1.2	400
	Isotropic V	1[d]	71.1	14.4	144	11.2	11.6	(c)	(c)
	Isotropic V	2	126	25.2	126	11.9	11.4	(c)	(c)
	Isotropic VI	1	95	14.5	145	2.53	2.07	0.06	22
	Isotropic VII	1	68.0	9.1	91	2.19	2.91	0.31	100
	NCC-217	1	84	14.4	144	0.25		(c)	(c)
	NCC-217	1[d]	95	16.1	161	1.26		0.37	100
	NCC-217	2	106	18.2	91	1.11		(c)	(c)
	NCC-217	4	187	31.6	79	8.6		(c)	(c)

[a]Reaction rate in mg of carbon per gram of carbon as pyrolytic carbon per hour.

[b]Obtained with nitrogen.

[c]Not determined.

[d]Fuel particles supported on Al_2O_3; platinum support used in other runs.

cases, however. The surface area data obtained for oxidized particles from the various batches also are extremely variable. For example, at a partial pressure of 45 torr the reaction rates given for particles from batches laminar 1 and laminar III are about equal, but the surface areas vary by a factor of 8 to 10. At a partial pressure of 567 torr, reaction rates vary at most by a factor of 2 for all the batches studied, but considerably larger variations are evident in the surface areas. Runs were made in which the particles were supported on aluminum oxide instead of platinum to establish any effect of the supporting medium. The results indicate that no significant effect resulted from changing the support medium. The incidence of failure of the coatings as determined from acid leaching data is quite variable for the various batches of particles. In general, only a few particles failed at a partial pressure of 4.5 torr, whereas at 567 torr appreciable fractions failed in all cases. No correlation between reaction rate and incidence of failure is evident.

Microscopic and metallographic examinations were performed on the particles following exposure to steam and subsequent acid leaching. Photomicrographs of particles from two batches following exposure under the designated conditions are shown in Figs. 2.24 and 2.25. Although exposure conditions were similar and both batches had laminar coatings, laminar III particles show more evidence of attack and more pronounced pitting than laminar I particles. Higher reaction rates were found for laminar III particles at a partial pressure of 45 torr than for laminar I particles. The rates, however, were about the same at a partial pressure of 570 torr. Photomicrographs of the isotropic VI and VII particles show very little evidence of attack at a partial pressure of 45 torr. Isotropic VII particles, which appeared to be as resistant to attack as any batch, were found to crack open to a limited extent when exposed to a partial pressure of 570 torr. This could be due to a pin-hole type of attack which, after reaching the core, caused expansion of the core as it reacted with steam. However, photomicrographs of the few particles examined failed to show any deep holes.

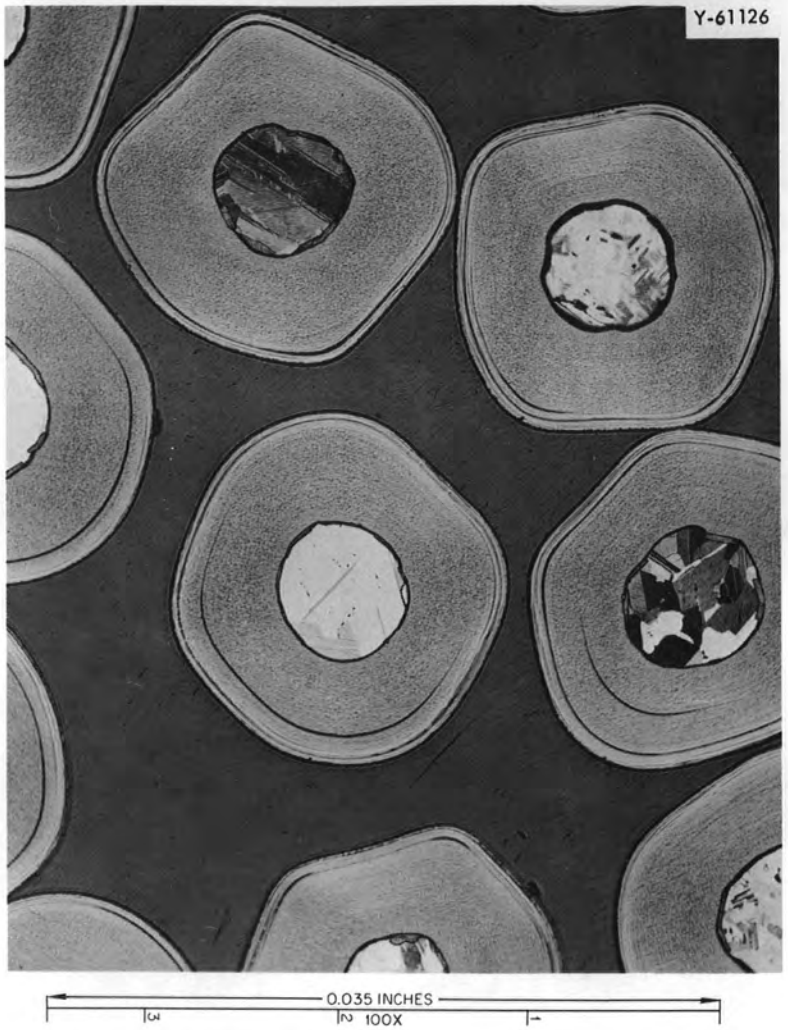

Fig. 2.24. Laminar I Pyrolytic-Carbon-Coated Particles (Batch 2701-109N) After Exposure to a Partial Pressure of Steam of 45 torr at 1000°C for 5 hr. As polished. 100×

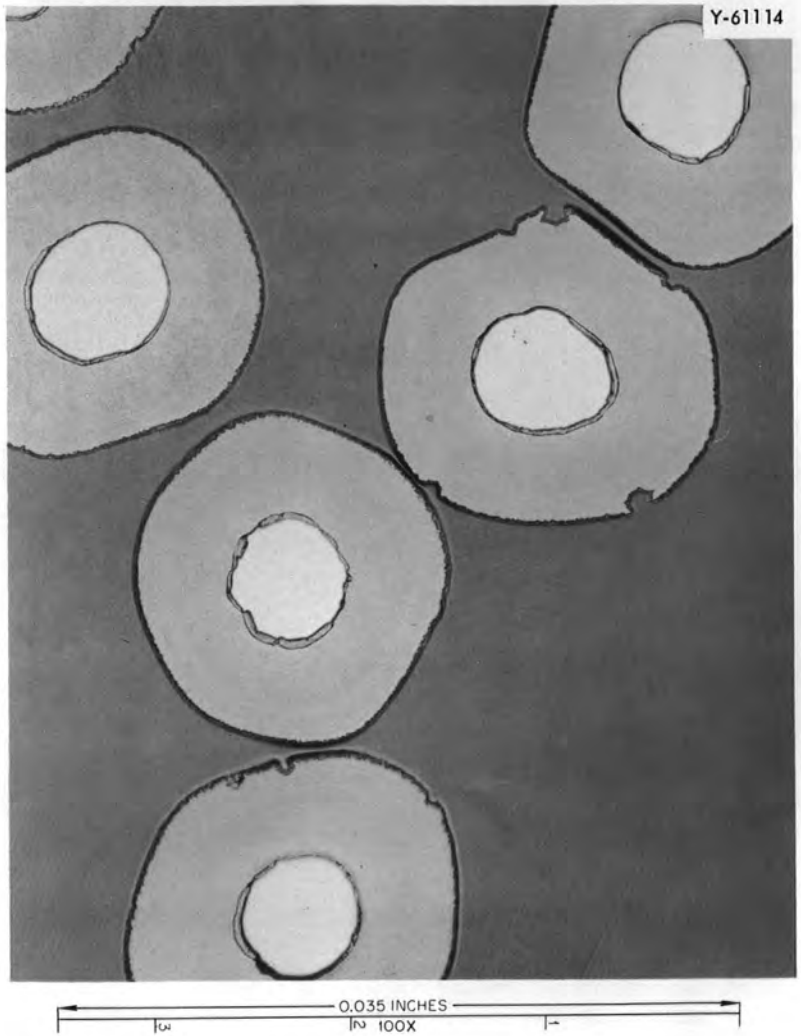

Fig. 2.25. Laminar III Pyrolytic-Coated Particles (Batch 2701-111N) After Exposure to a Partial Pressure of Steam of 45 torr at 1000°C for 6 hr. As polished. 100×

Recoil of Fission Products in Pyrolytic Carbon

R. B. Evans III J. L. Rutherford
R. B. Perez*

In utilizing carbon-coated UO_2 and ThO_2-UO_2 particles as nuclear fuels, virtually no gross migration of fuel would be expected. Experiments at high temperatures and exposures longer than 500 hr at 1900°C (see Chap. 1, this report) have indicated this. Thus, any major damage to the inner portions of the pyrolytic-carbon coatings will be the result of direct fission recoils. The inner layer is designed (1) to absorb such damage in a sacrificial manner while protecting the outer coating layer and (2) to shrink and provide expansion volume within the particle. We anticipate a high degree of damage to the inner layer over the entire average recoil distance (called the "range") with a small degree of damage beyond this distance. It is clear that the ratio of layer thickness to recoil range should be greater than unity for maximum adsorption efficiency. The immediate task is the determination of this ratio for various layer materials through range measurements. Information of this type should augment the data that currently form the basis for specifying inner-layer characteristics and dimensions.

However, there are other motivations, aside from immediate applications, that have prompted us to undertake these studies. For example, there is currently research emphasis on diffusion of fission products through pyrolytic-carbon matrices. The associated mechanisms may well be strongly influenced by the history of the diffusing atom prior to the diffusion process. We would not be surprised if the diffusion mechanisms for atoms placed in the matrix via recoils would be somewhat different than the diffusion mechanisms associated with the conventional means of placing these atoms on specimen surfaces. If such an investigation were carried out, recoil data that would specify the distribution of fission fragments would be required to specify the initial boundary conditions for the associated diffusion experiments.

---

*Consultant, University of Florida, Department of Nuclear Engineering.

Still another justification is the development of capability for accurate determination of concentration profiles for atomic species that exhibit almost negligible penetration. Techniques have been developed for many solids; however, pyrolytic carbon and graphite pose special problems in this respect. Thus we consider the present investigations to be necessary and logical activities that complement our long-range diffusion studies.

In summary, our present objective is the determination of the distribution of fission fragments that have recoiled to average positions within pyrolytic-carbon specimens. The fragments emanate (during neutron irradiation) from a specimen surface coated with a very thin ^{235}U layer. From the distribution curves we can extract values of the average recoil distance, or range, denoted as R, and a distribution parameter associated with the recoil range called the straggling factor, α. Present experiments have been restricted to General Electric (columnar) pyrolytic-carbon specimens, with emphasis on the development of grinding and counting techniques.

Basic Considerations

Scope and Orientation. Studies of recoil phenomena may be directed along either applied or fundamental paths, depending on the overall objectives of the investigation. The more fundamental approach involves research pertaining to microscopic details, such as the charge and energies of the moving particles, as well as the structure of the absorbing medium. The objective is to correlate such information from a microscopic point of view. Associated experiments involve particle beams that are composed of a single atom species. These beams are well collimated and frequently monoenergetic. The stopping or absorbing media are generally pure gases or nearly perfect solid crystals (called targets). At great expense, the fundamental experiments are arranged to place the transport theory in a convenient but secondary role.

The second approach, which is the one we have adopted, places primary emphasis on the transport parts of the problem. An orientation of this type is dictated by the ultimate applications of our data and also by the

characteristics of the stopping media under investigation. Even the best materials scheduled for investigation in our work are far removed from the category of nearly perfect crystals. Furthermore our specimens will contain all possible atomic species resulting from ^{235}U fissions induced by thermal neutrons.

While the importance of microscopic details is recognized, we anticipate that the major parameter of present interest will be simply the density of the material. Any unusual effects that we might observe will result primarily from the gross defects present in the ill-defined structure of our carbonaceous targets. We shall approach the problem from a macroscopic viewpoint; thus, we see the range and straggling factors as phenomenological coefficients that will hopefully show empirical correlations with the characterization data corresponding to the various targets.

Discussions of the transport phases of the recoil phenomena can be presented in terms of the applicable mathematical relationships or, in more simple fashion, in terms of graphical treatments. In general we prefer the former; indeed we have prepared such a discussion which incorporates a satisfying degree of elegance. Initial experimental results, however, suggest α/R ratios and target-source configurations that force us to regimes wherein the classical mathematical expressions break down completely. Since we will eventually employ graphical solutions* in our more advanced experiments, we have decided to stress such solutions in all discussions, including the present report.

Fission Fragment Distributions in r Space. We start by giving consideration to a point source located somewhere along the plane that defines the interface of two pyrolytic-carbon specimens. We assume that the source can provide enough fission fragments to adequately describe the typical fragment distribution (in spherical coordinates). The experimental technique consists of a grinding procedure whereby hemispherical cavities of ever-increasing size, starting at the source position in one of the specimens, can be removed. Measurements of the total activity after each grinding result in a curve such as that shown in the upper

*The utility and adaptability of graphical solutions was suggested to us by O. S. Oen of the ORNL Solid State Division.

right-hand corner of Fig. 2.26. Here F.R. denotes fraction of total activity remaining after grinding. The total activity is proportional to the total number, n_0, of ith species fragments. Without straggling, this curve would be a simple step function; with straggling, the step is rounded off in a symmetrical fashion, as shown.

It is clear that the majority of the fragments arrive within a hemispherical shell with a mean radius R_i. Nevertheless, small fractions of the fragments do not reach this shell, while other fractions pass beyond it. The degree of "under-and-over" shooting is measured by the straggling factor, α_i; the subscript i denotes a particular fragment species. The effect of straggling is clearly shown by the distribution curve at the lower right-hand corner of Fig. 2.24. The symbol n_i denotes the number of ith fragments at a particular r/R_i. This distribution curve, often

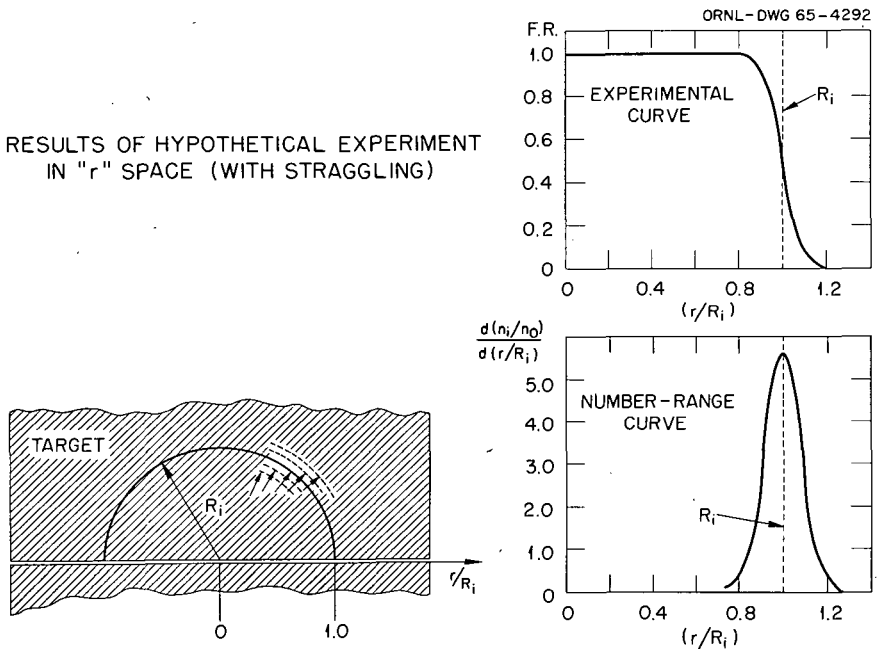

Fig. 2.26. Fission-Fragment Vector Diagrams and Penetration Curves Referred to a Reduced Spherical Coordinate System. A point source is assumed to be located at the origin, O. Fragments emanate from the origin in all possible directions. The curves correspond to the distribution in one hemisphere in the target in which a majority of a particular group of fragments comes to rest at range R_i. The symbol F.R. denotes the fraction of total fragments that reside beyond a particular reduced radius r/R_i.

called a number-range curve, is a plot of the derivative of the fraction-remaining curve and is analogous to a concentration profile in diffusion studies.

All our graphical treatments are based on the usual assumption that the concentration profiles follow normal-distribution curves, as indicated in Fig. 2.27, where it is shown that α_i is the square root of two times the standard deviation. For mathematical treatments, one generally starts with an expression for the distribution curve (Fig. 2.25) and integrates to obtain the equations that will describe the fraction-remaining curves (Fig. 2.28). A similar procedure is followed in the graphical treatment, for we must use properly weighted fractions of total fragments to obtain the curves in Fig. 2.26.

Since recoil ranges in solids are generally less than 1 mil (0.001 in.), we could not hope to perform an experiment of the type under discussion. In other words, we cannot carry out grinding operations in r space, although such an experiment is highly desirable because of the well-defined curved shapes shown in Figs. 2.26, 2.27, and 2.28. With expensive accelerating devices, this shortcoming could be overcome, since

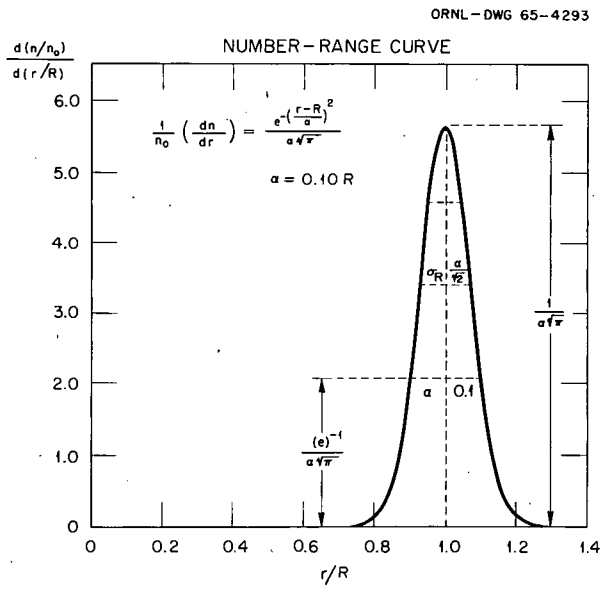

Fig. 2.27. Details of the Number-Range or Distribution Curve for r Space. An integral form of this curve is shown in Fig. 2.28.

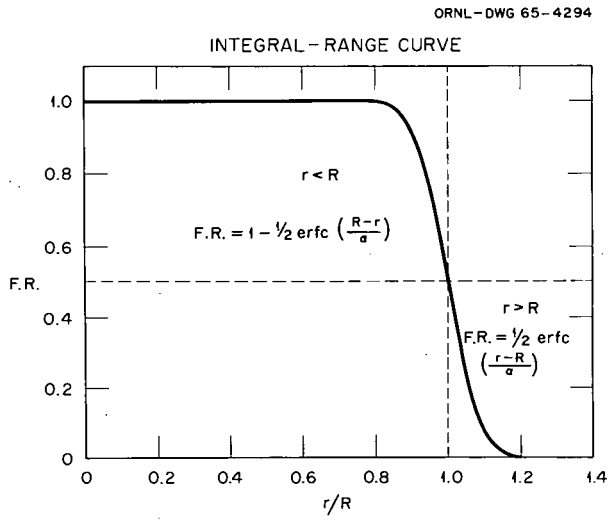

Fig. 2.28. Details of the Integral-Range Curve for r Space. This curve is referred to as the F.R. curve in the text. The analytical solutions correspond to particular regions. These solutions are not valid when α/R is greater than 0.1.

the distribution of fragments (along z) originating from a well-collimated beam impinging on a target is identical to the distribution (along r) for our hypothetical point-source experiment.

It is important to note that the distribution within the inner layer of a particle coating will not resemble the distribution curve shown in Fig. 2.27 because the source in a particle is not a point. Rather, the distribution within the inner layer will closely resemble the integral curve that will be obtained when the coupon is sectioned by grinding away rectangular sections in a direction normal to the interface, that is, along the z axis of the hemisphere mentioned in the discussion.

Fission Fragment Distributions in z Space. In considering a distribution curve obtained by grinding along the z direction of a spherical system* such as described in the previous section, it is convenient to visualize an array of vectors emanating from a point source (Fig. 2.29).

---

*For the special case of grinding along the z axis, the results for a specimen surface containing a single (but strong) point source are the same as the results for a specimen with several individual weak sources (actually ^{235}U atoms) scattered uniformly over the surface.

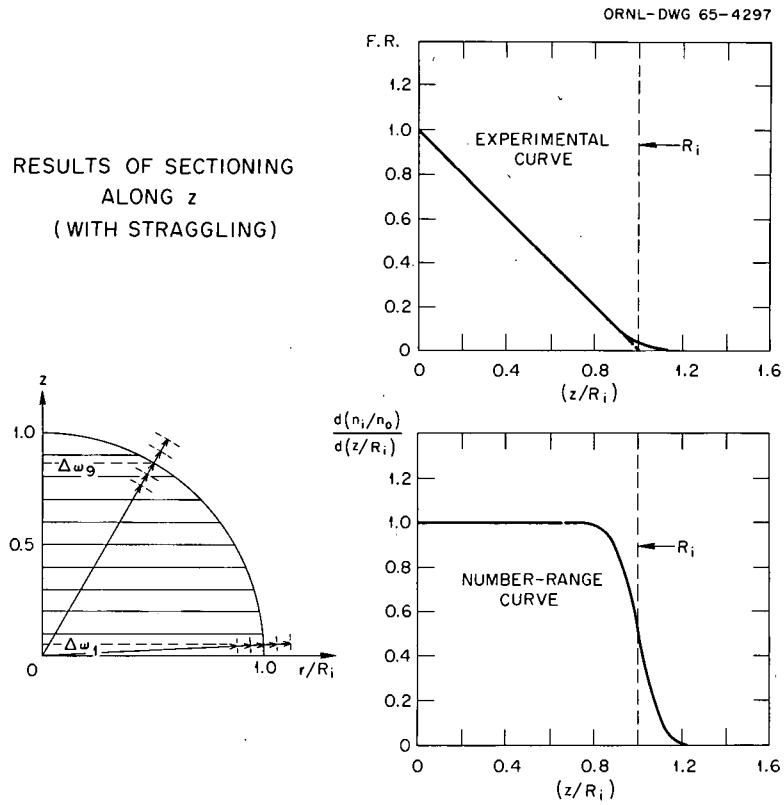

Fig. 2.29. Vector Diagrams and Penetration Curves Referred to the Linear Coordinate z.

These vectors represent all possible directions and lengths of flight of a particular fragment. After a reasonable period of time, each unit surface of our hemisphere (actually five hemispheres in our graphical treatment) should have an equal number of vectors normal to the surface. Specification of direction and average position of the vectors lends itself well to graphical treatments. The only trick involved concerns the relationship between increments of length along z, Δz, and increments of area, $\Delta\omega$, over the surface.

The key to this problem is the simple relationship for any sphere of radius r, namely,

$$\Delta\omega = 2\pi \frac{\Delta z}{r} .$$

It is fortunate that the spherical coordinate system is defined so that

when the z axis is proportioned into equal increments, as shown in Fig. 2.29, the surface area is also proportioned into equal increments. The latter feature was not at all clear to us by graphical means alone.

For a negligible degree of scattering, this means that each Δz carries with it an equal number of vectors that may be resolved to a single vector for each particular Δz or $\Delta\omega$. Thus, the subsequent cumulative removal of equal Δz's (without straggling) will produce a linear fraction-remaining curve with a slope of minus one. The corresponding distribution curve (without straggling) will be a step function. As indicated by the vector diagram in Fig. 2.29, we have considered five spheres to account for the straggling. The details of this procedure are given in Table 2.5.

Table 2.5. Characteristics of Representative Spheres Used for Graphical Determinations of $\alpha/R = 0.1$

Sphere No.	Increment of Total Fragment, n_0 (%)	Radius Position,[a] R (%)
1	12.5	88.4
2	12.5	96.3
3	50	100.0
4	12.5	106.4
5	12.5	111.6

[a]These values may be obtained from the curves in Figs. 2.27 and 2.28.

Several interesting and important facts are evident through comparison of plots in Figs. 2.26 and 2.29. It is clear that grinding in z space rather than r space is equivalent to integrating the r-space curves to obtain the z-space curves. For example, the differential curve in z space is the same as the integral curve in r space. Because of this, a large portion of the detail concerning α_i is lost to our experiments. On the other hand, we can carry out good determinations of R_i by extrapolations based on the nearly straight-line relationship exhibited by the z-space

F.R. curves. It is somewhat surprising that only a small contribution of α_i appears in the z-space F.R. curves. This constituted a very important part in our experimental program and warrants additional explanation.

With the aid of the vector diagram in Fig. 2.29, it may readily be seen that, at high polar angles (measured from the z axis), for example, at $\Delta\omega_1$, all vector tips are situated in the same $\Delta\omega_1$. Thus, the straggling has little effect over polar angles ranging from 45 to 90°, and in fact over angles much lower than 45° ($\Delta\omega_9$), because the over-and-under shooting compensates in nearly all the increments within this region. The only straggling effect seen by the F.R. curves are the overshoots of the last increment (near the pole of the hemisphere) plus a few from the next to the last increment.

Comparison of the F.R. and distribution curves in Fig. 2.29 suggests that the data should be correlated in terms of distribution profiles rather than F.R. plots in order to detect details pertinent to α_i. This turns out to be somewhat of a chore in the present work because of the small penetrations involved. A more fruitful method for increasing α_i sensitivity may be realized through the use of screens to partially collimate the beam. Hopefully, the screens will block off large fractions of high-angle vectors and will allow only the low-angle vectors to pass to the target.

These observations have formed the guidelines for our experimental efforts. At present we are trying to refine our grinding procedure so that we can plot distribution or number-range curves directly from the data. It is important to note that a multitude of experimental inadequacies can be well hidden through the use of F.R. curves, and for this reason these curves have been our favorite means of correlating penetration data. When such data are converted to differential plots, the results look quite bad. For diffusion studies the discrepancies can again be hidden by a standard trick, namely, the use of a log [Δ(activity)/Δz] as a function of $\langle z \rangle^2$. However, our data do not follow this relationship. It must be plotted on rectangular coordinates, and we have been forced to the realization that our earlier procedures require considerable refinement for the present investigations. We have also given considerable

thought and effort to the screen experiments that are in progress, although most of our experimental effort has been directed to grinding techniques.

Experimental Procedures and Results

Overall Procedure. The experimental methods used in this phase of the investigation are based on the classical thin-layer diffusion experiment for solid-state systems. Actinides (^{235}U and/or ^{232}Th) are embedded on carbon specimen surfaces by means of an ion-bombardment procedure[17] and then subjected to neutron activation in the ORNL Low-Intensity Test Reactor (LITR). Subsequent lapping, sectioning, and counting operations yield data related to the fission-fragment distributions. In all cases assay for the fission fragment is based on gamma activity. Our present experiments involve only ^{140}La (and ^{233}Pa), although we shall attempt some ^{95}Zr assays in the future. In this way, data will be generated for both the light and heavy fission fragments.

Preparation of Thin-Layer Specimens. The degree of care to be exercised in the placement of actinides as thin layers on specimen surfaces should be governed by the magnitudes of penetrations resulting from the phenomenon under observation. In our experiments, the fission fragments reside within 1 mil (25 μ) of the original surface. Obviously, very smooth surfaces containing uniform amounts of actinides with low initial penetrations are required. With these requirements in mind, the graphites and carbons to be investigated are cut and machined to produce several individual coupons that are 0.375 in. square, with a thickness of 0.150 in. The 0.375-in.-square surfaces normal to the z direction are ground flat and parallel to within ±0.0001 in. (±2.5 μ).* At this point the

*Surfaces of ⟨a⟩ direction pyrolytic-carbon specimens (wherein the z grinding direction is roughly parallel to the basal planes) are polished until they are optically flat. The optical method cannot be used for ⟨c⟩ direction specimens.

[17] J. Truitt, G. D. Alton, and C. M. Blood, Thorium Diffusion in Pyrolytic Carbon and Porous Graphite, Applied Physics Letters, 3(9): 150–152 (November 1963).

coupons are heated to temperatures around 1800°C for 15 min (under vacuum) to remove adsorbed volatile impurities.

The source region is created by mounting the out-gassed coupons on a rotating-target device[17] and bombarding one surface of the coupons with singly charged ^{235}U ions at an energy of 40 kev. The bombardments are carried out within an electromagnetic separator. The ^{235}U thus embedded on or near the graphite surfaces is quite pure from both chemical and isotopic standpoints. Since the flux of the ion beam is uniform over the target area, simultaneous bombardment of several coupons allows preparation of a series of specimens with identical n_0 values. Purity and equal n_0 values are deemed important for reasons pertaining to activation and counting.

Each range experiment involves several coupon pairs, with one member bearing a ^{235}U layer — called the source — and the other without ^{235}U — called the target. In addition to the ^{235}U specimens, we prepare ^{232}Th specimens that serve as blanks. These establish the "as-deposited" penetration of actinides in the source.

Determination of the Extent of Penetration. Both the precision and accuracy of the actinide penetration data depend heavily on accurate sectioning techniques. In our initial experiments we used the micrometer grinding jig[18] shown in Fig. 2.30.

To initiate determination of an F.R. curve, activated coupons are mounted in the grinding device. After the total activity of the coupon is determined, the first section of the coupon is removed and the activity redetermined. This process is repeated until there is no change in count with grinding. The coupon is never removed from the lapping device while grinding. For the determination of removal depths we use a direct-reading optical gage (Model DR-25B, Bausch and Lomb, Inc., Rochester, New York). Results obtained* with the micrometer grinding jig are shown in Fig. 2.31.

---

*The data obtained with the micrometer grinding jig were collected some time ago by J. Truitt of the ORNL Reactor Chemistry Division. These results established the feasibility of performing range experiments in pyrolytic carbons.

[18]H. J. de Bruin and R. L. Clark, A Precision Grinding Device for Solid State Diffusion Studies, Rev. Sci. Inst., 35(2): 227 (1964).

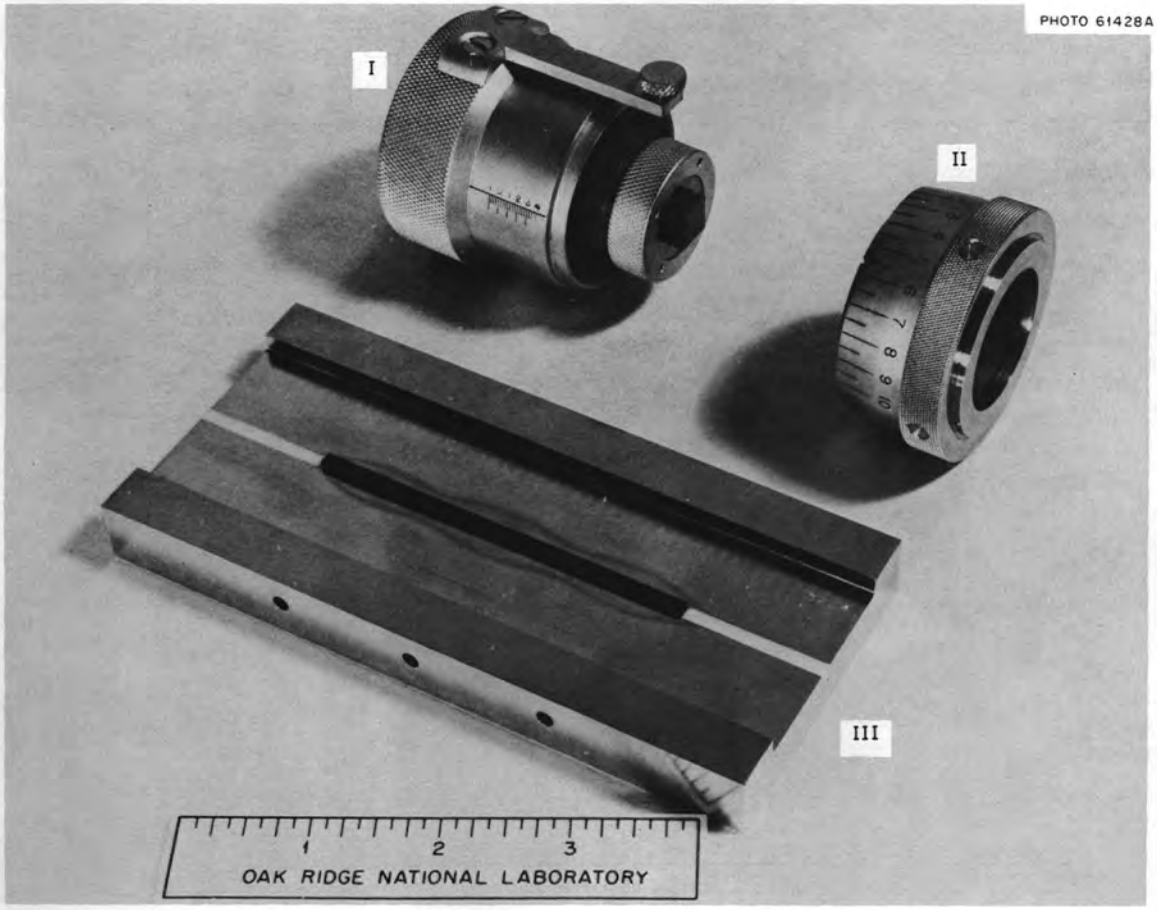

Fig. 2.30. Components of a Micrometer Grinding Jig. This device is used for the determination of F.R. curves pertinent to diffusion experiments and initial range measurements. The frame anvil is shown at I; the thimble spindle is at II; the base plate is at III. During use, parts I and II are engaged.

Modified Sectioning Techniques. An examination of the results presented in Fig. 2.31 clearly indicates that the micrometer grinding jig does not lead to the precision required for the present experiments, although it is quite adequate for diffusion experiments that produce relatively deep penetrations. To obtain a distribution curve we must take differences of two large numbers, and this amplifies the uncertainty of the data. Therefore, we have turned to grinding procedures with which the increments removed can be quantitatively recovered and counted. The device used to prepare the specimens and to carry out some of the sectioning operations is shown in Fig. 2.32. We refer to this device as the

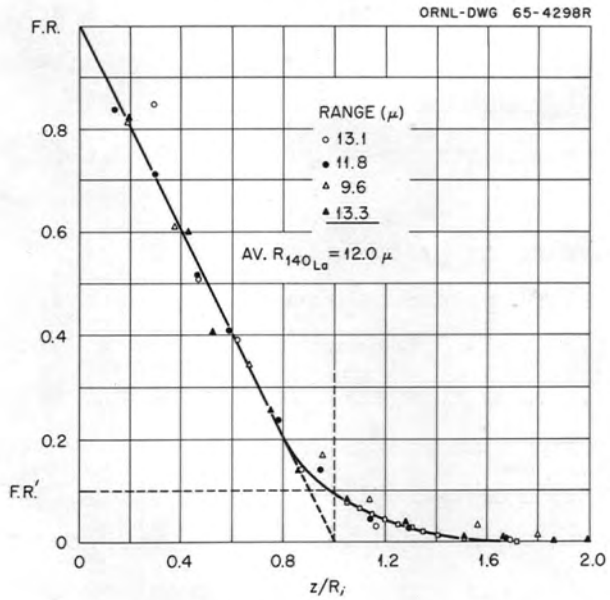

Fig. 2.31. Results of the Initial Recoil Range Experiments. These data were obtained by sectioning with the micrometer grinding jig shown in Fig. 2.30. The points shown as open squares (at z/R_i greater than 1) represent smooth data picked off to estimate a straggling-factor value. The F.R. represents a new percentile base required by such estimates.

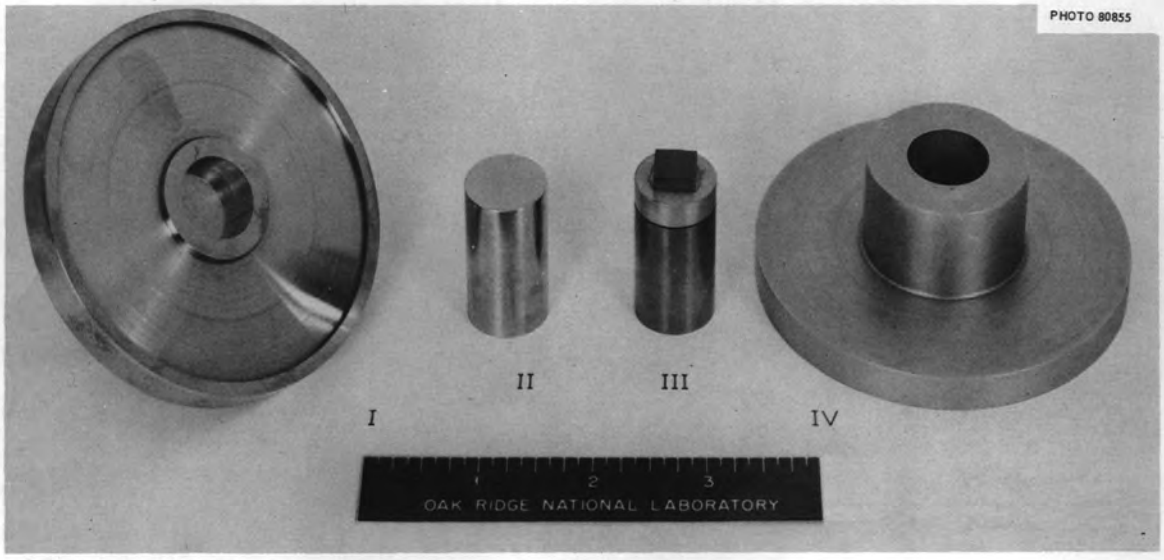

Fig. 2.32. Components of the Piston Lapping Jig. This device was used in some of the more recent range experiments. A bottom view of the cylinder frame is shown at I; the solid steel piston is at II; the magnesium piston with a steel sleeve (coupon mounted) is at III; the cylinder frame in the lapping position is at IV.

piston lapping jig.[19] For specimen preparation, a solid steel piston is used; for sectioning, we use a steel cylinder machined to accommodate a smaller magnesium piston. The light magnesium piston permits us to base the penetration measurements on weight loss as determined with a microbalance.

Two types of grinding procedures have been employed with the piston lapping jig. The first procedure removed increments by moving the jig in "figure 8" motions over 3/0 emery paper, and a depth measurement followed each removal. More recently, we adopted the technique suggested by Lonsdale and Graves[20] in which the entire region of penetration is removed by one continuous swipe across the 3/0 emery paper. The total depth of removal is determined by a single weight-loss measurement. Rather than sectioning the sample, the strip of emery paper containing the sample is sectioned. This operation is depicted graphically in Fig. 2.33. The validity of this procedure is based on the carbon removal rate along the strip being constant. Results from both the incremental — "figure 8" — sectioning and the swipe procedure are presented in Fig. 2.34; comparison of these results verifies a constant removal rate for the swipe method.

The opposite faces of one range and three blank specimens were not parallel, and it was necessary to carry out the swipe method without the aid of the piston-lapping jig. Much to our surprise we found that some of our best results were obtained by merely placing a copper cap over the specimen (shown as item II, Fig. 2.33) and then making a single swipe while rotating and maintaining a constant downward pressure on the specimen.

It appears therefore that the right forefinger and thumb comprise the best sectioning instrument of jig evaluated thus far. It is difficult to maintain a constant downward pressure with the present piston-lapping jig. This, coupled with the fact that our specimen surfaces are never

---

[19]F. H. Eisen and C. Ernest Birchenall, Self-Diffusion in Indium Antimonide and Gallium Antimonide, Acta Met., 5: 265–274 (May 1957).

[20]H. K. Lonsdale and J. N. Graves, Diffusion of Thorium in Pyrolytic Carbon Coatings, pp. 18–35 in Coated-Particle-Fuels Research at General Atomic, from October 30, 1964 Through April 30, 1965 (April 1965).

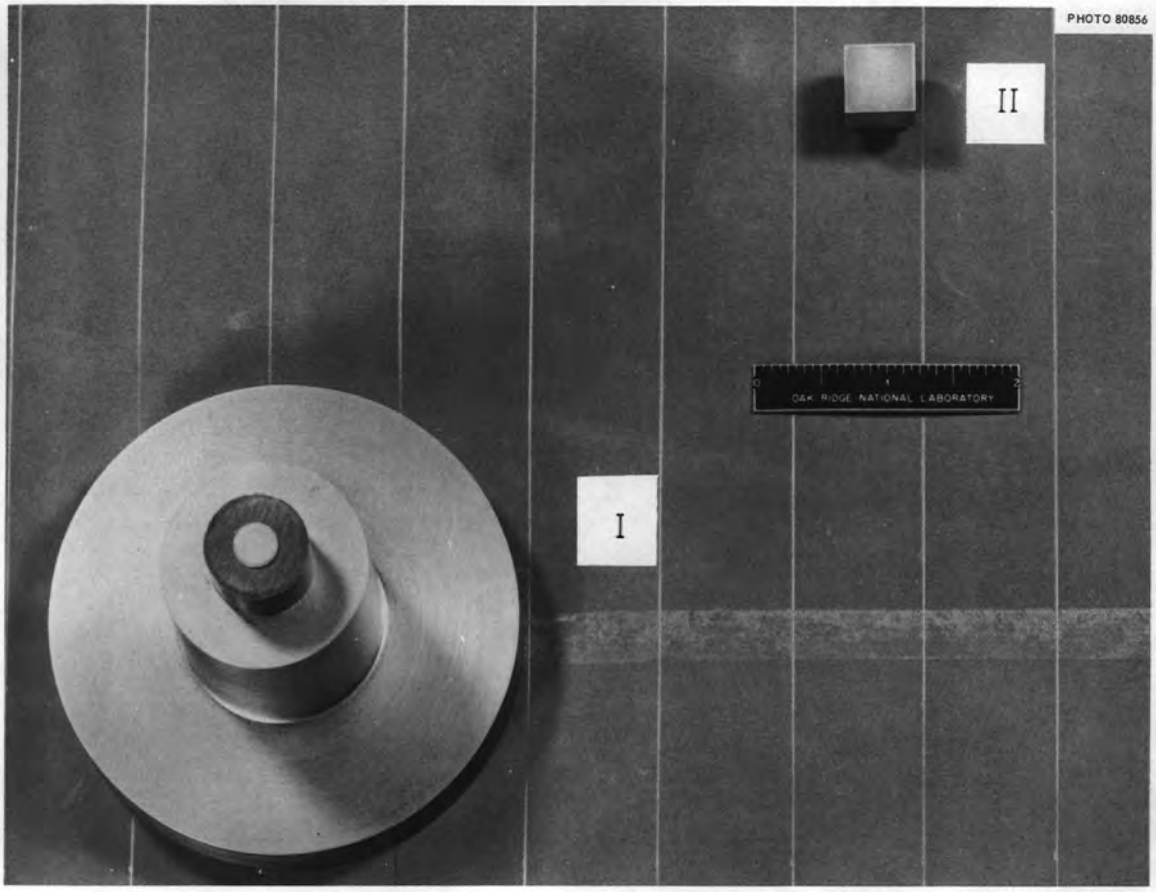

Fig. 2.33. View of the Lapping Jig Resting on Emery Paper at the Completion of a Sectioning Operation. The removed graphite appears as a light horizontal streak at the right of the jig at I. The apparent non-uniformity of the streak (or swipe) results from a photographic effect. Removal is carried out with the aid of either the piston lapping jig at I or the copper protective cap at II. After removal, mending tape is placed over the embedded graphite, and the emery paper is sectioned along the divisions shown.

perfectly parallel (a requirement for the piston jig), may explain the superiority of the manual grinding procedure for sectioning. The reverse is true with respect to specimen fabrication and preparation. In this operation, the degree of parallelism and flatness obtained on specimen surfaces with the piston jig is far superior to that which can be obtained manually. Thus, utilization of the piston jig continues to be an important feature of our experimental techniques.

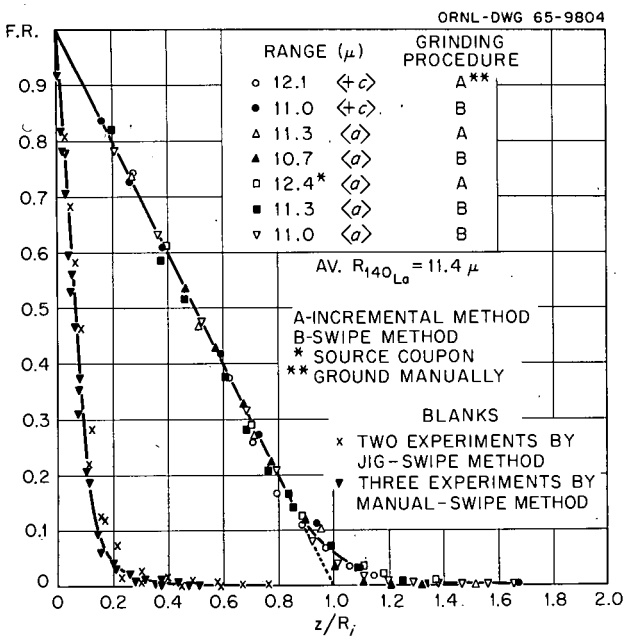

Fig. 2.34. Results of Recent Recoil Range Experiments, Including New Blank Data. All data were obtained with the devices shown in Fig. 2.33. Grinding procedure A involves removal of small sections and individual depth determinations; procedure B involves the swipe technique depicted in Fig. 2.33.

Additional Findings

When this investigation was initiated we were anticipating a measurable orientation effect on the range parameters. We were overly impressed by the high rates of actinide diffusion observed along basal planes as compared with those observed across basal planes. Although many properties of the pyrolytic carbons under study are very anisotropic, the data of Fig. 2.34 suggest that the range parameters relative to the ⟨a⟩ and ⟨c⟩ directions of the material are essentially the same. Accordingly, we plan to perform most of our subsequent experiments with ⟨a⟩ direction specimens, which are sectioned across basal planes. It is well known that polishing and sectioning parallel to basal planes is a difficult operation for pyrolytic carbons because basal planes are cleavage planes in these materials. Furthermore, the fact that these planes are wrinkled and irregular may explain our high rejection rate of data pertaining to ⟨c⟩ direction specimens.

We have assigned minimum values of the α/R ratios as a good criterion for an evaluation of our grinding techniques. The ratio obtained from the initial experiments with pyrolytic carbon obtained from High-Temperature Materials was 0.60, whereas the ratio obtained from the average curve for GE material (Fig. 2.34) was 0.25. The densities (HTM, 2.202 and GE, 2.192 g/cm^3) and other properties of these materials are comparable and consequently their recoil parameters should be nearly the same. Therefore we conclude that the modified techniques improved our measurements. Nevertheless the 0.25 α/R value cited above remains a doubtful value because it can be based only on the data corresponding to residual activity beyond $z/R = 1$.

To make estimates of α from F.R. data, we take the F.R. at $z/R_i = 1$ as representative of a new 1.00 F.R. value for penetrations greater than $z/R_i = 1$. Then we plot these residuals (or tails) on an exploded scale. The new ordinate is F.R.$'$; the new abscissa is $z-R_i$. If α/R is less than 0.10 the applicable equation is

$$\text{F.R.}' = \sqrt{\pi}\ \text{ierfc}\ (u)\ ,$$

where

$$u = [(z - R_i)/\alpha_i]\ .$$

Graphical comparisons of this function and the experimental curves allow estimates of α_i values. Of course 0.25 is greater than 0.10, and we realize that use of the equations is questionable.

The greatest uncertainty arises from the fact that α or α/R must be evaluated on the basis of the tails of the experimental curves. A large tail gives a high α value. In all our diffusion and range experiments we have never experienced great difficulty in obtaining large tails. Thus, we have little confidence in the α values obtained from such curves.

More reliable estimates of α can be obtained from the distribution curves because the presentation of the data in this form forces the rejection of all data that exhibit high degrees of variations about the average curve. Data thus selected and correlated are presented in Fig. 2.35. Note that portions of the curve within the interval $0.7 > \text{F.R.} > 1.0$ are the inverted-mirror image of portions within $1.0 > \text{F.R.} > 1.3$.

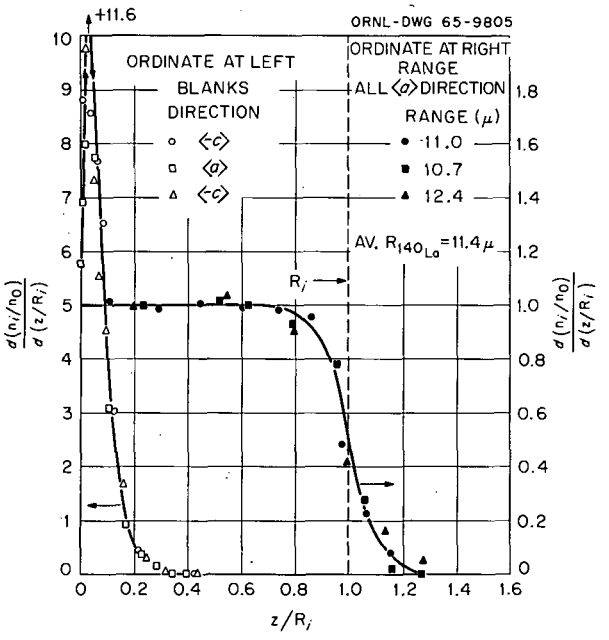

Fig. 2.35. Differential Curves Showing ^{140}La Distribution After Fissioning. The distribution curve for ^{235}U in the source coupons prior to fissioning, as indicated by ^{232}Th $\rightarrow$ ^{233}Pa*, is also shown (open symbols). These plots were prepared using the best data with respect to minimum deviation from the F.R. curve. While deviations of this type do not affect the average range value, they have a marked effect upon the shape of the distribution curve.

This condition is dictated by both graphical and analytical solutions. Tendencies to overemphasize the tails when the "average curve" is drawn through the points are tempered by this condition. The procedure for extracting an α value is the same as described before, with the one exception that the function erfc (u), rather than $\sqrt{\pi}$ ierfc (u), must be employed. The α_i/R_i value obtained from the curve in Fig. 2.31 is 0.126. Thus, we are beginning to approach an acceptable value of α/R; a value ranging about 0.07 was anticipated[21] prior to the experiments.

Another demonstration of the amount of detail that can be obtained through the use of distribution curves, as opposed to F.R. curves, is obtained through comparison of the blank data as they appear in Figs. 2.34 and 2.35. The curves of Fig. 2.34 suggest that the blank distribution is quite similar to the range distribution, except that the former

[21] R. D. Evans, The Atomic Nucleus, p. 671, McGraw-Hill, New York, 1955.

is much steeper over 1 > F.R. > 0.2, but the data are quite different, as indicated in Fig. 2.35. Two of the three experiments show "peak out" at an ordinate value of +11.6, which corresponds to a z/R_i value of 0.05 ($z = 0.57\ \mu$). Thus, the majority of the actinide resides 0.57 μ beyond the surface of the source coupons.

Practically all our grinding experiments are carried out with targets. If the 0.57-μ value were to be applied as a correction for the initial distribution, it would be added to the average $R^{140}La$ value of 11.4 μ. We feel that such a correction is beyond the present precision of our experiments. Our major interest concerns the total penetration of the actinide (the average width of the peak). This width is quite small; therefore, our assumption as to the existence of a very thin layer at or near the surface is a valid one.

A blank distribution as shown in Fig. 2.34 would be predicted, since the beam associated with the placement of the actinide was monoenergetic and collimated (to within ±9°). Nevertheless we are quite pleased and somewhat surprised that we could detect a peak at such low penetrations.

3. STUDIES FOR AVR — GERMAN PEBBLE-BED REACTOR

H. C. McCurdy O. Sisman J. H. Coobs

Introduction

D. B. Trauger

During the three years 1962 to 1965, a substantial test and development effort was maintained at ORNL in support of pebble-bed reactor design. Early work pertaining to the PBR included a conceptual design for a reactor and some component development studies.[1] Later studies and development were referenced to the German pebble-bed reactor, the AVR at Jülich. The PBR work is now drawing to a close, and it seems appropriate to provide a brief summary in this report, although some work will remain for reporting in later issues. The change from pebble bed to prismatic forms for fuel development should not be interpreted as resulting from an unfavorable evaluation but rather from a separation of ways wherein the U.S. effort and the German-Euratom efforts should provide bases for later comparison of the two systems when reactor experience has been obtained.

The fuel development and testing that constituted the major effort related to the AVR was keyed to the development of specifications whereby procurement from commercial U.S. sources would be possible for the reactor first-core loading. Pyrolytic-carbon-coated $(Th\text{-}U)C_2$ particles embedded in a matrix and encased in a spherical 6-cm-OD container constituted the basic fuel element. All fuel particle development was done by laboratories associated with commercial fuel suppliers. Most development of spherical element assemblies also was by these laboratories, although ORNL did undertake some investigation of matrix formulation and of structural features for spheres. Irradiation testing was the principal tool employed in the evaluation of fuel elements in the ORNL program.[2]

---

[1]Oak Ridge National Laboratory, Conceptual Design of the Pebble-Bed Reactor Experiment, USAEC Report ORNL-TM-201, May 1962.

[2]D. B. Trauger, Some Major Fuel-Irradiation Test Facilities of the Oak Ridge National Laboratory, USAEC Report ORNL-3574, Oak Ridge National Laboratory, April 1964.

Specialized irradiation test equipment and facilities were developed to accommodate the spheres at the AVR reference operating conditions. In addition, both destructive and nondestructive out-of-pile tests were developed. These included sphere and particle crushing strength and sphere impact (including gravity drop) tests,[3] low-voltage radiography of both particles and spheres,[4] ultrasonic tests, chemical leaching[5] to determine uranium contamination, and various physical property measurements.

A considerable investigation also was made of materials compatibility problems to be encountered in a helium-cooled reactor of the AVR type from impurities to be expected, such as water, oxygen, and CO_2. These investigations were conducted both on coated particles and spherical fuel elements.[6–7] They showed satisfactory performance for the conditions anticipated in the AVR.

In addition to fuel development, fuel-handling mechanisms were studied in the early efforts.[8] Flow distribution in pebble beds was investigated experimentally.[9] Several studies were made of the reactor physics to

---

[3]C. O. Smith and J. M. Robbins, Impact Resistance of Fueled Graphite Spheres for Pebble-Bed Reactor Applications, USAEC Report ORNL-3723, Oak Ridge National Laboratory, January 1965.

[4]R. W. McClung, E. S. Bomar, and R. J. Gray, Use of Microradiography Combined with Metallography for Evaluation of Coated Particles, USAEC Report ORNL-3577, Oak Ridge National Laboratory, June 1964.

[5]J. L. Cook and R. L. Hamner, The Removal of Uranium and Thorium from Fueled-Graphite Materials by Chlorination, USAEC Report ORNL-3586, Oak Ridge National Laboratory, April 1964.

[6]J. P. Blakely, J. L. Rutherford, and L. G. Overholser, Reactivity of Graphite and Fueled Graphite Spheres with Oxidizing Gases, USAEC Report ORNL-TM-751, Oak Ridge National Laboratory, February 1964.

[7]J. P. Blakely, N. V. Smith, and L. G. Overholser, Compatibility of Unsupported Pyrolytic-Carbon Coated Uranium Dicarbide Particles with Water Vapor, USAEC Report ORNL-3598, Oak Ridge National Laboratory, April 1964.

[8]S. E. Bolt, Fuel-Handling System, pp. 134–140, GCRP Semiann. Progr. Rept. Sept. 30, 1962, USAEC Report ORNL-3372, Oak Ridge National Laboratory.

[9]K. O. Wilmoth and F. N. Pebbles, Mass Transfer Variations in Randomly and Regularly Packed Sphere Beds, University of Tennessee Report EM 65-5-1, May 1965.

determine suitable ratios of C:U:Th and to evaluate desirable fuel-cycle schedules.[10,11] These studies led to a recommendation for the use of boron carbide as a burnable poison. It was recommended that pyrolytic-carbon-coated particles of boron carbide be embedded in unfueled spheres to aid in the reactivity control and to obtain a more favorable reactor startup schedule. Other more general studies of fuel cycles and economics were conducted for large pebble-bed reactors.[12–14]

During the past year, the AVR effort has been reduced to irradiation testing of coated particles and spheres. This semiannual progress report includes a description of the last two developmental type irradiation tests and a summary of the evaluation studies for several of these fuel elements.

In 1964, the AVR project placed an order for their first-core fuel with a U.S. commercial firm, the Carbon Products Division of Union Carbide Corporation. Fuel particles and elements produced under this contract have been submitted to ORNL for irradiation testing under a provision of an exchange agreement between the USAEC, Euratom, the German Ministry, and the German firm Brown Boveri/Krupp. The first of these tests for prototype spheres was conducted in an ORR poolside capsule, 01A-8, during the period September 1964 to March 1965. Results of this test also are included below. A test of loose coated particles from the first AVR fuel production run is now under way and is producing satisfactory performance data.

---

[10]A. M. Perry, R. S. Carlsmith, and J. G. Delene, AVR Fuel Management Study, pp. 279–283, GCRP Semiann. Progr. Rept. Mar. 31, 1963, USAEC Report ORNL-3445, Oak Ridge National Laboratory.

[11]R. S. Carlsmith and J. G. Delene, Fuel Composition and Fuel Management, pp. 279–284, GCRP Semiann. Progr. Rept. Sept. 30, 1963, USAEC Report ORNL-3523, Oak Ridge National Laboratory.

[12]A. M. Perry, H. F. Bauman, and J. G. Delene, Fuel-Cycle Cost Study for a Large Pebble-Bed Reactor, pp. 265–278, GCRP Semiann. Progr. Rept. Mar. 31, 1963, USAEC Report ORNL-3445, Oak Ridge National Laboratory.

[13]R. S. Carlsmith, Parametric Study of Fueled-Graphite Reactors, pp. 383–394, GCRP Semiann. Progr. Rept. Sept. 30, 1963, USAEC Report ORNL-3523, Oak Ridge National Laboratory.

[14]R. S. Carlsmith, Fuel Cycles for an 800 Mw(t) Pebble-Bed Reactor, USAEC Report ORNL-TM-314, Oak Ridge National Laboratory, August 1962.

Under the terms of the AVR exchange agreement, information concerning the fuel will be made available to the USAEC and thereby to ORNL as it is obtained from operation of the reactor through the expected life of the first core. This transmittal is expected to occur through reporting and through the presence of U.S. observers, who may visit the AVR site.

Fueled-Sphere Experiments — Capsule 05-8

Irradiation in ORR Poolside Facility (V. A. DeCarlo, F. R. McQuilkin)

Final irradiation data for capsule 05-8, which was discharged from the ORR Poolside Facility late in the previous reporting period,[15] are given in Table 3.1.

Postirradiation Examination (D. R. Cuneo, J. G. Morgan, E. L. Long, Jr., H. E. Robertson, C. D. Baumann)

Disassembly of the static capsule revealed that sphere 1 was split open and divided into two portions of approximately one-third and two-thirds. Preirradiation radiography had shown that it was likely that the central thermowell hole in this sphere was not perpendicular to the center of the sphere, and when the thermocouple was inserted perpendicularly, its sheath was broken. While it would seem unlikely that sufficient force was involved to split the sphere, this factor must be considered in searching for a reason for the broken sphere. The thermocouple is shown in its thermowell in Fig. 3.1 after removal from sphere 1. There was no evidence of a thermowell-graphite reaction, as was noted for two spheres that broke during irradiation in position 1 in two earlier experiments. Figure 3.2 shows the larger portion of the sphere with the broken thermowell hole.

Sphere 2 had some hair-line cracks over its surface. Two such cracks are shown in Fig. 3.3. Similar, but fewer, such cracks were present on sphere 3, which had the poorest compression resistance we have found.

---

[15] V. A. DeCarlo and F. R. McQuilkin, Fueled-Sphere Irradiations in ORR Poolside Facility, pp. 41–43, GCRP Semiann. Progr. Rept. Mar. 31, 1965, USAEC Report ORNL-3807, Oak Ridge National Laboratory.

Table 3.1. Summary of Operating Data for 6-cm-diam Fueled Spheres in ORR Poolside Capsule 05-8

Capsule type	Static upper compartment (spheres 1 and 2); sweep lower compartment (sphere 3)
Fuel identification	(a)
Irradiation starting date	4-10-64
Irradiation ending date	3-6-65
Irradiation time normalized to operation at 30 Mw, days	272.49
Effective thermal-neutron flux in sweep sphere, neutrons/$cm^2 \cdot sec$	1.62×10^{13}
Fast-neutron exposure (E > 0.18 Mev), neutrons/cm^2	$\sim 4 \times 10^{19}$
Self-shielding factor[b]	0.81
Fuel loading per sphere, g	
^{235}U	5.78
Uranium	6.2
Thorium	3.8
Total heavy metal	10.0
Thorium-to-uranium atom ratio	0.61
Density of sphere, g/cm^3	1.79
Volume of fueled matrix, cm^3	55.5
Fission power density[c] of fueled matrix, w/cm^3	
Sphere 1	47.2
Sphere 2	54.5
Sphere 3	57.2
Burnup,[c] at. % heavy metal in enriched particles	
Sphere 1	7.3
Sphere 2	8.3
Sphere 3	8.6
Average temperature,[d] °F	
Sphere 1	1461 (794°C)
Sphere 2	1538 (836°C)
Sphere 3	1536 (835°C)
Maximum central temperature of sphere 1, °F	2510 (1377°C)

[a]Sphere 1 (static) is designated 3M-VS16-2; sphere 2 (static) is 3M-VS16-4; and sphere 3 (sweep) is 3M-VS16-3. All spheres have 0.635-cm-thick molded unfueled shells and contain laminar-coated $(Th,U)O_2$ particles from batch 3M-120.

[b]Calculated value based on neutron diffusion theory.

[c]Calculated values based on stainless steel flux monitors placed near the fuel and corrected for self-shielding of fuel.

[d]Temperatures are measured in the graphite structure that holds the spheres by two thermocouples for each sphere. Approximately 100°F (56°C) must be added at design conditions to obtain surface temperatures of spheres.

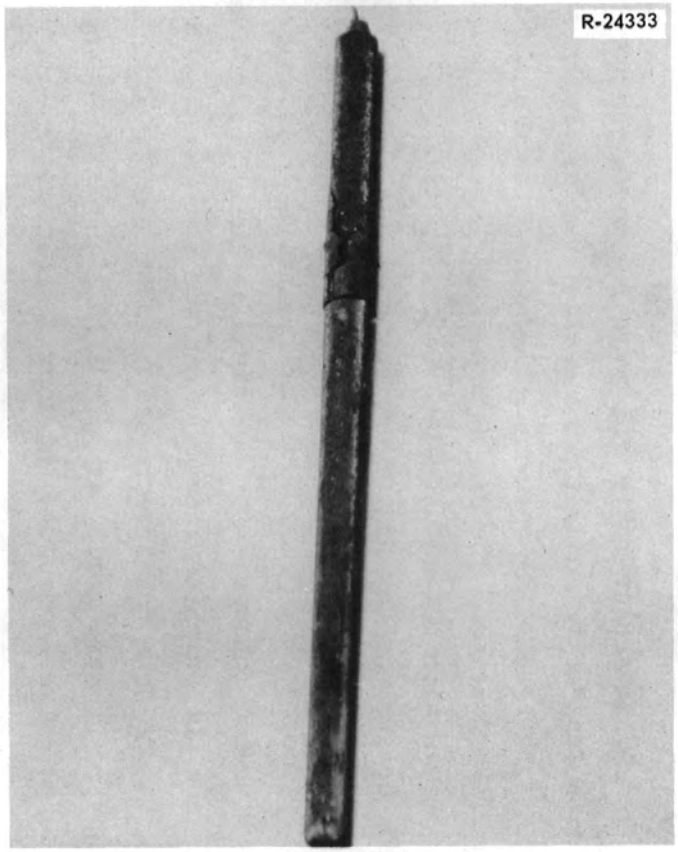

Fig. 3.1. Thermowell Containing the Thermocouple Removed from Sphere 1 of Capsule 05-8 After Irradiation. 2×

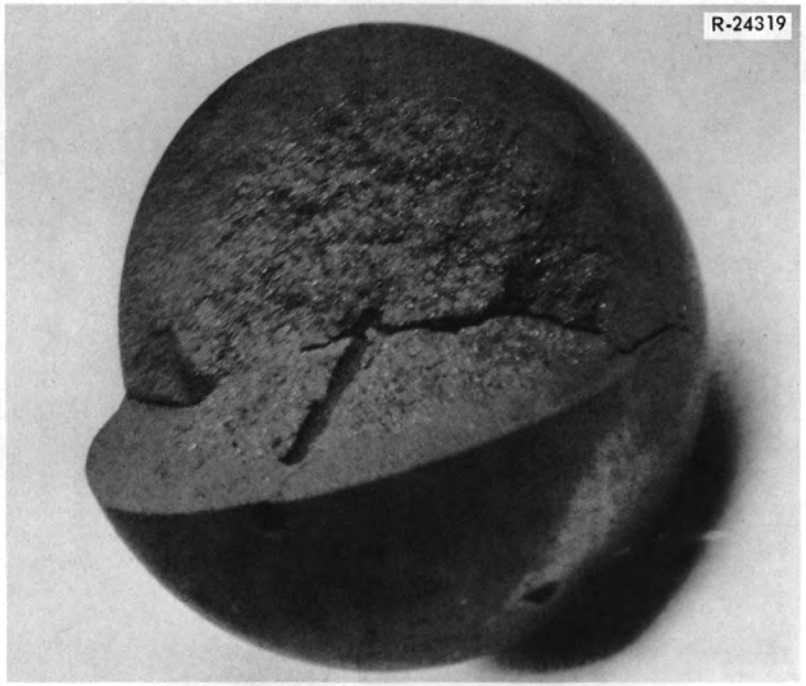

Fig. 3.2. Portion of Sphere 1 of Capsule 05-8 Showing the Thermowell Hole. 1.4×

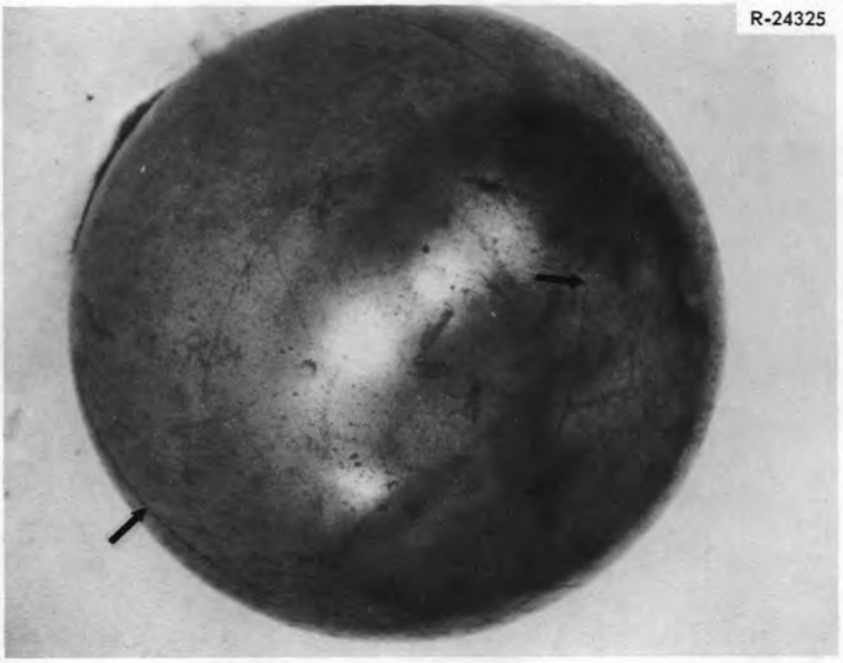

Fig. 3.3. Equator Region of Sphere 2 from Capsule 05-8 Showing Two Hair-Line Cracks Observed on Surface When Removed from Graphite Holder (3M-VS16-4). 1.4×

It broke under a 200-lb load. Sphere 2 was stored after weighing and dimensioning for possible use at a later date in a study of reaction with steam.

The weight gains, listed in Table 3.2, were relatively large when compared with those that occurred in previous experiments. Perhaps the cracked surfaces of these spheres allowed inclusion of the graphite powder packed around the spheres. The dimensional shrinkage for sphere 3 is typical for spheres with molded unfueled shells.

Thermal flux determinations from flux monitor wires are given in Table 3.3, as well as integrated exposures and burnups calculated from the flux values. Also shown in this table are relative areas under the gamma scan made with the spheres still contained in their respective graphite holders and the graphite sleeve. This was done to allow scanning the spheres in the same relative position to each other as during irradiation. Four scans were made: at 0, 90, 180, and 270°. Very little difference was noted between scans in the four positions. The results

Table 3.2. Weight and Dimensional Changes of 6-cm-diam Spheres Irradiated in Capsule 05-8

Sphere No.	Batch Designation	Dimensional Changes						Weight Gains	
		Pole		Equator		Temperate Zone			
		mils	%	mils	%	mils	%	mg	%
1	3M-VS16-2[a]							527	0.26
2	3M-VS16-4	−3.7	−0.16	0	0	−1.7	−0.07	375	0.19
3	3M-VS16-3	−2.7	−0.11	−4.2	−0.18	−6.4	−0.27	475	0.24

[a]Sphere broken; pieces assembled for weight-change measurements.

of the analyses for fission products in the graphite powder around the spheres are given in Table 3.4.

Specimens were sectioned from spheres 1 (3M-VS16-2) and 3 (3M-VS16-3) for metallographic examination. Both of these spheres were fueled with laminar-coated enriched $(Th,U)C_2$ particles from batch 3M-120, and metallographic examination yielded similar results. No failed particles were found in either specimen; 280 particles were examined. Wedge-shaped fractures originating at the fuel-coating interface were found in the coatings, and in some instances these fractures penetrated about one-third of the coating thickness. The formation of the wedge-shaped fractures was accompanied by partial delamination of the coatings. Except for a loss in crystalline detail and swelling of the fuel, no other major microstructural changes were noted after irradiation. A typical fuel particle is shown in Fig. 3.4.

In addition, a transverse section was made through the central thermocouple assembly of sphere 1 and examined metallographically; the section was taken near the thermocouple bead. The assembly comprised BeO-insulated W–5% Re and W–26% Re thermoelements sheathed in tantalum and placed in a pyrolytic-tungsten sleeve. The various components are shown after irradiation in Fig. 3.5. A very thin layer (less than 0.5 mil) of tungsten carbide was found on the outer surface of the tungsten well. The tantalum sheath had reacted severely to form nonmetallic compounds; however, there was no apparent change in the thermocouple wires or the insulation.

Table 3.3. Flux, Burnup, and Gamma-Scan Data from Experiment 05-8

Sphere	Batch Designation	Thermal-Neutron Flux (neutrons/cm^2·sec[a])	Total Thermal-Neutron Exposure (neutrons/cm^2)	Burnup		Normalized Gamma-Scan Areas
				% Heavy Metal	Normalized	
		$\times 10^{13}$	$\times 10^{20}$			
1	3M-VS16-2	1.3	3.13	7.3	85	88.5
2	3M-VS16-4	1.54	3.63	8.3	97	100
3	3M-VS16-3	1.62	3.81	8.6	100	99

[a]From analysis of cobalt in flux monitor wires.

Table 3.4. Results of Analyses for Fission Products and Uranium in Graphite Powder Around Spheres in Capsule 05-8

Sphere	Fraction of Total Fission Product Generated						Fraction of Uranium in Powder
	^{95}Zr	^{103}Ru	^{106}Ru	^{137}Cs	^{140}Ba	^{144}Ce	
1	1.3×10^{-4}	1.9×10^{-6}	7.4×10^{-6}	1.6×10^{-4}	2.4×10^{-4}	5.0×10^{-4}	2.2×10^{-5}
2	6.9×10^{-7}	6.2×10^{-7}	5.2×10^{-6}	2.4×10^{-5}	2.6×10^{-4}	1.8×10^{-5}	2.9×10^{-5}
3	7.0×10^{-7}	3.6×10^{-7}	3.1×10^{-7}	1.8×10^{-4}	1.1×10^{-4}	1.1×10^{-6}	3.0×10^{-5}

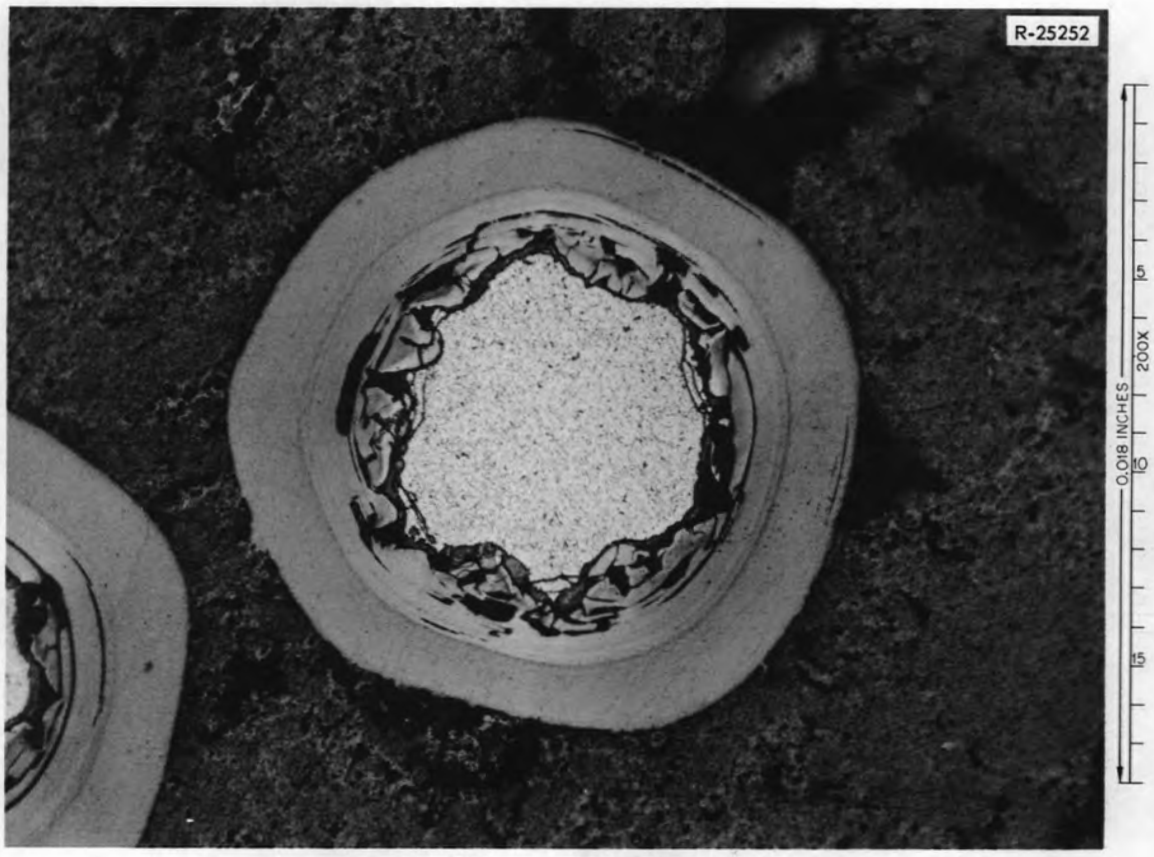

Fig. 3.4. A Pyrolytic-Carbon-Coated $(Th,U)C_2$ Particle (Batch 3M-120) Representative of Those Examined in Spheres 1 and 3 from Capsule 05-8. As polished. 200×

Eight-Ball Capsule F1-8B-5 Experiment

Irradiation in ORR Core (V. A. DeCarlo, F. R. McQuilkin)

Revised data for irradiation of the last-scheduled eight-ball assembly in capsule F1-8B-5 are given in Table 3.5. The capsule was discharged from ORR core position F-1 January 10, 1965.[16] These data have been revised to include neutron flux dosimetry and burnup results obtained after irradiation was completed.

---

[16]V. A. DeCarlo and F. R. McQuilkin, Eight-Ball Irradiation in ORR Core Position F-1, pp. 43–46, GCRP Semiann. Progr. Rept. Mar. 31, 1965, USAEC Report ORNL-3807, Oak Ridge National Laboratory.

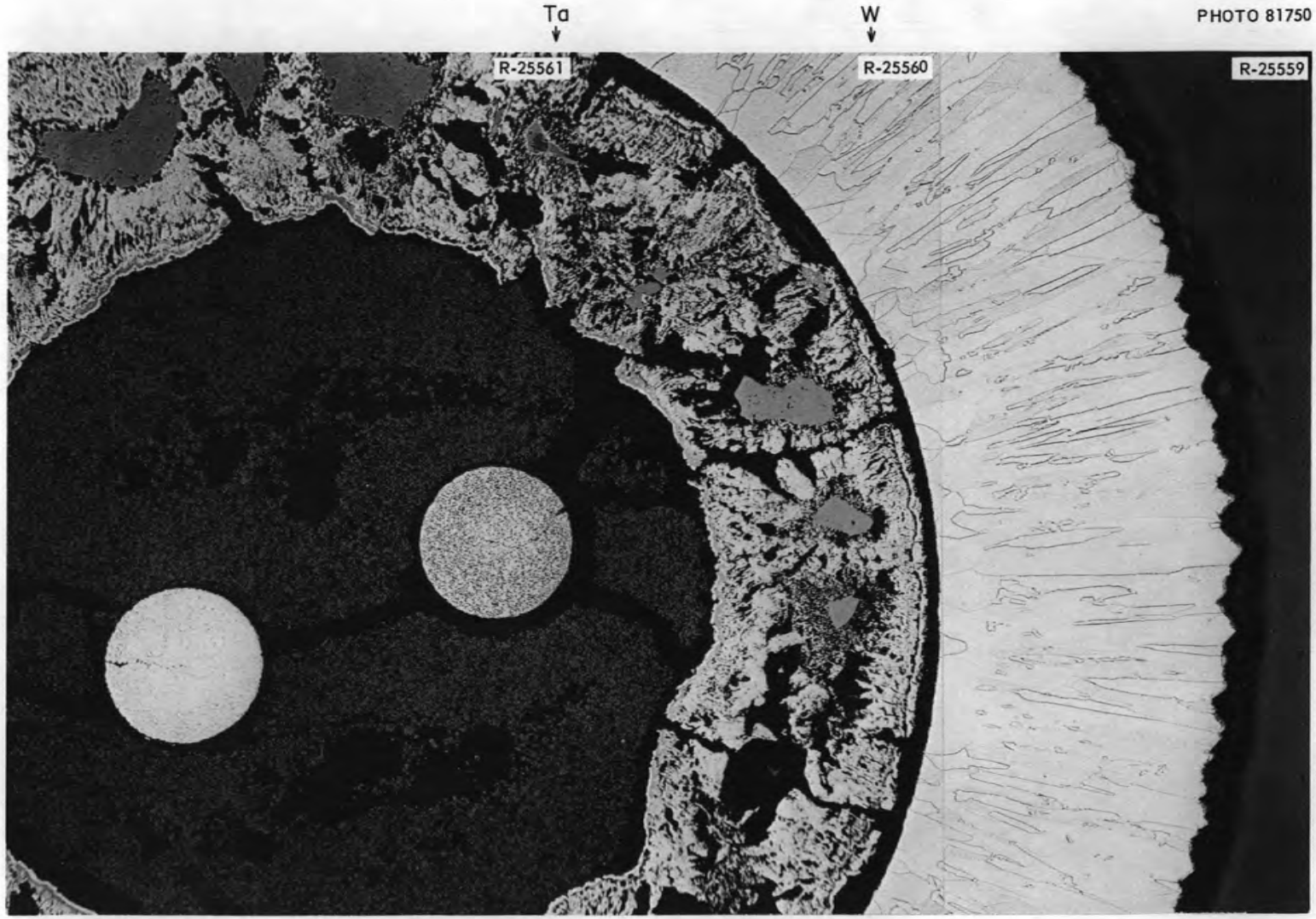

Fig. 3.5. Transverse Section Through Central Thermocouple Assembly from Sphere 1 After Irradiation in Capsule 05-8. Etched. 100×

Table 3.5. Summary of Operating Data for Eight-Ball Experiment F1-8B-5

Fuel identification	(a)
Irradiation starting date	4-10-64
Irradiation ending date	1-10-65
Irradiation time normalized to operation at 30 Mw, days	237.88
Effective thermal-neutron flux,[b] neutrons/cm^2·sec	5.55×10^{13}
Fast-neutron exposure (E > 0.18 Mev), neutrons/cm^2	$\sim 1.5 \times 10^{21}$
Fuel loading of typical sphere,[a] g	
^{235}U	0.29
Uranium	1.6
Thorium	1.0
Total heavy metal	2.6
Thorium-to-uranium atom ratio	0.61
Density of sphere, g/cm^3	1.75
Volume of sphere, cm^3	28.96
Average power density,[b] w/cm^3	26
Approximate burnup in enriched particles,[c] at. %	
^{235}U	44.0
Heavy metal	25.4
Operating temperature at center of fuel in sphere 1, °F	
Maximum	2080 (1138°C)
Minimum	1580 (860°C)
Sphere surface thermocouple readings[d] averaged for entire experiment, °F	
Sphere 1	1393 (756°C)
Sphere 2	1540 (838°C)
Sphere 3	1605 (874°C)
Sphere 4	1567 (852°C)
Sphere 5	1510 (821°C)
Sphere 6	1554 (846°C)
Sphere 7	1451 (788°C)
Sphere 8	1368 (742°C)

[a]A more complete description of the composition of each sphere is given in Table 3.6 following and in Table 1.15 of Ref. 17.

[b]Based on stainless steel flux monitors placed near the fuel and corrected for self-shielding of fuel. This value is the average of all eight spheres for the entire run. Fluxes in individual spheres ranged from 6.10×10^{13} to 4.58×10^{13} neutrons/cm^2·sec.

[c]For burnup in individual spheres see Table 3.7, this report.

[d]Approximately 100°F (56°C) must be added to obtain sphere surface temperatures at a power density of 35 w/cm^3.

Postirradiation Examination (D. R. Cuneo, J. G. Morgan, E. L. Long, Jr., H. E. Robertson, C. D. Baumann)

The highest neutron exposure and burnup yet attained for graphite-matrix fuel occurred in experiment F1-8B-5. The fuel, which was irradiated in the F-1 position of the ORR for 237.88 days, was in the form of 1 1/2-in.-diam fueled spheres, as described in Table 3.6. A more complete description was given previously.[17] It was suspected that this capsule leaked near the end of the irradiation period. However, a post-irradiation gas sample showed krypton and xenon activity, and pressure testing of the capsule did not reveal any leaks. The appearance of the capsule inner container was poor; numerous surface cracks were apparent.

The capsule also contained pyrolytic-carbon-coated B_4C particles in order to test their stability for use in control elements. A small 3/8-in.-diam, 4-in.-long graphite rod above the sealed portion of the capsule had been drilled to form two 0.5-in.-long compartments to hold the B_4C particles. The upper compartment was wrapped with three thicknesses of 0.020-in.-thick silver foil to shield this batch of B_4C particles from about one-half the reactor flux. A preirradiation radiograph showed that the foil had been displaced slightly downward. A gamma scan of the entire capsule after irradiation but before disassembly revealed that the foil was lying in the bottom of the space containing the holder for the B_4C particles. However, activity measurements showed that the B_4C particles from the upper compartment were approximately one-half as radioactive as those from the lower compartment (300 mr upper versus 700 mr lower). From this semiquantitative measurement we feel that it is likely that the silver foil provided screening throughout the irradiation.

Weight, dimensional, and compression test data are also reported in Table 3.6. These spheres showed the greatest dimensional changes yet observed in our fueled-graphite sphere examinations. Consistent with previous observations, the spheres without unfueled shells underwent larger shrinkages. Before irradiation sphere 2 had been subjected to 25

[17] C. Michelson and E. A. Franco-Ferreira, Preparation of Fueled-Graphite Irradiation Specimens, pp. 39–45, GCRP Semiann. Progr. Rept. Sept. 30, 1964, USAEC Report ORNL-3731, Oak Ridge National Laboratory.

Table 3.6. Weight, Dimensional, and Compression Test Data on 1.5-in.-diam Fueled Spheres Irradiated in Capsule F1-8B-5

Sphere Position	Sphere Designation	Unfueled Graphite Shell		Type of Coating on Normal and Enriched Uranium Particles[a]	Average Sphere Shrinkage (%)	Weight Losses		Compression Loading to Failure (lb)
		Thickness (in.)	Type			mg	%	
1	3M-S13-10	0.2	Molded	Laminar	1.38	(b)	(b)	
2	GA-S14-2	0.2	Machined ATJ	Triplex	0.84	69	0.14	
3	NCF-S24-L3	0	None	Duplex	1.49	3		2650
4	3M-S13-7	0.2	Machined ATJ	Laminar	0.77	51	0.1	900[c]
5	NCF-S25-V10	0	None	Duplex	2.32	5		3050
6	3M-S13-14	0.2	Molded	Laminar	1.54	26	0.05	1250
7	GA-S14-3A	0.2	Machined ATJ	Triplex	0.61	40	0.08	225[c]
8	3M-S13-9	0.2	Machined ATJ	Laminar	0.44	13	0.03	275[c]

[a]All particles were $(Th,U)C_2$. In spheres 1, 3, 4, 5, 6, and 8, Th/U = 0.61. In spheres 2 and 7, normal Th/U = 5.27 and enriched Th/U = 0.61.

[b]Thermocouple stuck.

[c]No bond between core and shell.

drops from a height of 4 meters onto a bed of 1 1/2-in.-diam graphite spheres. Visual examination of sphere 2 in the hot cell indicated that a crack caused by the preirradiation drop test did not propagate during irradiation. This was also confirmed from replicas of this sphere that were compared with preirradiation replicas.

The four spheres with machined shells had the least shrinkage of the three types in the capsule. The shrinkage of the machined shells ranged from 0.42% (pole of sphere 8) to 0.89% (poles of spheres 2 and 4), and sphere 8 had the least average shrinkage (0.44%). The two spheres with molded unfueled shells had fairly uniform shrinkages at the polar, equatorial, and temperate regions. The average was about 1.5%. The two spheres with no unfueled shells showed the greatest shrinkages. One of these averaged 1.5% and the other 2.3%. Compression test results were found to be in line with dimensional changes. For instance, the machined-shell spheres had no bond left between the core and shells, and consequently the compression resistance was very poor. The one sphere with a molded shell that was compression tested was appreciably better than the machined-shell spheres. As was expected, the one tested molded sphere without a shell had good compression strength. In order to check the relative strengths of a sphere and its core, where the overall compression strength of the sphere was very poor (225-lb load to failure), the core of sphere 7 was compression tested separately. It failed at a load of 1125 lb. Sphere 7, the weakest of those tested, is shown in Fig. 3.6, and sphere 5, the strongest, is shown in Fig. 3.7 after failure at a 3050-lb load.

Flux, burnup, and gamma-scan data for capsule F1-8B-5 are listed in Table 3.7. The spheres were stacked in a plastic tube and gamma scanned as usual. The tube was then rotated 90° three times and gamma scanned each time. Agreement for the four scans was quite close. Agreement of gamma-scan areas and values for the relative number of fissions that occurred in each sphere is quite good for most spheres. There is only 17% difference in the worst case (sphere 8).

The results of analyses for fission products and uranium in the graphite powder packed around the spheres are given in Table 3.8. When

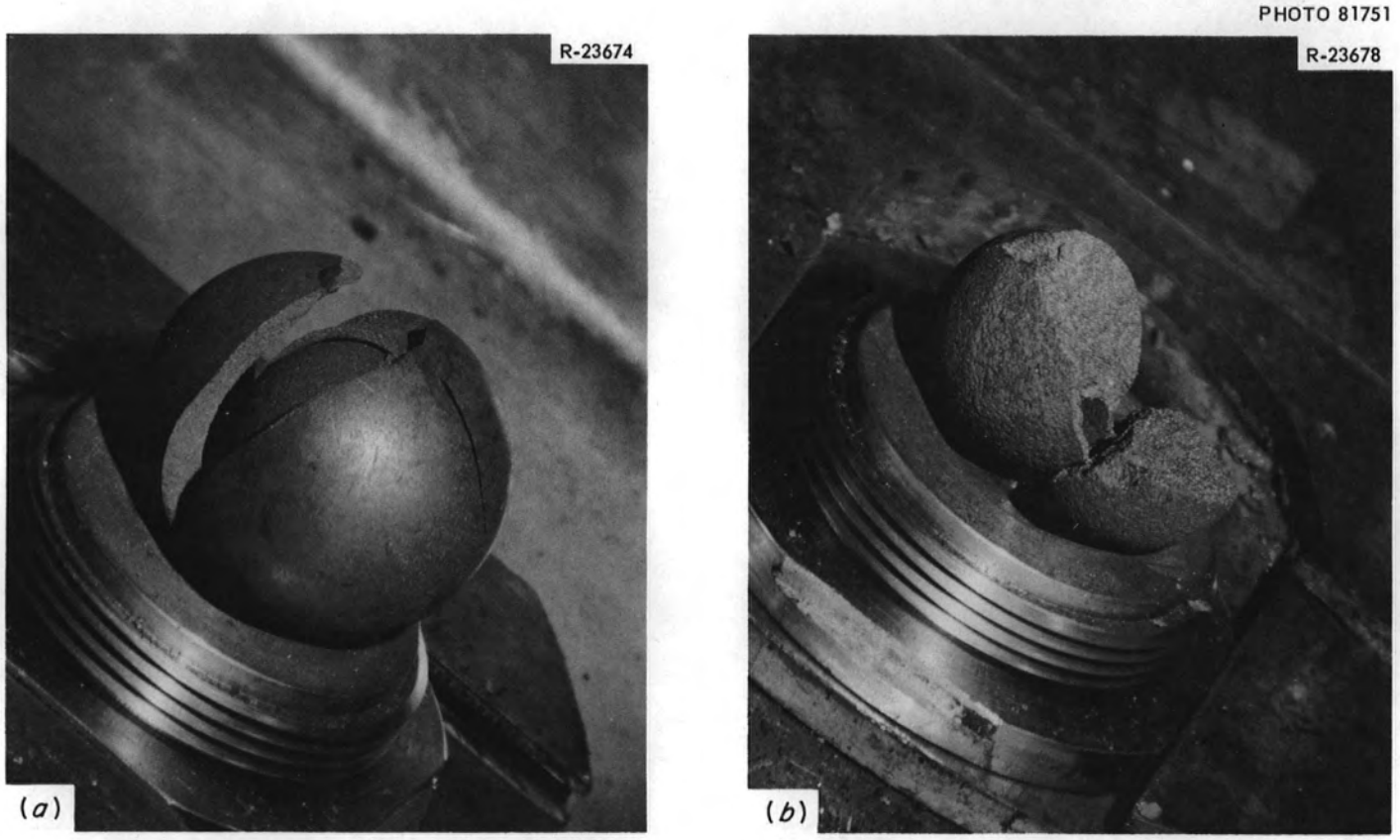

Fig. 3.6. Sphere 7 from Capsule F1-8B-5 After Compression Tests. (a) Entire sphere after failure at a load of 225 lb. (b) Core after failure at a load of 1125 lb. ~1.4×

Table 3.7. Flux, Burnup, and Gamma-Scan Data for Capsule F1-8B-5

Sphere	Normalized Gamma-Scan Areas					Average Thermal-Neutron Flux (neutrons/cm^2·sec)	Integrated Exposure (neutrons/cm^2)	Heavy-Metal Burnup[a]	Fraction of ^{235}U Fissioned	Normalized Burnup[b]
	At 0°	At 90°	At 180°	At 270°	Average for Four Positions					
						$\times 10^{13}$	$\times 10^{21}$			
1	83	82	82	82	82	5.74	1.18	0.256	0.450	96
2	100	98	100	99	99	6.08	1.25	0.266	0.461	95
3	97.5	100	96	100	98	5.85	1.20	0.270	0.467	99
4	90	88	88	91.5	89	6.10	1.25	0.270	0.468	100
5	94	97	91	97	95	5.76	1.18	0.267	0.463	99
6	88	89	84	89	88	(c)				
7	88	88	83	91	88	4.75	0.98	0.225	0.389	80
8	71	70	68	72	70	4.58	0.94	0.223	0.385	82
B_4C in top compartment						3.7	0.76			
B_4C in bottom compartment						5.09	1.05			

[a]Fraction of heavy metal that fissioned; enriched particles only.

[b]Based on product of fraction of ^{235}U that fissioned times initial ^{235}U content.

[c]Sample spilled during dissolution.

Table 3.8. Results of Analyses of Graphite Powder Around Spheres in Capsule F1-8B-5

Sphere Position	Sphere Designation	Unfueled Shells		Fraction of Total Fission Products Generated Found in Powder						Fraction of Uranium Found in Powder
		Thickness (in.)	Type	^{95}Zr	^{103}Ru	^{106}Ru	^{137}Cs	^{140}Ba	^{144}Ce	
1	3M-S13-10	0.2	Molded	3×10^{-6}	1.8×10^{-7}	2.7×10^{-7}	1.7×10^{-3}	3.6×10^{-4}	4.3×10^{-5}	3.6×10^{-6}
2	GA-S14-2	0.2	Machined ATJ	No powder						
3	NCF-S24-L3	0	None	No powder						
4	3M-S13-7	0.2	Machined ATJ	8.9×10^{-7}	8.5×10^{-8}	5.2×10^{-7}	8.1×10^{-5}	9.5×10^{-6}	1.1×10^{-6}	9.8×10^{-7}
5	NCF-S25-V10	0	None	9.9×10^{-7}	7.5×10^{-8}	1.3×10^{-7}	5.2×10^{-4}	1.0×10^{-4}	1.3×10^{-5}	1.1×10^{-6}
6	3M-S13-14	0.2	Molded	5.1×10^{-6}	4.6×10^{-7}	3.8×10^{-7}	3.6×10^{-3}	4.7×10^{-4}	6.8×10^{-5}	3.8×10^{-6}
7	GA-S14-3A	0.2	Machined ATJ	4.7×10^{-6}	1.6×10^{-7}	3.4×10^{-7}	4.7×10^{-3}	1.6×10^{-4}	3.8×10^{-5}	5.5×10^{-6}
8	3M-S13-9	0.2	Machined ATJ	2.8×10^{-6}	1.4×10^{-5}	1.0×10^{-4}	4.3×10^{-3}	1.3×10^{-4}	1.2×10^{-5}	7.3×10^{-6}

Fig. 3.7. Sphere 5 from Capsule F1-8B-5 After Compression Loading to Failure at 3050 lb. ~1.4×

the graphite stack was disassembled, large variations were found in the amounts of powder around the spheres, and there was no powder around the spheres in positions 2 and 3. Also, the graphite stack (sphere holders) was found to fit together quite loosely, probably due to radiation-induced shrinkage. It is likely that the loose-fitting holders allowed the powder to gradually sift downward during the experiment, as well as during postirradiation handling. No preirradiation determination of the powder weight was made; however, the total powder weight recovered was comparable with that recovered from the similar capsule F1-8B-4. The type of shell, or lack of one, did not seem to influence the fission-product content in the powder from any particular sphere; however, mixing of the powder may account for the similar results. An exception was the relatively high concentration of ^{103}Ru and ^{106}Ru in the powder around sphere 8. The 3M coated particles in spheres 1 and 4 are known to have failed badly, and

it is likely that those in spheres 6 and 8 did also. Cesium-137 was found in quantities of up to almost 0.5%, but the uranium content of the powder samples was uniformly quite low.

Metallographic specimens were sectioned from spheres 1 through 4, and samples were taken from the pyrolytic-carbon-coated B_4C particles in this capsule. Spheres 1 and 4 reached burnups of 25.6 and 27% heavy metal. Both spheres contained normal and enriched pyrolytic-carbon-coated $(Th,U)C_2$ particles from batches 3M-119 and 3M-120. Examination of 91 enriched particles (batch 3M-120) from sphere 1 revealed that 67% had failed. Examination of 88 enriched particles from sphere 4 showed 100% failure. The microstructural details of the particles from both spheres were similar. The enriched particles failed as a result of numerous wedge-shaped fractures that originated at the fuel-coating interface and extended through the coating. There was evidence of a reaction product in the peripheral regions of the particles and fuel swelling into the fractures. The fuel appeared to be amorphous after etching.

The particles of natural enrichment (batch 3M-119) from spheres 1 and 4 were similar in appearance. A slight loss in the crystalline detail of the $(Th,U)C_2$ was noted in comparison with the unirradiated particles. Also, there were wedge-shaped fractures in the coatings that originated at the $(Th,U)C_2$-coating interface and extended about one-third of the way through the coatings. This is the first time we have observed any damage to the coatings of particles containing normal uranium. There was no evidence of a reaction between the carbide and the coating, nor was there any evidence of swelling in the $(Th,U)C_2$. Typical particles from these two spheres are shown in Fig. 3.8.

Sphere 2 (GA-S14-2) contained both natural and enriched pyrolytic-carbon-coated $(Th,U)C_2$ particles from batches H2340-128 NC and N1736-121ECB, respectively. There were no failures in the 68 enriched particles examined. The only microstructural changes noted after irradiation were a loss in crystalline detail in the fuel, the presence of fine pores, and the formation of a reaction product at the fuel-coating interface. A typical enriched fuel particle is shown in Fig. 3.9. There was no

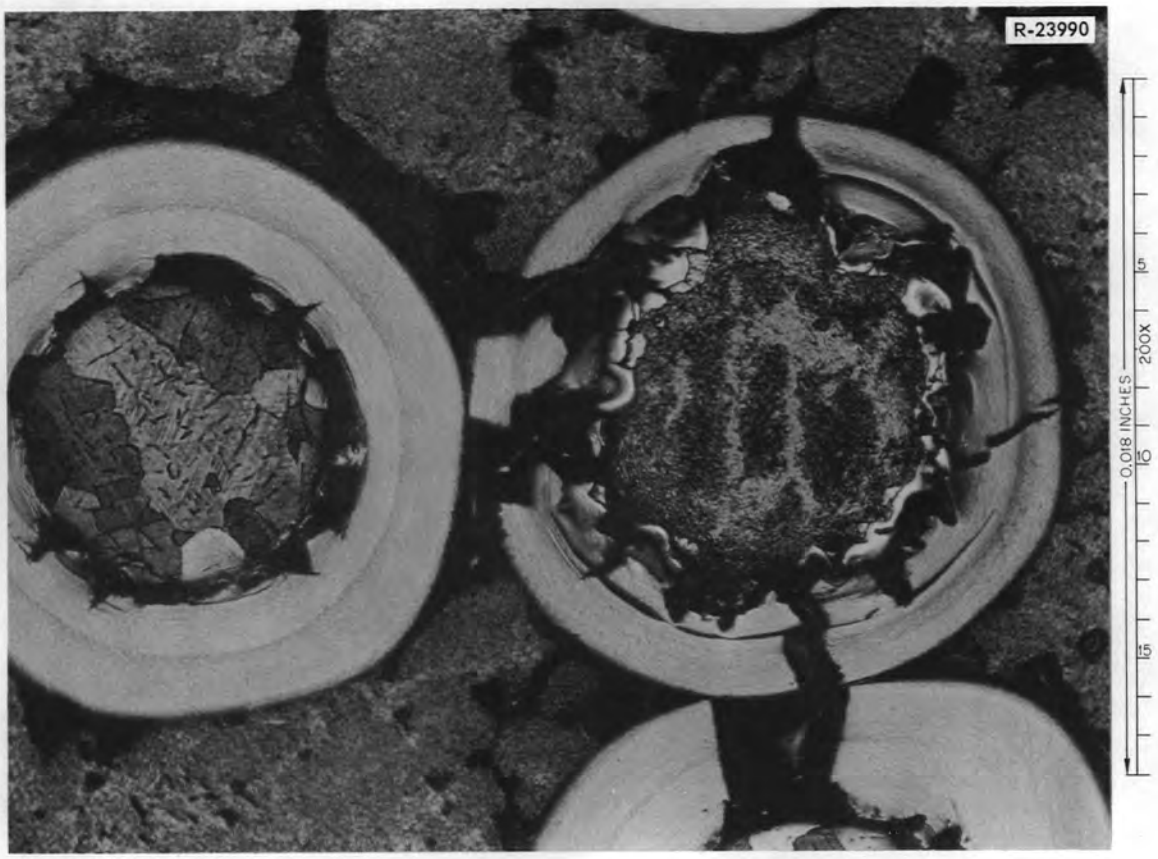

Fig. 3.8. Typical Particles from Spheres 1 and 4 from Capsule F1-8B-5. The coated particle on the left is $(Th,U)C_2$ of natural enrichment (batch 3M-119). The coated particle on the right is enriched $(Th,U)C_2$ (batch 3M-120). Etched. 200×

evidence of potential failure of the coatings. No unusual or unexpected changes were seen in the particles containing natural uranium.

Sphere 3 (NCF-S24-L3) also contained both natural and enriched pyrolytic-carbon-coated $(Th,U)C_2$ particles. The natural and enriched particles were from batches NCC-211 and NCC-210, respectively. No failures were noted in the 20 particles examined. There were numerous wedge-shaped fractures that originated at the fuel-coating interface. These extended through the inner coating and into the outer coating. The fuel appeared to be amorphous, contained numerous small pores, and had swelled considerably, as shown in Fig. 3.10. No unusual effects were noted in the natural particles.

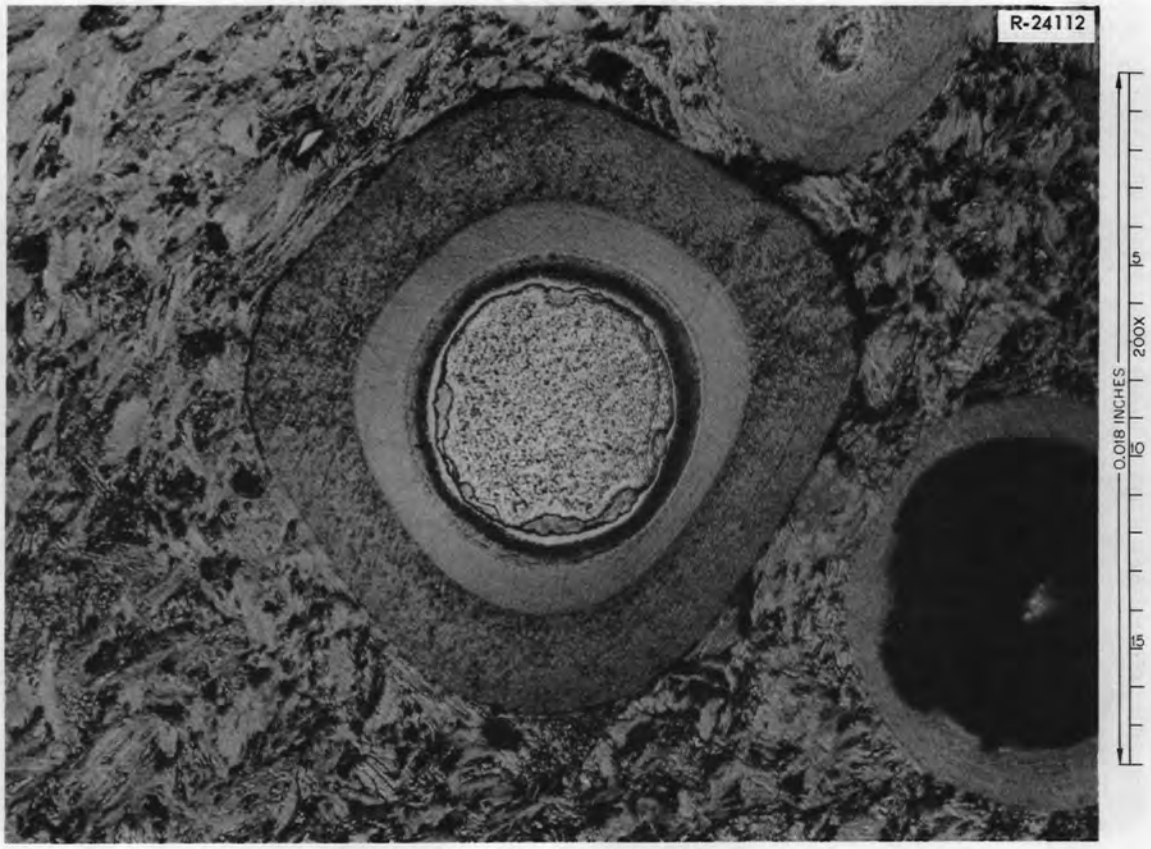

Fig. 3.9. Typical Enriched $(Th,U)C_2$ Coated Particle (Batch N1736-121ECB) from Sphere 2 of Capsule F1-8B-5. As polished. 200×

Samples of pyrolytic-carbon-coated B_4C particles were taken from both compartments in capsule F1-8B-5 and examined metallographically. The particles from both compartments were similar. Only slight differences were noted in the irradiated particles when compared with unirradiated control particles. No failed coatings were found, nor were there any signs of potential failures. The only change noted in the B_4C after irradiation was the presence of a few small grey-colored phases, both within the matrix and at the B_4C-to-coating interface. A highly anisotropic layer, about 3 to 4 μ thick was seen with the aid of polarized light along the inner surfaces of the coatings. We also observed that the coatings were more reflective after irradiation. Microhardness measurements showed that the irradiated coatings had increased in hardness

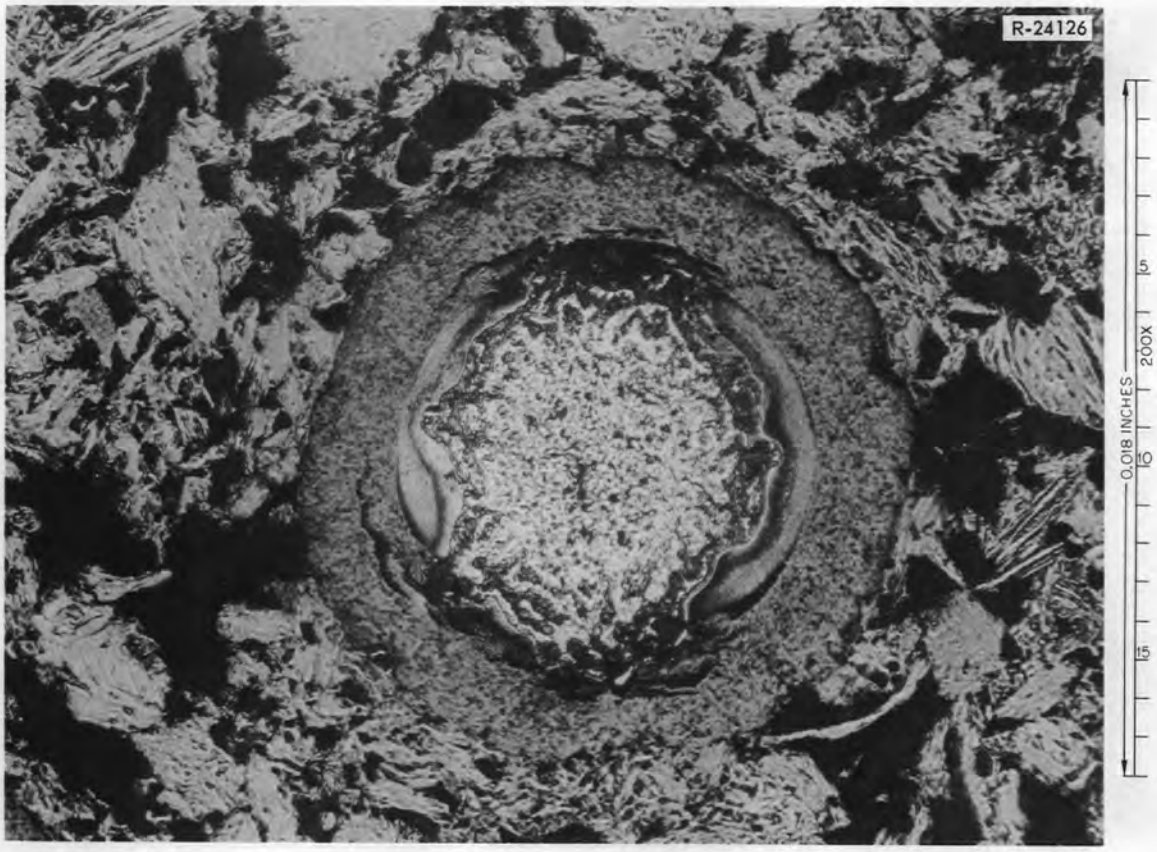

Fig. 3.10. Typical Enriched $(Th,U)C_2$ Particle (Batch NCC-210) from Sphere 2 of Capsule F1-8B-5. As polished. 200×

by 31 DPH-G,[18] where G indicates that this hardness value is for an elastic hardness. Representative particles are shown in Fig. 3.11 before and after irradiation.

The central thermocouple assembly that was used in sphere 1 was also included in the metallographic specimen section from that sphere. A transverse section near the thermoelement junction was examined. The assembly was comprised of MgO-insulated, Chromel-Alumel thermocouple wires sheathed in type 347 stainless steel. This assembly was then placed in a thin-walled type 304 stainless steel well. Metallographic examination showed both the sheath and the well material to be completely carburized, and there was evidence of melting. One of the thermoelements

[18]T. M. Kegley, Jr., and B. C. Leslie, How to Measure Hardness of Pyrolytic Carbon, Nucleonics, 21(12): 62–64 (December 1963).

was welded to the sheath material, and some of the well material was present in the graphite matrix. The transverse section through the thermocouple assembly is shown in Fig. 3.12.

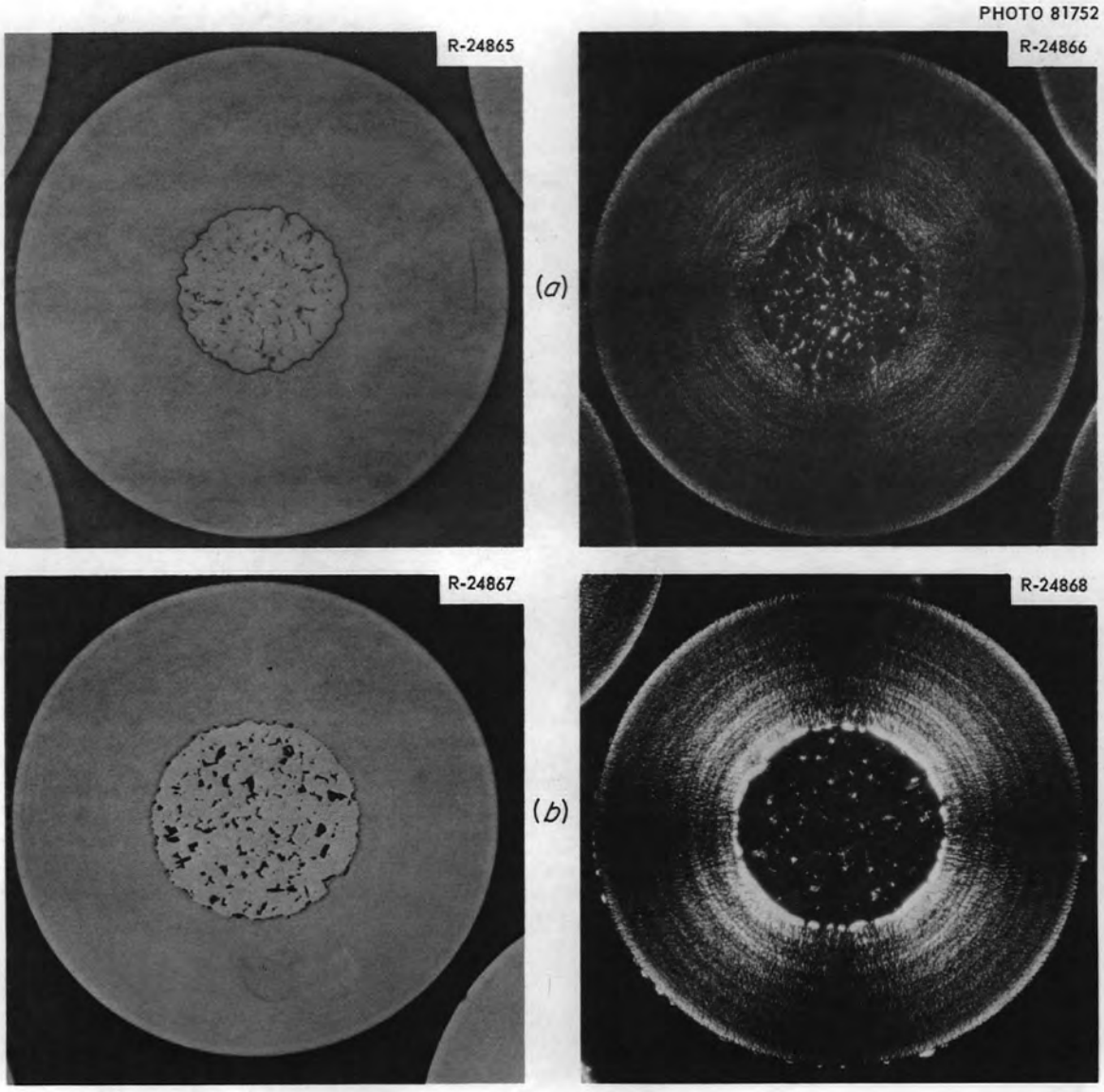

Fig. 3.11. Pyrolytic-Carbon-Coated B_4C Particles Irradiated in Capsule F1-8B-5. (a) Unirradiated control particle; left, bright field illumination; right, polarized light. (b) Irradiated particles; left, bright field illumination; right, polarized light. As polished. 200×

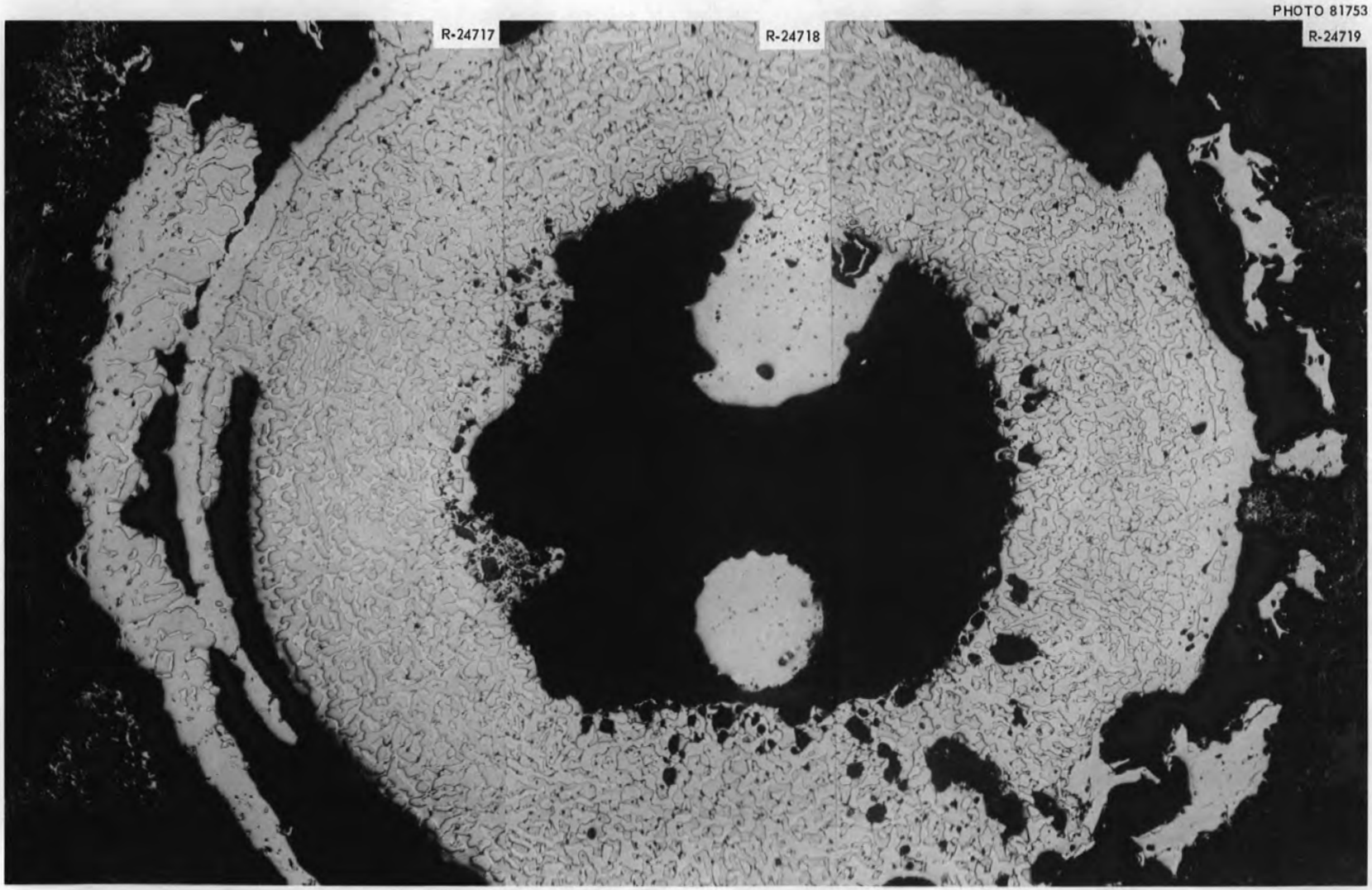

Fig. 3.12. Transverse Section Through the Central Thermocouple Assembly from Sphere 1 of Capsule F1-8B-5. Note the heavily carburized sheath and well material. As polished. 100× (Original reduced 14%)

AVR Prototype Sphere Experiments — Capsule 01A-8

Irradiation in ORR Poolside Facility (V. A. DeCarlo, F. R. McQuilkin)

The final irradiation data for capsule 01A-8, which was discharged late in the previous reporting period, are given in Table 3.9. Estimates

Table 3.9. Summary of Operating Data for AVR Prototype Fueled Spheres in ORR Poolside Capsule 01A-8

Capsule type	Static upper compartment (spheres 1 and 2); sweep lower compartment (sphere 3)
Fuel identification	(a)
Irradiation starting date	9-21-65
Irradiation ending date	3-7-65
Irradiation time normalized to operation at 30 Mw, days	145.76
Effective thermal-neutron flux in sweep sphere, neutrons/cm^2·sec	2.16×10^{13}
Fuel enrichment, wt % ^{235}U	93.2
Fuel loading, g	
Total ^{235}U	6.8
Total uranium	7.3
Self-shielding factor[b]	
Sphere 1	0.756
Sphere 2	0.756
Sphere 3	0.756
Volume of fueled matrix, cm^3	33.5
Fission power density[c] of fueled matrix, w/cm^3	
Sphere 1	52
Sphere 2	62
Sphere 3	59
Burnup,[c] at. % heavy metal in enriched particles	
Sphere 1	4.5
Sphere 2	5.3
Sphere 3	5.1
Average temperature,[d] °F	
Sphere 1	1433 (778°C)
Sphere 2	1550 (843°C)
Sphere 3	1574 (857°C)
Maximum central temperature of sphere 1, °F	2350 (1288°C)

[a]Sphere 1 (static) is designated NCL-VS8-E1; sphere 2 (static) is NCL-VS8-E2; and sphere 3 (sweep) is NCL-VS8-E3. All spheres have 1.0-cm-thick machined ATJ graphite shells and contain duplex-coated UC_2 particles from batch NCC-220.

[b]Values calculated with a simplified method based on neutron diffusion theory for rapid estimation of the average neutron flux in spherical fuel elements from burnup analyses of external flux-monitoring wires.

[c]Calculated values based on capsule thermal design and normalized gamma scans.

[d]Temperatures are measured in the graphite structure that holds the spheres by two thermocouples for each sphere. Approximately 100°F (38°C) must be added at design conditions to obtain surface temperature of spheres.

of power density and burnup have been adjusted from the values reported previously.[19] They are based on the capsule thermal design and on the normalized gamma scans of the irradiated spheres. Flux dosimeters included with the specimens indicate appreciably higher burnups (see Table 3.11), but these data are being evaluated further.

Postirradiation Examination (D. R. Cuneo, J. G. Morgan, E. L. Long, Jr., H. E. Robertson, C. D. Baumann)

Capsule O1A-8 contained three 6-cm-diam AVR-prototype fueled-graphite spheres manufactured by the Carbon Products Division of Union Carbide. Each sphere was fueled by 93.2% enriched uranium as pyrolytic-carbon-coated UC_2 particles from batch NCC-220. Each sphere had a 1.0-cm-thick unfueled machined ATJ graphite shell.

The spheres, their graphite holders, and the metal portions of the capsule were all normal in appearance. The static compartment (containing spheres 1 and 2) was punctured, and the contained gas was recovered and analyzed. The results are listed in Table 3.10. The presence of about 17 vol % air probably indicates leakage during the gas-sampling

[19]V. A. DeCarlo and F. R. McQuilkin, Capsule Irradiations in ORR Poolside Facility, pp. 143–144, GCRP Semiann. Progr. Rept. Mar. 31, 1965, USAEC Report ORNL-3807, Oak Ridge National Laboratory.

Table 3.10. Results of Mass Spectrometer Analysis of Gas Recovered from the Static Compartment of Capsule O1A-8

Constituent	Content (vol %)	Constituent	Content (ppm)
CO_2	0.01	H_2	~10
Ar	0.58	Xe	<100[a]
O_2	2.81	Kr	<100[a]
N_2 + CO	14.51		
He	81.74		

[a]Below limits of detection.

operation. Gamma counting the gas sample gave 3.2×10^4 dis/sec of ^{133}Xe and 6.3×10^4 dis/sec for ^{85}Kr.

The spheres were gamma scanned with the north pole regions up as during irradiation. Excellent agreement was found between the relative areas under the scan curves and normalized burnup values. These data, along with thermal-neutron flux values determined by the $^{59}Co(n,\alpha)^{60}Co$ reaction, are given in Table 3.11.

Weight and dimensional changes are reported in Table 3.12, as well as results of compression tests of spheres 2 and 3. Dimensional changes were uniform and relatively small. The weight changes were also insignificant. When broken under compression loading, spheres 2 and 3 showed some bonding between cores and shells. However, when we cut metallographic specimens from sphere 1, we usually found that the unfueled shell readily fell away from the core portion of the specimen. One unirradiated sphere (NCL-VS8-E4) of this type was available for testing. It broke at a compression loading of 3290 lb, and the unfueled shell fell away from the core. However, as shown in Fig. 3.13, there is evidence of some bonding between the core and shell of this sphere too.

Figure 3.14 shows spheres 2 and 3 after compression loading to failure, and Fig. 3.15 shows the cores of spheres 2 and 3 with the shells

Table 3.11. Burnup, Gamma-Scan, and Thermal-Neutron Flux Data for Capsule O1A-8

Sphere	Batch Designation	Thermal-Neutron Flux		Burnup		Normalized Area Under Gamma-Scan Curves
		neutrons/cm^2·sec	neutrons/cm^2	% Heavy Metal in Enriched Particles	Normalized	
		$\times 10^{13}$	$\times 10^{20}$			
1	NCL-VS8-E1	1.90	2.39	9.1	84	84
2	NCL-VS8-E2	2.28	2.88	10.8	100	100
3[a]	NCL-VS8-E3	2.18	2.75	10.2	93	95
		1.80	2.26			
		3.38	4.26			
		1.28	1.61			
		2.16 av	2.72 av			

[a]Four flux-monitoring wires analyzed as separate samples.

Table 3.12. Physical Properties of Spheres Irradiated in Capsule 01A-8

Sphere No.	Batch Designation	Dimensional Changes						Weight Losses		Compression Load to Failure[a] (lb)
		Pole		Equator		Temperate Zone				
		mils	%	mils	%	mils	%	mg	%	
1	NCL-VS8-E1	−5	−0.2	−3	−0.1	−5	−0.2	125	0.06	
2	NCL-VS8-E2	−5	−0.2	−4	−0.2	−5	−0.2	79	0.04	2500
3	NCL-VS8-E3	−4	−0.2	−4	−0.2	−5	−0.2	56	0.03	1600

[a]Unirradiated control broke at 3290 lb.

Fig. 3.13. Unirradiated Sphere (NCL-VS8-E4), Which Was Equivalent to Capsule 01A-8 Spheres, After Failure at a Compression Load of 3290 lb. 1.4×

removed. Generally, a good bond between the core and shell results in breakage of the core along with the shell. A comparison of Figs. 3.13, 3.14, and 3.15 leads to the conclusion that there was better bonding of the one unirradiated sphere than the two irradiated ones.

A portion of the graphite powder from each sphere holder was analyzed for uranium and fission products. The powder from sphere 1 contained 7.4×10^{-4}% of the total uranium in the sphere. The uranium content of the powder from spheres 2 and 3 was below limits of detection.

PHOTO 81754

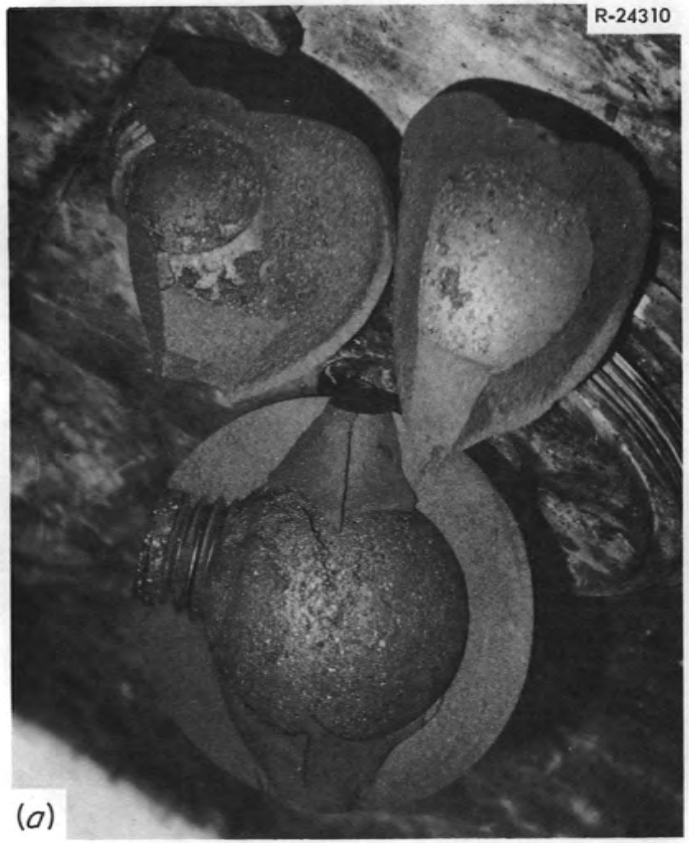

Fig. 3.14. (a) Sphere 2 of Capsule 01A-8 After Failure at a Compression Load of 2550 lb and (b) Sphere 3 After Failure at 1600 lb. 1.4×

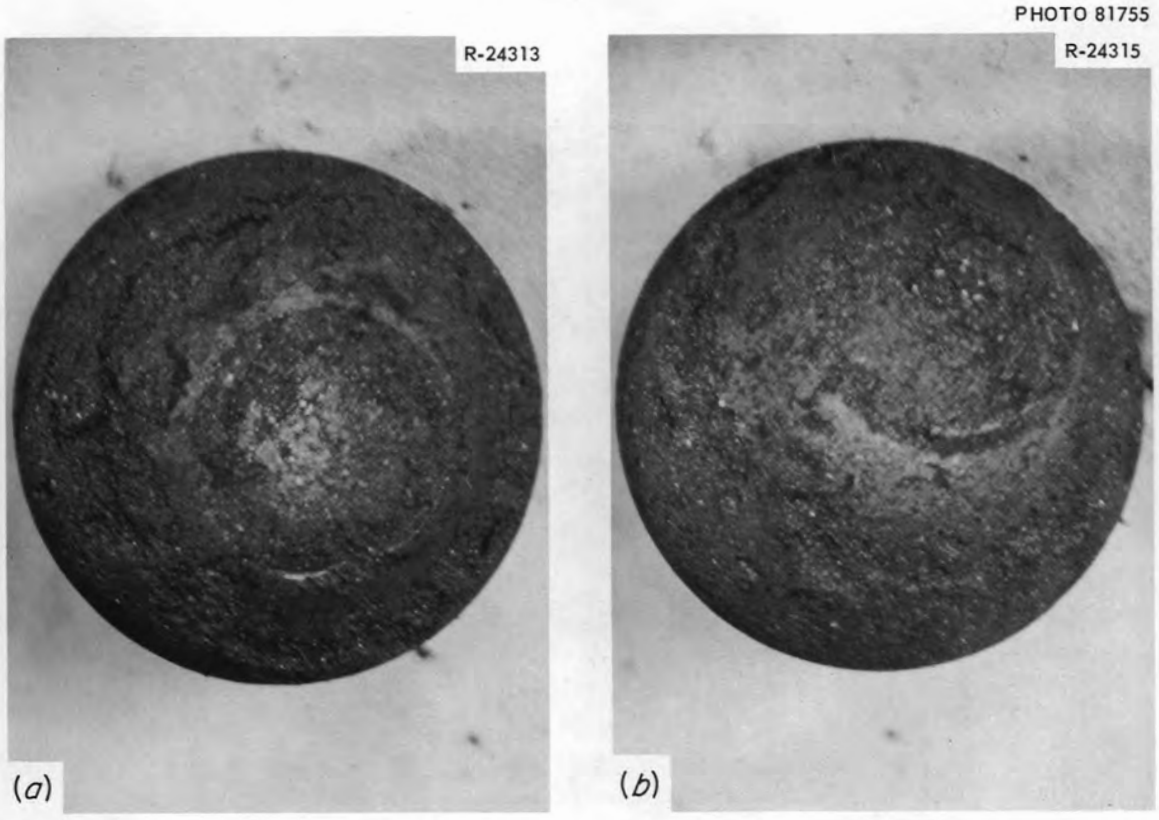

Fig. 3.15. Cores of Spheres 2 and 3 from Capsule O1A-8. (a) Sphere 2. (b) Sphere 3. 1.6×

The results of fission-product analyses of the graphite powder are given in Table 3.13.

Cesium-137 was generally found to have migrated into the graphite powder to a greater extent than the other nuclides. Powder from sphere 2 showed appreciably smaller concentrations of fission products than the powder from the other two spheres, except for ^{137}Cs.

Metallographic sections of an unirradiated control sphere are shown in Fig. 3.16. The fuel particles are duplex-coated UC_2 particles from batch NCC-220. Numerous inclusions, which appear to be graphite, are present in about half the fuel particles, and the particles that contain the inclusions have irregular surfaces that result in an inner coating of varying thickness. The particles that are free of inclusions are smoother than the others and have a thicker inner coating.

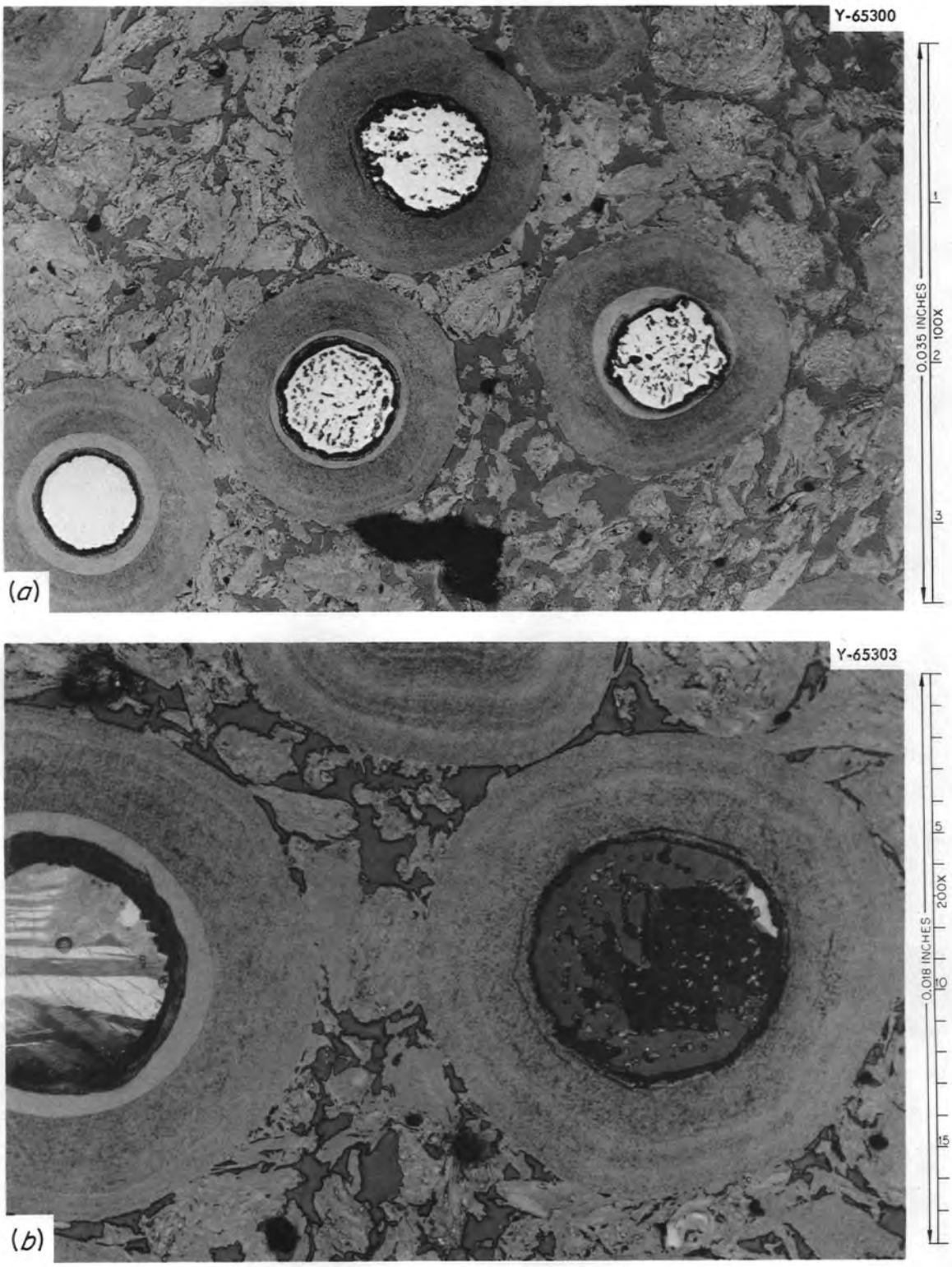

Fig. 3.16. Unirradiated Pyrolytic-Carbon-Coated UC_2 Particles from the Batch (NCC-220) Used in Fueling Spheres 1, 2, and 3 in Capsule O1A-8. These particles are contained in the graphite matrix of an unirradiated sphere. (a) About half the particles contained inclusions, as shown, that varied the thickness of the inner coating. As polished. 100× (b) Etched. 200×

Table 3.13. Fission Products Recovered from Graphite Powder Surrounding Spheres in Capsule O1A-8

Sphere	Fraction of Fission Product Generated Found in Powder					
	^{95}Zr	^{103}Ru	^{106}Ru	^{137}Cs	^{140}Ba	^{144}Ce
	$\times 10^{-6}$	$\times 10^{-6}$	$\times 10^{-6}$	$\times 10^{-6}$	$\times 10^{-6}$	$\times 10^{-6}$
1	2.6	0.9	8.3	7.4	0.7	7.1
2	0.08	0.01	0.08	13.1	0.07	0.15
3	1.5	0.5	7.4	22.3	0.3	2.2

Metallographic specimens were sectioned from each of the three irradiated spheres so as to permit examination of coated particles in the central as well as the peripheral regions of the cores of the spheres. Examination of 173 particles in the specimen from sphere 1 disclosed no failures. Short wedge-shaped fractures were observed in the coatings that originated at the fuel-coating interface and, in a few particles, the fractures extended into the outer coating. This effect was noted only in those particles that contained the inclusions in the fuel. Separation of the inner and outer coating was noted in the particles that were free of inclusions. Two typical particles are shown in Fig. 3.17. No microstructural differences were noted in the coated particles located in the central region as compared with those in the peripheral region of the fueled core.

No failed particles were found of the 176 examined metallographically in the specimen from sphere 2. However, one damaged particle was noted; the outer portion of the coating was broken, as shown in Fig. 3.18. We were unable to determine when the damage occurred, although we feel certain that the damage was not a result of specimen preparation. The microstructural features of the particles examined in this sphere were similar to those of the particles in sphere 1.

No failed particles were found of the 230 particles examined metallographically in the specimen from sphere 3. The microstructural details of the particles from this sphere were similar to those of the particles

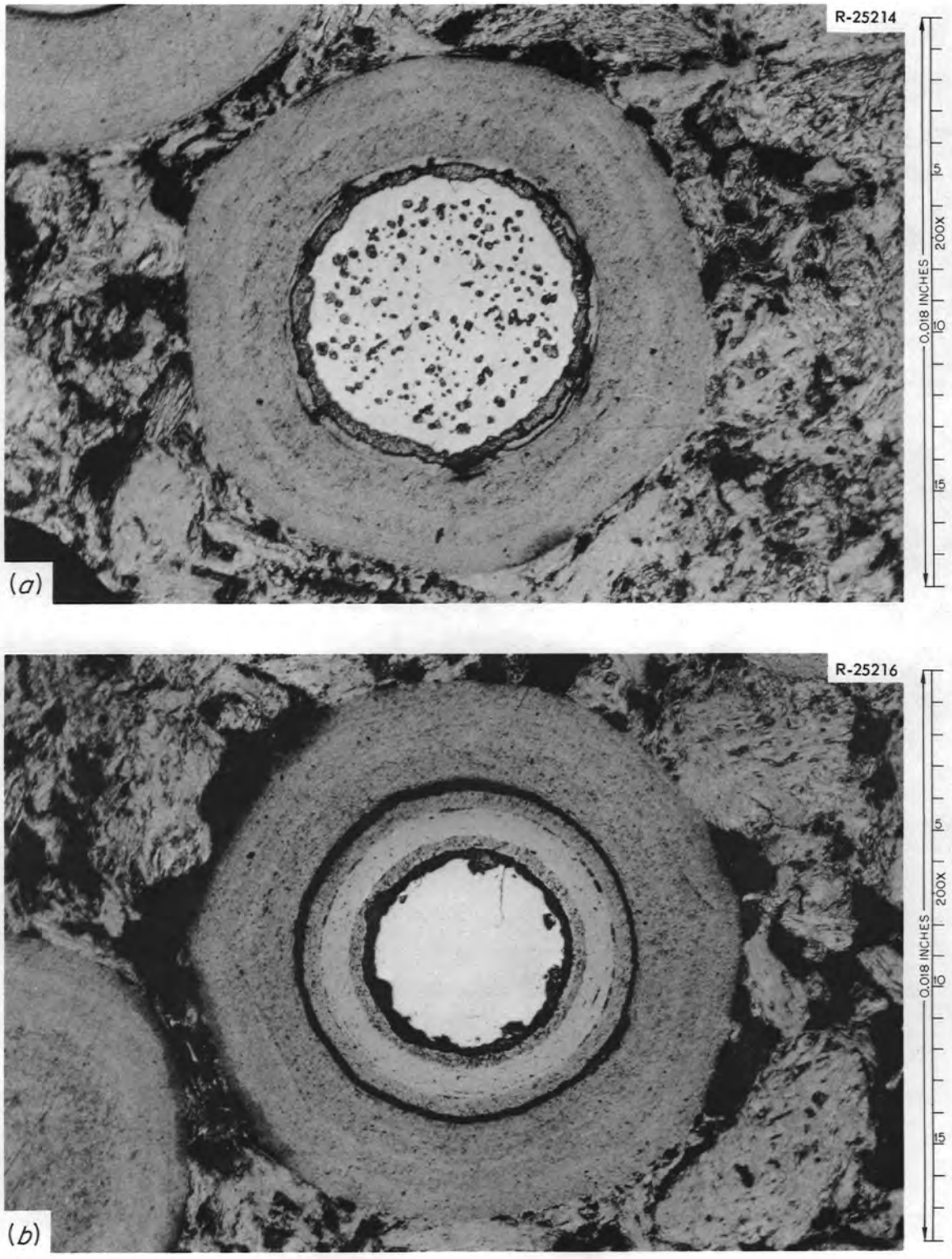

Fig. 3.17. Two Pyrolytic-Carbon-Coated UC_2 Particles from Sphere 1 of Capsule O1A-8. (a) Note the short wedge-shaped fractures that originated at the fuel-coating interface. (b) Typical coated particles that were free of inclusions in the UC_2. As polished. 200×

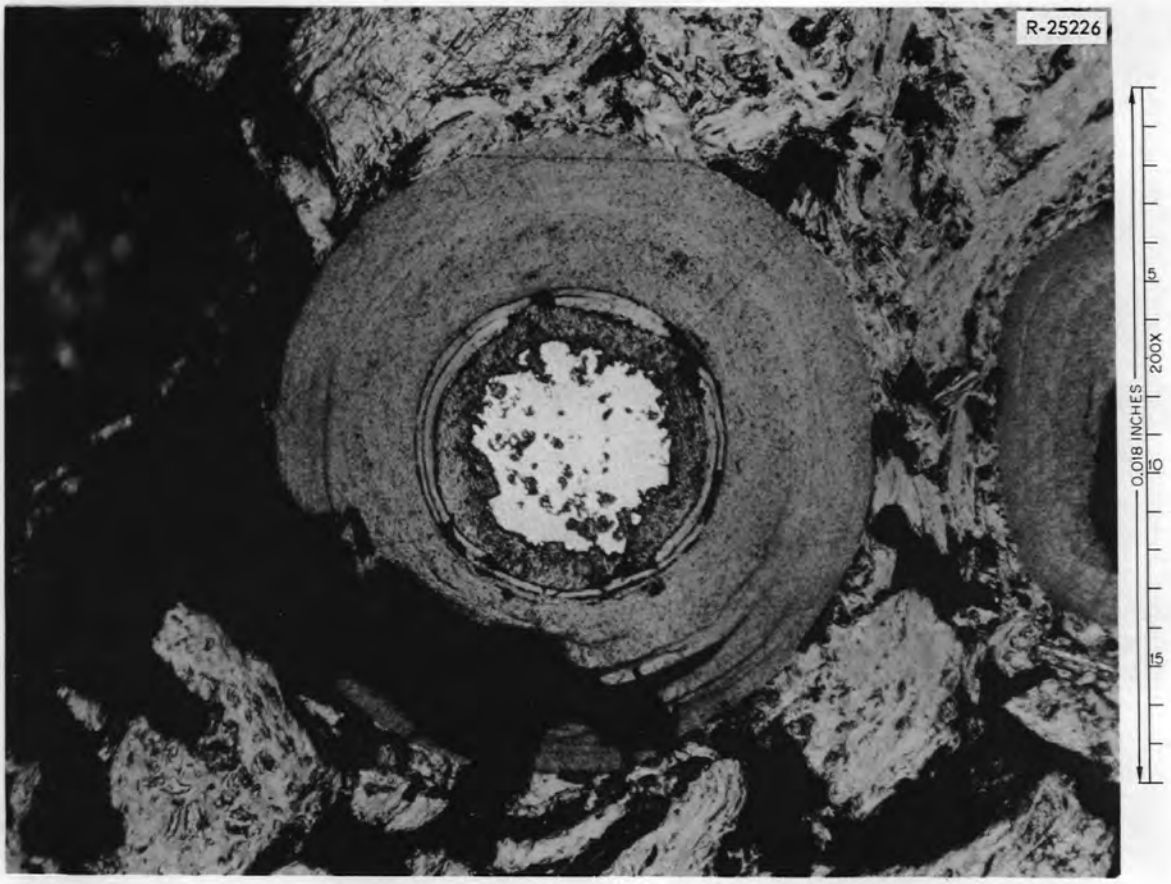

Fig. 3.18. Appearance of the Only Significantly Damaged Coated Particle Found in the 176 Particles Examined in Sphere 2 from Capsule O1A-8. As polished. 200×

in sphere 1, except that the wedge-shaped fractures that extended into the outer coatings were more pronounced. Typical coated particles from sphere 3 are shown in Fig. 3.19.

Fission-Gas Release from AVR Production Particles

P. E. Reagan J. W. Gooch
E. L. Long, Jr. J. G. Morgan

Capsule B9-28, which contained pyrolytic-carbon-coated thorium–uranium carbide particles from batch NCC-222, is being irradiated at 1300°C and has accumulated 1.2 at. % heavy-metal burnup. The particles are a sample of production particles for the AVR. An unirradiated

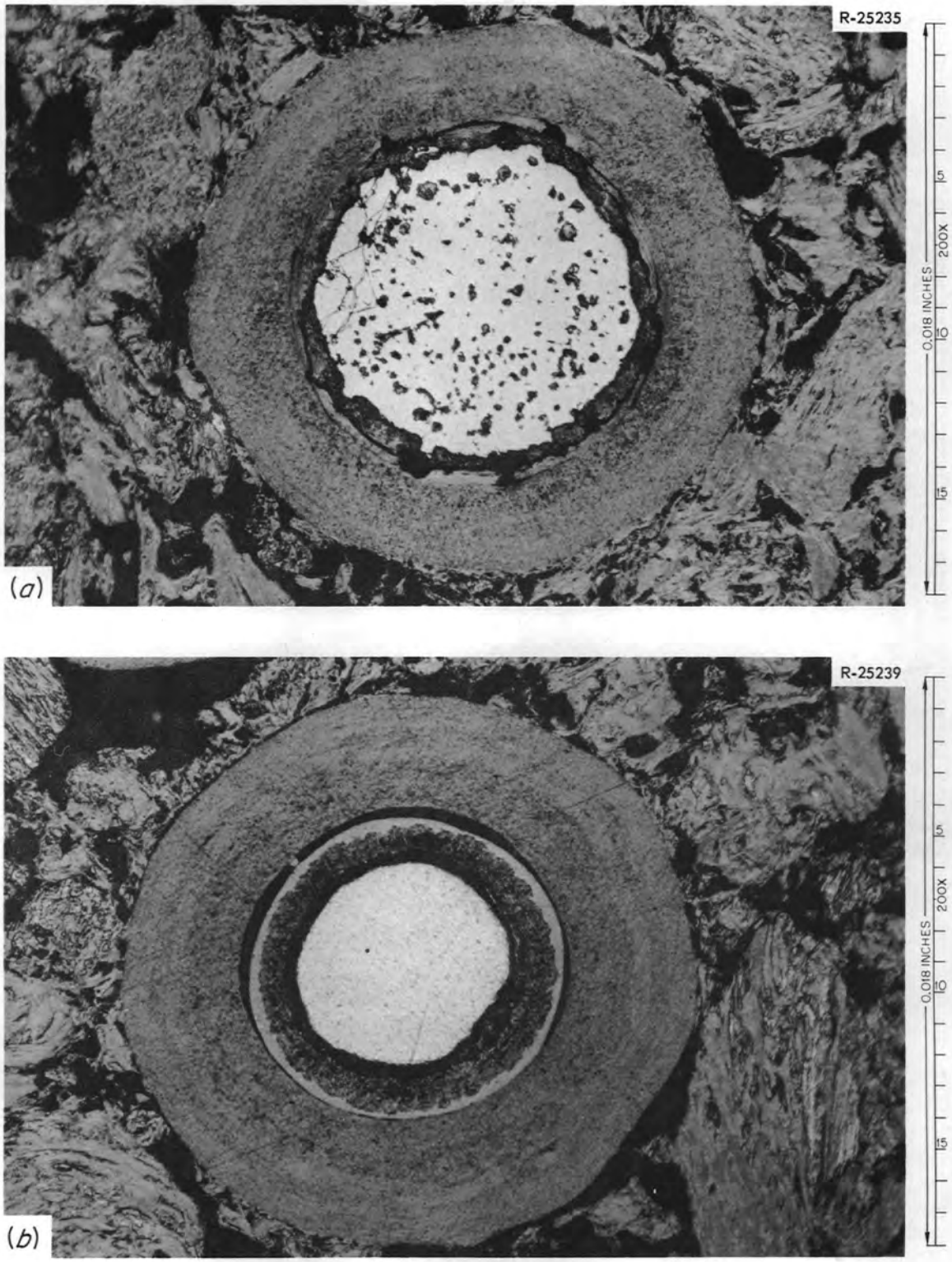

Fig. 3.19. Pyrolytic-Carbon-Coated UC_2 Particles from Sphere 3 of Capsule 01A-8. (a) Typical coated particle that contained inclusions in the UC_2. (b) Typical coated particle that contained inclusion-free UC_2. As polished. 200×

particle from batch NCC-222 is shown in Fig. 3.20. The fission-gas release rates have remained nearly constant, and there have been no bursts of fission gas or any other indications of coating failures.

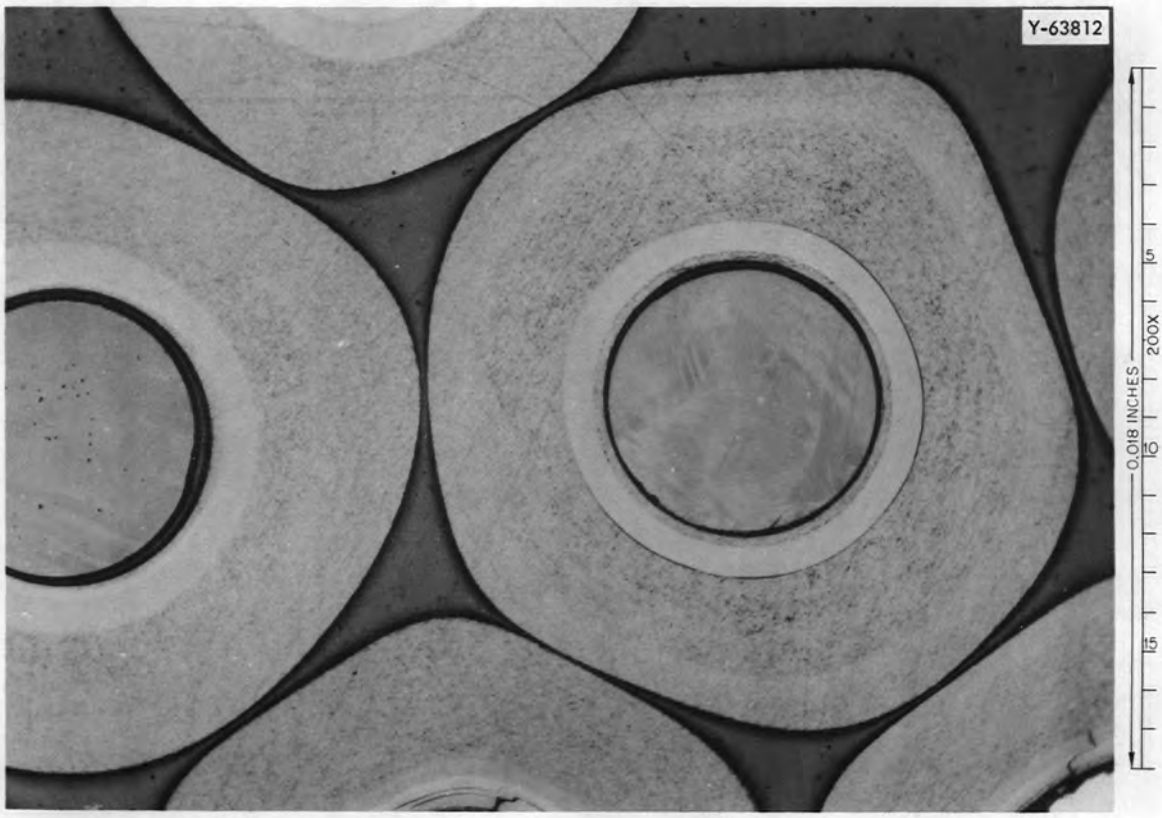

Fig. 3.20. Unirradiated Pyrolytic-Carbon-Coated Thorium Uranium Carbide Particle from Batch NCC-222. As polished. 200×

Evaluation of Fueled-Graphite Spheres

J. L. Scott

The results of thermal conductivity calculations on instrumented 6-cm-diam fueled-graphite spheres, which were reported previously,[20] showed

[20] J. L. Scott and J. W. Prados, Thermal Conductivity of Fueled-Graphite Spheres During Irradiation, pp. 34–36, GCRP Semiann. Progr. Rept. Mar. 31, 1965, USAEC Report ORNL-3807, Oak Ridge National Laboratory.

an interesting anomaly. In two of three spheres tested, the apparent thermal conductivity was unaffected by radiation, whereas the third sphere showed a definite reduction in the apparent thermal conductivity with increasing irradiation dose. This effect is shown graphically in Fig. 3.21. One of the two spheres that was unaffected by irradiation, sphere 08-8, had a machined ATJ graphite shell. The other, sphere 08-7, had a molded unfueled shell. The sphere that showed the reduction in the apparent conductivity, sphere 05-7, also had a machined ATJ graphite shell. In addition, this sphere was irradiated at a significantly higher temperature than the others.

We postulate that the reduction in the apparent thermal conductivity was the result of differential shrinkage between the molded fueled core and the machined unfueled shell. This effect would not be expected for an all-molded sphere, such as sphere 08-7, because the shrinkage rate of the shell should be about the same as that of the core. The fact that the effect was observed in one sphere with a machined shell and not the other is attributed to the higher operating temperature of sphere 05-7. Above 1000°C an increasing shrinkage rate is expected with increasing temperature.

Reexamination of the dimensional data for irradiated fueled-graphite spheres substantiates our hypothesis. A plot of the volume changes in

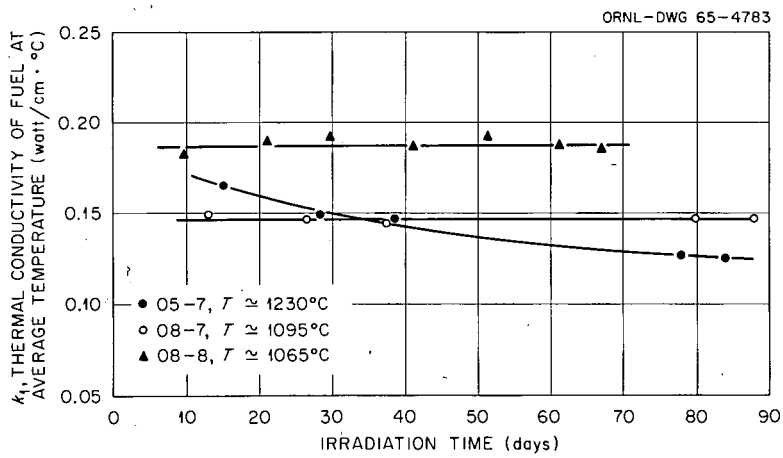

Fig. 3.21. Effect of Irradiation Time on the Apparent Thermal Conductivity of Fueled-Graphite Spheres.

1 1/2-in.-diam spheres as a function of neutron dose above 0.18 Mev is shown in Fig. 3.22. The spheres were irradiated at surface temperatures in the range 600 to 800°C. The volume changes were computed from the dimensional changes by use of the following equation:

$$\text{Volume change } (\%) = \% \frac{\Delta P}{P} + 2 \times \% \frac{\Delta E}{E} , \qquad (1)$$

where $\% \Delta P/P$ is the percentage change in polar diameter and $\% \Delta E/E$ is the percentage change in the equatorial diameter. After an initial volume increase at low doses, molded spheres with and without unfueled shells showed an approximately linear decrease in volume with increasing dose. Within the scatter of the data, there was no significant difference between spheres with molded shells and those without shells. The scatter is attributed to difference in matrix composition and baking temperature.

Spheres with machined shells showed a significantly lower rate of volume decrease with increasing dose. The scatter in the data is also significantly lower. Thus, definite evidence of differential shrinkage between the molded core and a fully graphitized machined shell is indicated.

The data are in excellent agreement with the results of Yoshikawa[21] for lampblack-based graphites annealed at different temperatures. His results showed that lampblack-based carbon processed at 1400°C shrinks

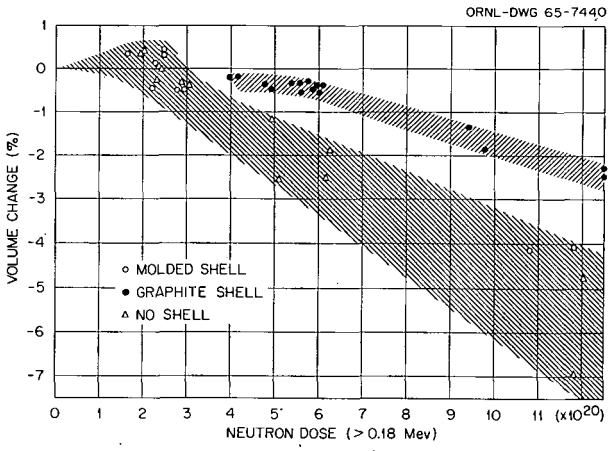

Fig. 3.22. Irradiation-Induced Volume Changes in 1 1/2-in.-diam Fueled-Graphite Spheres in Eight-Ball Capsules in the ORR.

at a much higher rate upon irradiation at 650°C than does the same material after annealing at 3000°C. The lampblack-based carbon annealed at 3000°C, in turn, shrinks at a much higher rate than a fully graphitized CSF-grade graphite; thus, an increased shrinkage rate is to be expected with a lower baking temperature or a higher fraction of ungraphitized carbon. The baking temperatures of the molded regions of the fueled spheres were limited to a maximum of 1900°C to avoid fuel migration through particle coatings. Thus, the molded cores would be expected to shrink at a higher rate than the graphite shells, which are baked at temperatures near 3000°C.

One consequence of the differential shrinkage between the molded core and the graphitized unfueled shell is the reduction of crushing strength as a result of irradiation. To check this point, we crushed a number of control spheres to compare their crushing loads with those for irradiated spheres. Our results are given in Table 3.14. The crushing strength of spheres having no unfueled shell was not reduced significantly by irradiation and even appeared to increase with increasing fast-neutron dose. Spheres with machined shells, on the other hand, show a marked reduction in the crushing strength, particularly at the highest integrated fast-neutron doses. Some reduction is also noted for spheres with molded shells, but the data are too limited to permit conclusions. For machined-shell spheres, crushing strength data support the hypothesis of differential shrinkage between molded cores and graphite shells.

The appearance of the unirradiated spheres after crushing was interesting. Typical specimens are shown in Figs. 3.23 through 3.26. Figure 3.23 shows sphere NCF-S25-V12, which had no unfueled shell. Sphere 3M-S8-19, which had a molded unfueled shell, had a similar fracture pattern that was indicative of good bonding between the core and shell, as shown in Fig. 3.24. Figures 3.25 and 3.26 show two spheres with fully graphitized machined shells that were cemented to molded cores. It is evident that in the as-fabricated condition the core and the shell were poorly bonded; this is attributed to a problem with the P 514 cement.

---

[21] H. H. Yoshikawa, High-Temperature Radiation Effects in Lampblack-Based Graphite, Carbon, 1: 201–207 (1964).

Table 3.14. Comparison of Crushing Loads of Irradiated and Unirradiated 1 1/2-in.-diam Fueled-Graphite Spheres

Sphere Designation	Unfueled Shell		Irradiation Dose, E > 0.18 Mev (neutrons/cm^2)	Crushing Strength (lb_f)
	Thickness (in.)	Type		
			$\times 10^{20}$	
3M-S10-5	0		0	2490
3M-S10-6	0		0	2340
3M-S10-14	0		0	2610
3M-S10-8	0		5.1	2040
3M-S10-10	0		6.2	1945
GA-S17-4	0		0	2800
GA-S17-10	0		0	2240
GA-S17-7	0		0	2790
GA-S17-2	0		6.2	2025
NCF-S24-L4	0		0	1560
NCF-S24-L1	0		0	2280
NCF-S25-V9	0		0	2010
NCF-S25-V6	0		0	1095
NCF-S24-L3[a]	0		12.0	2650
NCF-S25-V10[a]	0		11.8	3050
3M-S13-1	0.25	Molded	0	2220
3M-S13-2	0.25	Molded	0	2040
3M-S13-5	0.25	Molded	0	2320
3M-S13-14[a]	0.25	Molded	10.8	1250
GA-S6-8	0.2	ATJ	0	1575
GA-S6-4	0.2	ATJ	0	1880[b]
GA-S14-4	0.2	ATJ	5.6	490
GA-S14-3	0.2	9050	6.1	1270
GA-S14-5	0.2	ATJ	5.8	1290
GA-S14-6	0.2	ATJ	4.1	1000
GA-S14-3A[a]	0.2	ATJ	9.8	225
3M-S8-19	0.2	ATJ	0	1750
3M-S8-15	0.2	ATJ	0	1220
3M-S13-7[a]	0.2	ATJ	12.5	900
3M-S13-9[a]	0.2	ATJ	9.4	275

[a]Sphere irradiated in capsule F1-8B-5. See preceding section of this chapter for additional postirradiation examination results.

[b]The sphere was crushed along the polar axis. All other spheres with machined shells were crushed in a direction normal to the polar axis. This latter orientation is expected to be the weaker for elements with machined shells.

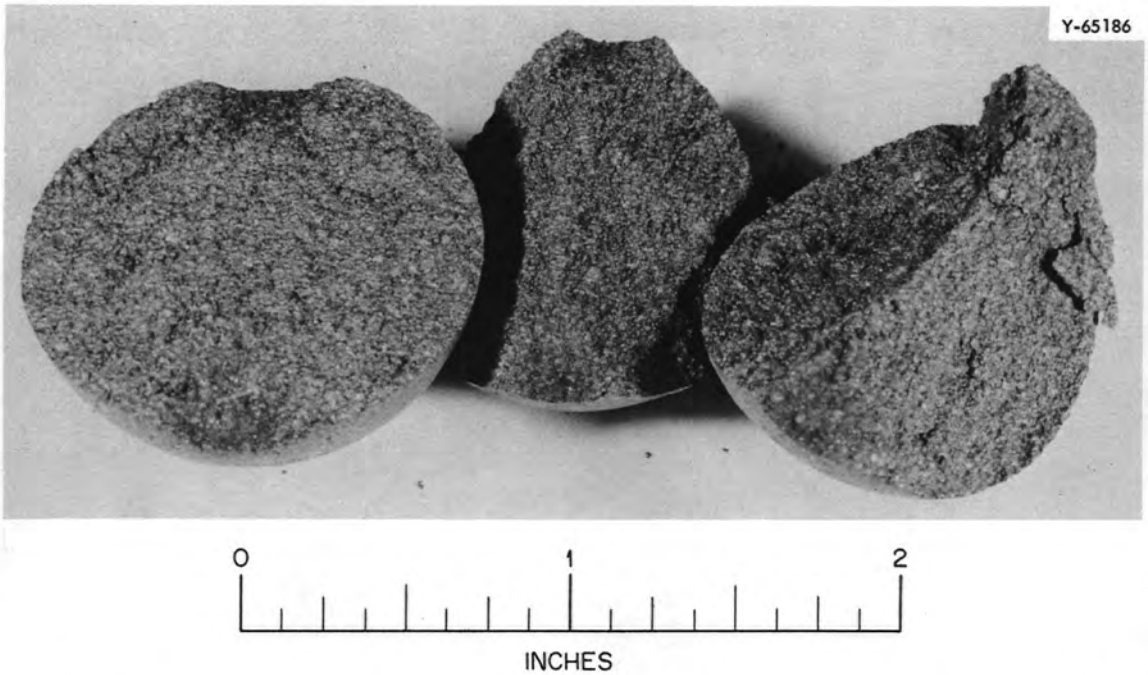

Fig. 3.23. Fueled-Graphite Sphere with No Shell (NCF-S25-V12) After Crushing.

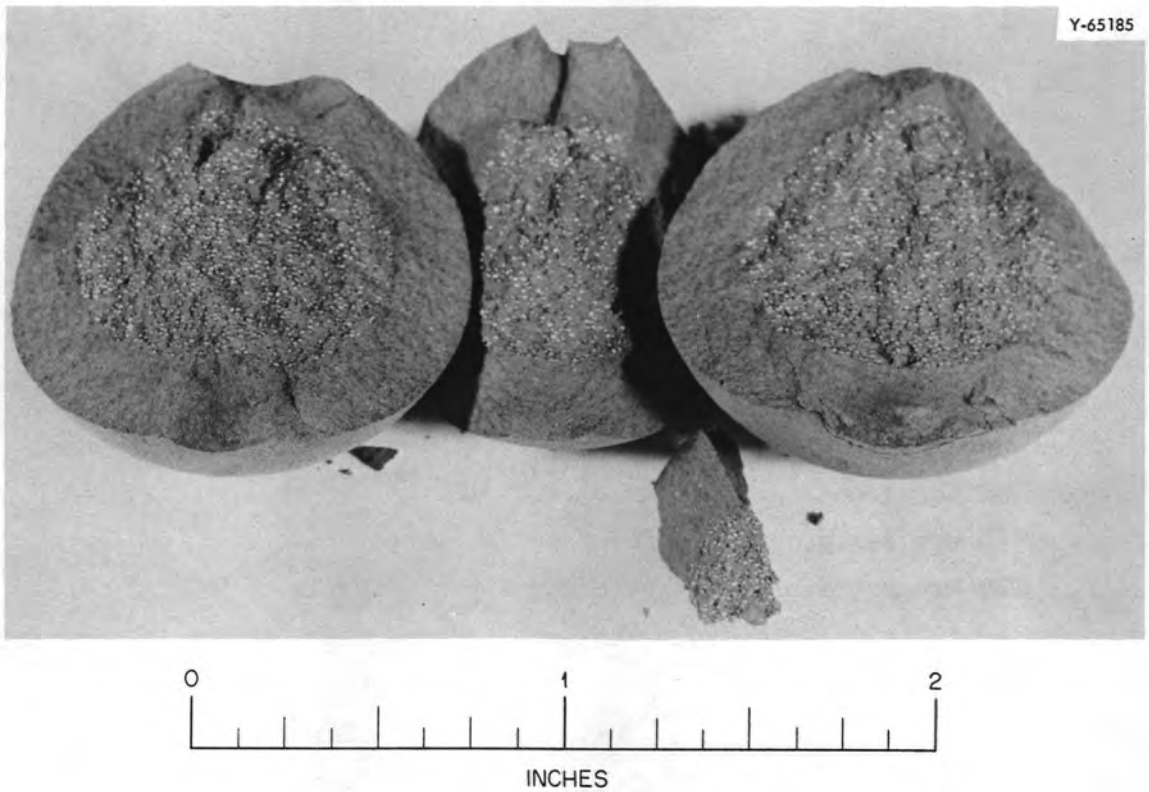

Fig. 3.24. Fueled-Graphite Sphere with a Molded Unfueled Shell (3M-S8-19) After Crushing.

Fig. 3.25. Fueled-Graphite Sphere (3M-S8-12) with a Machined-Graphite Shell After Crushing. Note poor bonding between core and shell.

Further developmental work on cements is needed, if the machined shell concept is to be considered further.

Reference design spheres for the AVR reactor have machined-graphite shells but are not fabricated by cementing the shells to molded cores. Instead a mix is injected into the machined-graphite shells. An end cap is then screwed into the hole provided for injection of the mix and the element is subsequently baked. Data on the crushing strength of AVR spheres, given in the preceding section of this chapter, show a mild reduction of the crushing strength with irradiation. Unfortunately, we

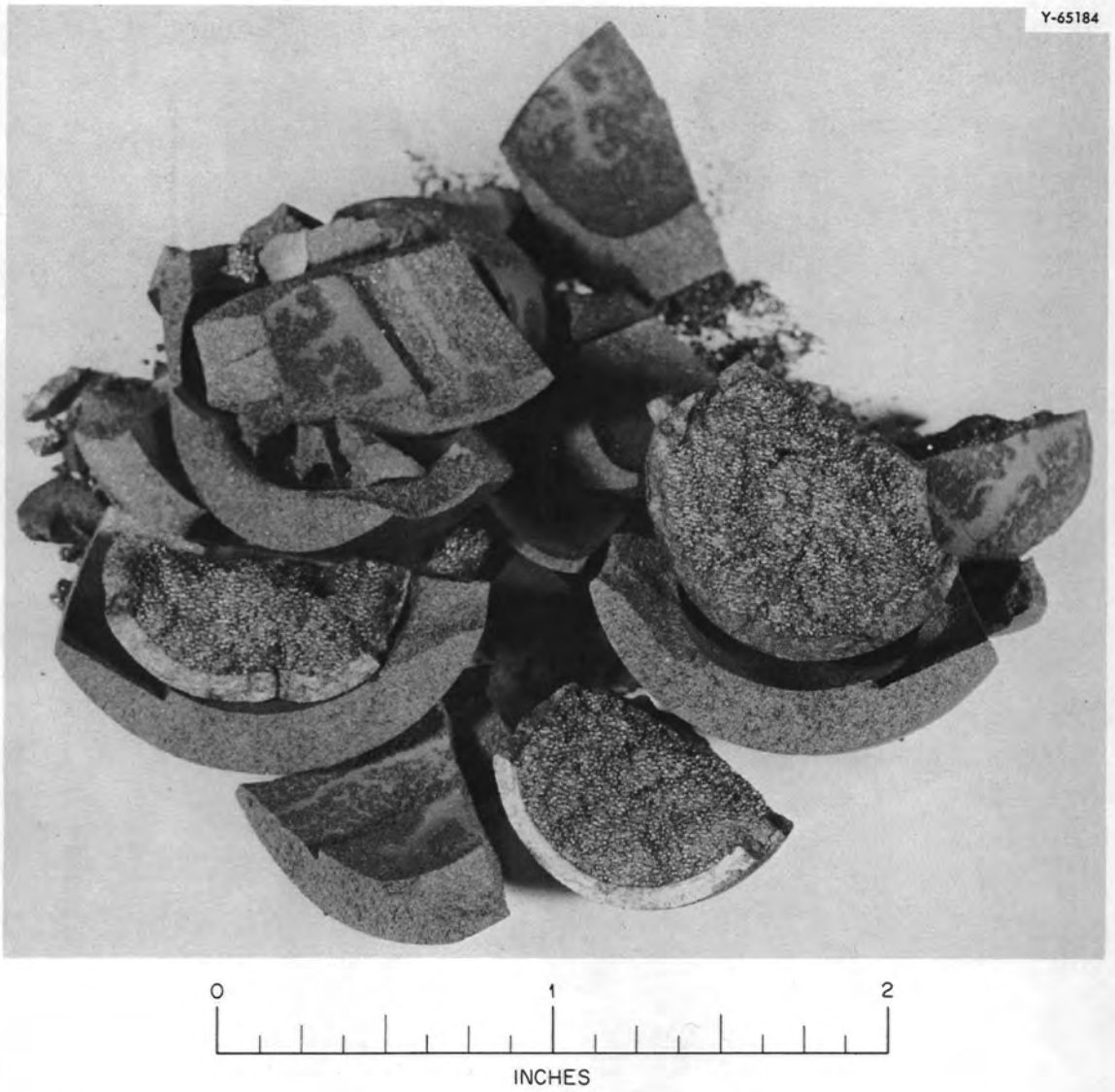

Fig. 3.26. Fueled-Graphite Sphere (GA-S6-7) After Crushing. Bonding is somewhat improved over that of sphere 3M-S8-12 (Fig. 3.25), but it is still poor.

do not have a good estimate of the damage flux in ORR poolside positions, where the AVR spheres were irradiated. Since the poolside positions are outside the reactor core, most of the neutrons are thermalized. The fast flux is about 20% of the thermal flux or, for the capsule where these spheres were irradiated, about 8×10^{19} neutrons/cm^2 ($E > 0.18$ Mev). To this, the effects of the very energetic neutrons produced by fissioning

within the fueled spheres themselves must be added. To date, the fast flux due to these neutrons has not been determined.

The appearance of an unirradiated AVR sphere after crushing is shown in Fig. 3.13. There was poor bonding between the core and the shell and between the threaded plug and the shell.

4. INVESTIGATIONS OF MODERATOR MATERIALS

J. H. Coobs H. C. McCurdy
G. M. Watson F. J. Witt

Thermal Conductivity of AGOT Graphite

J. P. Moore R. S. Graves

We are studying the high-temperature thermophysical properties of some grades of graphite that are used or proposed for nuclear components; all these grades are anisotropic due to the hexagonal structure and to preferred orientations developed during extrusion. We found that the total thermal resistivity of an AGOT specimen perpendicular to the extrusion direction could be described to ±0.5% by

$$R = 0.1935 + (1.6246 \times 10^{-3})\ T - (1.229 \times 10^{-7})\ T^2 ,$$

where T is in °K and R is in cm·°C/w. The thermal conductivity of this specimen in this direction was 30% greater at 50°C than that of the CGB graphite that we previously measured,[1] but it was only 5% greater at 900°C. Since the AGOT specimen was significantly less dense than the CGB, the difference in thermal conductivity must be attributed to a preferred orientation effect. These AGOT graphite results form the base-line comparison for low-temperature thermal conductivity measurements on the AGOT graphite specimens to be obtained for testing during the EGCR graphite surveillance program.

Dimensional Stability of AGOT Graphite

D. G. Harman

Structural graphite, because of its pronounced anisotropy, shows dimensional instabilities when subjected to thermal cycling. This behavior is related to the anisotropic thermal expansion and to the deformation characteristics of the material.

---

[1]J. P. Moore and T. G. Godfrey, Thermal Conductivity of UO_2, pp. 199–200, Metals and Ceramics Div. Ann. Progr. Rept. June 30, 1964, USAEC Report ORNL-3670, Oak Ridge National Laboratory.

In our study of AGOT, a coarse-grained nuclear-grade graphite, we thermally cycled a specimen at temperatures up to 1800°C. A constant tensile stress of 600 psi was applied to the 0.5-in.-diam tensile specimen while it was being heated by an induction-heated tantalum susceptor. The graphite was protected from oxidation by flowing argon. A 10-in. section of the specimen was heated to temperature, held for 15 min, and cooled to room temperature. The strain was continuously monitored by recording the output of a transducer fixed to the bottom pull rod.

The plastic strain due to the thermal cycle was determined by comparing the room-temperature strain measured before the thermal cycle with that measured after the thermal cycle. The plastic strain obtained with a single specimen is shown as a function of maximum temperature in Fig. 4.1. The spread in the data is shown by the vertical lines, and the

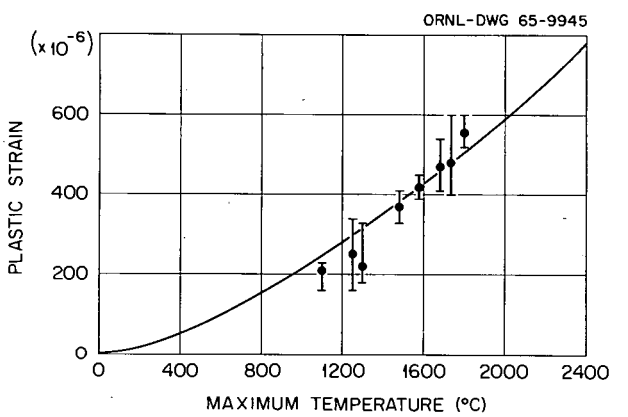

Fig. 4.1. Plastic Strain in AGOT Graphite Due to Thermal Cycling from Room Temperature with 600-psi Applied Stress. Vertical lines indicate data spread and filled circles represent average values; solid line represents theoretical relationship.

filled circles are the average values. The specimen was returned to its initial state by a high-temperature anneal after each cycle. Without this anneal, no plastic strain was noted beyond the first cycle.

The macroscopic stress-strain behavior of graphite is given according to Jenkins and Williamson[2] by

[2]G. M. Jenkins and G. K. Williamson, J. Appl. Phys., 34: 2837–2841 (1963).

$$\epsilon = A\sigma + B\sigma^2 , \tag{1}$$

where A is the elastic compliance at infinitely small stresses (the reciprocal of the elastic modulus) and B is a parameter measuring the extent of the plastic behavior. By including similar unloading and reloading relationships, the plastic strain due to thermal cycling is predicted by Jenkins and Williamson as

$$\epsilon_{plastic} = 2B\sigma_m \Delta\sigma - B\sigma_m^2 \qquad \text{for } \Delta\sigma > 2\sigma_m , \tag{2}$$

where σ_m is the applied stress and $\Delta\sigma$ is the change in local stress due to thermal effects.

For the tensile situation the thermal stress can be approximated as

$$\Delta\sigma = (\alpha_c - \alpha_a)E \frac{\Delta T}{2} ,$$

where α_c and α_a are the expansion coefficients of the individual crystallites in the c and a directions, E is the elastic modulus, and ΔT is the temperature cycle.

From the data of Mason and Knibbs[3] and that tabulated by Carbon Products Division of Union Carbide Corporation,[4] $(\alpha_c - \alpha_a)$ is given by $(3.0 \times 10^{-6}) + (4.45 \times 10^{-10})$ T, and E is given, in psi, by $(1.5 \times 10^{-6}) + (2.0 \times 10^{-4})$ T. The expansion coefficient data are macroscopic and thus account for the presence of microcracks. The parameter B has been measured[5] to be 0.7×10^{-10} $(\text{psi})^{-2}$ for AGOT graphite. With these values and Eq. (2), we obtain the relationship shown as a solid line in Fig. 4.1.

The fact that the data indicate a steeper slope than that of the theoretical curve suggests that the B parameter changes with temperature (which could be caused by crack closure, for example) or that the model proposed by Jenkins and Williamson does not apply.

---

[3] I. B. Mason and R. H. Knibbs, J. Nucl. Energy Pt AB, 18: 311–329 (1964).

[4] The Industrial Graphite Engineering Handbook, Carbon Products Division, Union Carbide Corporation (1959).

[5] C. R. Kennedy, unpublished data.

Creep of Graphite Under Irradiation

C. R. Kennedy

Graphite grades CGB and AGOT have been creep tested under irradiation from 130 to 370°C. Some details of the parabolic beam creep specimens, experimental procedures, and data from creep tests at the higher temperatures were reported previously.[6]

The creep curves obtained from the latest experiment at temperatures of 130 to 180°C are given in Figs. 4.2 and 4.3. As shown in the figures, the stresses were altered during the experiment to determine the effect of variable stress. The general shapes of the curves are much different from those obtained previously;[6] however, the deflection readings obtained from the creep specimens are actually sums of both creep deformation and differential growth. The differential growth that opposes the creep deformation was caused by a 10% flux gradient across the creep specimen. While this differential growth was small and insignificant at the higher test temperatures, it is quite large and must be considered at the present test temperatures.

[6]C. R. Kennedy, In-Pile Creep of Graphite, pp. 145–150, GCRP Semiann. Progr. Rept. Mar. 31, 1965, USAEC Report ORNL-3807, Oak Ridge National Laboratory.

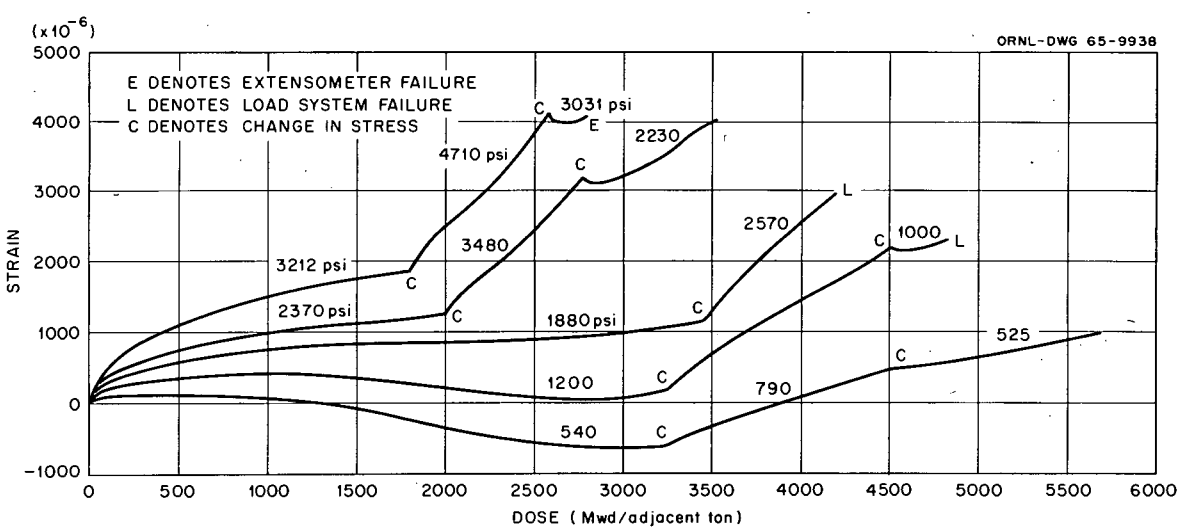

Fig. 4.2. Creep of EGCR-Type AGOT Graphite Under Irradiation at 130 to 180°C.

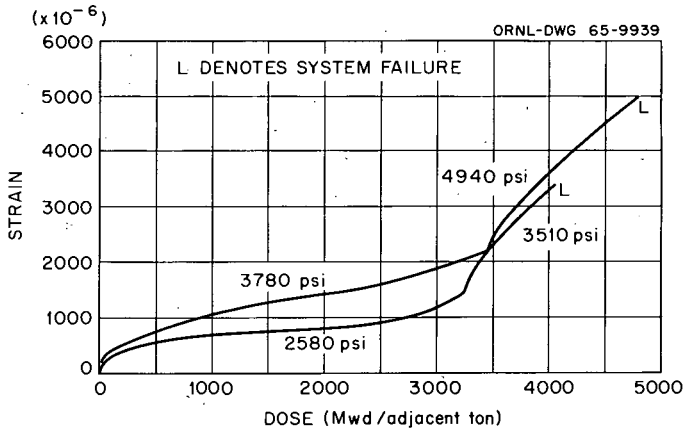

Fig. 4.3. Creep of CGB Graphite Under Irradiation at 150 to 180°C.

The differential growth was separated from the total deformation by two methods. First, the total deformation was plotted versus stress at 100-Mwd/adjacent ton dose intervals. The deformation extrapolated to zero stress was the deflection caused by differential growth. A second method was required after the stress levels were altered in the experiment. This method was essentially the same, except that tangent deformation rates were used in place of the total deformation. The tangent deformation rates were also plotted versus stress at 100-Mwd/adjacent ton dose intervals. The slope is the creep coefficient and the zero intercept is the deflection rate due to the differential growth.

The results of these two methods are given in Figs. 4.4 and 4.5. The curves for the AGOT and CGB grades show very marked similarity, with CGB graphite having a lower creep rate. The very important difference from previous results is the variation of creep coefficient with dose.

The change in creep coefficient with dose was predicted by Hesketh[7] based on the Cottrell model of continuous yielding. The implication is that cooling or Mrozowski cracks reduce the internal stress intensity produced by the anisotropic growth of the crystallites. As the cracks are closed, this stress-relaxation process may cease and thus create higher internal stresses, which should increase the creep rate. The dose required to close the cracks will vary with the growth rate of the crystallites and thus with temperature. The dose level required for crack

[7]R. V. Hesketh, Phil. Mag., 11: 917–927 (1965).

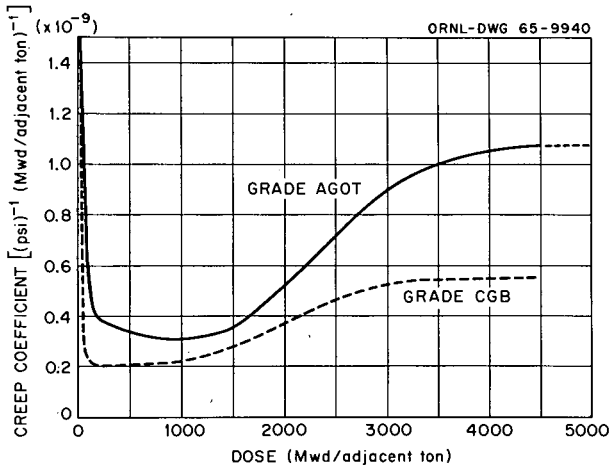

Fig. 4.4. Creep Coefficient of Graphite Under Irradiation at 130 to 180°C.

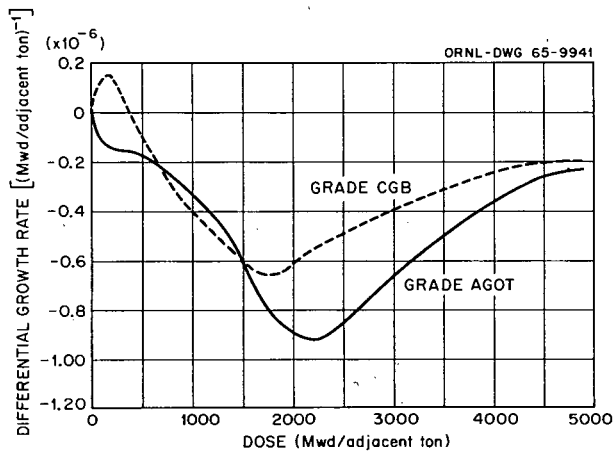

Fig. 4.5. Differential Growth Rate of Creep Specimens at 130 to 180°C.

closure equivalent to 2×10^3 Mwd/adjacent ton at 150°C would be about 3×10^4 Mwd/adjacent ton at 400°C and 2.5×10^4 Mwd/adjacent ton at 300°C.

The previous creep specimens did not receive neutron dosages of this level and thus did not demonstrate a change in the creep coefficient. There are, however, recent creep results[8,9] at 400°C to dose levels of 10^5 Mwd/adjacent ton. These creep test data should verify this concept, but on the contrary they indicate a continuous creep-rate coefficient. Also in conflict with this concept are data from thermal-cycling tests

by Harman, reported in part in the preceding section, which show plastic yielding from 1000 to 2000°C without an abrupt change due to crack closure. The explanation of increased creep rate by crack closure does not appear to be verified and is therefore subject to doubt. These results do not detract from the Cottrell model for creep; they only cast doubt on the effect of crack closure on stress relaxation.

The concept of the Cottrell model for creep does offer a second possible explanation for the creep-rate variation. The rate of continuous yielding or creep depends on the reistance of the material to deformation. Since the elastic modulus measures the dislocation mobility in graphite, the creep coefficient should be inversely proportional to the elastic modulus. Figure 4.6 demonstrates very close agreement with this for six grades of graphite. Also, at the lower temperature the elastic modulus increases sharply with dose and then decreases to a lower value almost

---

[8]B. S. Gray, J. E. Brocklehurst, and A. A. McFarlane, Irradiation Induced Plasticity in Graphite, Paper 182, presented at Seventh Biennial Conference on Carbon, Case Institute of Technology, Cleveland, June 21–25, 1965.

[9]A. H. Perks and J. H. W. Simmons, Dimensional Changes and Radiation Creep of Graphite at Very High Neutron Doses, Paper 188, presented at Seventh Biennial Conference on Carbon, Case Institute of Technology, Cleveland, June 21–25, 1965.

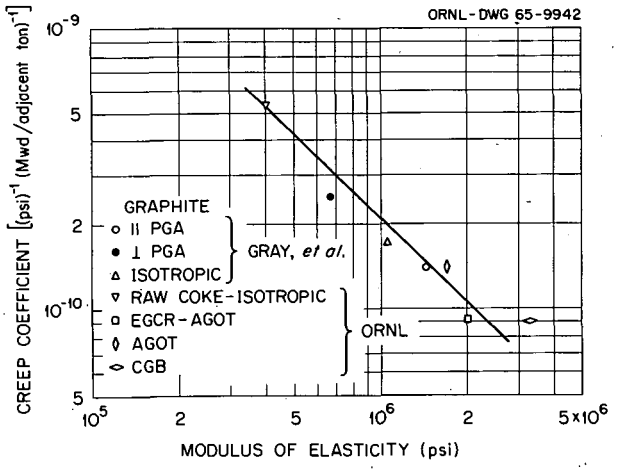

Fig. 4.6. Relationship of the Creep Coefficients of Various Grades of Graphite to Young's Modulus at 400°C.

equal to the high-temperature value, as shown in Fig. 4.7. We would therefore expect that the lower initial creep-rate coefficient is a result of increased strength, as evidenced by the modulus changes. If this is the proper analysis of the variation in creep coefficient, the later creep coefficient obtained at higher doses is the value that should be compared with the higher temperature data. However, if the proper analysis is based on crack closure, the initial lower value of the creep coefficient should be compared with the higher temperature data.

The variation of creep coefficient with temperature is shown in Fig. 4.8. This figure includes, for comparison, both the initial and final

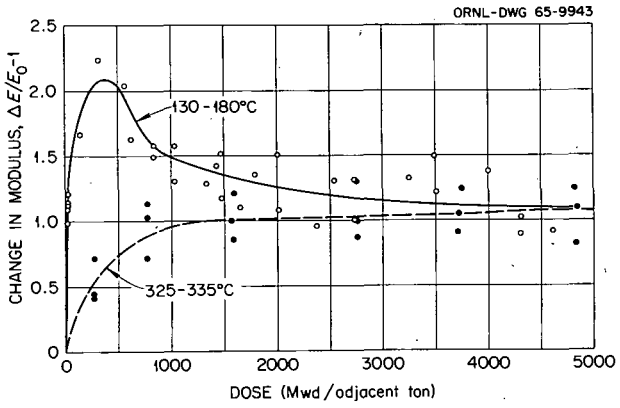

Fig. 4.7. Effect of Irradiation on the Modulus of Elasticity of EGCR-Type AGOT Graphite.

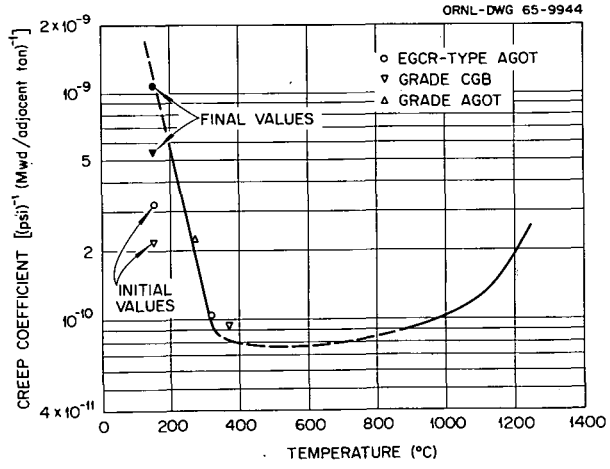

Fig. 4.8. Effect of Temperature on the Irradiation Creep of Graphite. The curve is based on the Cottrell model.

values obtained at the lower temperature. Regardless of which values are used, the data appear to support a Cottrell model for the creep of graphite. If the higher values are used, the Cottrell model appears to be quite accurate; however, if the lower values are used, the Cottrell model has to be modified to some degree.

These results help relieve our concern over the stress intensity generated by differential growth in moderator structures. That is, as the growth rates increase, the creep rate coefficient also increases, so creep compensates for differential growth by reducing stress intensity. These experiments have also demonstrated a significant increase in strain absorption without fracture. Several of the specimens absorbed creep strains of greater than 0.6% and total strain of greater than 0.8%. These values are considerably greater than obtained out of pile but are not quite as significant as the 1.5 to 2% tensile strains obtained by Perks and Simmons[9] for PGA graphite. Apparently strains of this magnitude can be sustained without loss of the mechanical integrity of the material. The strain limit has not yet been reached.

Deposition of Carbon on ATJ Graphite

L. G. Overholser J. P. Blakely

Experimental results obtained from studies of the oxidation of ATJ graphite by low concentrations of water vapor and carbon dioxide in flowing helium at a total pressure of 1 atm were presented previously.[10,11] Strong retardation of the H_2O-graphite reaction by hydrogen and carbon monoxide was noted. Prior to concluding the experiments with ATJ graphite, brief studies were carried out using methane additions to ascertain whether methane also retarded the H_2O-graphite reaction. Some

[10] L. G. Overholser and J. P. Blakely, Oxidation of ATJ Graphite by Low Concentrations of Oxidants in Helium, pp. 161–167, GCRP Semiann. Progr. Rept. Sept. 30, 1964, USAEC Report ORNL-3731, Oak Ridge National Laboratory.

[11] L. G. Overholser and J. P. Blakely, Oxidation of ATJ Graphite by Low Concentrations of Oxidants in Helium, pp. 150–155, GCRP Semiann. Progr. Rept. Mar. 31, 1965, USAEC Report ORNL-3807, Oak Ridge National Laboratory.

experiments also were performed in which methane was added to helium in the absence of water vapor to establish cracking rates for methane. Comparison of these results with those obtained in the presence of water vapor was expected to indicate the effect of water vapor on the deposition of carbon. A brief study was also made of the stability of helium-carbon monoxide mixtures in contact with ATJ graphite. All studies were made with a 1-in.-diam sphere of ATJ graphite in the equipment used previously.[10]

Results obtained from runs with various methane—water vapor mixtures are listed in Table 4.1. Included are (1) the loss of carbon by reaction with water vapor, as calculated from the $CO + CO_2$ concentration found in the effluent gases, (2) the carbon formed by cracking of methane, as calculated from the hydrogen produced by the reaction $CH_4 \rightleftharpoons C + 2H_2$ (total hydrogen less that formed by water vapor reaction), (3) the net gain or loss of carbon from these processes, and (4) the weight change recorded by the analytical balance. Weight losses calculated from $CO_2 + CO$ concentrations show that the H_2O-graphite reaction is retarded by the addition of methane, although to a lesser degree than by an equal concentration of hydrogen.[11] A continuous increase in the amount of carbon deposited with increasing methane concentration is evident at 800°C. Based on the calculated net gain or loss of carbon, it may be seen that at methane concentrations of approximately 300 ppm no net change occurs. If only weight changes are determined, it might be concluded that the oxidation by water vapor is completely suppressed. Data obtained from the effluent gases show that both oxidation and deposition occur but at about the same rate. Comparisons of the calculated and observed weight changes show fair agreement for weight losses and small weight gains. However, the calculated weight changes are significantly larger than the observed weight changes in those instances where large weight gains prevail. This behavior could be due to cracking of methane in the gas phase and/or on surfaces other than the graphite. Another and probably more plausible explanation is that part of the low-density carbon deposited on the graphite specimen does not adhere rigidly to the graphite surface. The few runs made at temperatures below 800°C show that both the oxidation by

Table 4.1. Carbon Deposition from Methane—Water Vapor—Helium Mixtures with an H_2O Concentration of 110 ppm

Temperature (°C)	Flow (cm^3/min)	CH_4 Concentration (ppm)		Effluent Concentration (ppm)				Loss and Gain of Carbon ($mg/cm^2 \cdot hr$)			Observed Weight Change ($mg/cm^2 \cdot hr$)
		Influent Gases	Effluent Gases	CO_2	CO	Total H_2	Corrected H_2	Loss Calculated from CO_2 + CO	Gain Calculated from Corrected H_2	Net Gain or Loss	
								$\times 10^{-3}$	$\times 10^{-3}$	$\times 10^{-3}$	$\times 10^{-3}$
800	280			18	2	37		8.1		−8.1	−8.0
800	275	142	132	15	<1	46	16	6.0	3.2	−2.8	−3.9
800	300	270	255	14	<1	46	18	6.1	3.9	−2.2	−1.8
800	275	335	320	14	1	63	34	6.0	6.7	+0.7	+0.8
800	300	560	520	11	<1	62	40	4.8	8.6	+3.8	+2.0
800	300	635	610	9	<1	63	45	4.0	9.7	+5.7	+2.8
800	275	680	650	10	<1	78	58	4.0	11.1	+7.1	+4.7
750	285	290	280	6	<1	20	8	2.5	1.7	−0.8	−0.6
750	285	560	550	6	<1	29	17	2.5	3.5	+1.0	+1.2
700	300	260	260	2	<1	10	6	0.9	1.3	+0.4	−0.7

water vapor and cracking of methane decrease with decreasing temperature. The rates are not measurable at temperatures much below 700°C.

Results obtained from runs with various methane concentrations in the absence of water vapor are given in Table 4.2. It may be seen that the cracking rate of methane generally increases with both increasing temperature and methane concentration. (There are a few inconsistencies in the data that arise from the poor precision obtainable for this system.) Measurable rates were found at temperatures above approximately 650°C. Fair agreement between the calculated and observed rates of carbon deposition is evident. The calculated rates are, in most instances, higher than the observed rates, particularly at the higher rates. The differences are, however, not as great as those observed in the presence of water vapor. A comparison of the calculated rates of carbon deposition given in Table 4.2 with those found in the presence of water vapor (Table 4.1) shows that water vapor has very little, if any, effect on the cracking of methane. However, the overall rates are different in the two cases because carbon is lost through oxidation in the presence of water vapor.

Results obtained from runs with various helium–carbon monoxide mixtures are reported in Table 4.3. The outstanding feature of these data is the complete lack of agreement between the deposition rates calculated from the carbon dioxide found in the effluent gases and those obtained from measured weight changes. This behavior is not understood. It is possible that disproportionation of carbon monoxide occurred on surfaces other than the ATJ graphite specimens or that carbon was deposited on the graphite surface but was not adherent. Based on the rates of deposition calculated from the carbon dioxide formed, it is evident that the deposition rates increased with increasing carbon monoxide concentration. The deposition rates at constant carbon monoxide concentration increased upon raising the temperature from 550 to 750°C and then remained constant or decreased when the temperature was raised to 850°C. Increasing the flow rate appears to have increased the deposition rate slightly. These results suggest that ATJ graphite is not an efficient medium for promoting the disproportionation of carbon monoxide under the experimental conditions examined.

Table 4.2. Deposition of Carbon from Methane-Helium Mixtures

Temperature (°C)	Flow (cm^3/min)	CH_4 Concentration (ppm)		H_2 Concentration in Effluent Gases (ppm)	Carbon Deposited ($mg/cm^2 \cdot hr$)	
		Influent Gases	Effluent Gases		Calculated from H_2 Produced	Observed from Weight Change
					$\times 10^{-3}$	$\times 10^{-3}$
450	300	102	100	<1	<0.2	<0.1
550	280	108	104	<1	<0.2	<0.1
650	280	118	120	<1	<0.2	0.6
700	270	123	125	<1	<0.2	0.4
700	260	111	112	~2	~0.4	0.5
750	250	125	124	7	1.2	1.0
750	250	121	118	8	1.4	0.9
800	250	127	112	28	5.0	3.2
850	260	115	90	70	13	10
700	300	295	300	4	0.8	0.3
750	300	310	300	9	2.0	3.2
800	300	310	285	29	6.2	5.3
850	300	310	270	90	19	16
650	300	510	500	<1	<0.2	0.3
700	300	570	570	4	0.8	0.9
750	300	550	530	15	3.2	3.0
800	285	565	540	48	9.5	6.0
850	285	560	495	140	29	23
800	275	700	690	46	9.2	7.0

Table 4.3. Deposition of Carbon by Disproportionation of Carbon Monoxide

Temperature (°C)	Flow (cm^3/min)	CO in Influent Gases (ppm)	CO_2 in Effluent Gases (ppm)	Carbon Deposited, Calculated from CO_2 Produced ($mg/cm^2 \cdot hr$)	Observed Weight Change ($mg/cm^2 \cdot hr$)
				$\times 10^{-3}$	$\times 10^{-3}$
550	100	130	3	0.4	<0.1
650	100	130	8	1.1	−0.2
750	100	120	10	1.4	−0.2
850	100	120	4	0.6	−0.5
550	100	660	6	0.9	<0.1
650	120	640	13	2.2	−0.2
750	100	580	13	1.9	+0.2
850	100	640	10	1.5	−0.1
350	100	1550	4	0.5	<0.1
450	100	1500	9	1.3	<0.1
550	100	1450	13	1.9	<0.1
650	100	1300	27	3.9	<0.1
750	100	1250	30	4.4	+0.2
850	100	1550	30	4.4	−0.5
550	270	695	3	1.3	−0.5
650	280	620	5	2.1	+0.1
650	275	650	6	2.4	−0.5
750	300	660	6	2.6	+0.1

BeO-Graphite Compatibility

C. A. Brandon I. T. Dudley
J. A. Conlin W. R. Mixon

Irradiation of the Mark II BeO-graphite compatibility test capsule began March 14, 1965 and is continuing. This capsule, described previously,[12] was designed to evaluate the overall feasibility of employing BeO in a TARGET-type reactor as a means of increasing the conversion ratio. The capsule contains a central BeO cylinder surrounded by a graphite sleeve and a pair of BeO and graphite rings having a known contact area. The specimens are being irradiated in a continuously flowing inert gas atmosphere at a design temperature of 2750°F (1500°C) achieved by

[12] C. A. Brandon, J. A. Conlin, I. T. Dudley, and W. R. Mixon, BeO-Graphite Compatibility, pp. 172–176, GCRP Semiann. Progr. Rept. Mar. 31, 1965, ORNL-3807, Oak Ridge National Laboratory.

gamma heat. Accumulation of the desired neutron exposure of 1×10^{21} to 2×10^{21} neutrons/cm^2 ($E > 0.18$ Mev) will require approximately one year.

From the beginning of the irradiation period a progressive increase in the argon content of the argon-helium sweep-gas mixture was required to maintain the capsule design temperature. This has been interpreted as indicating an increase in the radiant heat transfer within the capsule as a consequence of a progressive degradation of the internal heat-reflective baffles. The design temperature of the BeO-graphite specimen interface was maintained through the early part of July. Since then the sweep gas has been 100% argon and the specimen temperature has shown a continual slow decrease. The specimen temperature is presently 2530°F (1390°C). Although this is below the design temperature, it is still in the region of interest, which extends to 2370°F (1300°C). Of the six W–5% Re vs W–26% Re thermocouples located in the high-temperature region of the capsule, only one has become inoperative.

Eight days after the test began, a small internal leak developed between what were originally two independent regions of the capsule, the gas-swept specimen region and a secondary "temperature-control gas" region. The secondary region was isolated from its gas supply system to prevent possible contamination of the specimen region by the unpurified temperature-control gas. Diffusion of argon from the sweep-gas system into the temperature-control gas region caused the temperature of the primary container to increase to 1460°F (790°C), a condition which is not important to the experiment.

The Analytic Systems Company's infrared CO analyzer was installed in the sweep-gas system downstream of the capsule. Use of the analyzer on the capsule effluent was hampered by the radioactivity of the argon purge, which caused a negative CO indication. Apparently, the absorption of photon energy by the walls of the detector raised the temperature of the gas within the sample side of the detector. An increase in temperature has the same effect on the instrument as a decrease in CO concentration. The capsule was operated with pure helium sweep gas for 20 hr at a temperature of 1750°F (954°C) to allow measurement of CO concentration without the presence of radioactive gases. No CO was detected.

A moisture monitor was installed in the capsule sweep-gas supply line during a reactor shutdown in May 1965. Since that time the indicated moisture level has been in the range 1.2 to 3.6 ppm.

The neutron flux exposure is monitored by tubular monitor-cane assemblies held vertically on the surface of the outer shell of the experimental assembly. Each cane contains three sealed quartz ampules, spaced 0.80 in. apart, with the center ampule at the same elevation as the BeO sample rings within the capsule. Each ampule contains three monitor wires: a 0.0964% Co-Al wire to indicate gross thermal-neutron flux from $^{59}Co(n,\gamma)^{60}Co$ activation, and nickel and iron wires to indicate fast-neutron flux from $^{58}Ni(n,p)^{58}Co$ and $^{54}Fe(n,p)^{54}Mn$ activation. A monitor cane is normally exposed for about two weeks of each reactor cycle.

Nickel and iron are activated by neutrons with energies greater than about 3 Mev, but the exposure to neutrons with energies greater than 0.18 Mev was desired. One quadrant of the ORR core was homogenized, and the fast-neutron spectrum and flux-averaged activation cross sections of ^{58}Ni and ^{54}Fe for neutrons with energies greater than 0.18 Mev were computed with the GAM code.[13] Based on these effective cross sections and the activation analysis data, integrated neutron exposures were computed with the FOILS program.[14] The estimated total exposure of the sample rings to neutrons with kinetic energies greater than 0.18 Mev was 1×10^{21} neutrons/cm^2 as of September 20, 1965.

Failure Characteristics of EGCR-Type AGOT Graphite

F. J. Witt

Our experimental investigations of EGCR-type AGOT graphite were described previously[15–17] and, with the results presented below, the

---

[13] G. D. Joanou and J. S. Dudek, GAM-1: A Consistent P-1 Multigroup Code for the Calculation of Fast Neutron Spectra and Multigroup Constants, USAEC Report GA-1850, General Atomic, 1961.

[14] W. C. Morgan, FOILS: A Program for Computing Neutron Exposures from Foil Activation Data, USAEC Report HW-81367, Hanford Atomic Products Operation, 1964.

testing program is now essentially complete. The more recent results were obtained in experimental studies relative to crack propagation and multiaxial stress states. Hardness and density measurements were obtained for the uniaxial and flexure test specimens, and all the data were correlated. The applicability of the Weibull statistical theory to the strength of graphite was investigated.

Crack Propagation and Fracture Characteristics of EGCR-Type AGOT Graphite (J. M. Corum)

The Griffith-Irwin fracture mechanics concept[18,19] is one of the most promising engineering approaches to the study of brittle fracture. Briefly, the concept involves the principle and practice of controlling brittle fracture by limiting the stress to a value compatible with defect size.

According to the Griffith-Irwin concept, rapid crack propagation will commence from a stationary or slowly propagating crack when a small extension of the crack releases as much elastically stored energy as the total energy used to form the new crack increment. The rate of strain-energy release per unit area of new crack surface is called G and, at the point of impending fracture, G is called G_c, the critical rate of strain-energy release. Often G_c is alternately referred to as the fracture toughness or the crack-extension force. Irwin has suggested that the critical strain-energy-release rate is a fundamental property of a

---

[15]B. L. Greenstreet, Failure Characteristics of Graphite, pp. 168–180, GCRP Semiann. Progr. Rept. Mar. 31, 1964, USAEC Report ORNL-3619, Oak Ridge National Laboratory.

[16]B. L. Greenstreet and F. J. Witt, Failure Characteristics of Graphite, pp. 177–196, GCRP Semiann. Progr. Rept. Sept. 30, 1964, USAEC Report ORNL-3731, Oak Ridge National Laboratory.

[17]B. L. Greenstreet et al., Room-Temperature Mechanical Properties of EGCR-Type AGOT Graphite, USAEC Report ORNL-3728, Oak Ridge National Laboratory, January 1965.

[18]A. A. Griffith, The Phenomena of Rupture and Flow in Solids, Phil. Trans. Roy. Soc., 221: 163–198 (1920).

[19]G. R. Irwin, Fracture Mechanics, pp. 557–594 in Structural Mechanics, J. N. Goodier and N. J. Hoff (Eds.), Pergamon Press, New York, 1960.

material in that it is independent of the size, shape, and type of loading of the specimen.

The Griffith-Irwin fracture mechanics concept has possible practical applications to graphite in design as well as in basic investigations. For example, the load required to cause fracture of a component that is cracked or has a significant initial flaw might be determined. In addition, G_c measurements can serve as a convenient means of comparing the fracture toughness of various graphites as well as the fracture resistance of a single graphite to initial cracks with different orientations. Consequently, graphite fracture studies were made.

Two sets of notched-bend tests were performed on EGCR-type AGOT graphite, and the results were used to determine values of G_c. The specimens for both sets were beams taken from EGCR core column 246 with their long dimension parallel to the axis of extrusion. Each beam had a single lateral crack cut in it with a 0.0095-in.-wide jeweler's saw, as shown in Fig. 4.9. All specimens were tested by the two-point loading method with the artificial crack placed on the tension side of the beam. The beams were loaded until fracture or rapid crack propagation occurred, and load-deflection data were recorded throughout each test.

Seventy-four specimens were tested. In the first series of tests all the beams were 1 ft long and 1 1/4 in. wide, and each had a depth h of 1 in. at the root of the crack. The total depth d was varied to

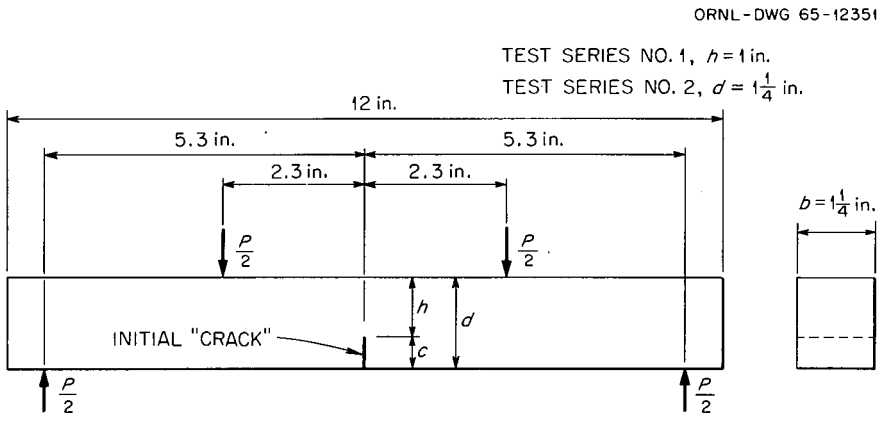

Fig. 4.9. Graphite Notched-Bend Test Specimen.

produce seven different ratios of crack depth to beam depth, including zero. Six beams of each type were tested.

The mean load-deflection curves for each of the seven sets of beams used in the first test series are shown in Fig. 4.10 (the variation from linearity is shown by the straight lines). Specimen sets 1 and 2 broke completely into two pieces very suddenly. In the tests of the third and fourth sets, the beams cracked suddenly, but they did not break completely apart. The tests were stopped when this sudden cracking occurred. In the tests of the three remaining sets, 5, 6, and 7, the crack propagated very slowly across the beam. Fracture was assumed to occur when the maximum load was reached.

In the second series of tests, the beams were again 1 ft long and 1 1/4 in. wide, but the total depth was 1 1/4 in. in every case, and the cracks penetrated the beams to various depths to produce six different ratios of crack depth to beam depth. The mean load-deflection curves for the second test series are shown in Fig. 4.11. Specimen sets 8, 9, and 10 all broke suddenly into two pieces, while specimen sets 11 and 12 never broke apart. As deflection pressure was applied, the cracks propagated slowly across the beams. Most of the deflection pressures were at least twice those of unnotched specimen set 8 when the tests were stopped.

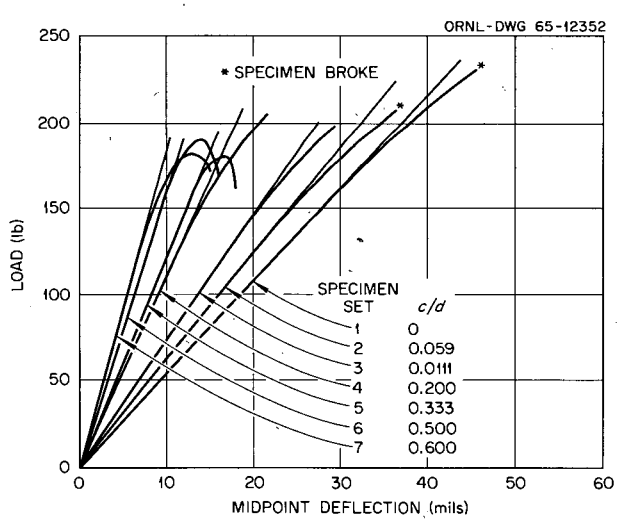

Fig. 4.10. Mean Load-Deflection Curves for Graphite Notched-Bend Test Series 1 (h = 1 in.).

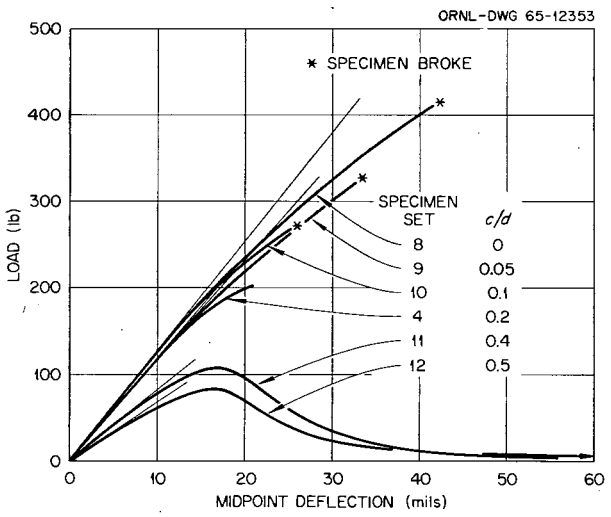

Fig. 4.11. Mean Load-Deflection Curves for Graphite Notched-Bend Test Series 2 (d = 1 1/4 in.).

Two different methods were used to determine values of G_c from the notched-bend test data. The first, which is referred to as the analytical method, makes use of a theory of elasticity solution for G in terms of the dimensions of the specimen, the crack depth, the applied load, and the elastic constants of the material.[20] The relation is

$$G = \frac{1 - \nu^2}{E} \frac{36M^2}{b^2h^3} f(c/d) , \qquad (1)$$

where E is the modulus of elasticity, which was taken to be 1.8×10^6 psi, ν is Poisson's ratio, which was taken to be 0.09, M is the bending moment, which by Fig. 4.9 is equal to 3/2 P, b is the width of the beam, and f(c/d) is a function whose values can be obtained from Ref. 20. The critical value of G is obtained by using, in the above relation, the value of the applied load that results in rapid propagation of the initial crack.

The second method, which is referred to as the direct experimental method, utilizes the experimentally measured change in the spring constant

[20]B. Gross and J. E. Srawley, Stress-Intensity Factors for Single-Edge-Notch Specimens in Bending or Combined Bending and Tension by Boundary Collocation of a Stress Function, Report NASA-TN-D-2603, National Aeronautics and Space Administration, January 1965.

of a set of beams with crack depth to determine G. The relation for G here is

$$G = \frac{1}{2b} P^2 \frac{d}{dc} (1/K) , \qquad (2)$$

where K, the spring constant, is the slope of the load-deflection curve with the deflection measured under the load. For this second method, the entire set of beams must have the same total depth. Consequently, the direct experimental method was used only for the second test series, while the analytical method was used for both series.

Table 4.4 gives the average G_c values for each crack depth tested. The average maximum loads and the coefficients of variation of the loads are also given.

Table 4.4. Average Critical Rate of Strain-Energy Release, G_c, for Graphite Notched-Bend Specimens

Crack Depth (in.)	c/d Ratio	Average Maximum Load (lb)	Coefficient of Variation for Load (%)	Average Value of G_c (in.·lb/in.^{2})	
				Analytical	Direct Experimental
			Test Series 1		
0	0	234	6.9		
1/16	0.059	210	5.0	0.21	
1/8	0.111	196	3.4	0.30	
1/4[a]	0.200	202	5.6	0.42	0.35
1/2	0.333	180	4.8	0.39	
1	0.500	188	5.5	0.43	
1 1/2	0.600	182	1.6	0.40	
			Test Series 2		
0	0	412	15.0		
1/16	0.050	329	4.2	0.28	0.17
1/8	0.100	276	3.3	0.38	0.34
1/4[a]	0.200	202	5.6	0.42	0.35
1/2	0.400	110	2.5	0.35	0.43
5/8	0.500	88	4.4	0.39	0.32

[a]The results from this specimen set are applicable to both series of tests.

The G_c values are plotted as a function of c/d in Fig. 4.12. The values determined by the analytical and the direct experimental methods are in good agreement. However, both sets of values tend toward zero for values of c/d below about 0.1. This is probably an indication of the presence of slow crack growth prior to rapid crack propagation. A small

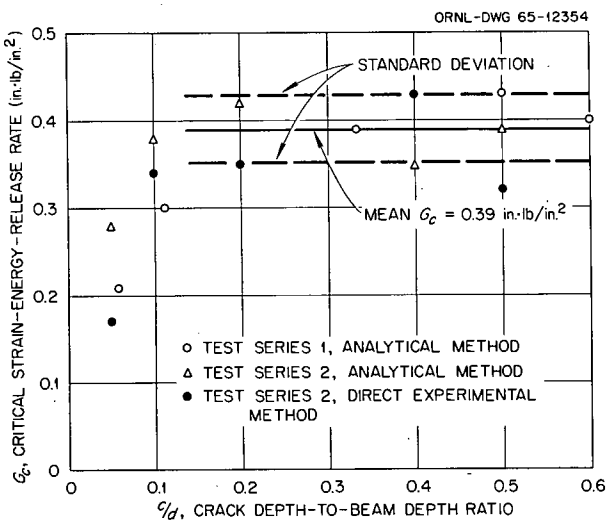

Fig. 4.12. Critical Strain-Energy-Release Rate Versus Crack Depth-to-Beam Depth Ratio.

increment of slow crack growth would significantly affect the G_c values for small c/d ratios. Considering only those values for c/d of 0.2 or greater, the average value of G_c is 0.39 in.·lb/in.^{2}, with a coefficient of variation of 10%. If the G_c values for c/d ratios above 0.1 are considered, the average value becomes 0.38 in.·lb/in.^{2}.

For comparative purposes, G_c for glass is about 0.06; for concrete, 0.1; for epoxy, 8; and for steels and aluminum alloys it ranges from below 100 to as high as 1000. Higher values, of course, indicate better toughness.

Theoretical and Experimental Investigation of the Applicability of Weibull's Statistical Theory of Strength to EGCR-Type AGOT Graphite Fracture Data (S. E. Moore)

One of the most widely discussed theories of failure for brittle materials is that proposed by Weibull.[21] Weibull's theory attempts to account for the variation in observed fracture strength values by treating the strength as a statistical variable. The theory is complete in the sense that, given a sufficient amount of laboratory data on a particular material, the probability that a component will fail under a given set of

[21]W. Weibull, A Statistical Theory of the Strength of Materials, Ingeniorvetenskapsakademiens, Handlingar NR 153, Stockholm, 1939.

service conditions can be calculated. Since one of the more important objectives of these graphite investigations is to validate a set of failure criteria for graphite as a structural material, Weibull's theory has been tested as a possible candidate.

Until very recently a number of obstacles prevented an objective evaluation of the theory. The most serious of these was the nonexistence of statistical test functions for the Weibull distribution function that could be used for small data samples. Without the small sample or exact test functions, it was necessary to gather a large amount of experimental data without a clear indication of how large a sample was needed. Since large samples of fracture data are not easily obtained, the result was that only a superficial examination of the theory was possible.

Recently it became possible for us to examine the two fundamental postulates upon which the Weibull theory is based with the use of fracture data from EGCR-type AGOT graphite. We arrived at the very interesting conclusion that for this particular material one of the postulates is valid and the other is not.

Weibull postulated that within every unit volume of material there were flaws, distributed at random, both in severity and position, that caused the material to be weaker at some locations than at others. The natural consequence of this postulate is that the larger the volume of material subjected to stress, the higher is the likelihood of failure. This is the <u>size-effect</u> postulate, or the weakest-link hypothesis. Expressed mathematically,

$$P(X < x) = 1 - \exp\left[-\int_V \sigma_n dV\right]; \qquad (3)$$

that is, the probability P that the strength X is less than some number x is given by 1 minus the exponential e raised to minus the volume integral of some function σ_n. The bracketed quantity is sometimes called the risk of rupture; σ_n is some, as yet unspecified, function that describes the state of stress in the volume and the parameters that govern failure of the material.

Weibull noted that the two parameters of the normal distribution function, the mean μ and the variance σ^2, were insufficient to characterize failure for brittle materials. He therefore chose a three-parameter function

$$\sigma_n = \left(\frac{x_v - x_u}{x_0}\right)^m , \tag{4}$$

where x_u, x_0, and m are constants peculiar to a given material and x_v is the stress distribution. This is the second postulate.

When Eqs. (3) and (4) are combined, the result is Weibull's statistical theory of strength, as expressed by

$$P(X < x) = 1 - \exp\left[-\int_V \left(\frac{x_v - x_u}{x_0}\right)^m dV\right] . \tag{5}$$

With the introduction of two transformations, defined as the critical volume kV, which is given by

$$kV = \int_{x=x_u}^{x} \left(\frac{x_v - x_u}{x - x_u}\right)^m dV , \tag{6}$$

where k is the stress distribution parameter and x is the maximum stress in the body, and the scale parameter θ, which is given by

$$\theta = x_0(kV)^{-1/m} , \tag{7}$$

the familiar form of Weibull's probability function is obtained; that is,

$$P(X < x) = 1 - \exp\left[-\left(\frac{x - x_u}{\theta}\right)^m\right] . \tag{8}$$

The distribution function is

$$\begin{aligned} f(x) &= \frac{m}{\theta}\left(\frac{x - x_u}{\theta}\right)^{m-1} \exp\left[-\left(\frac{x - x_u}{\theta}\right)^m\right] \qquad \text{for } x_u \leqslant x \leqslant \infty \\ &= 0 \qquad \text{elsewhere} . \end{aligned} \tag{9}$$

The mean is given by

$$\mu = x_u + \theta\Gamma\left(1 + \frac{1}{m}\right) , \tag{10}$$

and the variance is

$$\sigma^2 = \theta^2 \left[\Gamma\left(1 + \frac{2}{m}\right) - \Gamma^2\left(1 + \frac{1}{m}\right)\right] , \tag{11}$$

where Γ is the complete gamma function, x_u is the guaranteed minimum, and m is the shape parameter.

In order for the theory to hold, two conditions must be satisfied. First, experimental data must be distributed according to Eq. (9); that is, the failure stress for a sufficiently large number of specimens of equal volume must be distributed according to a Weibull distribution function. Second, if the first condition is met, the scale parameter θ must obey Eq. (7) for specimens with different volumes but like stress distributions. Testing these two conditions is equivalent to testing the hypotheses of the theory. If the data fit a Weibull distribution function, the second postulate concerning σ_n is valid. If the data fit a Weibull distribution function <u>and</u> the scale parameter θ is volume dependent according to Eq. (7), the weakest-link hypothesis, or the first postulate, is valid. These two conditions form a necessary and sufficient set for the validity of the theory.

Four samples of EGCR-type AGOT graphite fracture data[17] were used to test Weibull's theory. Four samples were necessary because of the dependence of the scale parameter θ on both the volume and the stress distribution. We used two sizes of tensile specimens and two sizes of flexure specimens taken from an EGCR graphite column core in such a way as to guarantee that all the data came from the same parent population (see Fig. 4.13). The specimens were designated ST, LT, SF, and LF for small and large tensile and small and large flexure, respectively. The volumes of both small specimens were 0.115 in.^{3}; the volume of each large specimen was eight times the small specimen volume, or 0.92 in.^{3}. Approximately 30 specimens of each kind comprised a sample.

In order to test the data against the distribution function, it was first necessary to estimate the numerical values of the three parameters

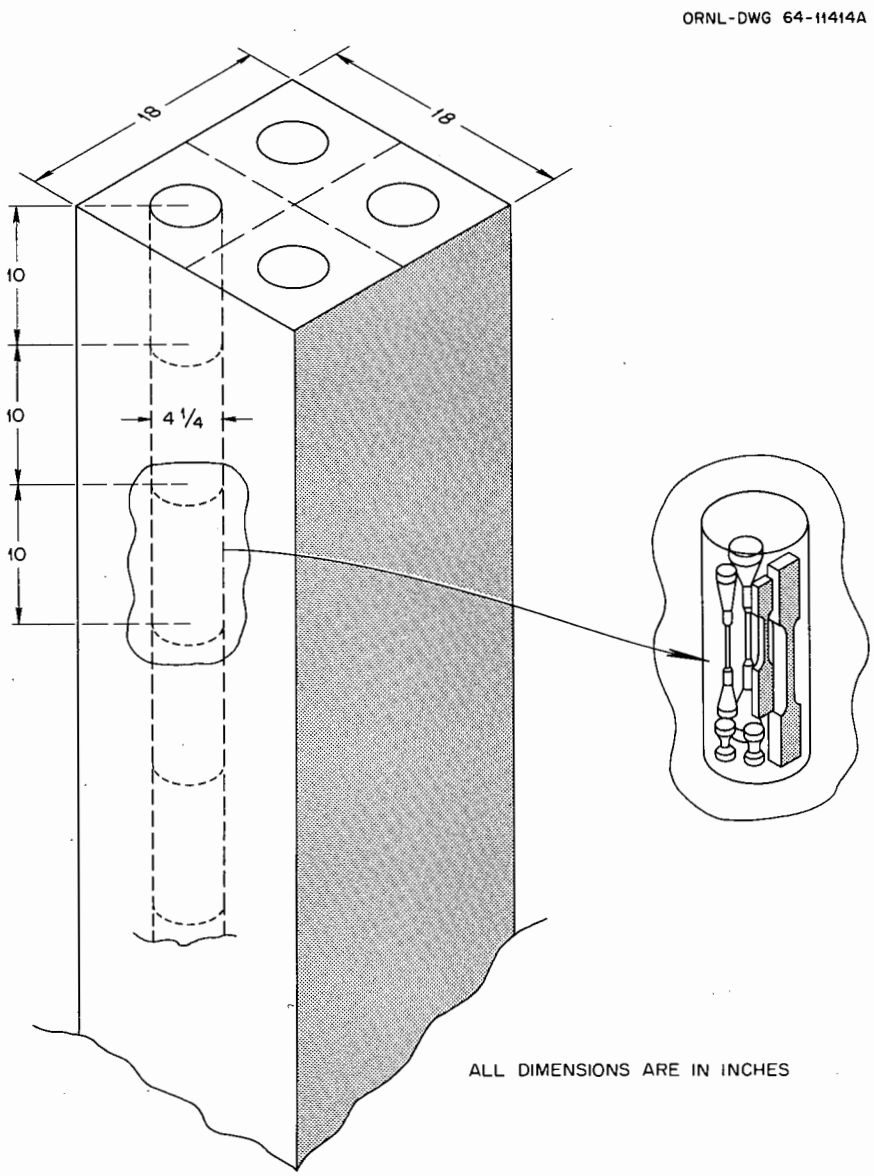

Fig. 4.13. Statistical Sampling Scheme for Taking Specimens of EGCR-Type AGOT Graphite.

x_u, m, and θ, and then to test the fit by performing a statistical hypothesis test. The parameters were estimated with the method of maximum likelihood, which is the standard method when it can be used. The advantage of this method results from two theorems by Cramér,[22] one of

[22]H. Cramér, Mathematical Methods of Statistics, pp. 499–506, Princeton University Press, 1946.

which guarantees uniqueness when certain regularity conditions are satisfied and one which states that for a given sample size the resulting parameter estimates, designated by $(.\hat{.}.)$, are the most nearly correct values that can be obtained by any method. Moreover, the second theorem leads to a method for estimating the error. For small samples the error estimate is crude; however, other methods do not have the error-estimating property. The difficulty with the maximum likelihood method is that for complicated distributions it often leads to equations that cannot be solved in closed form. Special numerical methods must then be devised to solve the equations. A computer code for solving the likelihood equations for the Weibull distribution function and for the variance estimates of the parameters was written.* Also the χ^2 goodness-of-fit test was incorporated into the code for checking the estimated distribution function against the data. The results of these calculations for the four samples of EGCR-type AGOT graphite data are listed in Table 4.5.

Several interesting observations are immediately apparent. First, and extremely important, is the consistently high value of α obtained from the χ^2 goodness-of-fit test. The value of α is the probable error in the null hypothesis H_0:; the distribution of the data is <u>not</u> that of Weibull. Stated another way, $(1 - \alpha)$ is the probable error in assuming that the data <u>are</u> distributed according to the Weibull distribution function. The variable $\chi^2(x)$ is the value of χ^2 computed from the data, whereas $\chi^2_n(\alpha)$ is the critical value for rejection of the hypothesis for a sample size of n. Taken together these numbers show that α is even larger than indicated. We have thus proved the necessary but not sufficient condition that the data do, in fact, fit a Weibull distribution function.

Two other immediate observations are in order. First, there is excellent agreement between the data mean and standard deviation, $\bar{x}$ and $s(x)$, respectively, and the estimated values, $\hat{\mu}$ and $\hat{\sigma}$, which were calculated using the likelihood estimates $\hat{m}$, $\hat{x}_u$, and $\hat{\theta}$ and Eqs. (10) and (11). Second, there is no strong indication of agreement between the individual

*R. B. Bullock, ORNL, wrote the computer program.

Table 4.5. Estimates and Tests of the Weibull Distribution Parameters[a]

Sample	n	$\hat{\mu}$	$\bar{x}$	$\hat{\sigma}$	s(x)	$\chi^2(x)$	$\chi^2_n(\alpha)$	α	$\hat{m}$	$\sigma(\hat{m})$	$\hat{x}_u$	$\sigma(\hat{x}_u)$	$\hat{\theta}$	$\sigma(\hat{\theta})$
SF	29	2117	2117	275	279	6.655	12.49	0.995	2.09	0.328	1569	24.2	618	65.4
LF	36	1890	1892	298	292	8.022	17.25	0.995	3.82	1.308	868	151.5	1129	329.7
ST	32	1596	1594	313	318	7.779	14.34	0.995	2.73	0.622	804	86.9	890	153.1
LT	30	1541	1539	276	283	9.313	13.14	0.995	3.39	1.085	694	124.5	943	248.5

[a]The notation is defined in the text.

parameter estimates for the different samples. This is to be expected from other statistical considerations and especially from the fact that the estimated values are strongly interrelated. In the absence of exact statistical test functions, useful information could be gained by assuming large-sample theory and a trinormal distribution function[23] for the estimated values $\hat{m}$, $\hat{x}_u$, and $\hat{\theta}$ when these numbers are considered as random variables. One such piece of information is an estimate of the variances, $\mathrm{Var}(\hat{m})$, $\mathrm{Var}(\hat{x}_u)$, and $\mathrm{Var}(\hat{x}_0)$, reflected in the table as standard deviations of the parameter estimates $\sigma(\hat{\ldots})$. The only important conclusion from these numbers is that the sample size is too small for conclusive testing of the individual parameters based on the assumption of trinormality. Further research along these lines would lead to prohibitively expensive experimental programs.

Recently Dubey[24] developed a number of exact test functions for the Weibull distribution function for testing null hypotheses. Two of these, the Weibull t test and the Weibull v test, were used to test the null hypothesis of the mean H_0: $\mu = \mu_0$, and the null hypothesis of the variance H_0: $\sigma = \sigma_0$, respectively. Weibull's statistical theory predicts a very definite relationship between the critical volume (kV) and the mean and variance, as seen from Eqs. (7), (10), and (11). If we assume that any one set of estimates is correct, we can compute the expected mean and standard deviation for any of the other samples. The results of this calculation, based on the small tensile specimen data, are shown in Fig. 4.14, with the corresponding observed values.

Each set of data was used to predict the mean and variance of every other set; $\mu_{0,i}$ and $\sigma_{0,i}$, $i = 1,2,3,4$. These null values were then tested against the observed values $\bar{x}_i$ and s_i, $i = 1,2,3,4$, respectively, and the results listed in Table 4.6 were obtained. The notation in the table shows whether the hypothesis could be rejected (denoted by R_α) at the indicated significance value of α or not (denoted by N_α). There is

---

[23] R. V. Hogg and A. T. Craig, Introduction to Mathematical Statistics, Chap. 11, p. 211, MacMillan, New York, 1959.

[24] S. D. Dubey, Tables for Tests of Significance of the Mean and the Variance of the Weibull Distribution, 1965, to be published.

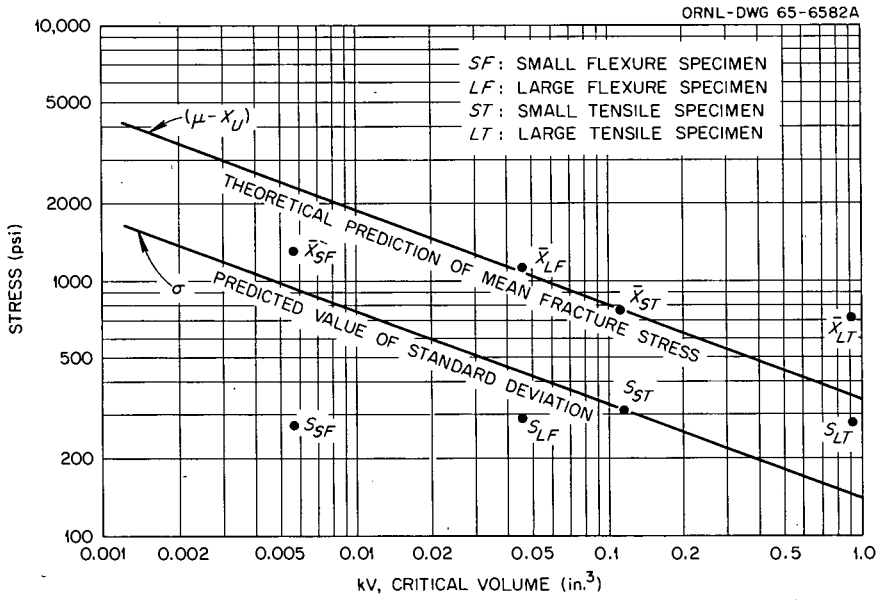

Fig. 4.14. Mean and Standard Deviations Predicted from Graphite Small Tensile Specimen Data.

Table 4.6. Significance Tests on the Mean and Variance[a]

Mean H_0: $\mu = \mu_0$					Variance H_0: $\sigma = \sigma_0$				
Ref[b]/P[c]	SF	LF	ST	LT	Ref/P	SF	LF	ST	LT
SF		R.01	R.01	R.01	SF		R.01	R.01	R.05
LF	R.01		N.85	R.01	LF	R.01		R.05	R.01
ST	R.01	N.85		R.01	ST	R.01	R.05		R.01
LT	R.01	R.01	R.01		LT	R.01	R.01	R.01	

[a]Tables used for significance tests based on Ref. 24.

[b]Samples used for reference.

[c]Expected values predicted from reference.

apparently no correlation between the theory and the data. This can mean only one thing — the initial assumption of the weakest-link hypothesis is <u>not</u> valid.

Since we have shown that Weibull's statistical theory of strength is not entirely valid, an apparent line of research is to attempt to modify the theory in such a way as to support observation. There are a

number of clues in the data that we now have; however, a valid theory should support more data than that used in this study. Additional fracture data on graphite are being gathered from as wide sources as possible. Hopefully, the statistical approach, as well as others, will lead to a comprehensive understanding of the nature of graphite component failure.

Correlation of EGCR-Type AGOT Graphite Properties Data
(G. T. Yahr)

Graphite exhibits considerable variability of mechanical properties even within the same block. Consequently, ultimate strength values used in graphite component design could be increased safely if there were a method for determining the portions of a specific block most capable of sustaining the highest stresses without failing. In order to test this possibility, hardness and density measurements were made on tensile, compressive, and flexure specimens of EGCR-type AGOT graphite. Strength data for these specimens were reported previously.[15–17] The specimens were radiographed before testing, and no significant flaws were found.

Simple correlations were made between the experimental data and density prior to testing, hardness prior to testing, initial modulus of elasticity (as defined in Ref. 17), fracture stress, fracture strain, and strain energy at fracture. Both the average hardness value and the minimum value were tabulated. Results for both the large and small specimens of each particular test were combined into a single large set by normalizing all the strength results to the mean obtained for the large specimens. The parallel uniaxial tensile data and the flexural tensile data were combined into one large set. The simple correlation coefficients are listed in Tables 4.7 and 4.8, and those significant at the 90, 95, and 99% significance levels are indicated.

Of particular interest is the degree of correlation between the nondestructive properties (modulus of elasticity, density, and hardness) and the fracture properties (fracture stress, fracture strain, and strain energy at fracture). The average hardness exhibits the best correlation with fracture properties, while the minimum hardness shows very little

Table 4.7. Simple and Partial Correlation Coefficients for EGCR-Type AGOT Graphite Parallel Tensile and Compressive Properties Data[a]

	Initial Modulus	Fracture Stress	Strain Energy at Fracture	Density	Minimum Hardness	Average Hardness	Fracture Strain
Parallel Tensile and Flexural Data (97 specimens)							
Initial modulus		0.546	0.331	0.210	0.080	0.220	0.157
Fracture stress	0.328		0.907	0.207	0.177	0.316	0.777
Strain energy at fracture	0.065	0.825		0.212	0.106	0.265	0.958
Density	0.136	−0.057	0.036		0.064	0.209	0.192
Minimum hardness	−0.172	0.123	−0.050	−0.103		0.766	0.075
Average hardness	0.157	0.011	−0.031	0.176	0.770		0.231
Fracture strain	−0.243	−0.613	0.939	0.002	−0.020	0.078	
Parallel Compresive Data (38 specimens)							
Initial modulus		0.375	−0.181	0.199	−0.344	−0.173	−0.344
Fracture stress	0.071		0.472	0.378	0.178	0.279	0.235
Strain energy at fracture	0.231	0.851		0.202	0.205	0.371	0.959
Density	0.096	0.290	−0.204		0.186	0.408	0.138
Minimum hardness	−0.416	0.206	−0.088	−0.258		0.833	0.206
Average hardness	0.238	−0.111	0.063	0.404	0.844		0.352
Fracture strain	−0.311	−0.806	0.986	0.190	0.026	0.003	

Partial correlation

Simple correlation

[a] ___ Indicates significance at the 90% level.

___ Indicates significance at the 95% level.

___ Indicates significance at the 99% level.

Table 4.8. Simple and Partial Correlation Coefficients for EGCR-Type AGOT Graphite Transverse Tensile and Compressive Properties Data[a]

	Initial Modulus	Fracture Stress	Strain Energy at Fracture	Density	Minimum Hardness	Average Hardness	Fracture Strain
Transverse Tensile Data (32 specimens)							
Initial modulus		−0.094	−0.236	0.228	0.155	0.032	−0.214
Fracture stress	0.163		0.681	0.171	0.020	0.205	0.620
Strain energy at fracture	−0.234	0.388		0.228	−0.082	−0.056	0.976
Density	0.335	−0.101	0.212		0.008	0.114	0.194
Minimum hardness	0.217	−0.175	0.079	−0.141		0.631	−0.126
Average hardness	−0.144	0.308	0.101	0.161	0.629		−0.134
Fracture strain	0.155	−0.205	0.961	−0.144	−0.044	−0.192	
Transverse Compressive Data (32 specimens)							
Initial modulus		0.052	−0.053	0.095	0.005	−0.033	−0.113
Fracture stress	0.002		0.778	0.359	0.327	0.224	0.718
Strain energy at fracture	0.239	0.544		0.294	0.496	0.410	0.980
Density	0.068	0.159	0.074		0.086	0.664	0.261
Minimum hardness	0.076	0.034	0.016	−0.047		0.790	0.448
Average hardness	−0.124	−0.223	0.320	−0.002	0.714		0.347
Fracture strain	−0.287	−0.381	0.966	−0.063	0.036	−0.303	

Partial correlation

Simple correlation

[a] ___ Indicates significance at the 90% level.

═══ Indicates significance at the 95% level.

▓▓▓ Indicates significance at the 99% level.

correlation. Correlations of density and modulus with fracture properties are good for the parallel specimens and especially for the combined parallel tensile and flexural set. Significant correlations in 16 of the 21 cases for the parallel tensile and flexural data strongly indicate that a sufficiently large sample size may not exist for the remaining data in Table 4.7 and in Table 4.8. The results in Table 4.8 show a marked lack of correlation. This probably results from the cross section of the specimen being anisotropic, as well as from the relatively small sample size.

Partial correlation coefficients are also shown in Tables 4.7 and 4.8. In this case two independent variables are correlated by assuming that the remaining variables are constant; that is, they are correlated when the influence of the other factors is removed. The only nondestructive property that shows any significant partial correlation with fracture properties is the modulus of elasticity. Again the significant correlations appear in the sets of data with the larger sample sizes. The average hardness exhibits no significant partial correlation in the largest sample size (parallel tensile and flexural results), which implies that the hardness is related to the other properties. It is interesting to note that while the simple correlation coefficients indicate that the specimens with the highest strength absorbed the greatest amount of strain, the partial correlation coefficients indicate the opposite.

Multiple correlation of the strength properties with hardness, density, and modulus are given in Table 4.9. Again good correlations exist for the parallel specimen data, with very little correlation for the transverse specimen results. Anisotropy in the cross section and sample size affects these results, as before.

In summary, these results indicate that with sufficient sample size the initial modulus, density, and hardness all correlate fairly well with strength properties. The average hardness shows the most consistent simple correlation; but when considered as a quantity devoid of the influence of other properties, it has little inherent significance. The modulus is the property related most strongly to the stress and strain at fracture. Although further investigations are anticipated, these results

Table 4.9. Multiple Correlation Coefficients of Combined Sets of Data for EGCR-Type AGOT Graphite[a]

Specimen Type	Number of Specimens	Dependent Variable		
		Fracture Stress	Fracture Strain	Strain Energy
Parallel tensile and flexure	97	0.585	0.286	0.402
Parallel compressive	38	0.539	0.462	0.401
Transverse tensile	32	0.288	0.363	0.382
Transverse compressive	32	0.412	0.440	0.494

[a]Independent variables are modulus of elasticity, density prior to testing, and average hardness prior to testing.
___ Indicates significance at the 95% level.
═══ Indicates significance at the 99% level.

indicate that it is possible to choose by nondestructive means the stronger components of EGCR-type AGOT graphite from a given set.

Compressive Modes of Failure in EGCR-Type AGOT Graphite
(J. G. Merkle, J. E. Smith)

Compressive specimens of two sizes (see Fig. 4.15) were tested and the results reported.[17] The average compressive strength of the smaller specimens was 5000 psi, while that of the larger specimen was 4600 psi. Since both sets of specimens had enlarged ends, it is possible that the lowest mode of compressive failure might have been inhibited; that is, the relatively larger end sections of the specimens might have restrained the gage section and increased their apparent strengths. Since the effect would be greatest in the specimens with the relatively largest ends, the results stated above are consistent with this concept. Actually, there are at least three phenomena that could obscure the lowest mode of failure, as follows:

1. nonparallel alignment of the ends, which would introduce a bending moment along the length of the specimen,

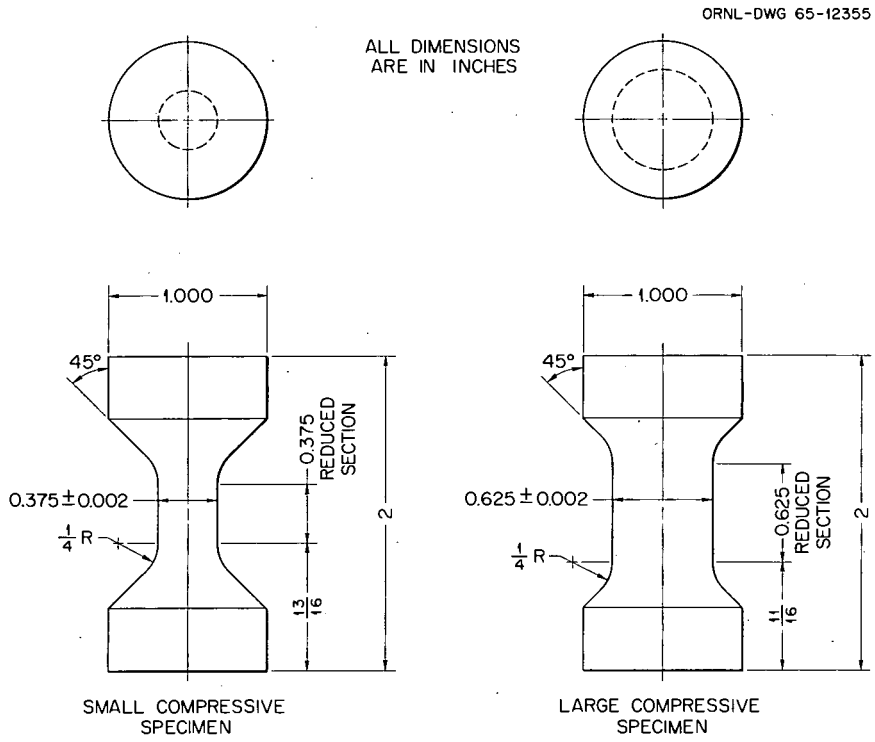

Fig. 4.15. Graphite Compressive Test Specimen Configurations.

2. stress concentrations in the transition region adjoining the gage section or at the sudden change in cross section between the loading platens of the testing machine and the specimen,
3. friction between loading platens and specimen.

A test rig was set up that practically eliminated these features that tended to invalidate the test results. The test setup is shown in Fig. 4.16. The specimen is a right circular cylinder with a height of 1.50 in. and a diameter of 0.625 in. In order to minimize the effects of change in cross-sectional area, end platens of a stronger graphite, 0.75 in. long and of the same diameter as the test specimen, were used.

Eleven specimens, all cut in the parallel direction, were tested. No strain measurements were made. Most of the specimens were unloaded immediately after passing the maximum load in order to determine the location of initial cracks. Where complete failure was obtained, the mode of failure was a series of jagged cracks running vertically and diagonally through the specimen (see Fig. 4.16); no vertical splitting occurred. The average strength of the 11 specimens was 3950 psi. This result is

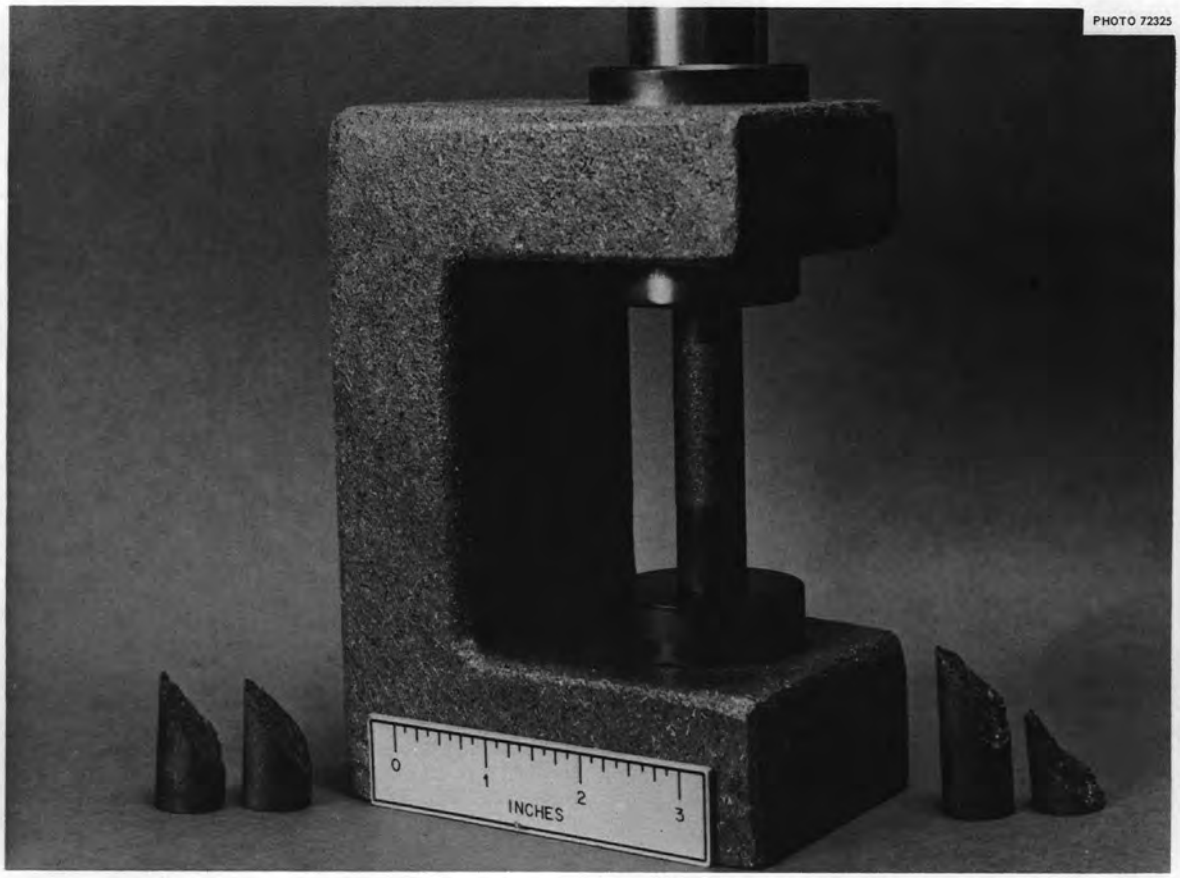

Fig. 4.16. Graphite Compressive Specimen in Test Rig and Typical Fractured Specimens.

from 15 to 20% smaller than the values given above. The most obvious conclusions from this experiment are that end conditions have affected the results reported previously and that a reduction in end restraint has been obtained for the tests described here. However, a plot of gage volume versus ultimate strength, as given in Fig. 4.17, is linear and suggests that perhaps still another mechanism affects the results. Further investigation of this phenomenon is anticipated.

Investigation of Multiaxial Stress States for EGCR-Type AGOT Graphite (J. G. Merkle, J. E. Smith, R. S. Valachovic)

In most design applications, graphite is subject to triaxial stresses, and the most likely mode of failure is either cracking or spalling at a surface at which the state of stress is biaxial or almost so. The

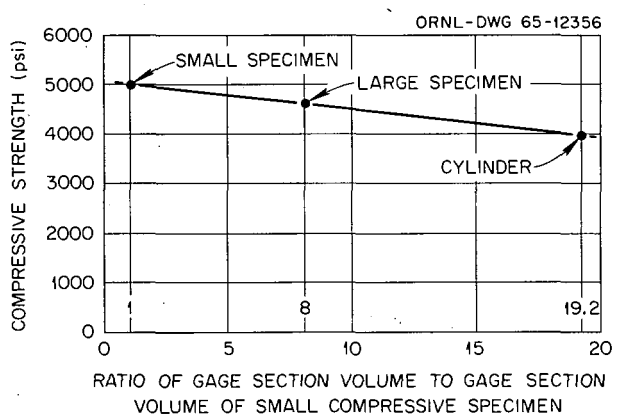

Fig. 4.17. Variation of Compressive Fracture Strength of Graphite with Volume of Gage Section.

behavior of graphite under multiaxial stress states and the applicability of uniaxial properties to the investigation of this behavior must be known before realistic analyses can be performed. As a first step in this direction, a series of biaxial tensile tests of thin-walled EGCR-type AGOT graphite tubes subjected to internal pressure and axial thrust was made. A sketch of the tube is shown in Fig. 4.18. The stresses are statically determinant for this type of loading. The wall thickness was 0.092 in., as compared with a maximum grain size of 0.032 in. for the graphite. The tubes were designed so that failure should occur randomly in the 4-in. gage section. However, failure was always shown to occur near the transition section due to stress concentrations. Since failure due to bending is inherent in this particular design, a small portion at the center of the tubes was further reduced in thickness to 0.065 in. As a result, the failure always initiated in this region.

The specimens were strain gaged so that a continuous monitoring of strain as well as pressure could be made. A specimen ready for testing in the biaxial tensile rig is shown in Fig. 4.19. Similar rigs for measuring compressive end loads and external and/or internal pressure were made. Thus, almost any combination of triaxial and biaxial stress conditions may be obtained.

A sketch of the test outline for biaxial stress states is shown in Fig. 4.20. Test series A, B, C, N, and M were performed on tubes having

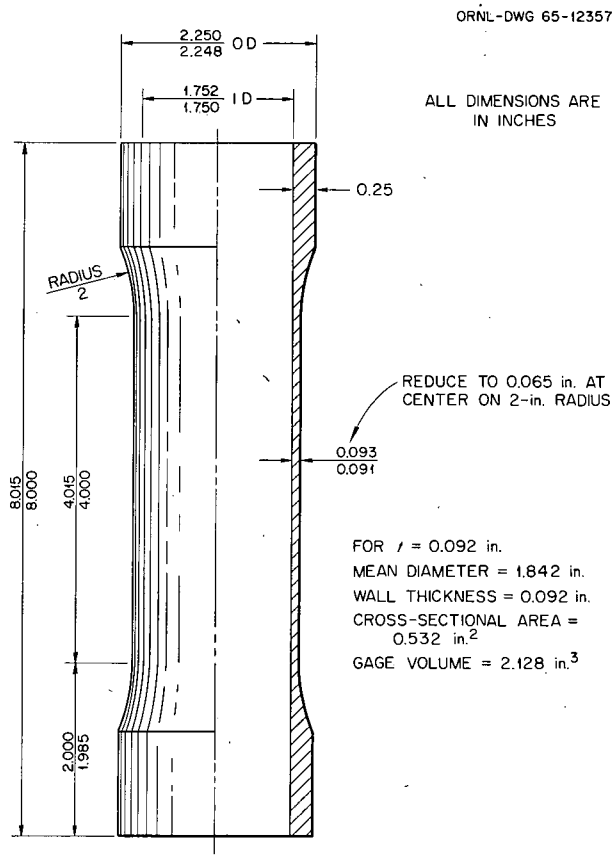

Fig. 4.18. Sketch of EGCR-Type AGOT Graphite Tube Specimen for Investigating Multiaxial Stress States. Combined or separate loadings: internal pressure, external pressure, axial tension, and axial compression.

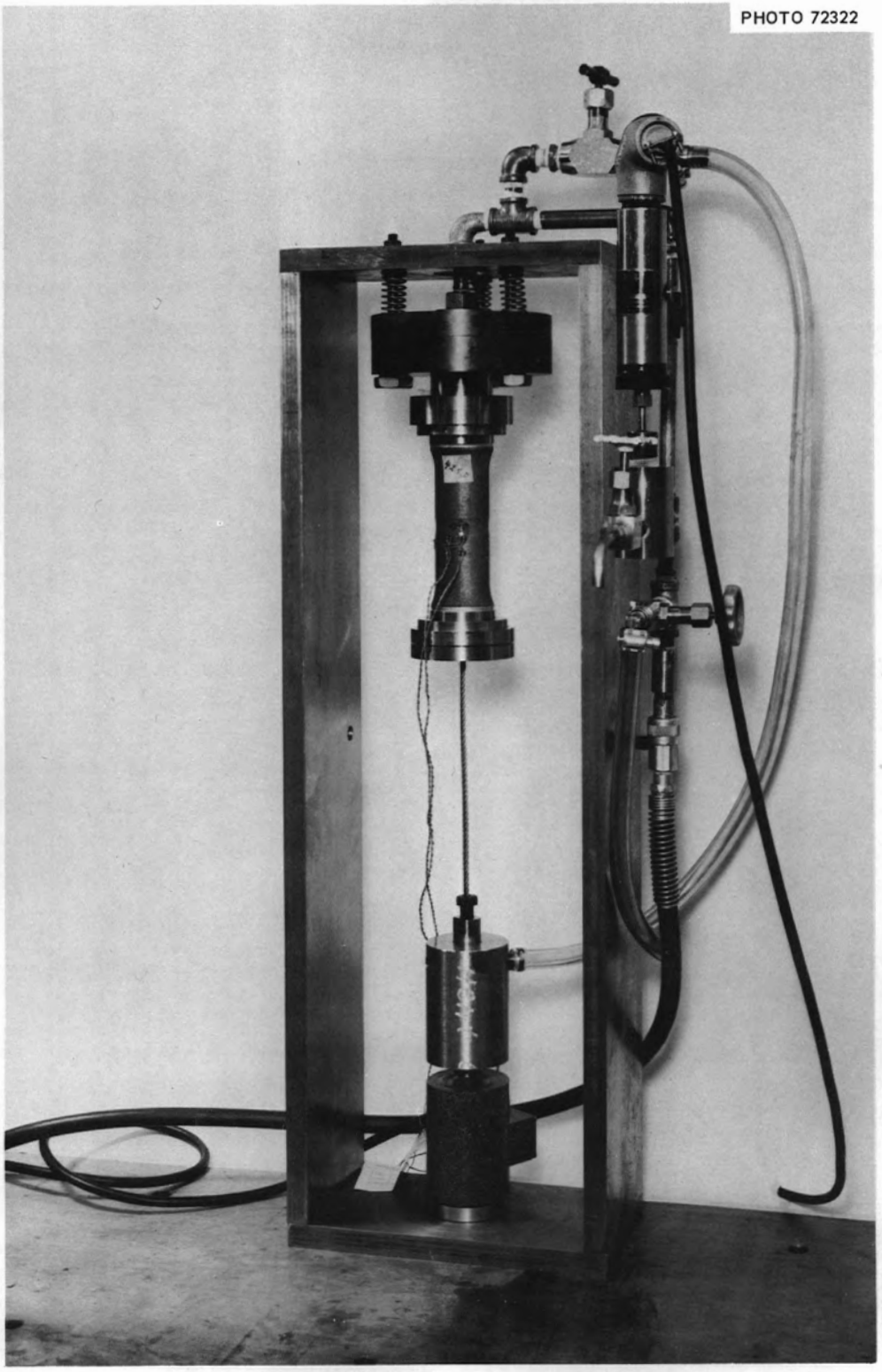

Fig. 4.19. Graphite Specimen in Biaxial Tension Rig Ready for Testing.

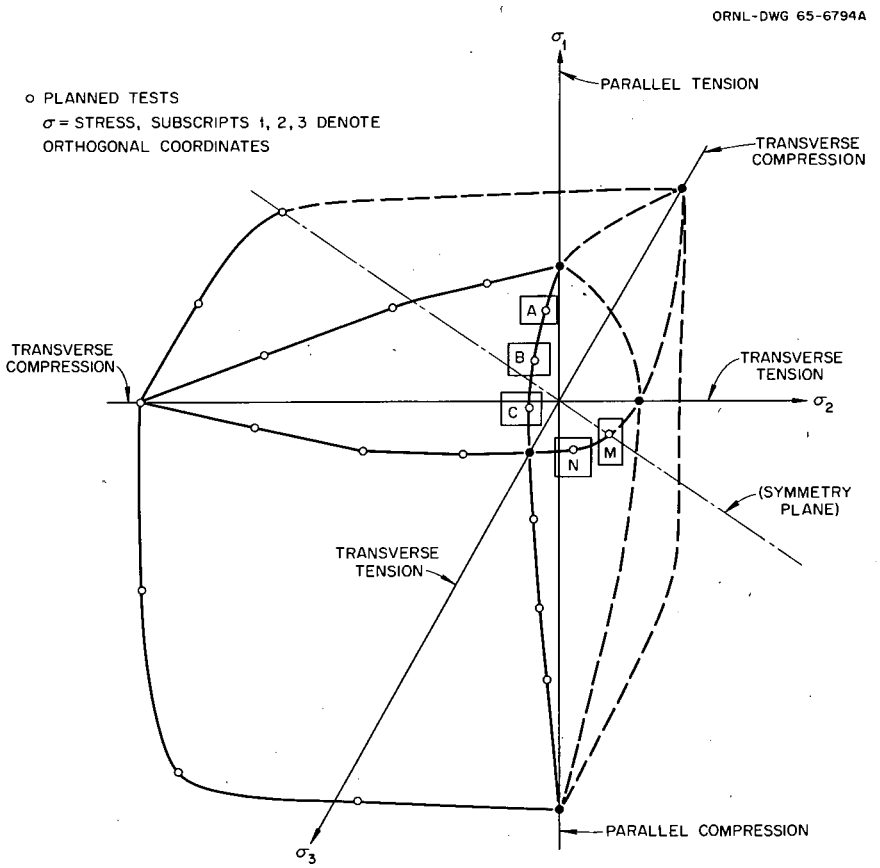

Fig. 4.20. Outline of Tests for Investigating Multiaxial Stress States in EGCR-Type AGOT Graphite. Tests A, B, C, N, and M performed on tubes with reduced thickness at the center.

the reduced thickness at the center. Since the strains are obtained in a discontinuity region, some procedure for calculating stresses from measured strains must be devised. Several such procedures were investigated, and some appear to be quite satisfactory; however, further investigations are necessary. New specimen configurations are also being investigated for producing a statically determinant state of stress at failure.

5. STUDIES FOR ADVANCED SYSTEMS

A. M. Perry F. J. Witt

Fuel Cycle for Fission-Product-Releasing Fuel

R. S. Carlsmith W. E. Thomas

We have investigated the effect on high-temperature gas-cooled reactor (HTGR) conversion ratios and fuel-cycle costs of using a fuel that rapidly releases the volatile fission products instead of retaining them. The advantage to be gained from release of the fission products is that they could then be removed from the active part of the core in order to reduce parasitic neutron capture and improve the neutron economy of the system. Our purpose in making the study was to provide a partial estimate of the incentive for developing such a fuel. In making cost comparisons we have not included any increase in operation and maintenance cost implied by the higher activity levels in the circulating gas nor the effect of the possibly lower fuel fabrication cost for this type of fuel element, though we recognize that these two factors may be important.

The fission products we chose to treat as being released were the noble gases and halogens, since it seems unlikely that a fuel element can be developed that would release any other groups of elements without at the same time allowing uranium migration. We also calculated the effect of the possible release of ^{6}Li, which occurs not as a fission product but as a product of the beryllium (n,α) reaction in the moderator. We investigated the limiting case in which the nuclides in question made no contribution to neutron absorption. Since ^{135}Xe is one of the principal nuclides involved, the removal of this nuclide or its precursor ^{135}I would have to be accomplished in a matter of hours.

We used as our reference the design of the General Atomic TARGET study.[1] The reactor has a 1000-Mw(e) power output, it is cooled by helium,

[1]General Atomic, Design Study Report for TARGET — A 1000 Mwe High-Temperature Gas-Cooled Reactor, USAEC Report GA-4706, rev., Mar. 9, 1964.

and it operates on a thorium—fully enriched uranium cycle with recycle of the bred uranium. The moderator is a combination of graphite and BeO, with an atomic ratio of about 2.4 times as much graphite as BeO. We made our calculations, as in previous studies,[2,3] for an equilibrium fuel cycle and graded exposure. We used a multigroup point-depletion computer code with a buckling specification to account for neutron leakage. Some of the principal ground rules for the study are given in Table 5.1. The fuel processing cost was allowed to vary with processing rate, and hence with burnup, as in previous studies.[2,3] Fuel fabrication costs of $50 and $100/kg were used. We consider $100/kg as a reasonable cost for current technology in a large industry, while $50/kg might ultimately be possible.

The net conversion ratios at a power density of 7 w/cm^3 are given in Fig. 5.1. The values always decrease at long burnup because of the accumulation of slowly saturating fission products. They also decrease for very short burnup because of excessive processing losses. The maximum conversion ratios occur at about 5000 Mwd/T, which is probably too low a burnup ever to be economical. In addition, the conversion ratio advantage of the releasing fuel is greater at high burnup because of the low-cross-section volatile fission products, principally in the mass 131 and 133 chains. At 50,000 Mwd/T the releasing fuel has a conversion ratio 0.07 higher than that of the retaining fuel. If ^{6}Li were also released, an additional increase of 0.04 would occur.

Some corresponding doubling times for the total fissile inventory are shown in Fig. 5.2. The total out-of-reactor time was assumed here to be 60 days, implying that reprocessing and refabrication would be done in an integrated on-site plant with very short cooling times. Even with this assumption, the minimum doubling times for releasing fuels occur at

---

[2]R. S. Carlsmith and W. E. Thomas, Comparison of Fuel Compositions for High-Temperature Gas-Cooled Reactors, p. 212, GCRP Semiann. Progr. Rept. Sept. 30, 1964, USAEC Report ORNL-3731, Oak Ridge National Laboratory.

[3]R. S. Carlsmith, C. M. Podeweltz, and W. E. Thomas, Fuel-Cycle Cost Comparisons for High-Temperature Gas-Cooled Reactor Fuels, USAEC Report ORNL-TM-1112, Oak Ridge National Laboratory, April 14, 1965.

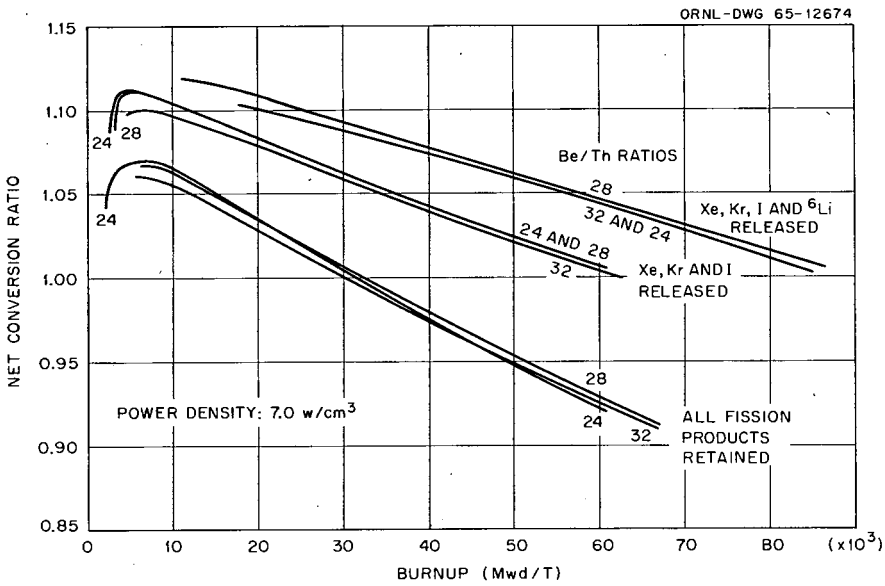

Fig. 5.1. Conversion Ratios for High-Temperature Gas-Cooled Reactors Operating with Fission-Product-Releasing Fuel Compared with Those for Same Reactors with all Fission Products Retained.

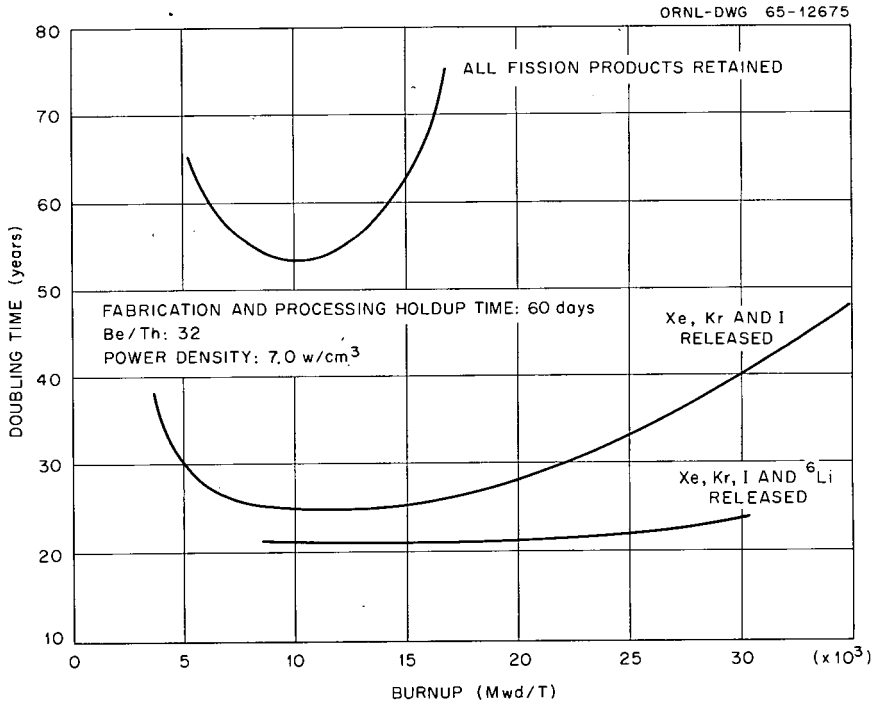

Fig. 5.2. Doubling Times for High-Temperature Gas-Cooled Reactors Operating with Fission-Product-Releasing Fuel Compared with Those for Same Reactors with All Fission Products Retained.

Table 5.1. Ground Rules for Study of HTGR Operating with Fission-Product Releasing Fuel

Power density, w/cm^3	5, 7, and 14
Thermal efficiency, %	44.4
Plant factor	0.8
Reactor electrical power, Mw	1000
Beryllium-to-thorium atomic ratio	24, 28, and 32
Fixed charges on fuel inventory, %/year	10
Fixed charges on working capital, %/year	10
Processing losses, %	
Uranium	1.0
Protactinium	3.1
Fabrication scrap losses, %	0.2

burnups as high as 15,000 to 20,000 Mwd/T. We have not found any doubling times for this reactor design of less than about 21 years.

Fuel-cycle costs at a power density of 7 w/cm^3 are listed in Table 5.2 for each of the types of fuel under several cost assumptions. All these cases are for a beryllium-to-thorium ratio of 32, which consistently gave slightly better fuel-cycle costs than the other fuel compositions. As one might expect, the releasing fuels optimize at higher burnups than the retaining fuel, so part of the cost advantage is in higher conversion ratio and part in lower processing and fabrication costs. With current ground rules for a large industry ($100/kg fabrication cost, $8/lb U_3O_8, and 300 days out-of-reactor time) the releasing fuels give 0.2 to 0.3 mills/kwhr(e) lower fuel cycle costs than the retaining fuels. This cost advantage increases with higher ore cost and with higher fuel fabrication cost. Perhaps the most striking difference between the fuel types is that the releasing fuels always optimize with conversion ratios above 1.0, whereas the retaining fuels nearly always optimize below unity.

We also varied the power density and obtained the results shown in Table 5.3. The optimum power density is generally in the range of 7 to 14 w/cm^3 and varies somewhat with the economic ground rules. At higher

Table 5.2. HTGR Minimum Fuel-Cycle Cost at a Power Density of 7 w/cm^3

Out-of-reactor holdup, days	300				60			
Fabrication cost, \$/kg (U + Th)	100		50		100		50	
Ore cost, \$/lb U_3O_8	8	20	8	20	8	20	8	20
All fission products retained								
Burnup, Mwd/T	57,000	45,000	45,000	33,000	53,000	41,000	37,000	24,500
Conversion ratio	0.93	0.96	0.96	0.99	0.94	0.97	0.98	1.014
Doubling time, years								180
Fuel-cycle cost, mills/kwhr(e)	0.91	1.15	0.79	1.01	0.87	1.08	0.75	0.91
Xe, Kr, and I released								
Burnup, Mwd/T	58,000	49,800	49,800	45,800	55,000	50,000	50,000	42,000
Conversion ratio	1.007	1.021	1.021	1.028	1.012	1.020	1.020	1.036
Doubling time, years	300+	143	143	107	221	110	110	66
Fuel-cycle cost, mills/kwhr(e)	0.73	0.90	0.62	0.78	0.70	0.85	0.59	0.72
Xe, Kr, I, and ^{6}Li released								
Burnup, Mwd/T	75,000	71,000	71,000	62,500	75,000	71,000	67,000	54,000
Conversion ratio	1.020	1.027	1.027	1.039	1.020	1.027	1.033	1.053
Doubling time, years	132	110	110	82	115	93	80	52
Fuel-cycle cost, mills/kwhr(e)	0.64	0.79	0.55	0.69	0.62	0.75	0.53	0.65

Table 5.3. Minimum Fuel-Cycle Cost at Several Power Densities for Fuel that Releases Xe, Kr, and I

Out-of-reactor time: 300 days
Fabrication cost: $100/kg
Ore cost: $8/lb U_3O_8

Power density, w/cm^3	5	7	14
Burnup, Mwd/T	59,000	58,000	65,000
Conversion ratio	1.017	1.007	0.925
Fuel-cycle cost, mills/kwhr(e)	0.8	0.7	0.7

power densities the conversion ratio is penalized excessively because of increased neutron leakage and ^{233}Pa absorptions. At lower power densities there is excessive inventory cost. We had previously[4] found minimum fuel-cycle costs at power densities of 5 to 10 w/cm^3 for fission-product retaining fuels.

Analyses of Nozzle-to-Spherical Shell Attachments

F. J. Witt R. C. Gwaltney
R. L. Maxwell

The first phase of the experimental work on analyses of nozzles attached to spherical shells was concluded[5] with the completion of the investigation of the six configurations described in Table 5.4. The results of previous theoretical and experimental work have been reported.[6,7]

[4]R. S. Carlsmith, Parametric Study of Fueled-Graphite Reactors, pp. 383–394, GCRP Semiann. Progr. Rept. Sept. 30, 1963, USAEC Report ORNL-3523, Oak Ridge National Laboratory.

[5]R. L. Maxwell, R. W. Holland, and J. A. Cofer, Experimental Stress Analysis of the Attachment Region of Hemispherical Shells With Radially Attached Nozzles, ME-7-65-1, Engineering Experiment Station, The University of Tennessee College of Engineering, June 1965.

[6]F. J. Witt, R. C. Gwaltney, and S. E. Moore, Shell Analysis Program, pp. 184–185, GCRP Semiann. Progr. Rept. Mar. 31, 1965, USAEC Report ORNL-3807, Oak Ridge National Laboratory.

[7]F. J. Witt, R. L. Maxwell, and R. C. Gwaltney, Analyses of Nozzle-to-Shell Attachments, pp. 185–188, GCRP Semiann. Progr. Rept. Mar. 31, 1965, USAEC Report ORNL-3807, Oak Ridge National Laboratory.

Table 5.4. Dimensional and Loading Data for the Six Configurations of Nozzle-to-Spherical Shell Attachments

Sphere radius: 15.2535 in.
Sphere thickness: 0.375 in.
Outside diameter of nozzle: 2.625 in.

Configuration No.	Internal Nozzle Length (in.)	Nozzle Radius (in.)	Nozzle Thickness (in.)	Nozzle Radius-to-Thickness Ratio	Loading		
					Internal Pressure (psi)	Axial Compressive Thrust (lb)	Bending Moment (in.-lb)
1	4.125	1.1875	0.25	4.75	400	6000	8000
2	4.125	1.25	0.125	10.0	300	3000	4500
3	0.75	1.25	0.125	10.0	300	3000	4500
4	0.375	1.25	0.125	10.0	300	3000	4500
5	0.0	1.25	0.125	10.0	300	3000	4500
6	0.0	1.28125	0.0625	20.5	200	1500	2400

The loading conditions used are also shown in Table 5.4. Not only were stresses obtained in the plane of loading for the moment loads but also at every 15° around the junction from the plane of loading. Theoretical analyses were made for all the types of loading and compared with the experimental results.

The most significant fact obtained from the comparisons is that for each configuration and all loadings the maximum experimental stresses were well approximated by the theoretical analyses. This is in spite of the fact that for the thickest nozzle configuration (configuration 1) the experimental and theoretical stresses on the sphere were in considerable disagreement for pressure loading. It is also noteworthy that for the thinner nozzles the agreement for the spherical stresses improves, and rather rapidly so, for the maximum values under pressure loading. For these cases (configurations 2 through 6) the only significant disagreement is for the meridional outer surface stresses for the sphere, and this disagreement exists for all three loadings considered.

6. FAST REACTOR DEVELOPMENT

Fuel Irradiation Tests in ORR Poolside Facility

F. R. McQuilkin V. A. DeCarlo
J. A. Conlin

An irradiation test program was initiated in support of the development of fuel elements for the fast gas-cooled reactor. The program consists initially of a series of capsule tests to be performed in the ORR poolside facility. The General Atomic fast gas-cooled reactor design (GCFR) was used as the first reference in the selection of test parameters.[1] Details of test design conditions and procedures were determined in cooperation with General Atomic. The tests presently planned are designed to investigate the effects of irradiation, thermal cycling, external pressure, and fuel-cladding interactions on the integrity and behavior of metal-clad oxide fuel elements having design features that approximate design variations for the GCFR element.

The reference element is a fuel rod consisting of a metal tube about 1 cm in outside diameter, with a 10-mil wall thickness and a 100-cm active length, fueled with UO_2 pellets and designed to generate 20-kw/ft fission heat. The fuel pellets are cored (inside diameter equal to about 20% of the outside diameter) to reduce fission-product gas pressure buildup as burnup increases. The element may have some type of radial restraint and a roughened outer surface to improve heat transfer. The operating pressure is to be 1000 psig, with a possible increase to 2000 psig, and the maximum cladding surface temperature is to be 1400°F (760°C). Because of the severe pressure and temperature requirements, attention during test work will be focused on fuel-cladding interaction problems and the effects of differential thermal expansion as thermal cycling occurs.

Two types of elements are under consideration. One is a "fuel-supported" clad type in which the cladding is designed to collapse on the

[1]P. Fortescue, R. T. Shanstrom, and H. Fenech, Development of the Gas Cooled Fast Reactor Concept, ANS-100, p. 89, Proceedings of American Nuclear Society National Topical Meeting on Fast Reactor Technology, Detroit, April 26-28, 1965.

fuel pellets essentially immediately upon being subjected to the operating pressure and temperature. To reduce interaction effects the outer surfaces of the fuel pellets may be contoured with a midsection undercut to enhance the tendency for the cladding to "lock" itself to the fuel. The second fuel element is of a pressure-equalizing design with all voids filled with sodium or NaK. This element has a specially deformed (flattened) unfueled upper region, or "flex tube," that is capable of flexing so as to transmit the reactor coolant system pressure to the inside of the element and thereby eliminate the collapsing stress from the fuel region.

The first test assembly, which is designated P4A-1 and is currently being irradiated, contains a three-section fuel pin supplied by General Atomic. As shown in Fig. 6.1(a) the topmost section is a detachable mockup of a flex tube, and the lower two sections are sealed elements of the fuel-supported type fueled with cored UO_2 pellets and clad with 9-mil-thick, 3/8-in.-OD Hastelloy X. The specimens are attached to each other with screw threads and are mounted in a NaK-filled irradiation test rig (similar to that used for EGCR fuel elements tests), as shown in Fig. 6.2. A summary of the design and planned operating conditions for capsule P4A-1 is given in Table 6.1. This capsule is being operated at a maximum cladding temperature of 1400°F (760°C), as estimated from temperatures indicated by six thermocouples located in the NaK coolant. The nominal external pressure is 800 psia. Thermal cycles are applied once per day at a maximum temperature change rate of 50°F/min (28°C/min) by manually repositioning the capsule in the poolside flux. The dummy flex-tube section is included in this assembly to provide temperature-effect information needed for the design of future capsules.

The next test assembly, designated P4A-2, will contain fuel-supported specimens similar to those in capsule P4A-1, but the two fueled sections will be longer and there will not be a flex section. As shown in Fig. 6.1(b), each fueled pin will contain 0.312-in.-OD cored UO_2 pellets within 0.315-in.-ID Hastelloy X tubes. The cladding thickness of the upper pin will be 0.015 in.; on the lower pin it will be 0.020 in. near the upper end and 0.010 in. near the lower end. The wall thickness variation was achieved by machining the tubing outside surface. A summary of the design

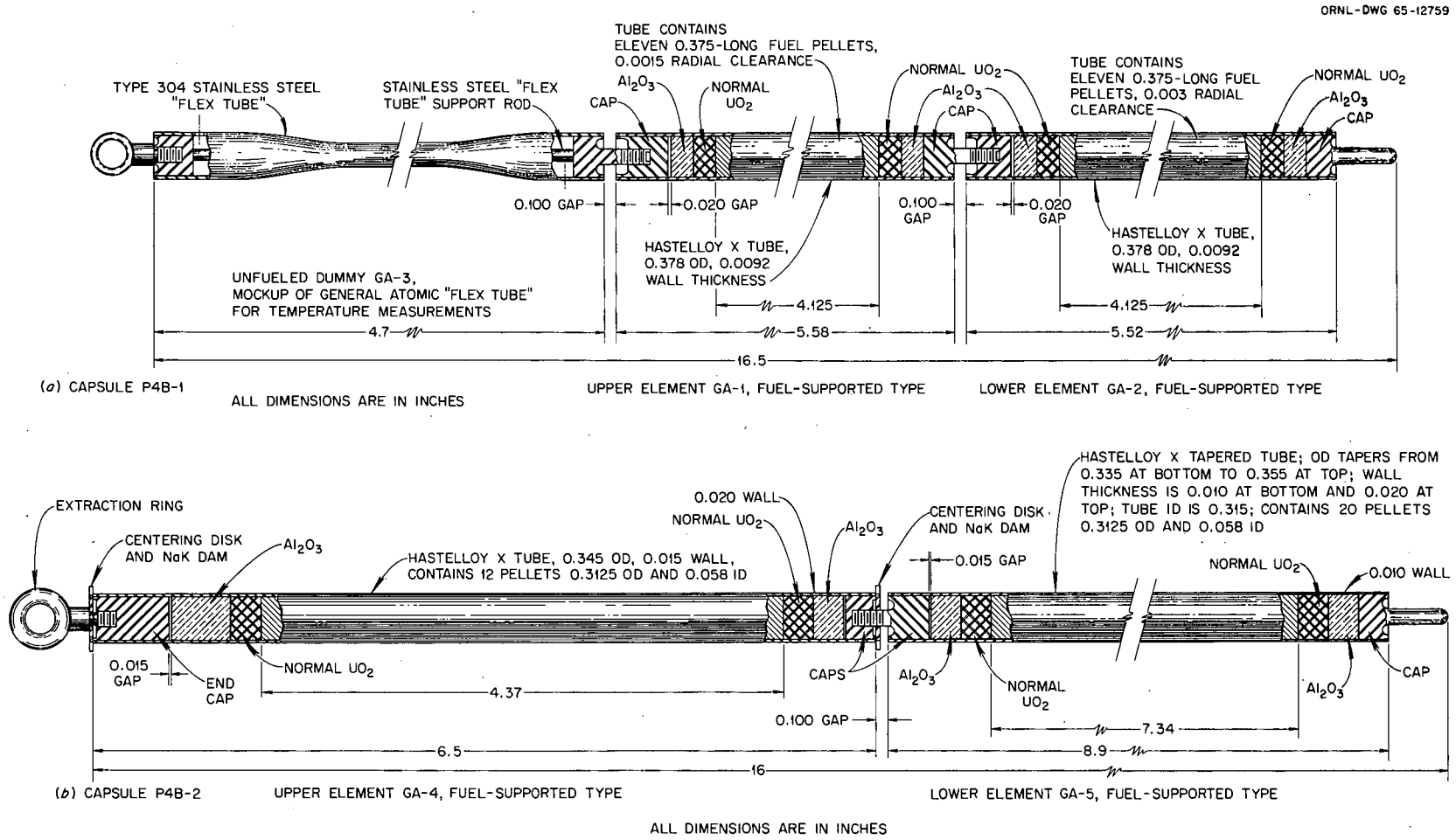

Fig. 6.1. First Fast Gas-Cooled Reactor Test Elements Irradiated in ORR Poolside Facility. Both sets of specimens were supplied by General Atomic. All UO_2 fuel pellets have dished ends and a 0.005-in.-deep groove at midplane.

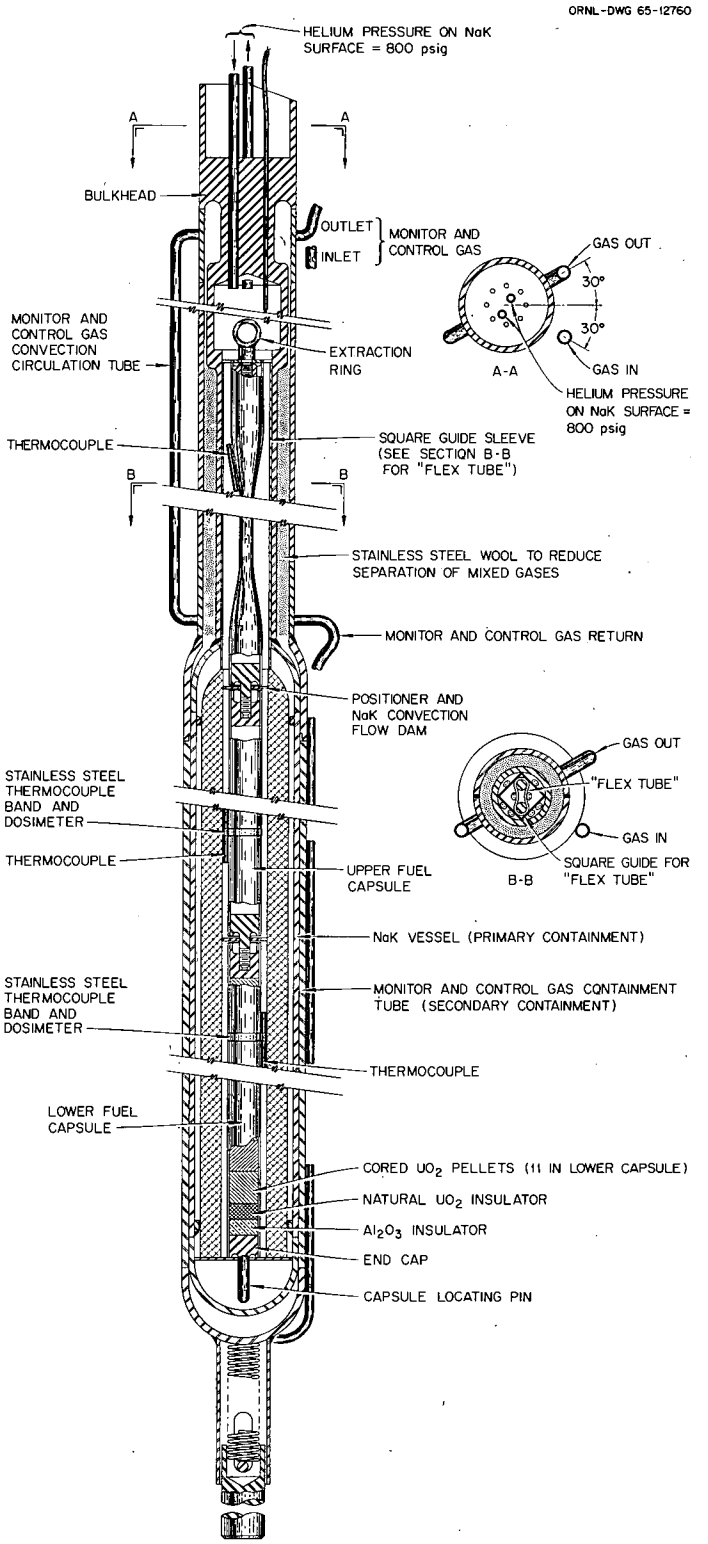

Fig. 6.2. Fast Gas-Cooled Reactor Irradiation Test Assembly P4A-1.

Table 6.1. Summary of Design and Planned Operating Conditions for Fast Gas-Cooled Reactor Fuel Test Capsule P4A-1

ORR poolside position: P4A
Insertion date: August 29, 1965
Estimated removal date: October 17, 1965

Fuel pin	Upper	Lower
Fuel data		
Fuel material	UO_2	UO_2
Fuel supplier	General Atomic	General Atomic
Number of fuel pellets	11	11
Fuel loading		
^{235}U, g	11.507	11.483
Uranium, g	53.028	52.917
UO_2, g	60.249	60.121
Fuel density, % of theoretical	90–91	90–91
^{235}U enrichment, %	21.7	21.7
Power data (calculated)		
Heat rate, kw/ft	20	20
Neutron flux		
Effective thermal flux, neutrons/cm^2·sec	1.37×10^{13}	1.37×10^{13}
Fast flux (>1 Mev), neutrons/cm^2·sec	1.37×10^{12}	1.37×10^{12}
Self-shielding factor	0.500[a]	0.500[a]
Dimensional data		
Fuel pellet OD, in.	0.357	0.355
Fuel pellet ID, in.	0.096	0.096
Fuel can OD, in.	0.378	0.378
Fuel can wall thickness, in.	0.009	0.009
Height of fuel stack, in.	4.134	4.117
Fuel cladding material	Hastelloy X	Hastelloy X
Planned operating conditions		
Maximum fuel cladding temperature, °F (°C)	1400 (760)	1400 (760)
Cladding external pressure, psia	800	800
Assembly drawing number	10392 R 002E	10392 R 002E

[a]As calculated with THERMOS code.

and planned operating conditions for capsule P4A-2 is given in Table 6.2. The NaK-filled irradiation test rig for capsule P4A-2 differs somewhat from that for P4A-1, as shown in Fig. 6.3. It is planned to insert capsule P4A-2 in the ORR during the October 17, 1965 shutdown.

Table 6.2. Summary of Design and Planned Operating Conditions for Fast Gas-Cooled Reactor Fuel Test Capsule P4B-2

ORR poolside position: P4B
Estimated start date: October 22, 1965
Estimated removal date: December 12, 1965

Fuel pin	Upper	Lower
Fuel data		
Fuel material	UO_2	UO_2
Fuel supplier	General Atomic	General Atomic
Number of fuel pellets	12	20
Fuel loading		
^{235}U, g	13.756	23.185
Uranium, g	44.090	74.311
UO_2	50.259	84.726
Fuel density, % of theoretical	90–91	90–91
^{235}U enrichment, %	31.2	31.2
Power data (calculated)		
Heat rate, kw/ft	20	20
Neutron flux		
Effective thermal flux, neutrons/cm^2·sec	1.43×10^{13}	1.43×10^{13}
Fast flux (>1 Mev), neutrons/cm^2·sec	1.43×10^{12}	1.43×10^{12}
Self-shielding factor	0.480[a]	0.480[a]
Dimensional data		
Fuel pellet OD, in.	0.3125	0.3125
Fuel pellet ID, in.	0.058	0.058
Fuel can OD, in.	0.342	0.3346–0.353[b]
Fuel can wall thickness, in.	0.015	0.010–0.020[b]
Height of fuel stack, in.	4.374	7.318
Fuel cladding material	Hastelloy X	Hastelloy X
Planned operating conditions		
Maximum fuel cladding temperature, °F (°C)	1400 (760)	1400 (760)
Cladding pressure, psia	1000	1000
Assembly drawing number	10406 R 002E	10406 R 002E

[a]As calculated with THERMOS code.

[b]Outside diameter of tube machined to produce a variable tube wall thickness that tapers from 20 mils thick at the top to 10 mils at the bottom.

ORNL-DWG 65-12761

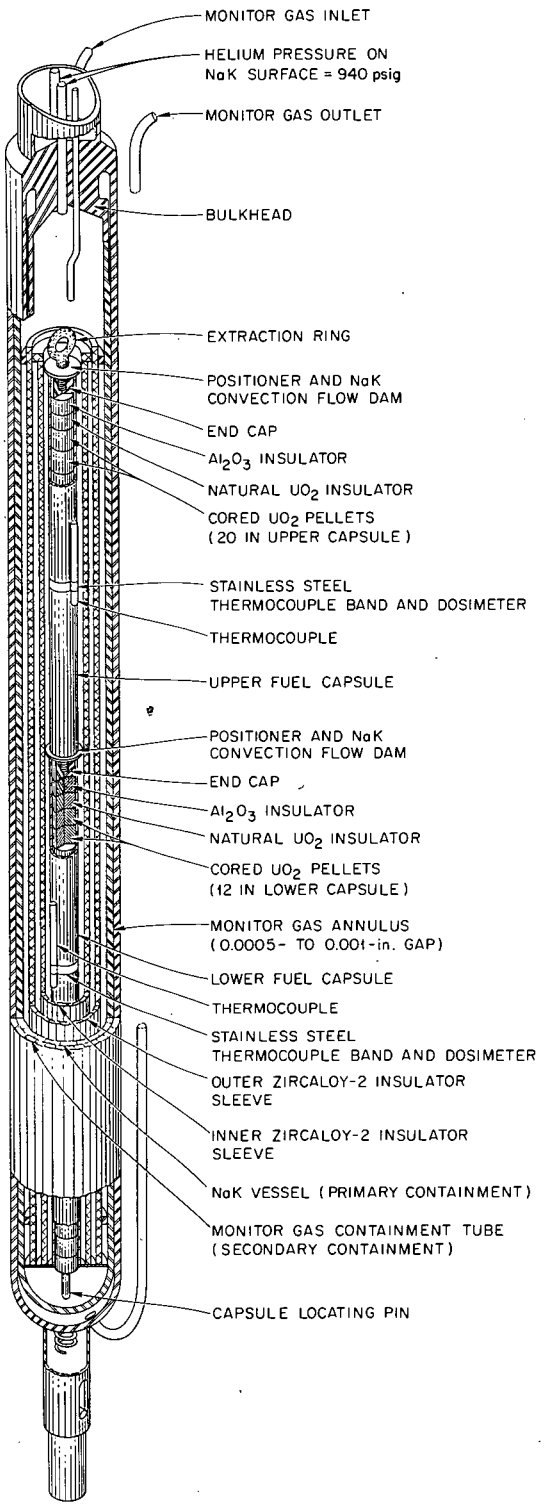

Fig. 6.3. Fast Gas-Cooled Reactor Irradiation Test Assembly P4B-2.

PART 2. EXPERIMENTAL GAS-COOLED REACTOR PROGRAM

7. PERFORMANCE ANALYSES

A. M. Perry W. B. Cottrell

Reactor Commissioning Program

C. A. Preskitt

Our activity in the past reporting period was devoted entirely to supporting and assisting the TVA physics staff in completing a large number of tasks relative to final safety reviews and preparations for the physics commissioning experiments. Calculations were performed and older work was summarized to provide a few remaining results needed for the selection of experimental conditions or initial interpretation of experimental results. The computer codes written for a quick initial data analysis were reviewed and a few improvements are presently being made.

As further preparation for the commissioning experiments, we assisted in the planning and performance of a series of experiments with the unfueled core. These largely consisted of pulsed-neutron experiments with a range of control rod patterns, axial and radial flux traverses with fixed sources, and studies of detector response to determine counting losses. We are presently assisting in the analysis of the data from these experiments.

Graphite–Air Oxidation Studies

J. O. Kolb

In the review of the EGCR hazards evaluation by the ACRS and the AEC Division of Licensing and Regulation, various situations following a rapid depressurization of the primary cooling system were proposed for investigation of core cooling requirements. Investigations completed during this reporting period are described below.

Core Cooling Requirements and Nitrogen Purge Effectiveness for Extreme Coolant Piping Ruptures

A study of circumferential ruptures in the primary loops and emergency cooling loop piping and nozzles was requested by ACRS to determine the worst consequences to the core. Circumferential ruptures had not been considered credible in the EGCR Hazards Summary Report,[1] except at dissimilar metal welds and isolation valve welds in the primary loops. The objective of this study was to determine the convective core cooling that would be required to prevent runaway air oxidation of graphite and excessive fuel cladding temperatures; in order to maintain the cladding as a barrier to fission-product release, the cladding temperature must not exceed 1800°F (982°C).

It was recognized at the outset of this study that piping ruptures near the pressure vessel could markedly reduce the effectiveness of the nitrogen purge from the emergency cooling loop. Investigation of the required time of continued circulation from the main blowers after a coolant depressurization accident and before circulating air from the emergency cooling loop was therefore given major emphasis. Consideration of nitrogen purge effectiveness and required air concentrations for the various core flow rates from emergency cooling loop operation were included in this study for situations when neither main blower was available after a depressurization accident.

Rupture Locations. The locations of coolant piping ruptures considered in this study were determined by the EGCR Hazards Evaluation Team. They were chosen so that core flow and nitrogen purge effectiveness were reduced the greatest amount. The deleterious effects of these piping ruptures on core flow and purge effectiveness satisfy the ACRS request with respect to core cooling and high core temperatures.

Of the five rupture locations chosen, three were in the primary cooling loop and two in the emergency cooling loop. Ruptures 1 and 2 were in the hot leg of the primary cooling circuit at the temperature-barrier coolant connection and the match line with the hot-leg pipe chase,

[1]Oak Ridge Operations Office, Experimental Gas-Cooled Reactor Final Hazards Summary Report, USAEC Report ORO-586, Oct. 10, 1962.

respectively. Rupture 3 was in the primary cooling circuit cold leg near the match line with the cold-leg pipe chase. These three circumferential ruptures in the reactor vault were assumed to have a completely offset configuration with chase air flow impinging on the pressure-vessel side of the rupture. In addition, rupture 1 would allow core bypass flow through the temperature barrier coolant annulus on the hot-leg nozzle. Completely offset ruptures were also assumed in the two failures in the emergency cooling loop doubly contained pipe. Rupture 4 was at the emergency cooling loop hot-leg nozzle so that there could be core bypass flow through the temperature-barrier cooling annulus. Rupture 5 was at the beginning of the first horizontal run of the emergency cooling loop cold-leg piping; nitrogen purge flow would discharge from the rupture before removing any core heat. Completely offset ruptures at these locations, though physically impossible because of pipe movement limits, would have deleterious effects on core cooling that would not be exceeded by the effects of ruptures at any other piping location because of the close proximity of the ruptures to the pressure vessel.

Nitrogen Purge Effectiveness. Nitrogen purge-gas flows of 1000 scfm for 1 1/2 hr followed by 200 scfm for 70 hr are the design capability of the emergency cooling loop. These are the requirements for maintaining an air concentration of less than 1 wt % in the core coolant in the event of the ruptures assumed to be credible in the EGCR Hazards Summary Report.[1] Purge-gas flow is concurrent with the core flow provided by the emergency cooling loop and hence is used only if adequate core flow cannot be supplied by the main coolant blowers.

The purge effectiveness of a 200-scfm nitrogen flow was examined for the ruptures described above. Forced circulation flows of 7500 and 2400 scfm are estimated for the hot- and cold-leg pipe chases, respectively, under containment isolation conditions, with flow being toward the reactor vault. Purge gas discharging at ruptures 1, 2, and 3 would have to prevent mixing of the chase air flow into the pressure vessel plenums. Since chase air flow could impinge directly into an exposed pipe if there were a complete offset of the ruptured pipe ends, the chase air velocity head would far exceed the velocity head of purge gas discharging uniformly across the pipe at these three rupture locations.

Therefore a mechanism was sought that would dissipate the chase air velocity head before reaching the interior of the pressure vessel. Energy losses by friction or mixing in the short nozzle length available could not be demonstrated to be sufficient to dissipate the chase air velocity head. Therefore it is concluded that air concentrations of several percent by volume may be attained in the core coolant if core cooling is provided by the emergency cooling loop for ruptures at locations 1, 2, or 3.

The nitrogen purge flow could be similarly ineffective in maintaining low air concentrations in the core coolant for the complete rupture of the doubly contained emergency cooling loop piping at locations 4 or 5. At these locations, external gas would be mixed with the nitrogen in the emergency cooling loop and be drawn into the recirculating flow. Since no mechanism exists to prevent air from returning to the rupture location after being displaced during the depressurization, a low equilibrium air concentration in the core coolant cannot be guaranteed for double-ended ruptures anywhere in the hot- or cold-leg piping of the emergency cooling loop.

The discussion here is concerned with preventing air concentrations in excess of several weight percent in the core coolant during operation of the emergency cooling loop. The air concentration in the core coolant would probably reach a level much less than 100%, even for the extreme rupture conditions assumed in this study. Purge flow plus oxidation removal of oxygen would ultimately balance oxygen inflow through a rupture. However, low air concentrations have been the basis for ultimately cooling the core with emergency cooling loop flows as low as 8000 lb of nitrogen per hour. Therefore with ruptures causing unacceptable air inleakage, the emergency cooling loop can only be utilized after core temperatures have been reduced (<800°F, 427°C) by cooling with a main blower. The investigation of coupled operation of main blowers and the emergency cooling loop is described in the following sections.

Core Flow from Emergency Cooling Loop Operation Under Various Conditions. Reasonable core flows for emergency cooling loop operation both with and without nitrogen purge flow were developed. A wide range of

core flow values exists because (1) emergency cooling loop operating conditions are determined by containment building pressure and the hot-leg gas temperature, (2) core flow is augmented by the purge-gas flow, and (3) there is bypass flow around the core through the temperature-barrier flow path for ruptures involving temperature-barrier locations 1 and 4.

Core flow information used in this study was based on either the use of nitrogen purge or no purge flow; the former situation was used to investigate acceptable air concentrations in the core coolant and the latter to investigate cooling with air circulated first by a main blower and then by the emergency cooling loop. Core flows delivered by the emergency cooling loop as a function of loop pressure and hot-leg temperature were obtained from design studies in which core flow was calculated with and without 1000-scfm nitrogen purge flow. The scheduled nitrogen purge flows of 1000 and 200 scfm correspond to mass flows of 4680 and 936 lb/hr, which would contribute to the core flow for rupture locations 1, 2, and 4. Core bypass flows for locations 1 and 4 were based on approximately 18 and 25% of the total flow, respectively, from TVA calculations.[2] A core flow was then estimated for a given situation by (1) obtaining the emergency cooling loop flow based on the containment pressure and the hot-leg outlet temperature, (2) adding the purge flow to the emergency cooling loop flow (for ruptures 1, 2, or 4), and (3) reducing the result of step 2 by the percentage of bypass flow (for ruptures 1 or 4). The net core flows obtained for all rupture locations with this procedure are summarized in Table 7.1 for situations with and without emergency cooling loop purge flow; containment pressure and hot-leg temperature conditions for which the core flows were estimated are included in the table.

The containment pressure and hot-leg temperature would actually vary during a particular accident. The 16-psia containment pressure is a reasonable value that requires no more than the helium released on depressurization for the accident pressure rise. A hot-leg temperature of 1100°F (593°C) was used for locations 1 and 2 with purge flow to improve the core flow and to see whether the emergency cooling loop flow would

---

[2] J. A. Coffey, Pressure Differentials and Damage to EGCR Components Due to Emergency Cooling Loop Nozzle Failures, Report 64-31 EAS, Tennessee Valley Authority, Oct. 1, 1964.

Table 7.1. Core Flows for Emergency Cooling Loop Operation After Ruptures at Various Locations

Rupture Location	Flow With Purge	Flow Without Purge
1	13,000 lb/hr during 1000-scfm purge and 9,000 lb/hr during 200-scfm purge (16 psia, 1100°F, 593°C)	8,000 lb/hr (16 psia, 1200°F, 649°C)
2	15,000 lb/hr during 1000-scfm purge and 11,000 lb/hr during 200-scfm purge (16 psia, 1100°F, 593°C)	10,000 lb/hr (16 psia, 1200°F, 649°C)
3	10,000 lb/hr (16 psia, 1100°F, 593°C)	10,000 lb/hr (16 psia, 1200°F, 649°C)
4	10,000 lb/hr during 1000-scfm purge and 6,750 lb/hr during 200-scfm purge (14.4 psia, 1350°F, 732°C)	6,000 lb/hr (14.4 psia, 1350°F, 732°C)
5	8,000 lb/hr (14.4 psia, 1350°F, 732°C)	8,000 lb/hr (14.4 psia, 1350°F, 732°C)

be satisfactory under somewhat favorable conditions. The most adverse conditions of 14.4 psia and 1350°F (732°C) were used for locations 4 and 5 without purge flow to investigate the maximum time requirement for main blower air circulation. The conditions of 16 psia and 1200°F (649°C) were used for locations 2 and 3 without purge flow so that an air flow of 10,000 lb/hr could be easily satisfied during emergency cooling loop operation following main blower operation.

Graphite-Air Oxidation Calculations. Core coolant flow requirements for the conditions of this study were determined by calculations performed with the EGCR Graphite Oxidation IBM-7090 Code. Variables determining graphite oxidation heat generation were assumed, as follows:

1. a reaction rate order, with respect to oxygen partial pressure, of 0.6,
2. a 50-kcal/mole activation-energy oxidation rate for graphite in air of twice the rate determined by Hanford experiments for unirradiated graphite (see Fig. 7.1),

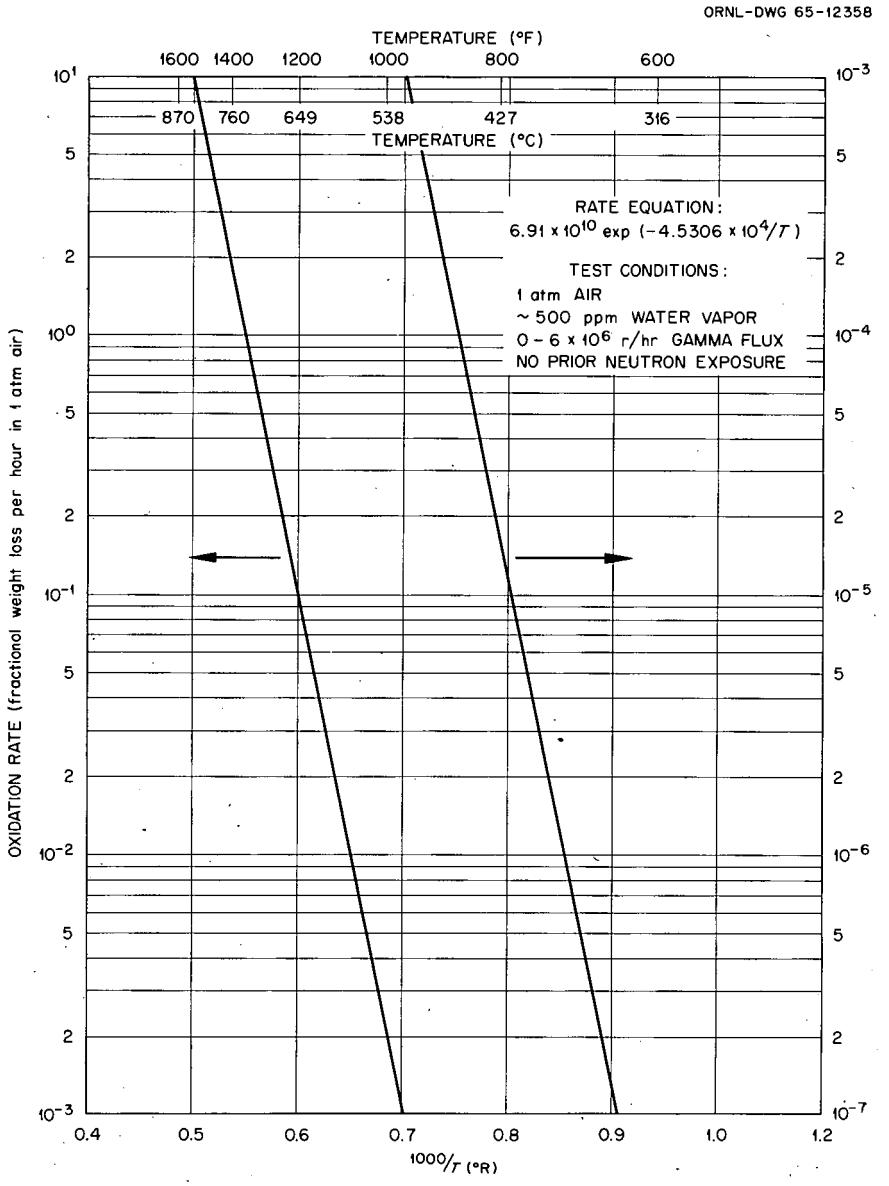

Fig. 7.1. Homogeneous Oxidation Rate of EGCR Moderator Block Graphite from Hanford Experimental Data.

3. flow in the annulus between the graphite sleeve and moderator block up to 10% of the total channel flow.

The first part of the calculational investigation dealt with the possibility of using the emergency cooling loop to purge and cool the core with coolant air concentrations in excess of 1 wt %. The highest core flows were obtained with ruptures at locations 1 and 2, as in Table 7.1; hence, flows of 13,000 and 15,000 lb/hr for 1 1/2 hr were followed

by 9,000 and 11,000 lb/hr, respectively, in calculations for a maximum power channel. Initial temperatures (see curve 2, Fig. 7.2, for sleeve temperatures) and afterheat for 1/2 hr after scram were used in calculations covering oxygen concentrations from 2 to 15% of normal air. Temperature profiles and oxidation depth conditions from the 15,000 and 13,000 lb/hr calculations were used as initial values for the 11,000- and 9,000-lb/hr calculations. The results for air concentrations of 5% and above showed runaway temperature rises; with 2% air, no runaway oxidation occurred, but the outlet coolant temperature exceeded the 1100°F (593°C) outlet temperature assumption involving the available core flow. Therefore the highest core flows estimated for the ruptures could not be demonstrated to be applicable for long-term core cooling with air concentrations of 2% or higher.

Maximum power channel calculations were then performed for air from main blower operation followed by emergency cooling loop operation. Air flows of 30,000 lb/hr at 30 sec and 50,000 and 100,000 lb/hr at 1 hr

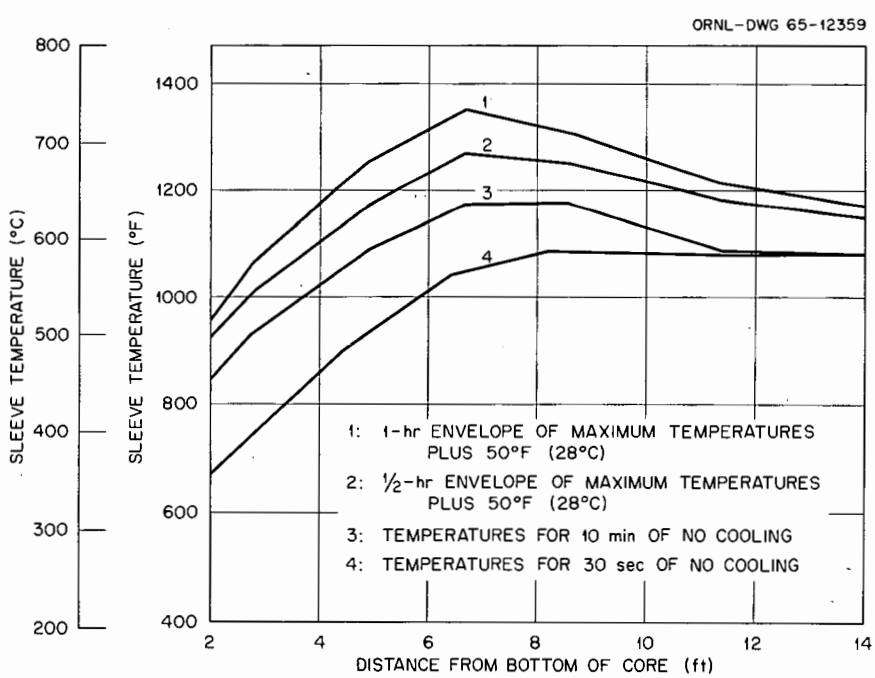

Fig. 7.2. Sleeve Temperature Profiles for Graphite Oxidation Calculations.

after scram were used in cases listed in Table 7.2 to obtain initial conditions for calculations with emergency cooling loop flows of 8,000 and 10,000 lb/hr. Initial sleeve temperatures for the 30-sec delay situation are shown in Fig. 7.2, curve 4. For the 1-hr delay situation, initial sleeve temperatures were reduced 50°F (28°C) below curve 2 of Fig. 7.2 to remove an arbitrary 50°F (28°C) increase added for conservatism in previous studies.[3] Calculations were performed with an inlet coolant temperature of 510°F (266°C) and 8,000 and 10,000 lb/hr emergency cooling loop flows starting from 6 to 30 hr after scram. Cases 14-N3, 56-D5, 57-D5, and 56-D7 (see Table 7.2) determined the earliest times after scram for which 10,000 and 8,000 lb/hr of air flow would be adequate. The operating time requirements on a main blower are summarized in Table 7.3.

Table 7.2. Core Cooling Conditions for Graphite Oxidation Calculations

Maximum power channel coolant: air

Calculation Case	Core Flow (lb/hr)	Central Channel Flow (lb/hr)	Annulus Flow (lb/hr)	Channel Heat Transfer Coefficient (Btu/hr·ft^2·°F)	Inlet Coolant Temperature		Time After Scram at Start of Transient
					°F	°C	
14-N	30,000	156.2	17.35	8.26	510	266	30 sec
56-D	50,000	258.0	28.66	12.2	510	266	1.0 hr
57-D	100,000	516.0	57.4	21.2	510	266	1.0 hr
56-E	50,000	258.0	28.66	12.2	350	177	1.0 hr
57-E	100,000	516.0	57.4	21.2	350	177	1.0 hr
14-N3	10,000	51.66	5.74	3.42	250	121	10.0 hr
56-D5	10,000	51.66	5.74	3.42	250	121	15.0 hr
57-D5	10,000	51.66	5.74	3.42	250	121	10.0 hr
56-D7	8,000	41.66	4.63	2.92	250	121	30.0 hr
56-E1	10,000	51.66	5.74	3.42	250	121	12.0 hr
57-E1	10,000	51.66	5.74	3.42	250	121	6.0 hr

Cases 56-E and 57-E, Table 7.2, for a 350°F (177°C) inlet coolant temperature, were used to investigate the incentive for lowering the inlet coolant temperature by reducing the steam generator pressure during

[3]J. O. Kolb and W. B. Cottrell, Graphite Oxidation, pp. 23–37, GCRP Semiann. Progr. Rept. Sept. 30, 1962, USAEC Report ORNL-3372, Oak Ridge National Laboratory.

Table 7.3. Earliest Time and Required Emergency Cooling Loop Air Flow for Various Main Blower Operating Conditions

Main Blower Flow Provided	Time (hours after scram)		
	For 10,000-lb/hr Flow	For 8,000-lb/hr Flow	For 6,000-lb/hr Flow
30,000 lb/hr starting 30 sec after scram	10	30	~100
50,000 lb/hr starting 1 hr after scram	15	30	~100
100,000 lb/hr starting 1 hr after scram	10	30	~100

the first hour after scram. The "runaway" results of cases 56-E1 and 57-E1 showed that 50,000 or 100,000-lb/hr time requirements would not be reduced from 15 to 12 hr or from 10 to 6 hr after scram, respectively, with 10,000-lb/hr flow from the emergency cooling loop. Hence the lower core inlet temperature condition would not reduce the main blower time requirement more than several hours for the situations investigated.

The main blower time requirement of 100 hr after scram was estimated for the 6000-lb/hr emergency cooling loop flow with a rupture at location 4. This time estimate was made by simply determining the time after scram when the core afterheat could be removed by 6000-lb/hr flow with a 250 to 800°F (121 to 427°C) temperature rise. This approach is valid because graphite oxidation heat generation is relatively unimportant for core temperatures up to 800°F (427°C). Hence core temperatures can be allowed to increase to the level required for removal of afterheat without any further concern for runaway graphite oxidation.

Discussion and Conclusions. This study brings into focus the limitations of the emergency cooling loop when the credibility of the initial system fault is disregarded so that the cooling and purge effectiveness are severely reduced. The emergency cooling loop was not designed to function effectively for all possible primary helium system faults, and

these initial failures are extremely unlikely because of the physical restraint provided to prevent significant displacement of the helium piping and the double wall design of the emergency cooling loop piping. If the emergency cooling loop were used as the initial preventive measure to control the consequences of the hypothetical accidents considered, uncontrolled graphite oxidation or excessive temperatures might occur. Another important area is the operating time required of a main blower on air before emergency cooling loop circulating air can be safely used. The main conclusion in this area is that 10 to 15 hr of main blower operation is sufficient for all ruptures considered in the primary cooling system and the emergency cooling loop except catastrophic ruptures of the hot-leg nozzles that allow flow bypass through the temperature barrier. As the bypass flow increases to a limit of about 25% of the total flow, the main blower operating time increases to about four days.

Effect of Increased Oxidation Rate, Higher Initial Temperatures, and Increased Oxidation Depth on Required Air Coolant Flow

The ACRS review of the graphite–air oxidation analysis has been mainly concerned with the degree of conservatism allowable in the air flow required to control graphite oxidation. Variables of particular interest were the oxidation rate, initial temperatures, and the initial oxidation depth for which the air coolant could be used and still control the oxidation heat generation.

Initial Graphite Temperatures. In the initial investigation of air flows required to prevent runaway oxidation, it was decided to consider time delays up to 1 hr in supplying flow from the main compressor. This extended period of uncontrolled core thermodynamic conditions allowed a wide variation in the graphite temperatures the air cooling was required to control. The variations in air flows and inlet air temperatures were determined by mechanistically examining the interrelated effects of main and vessel-cooling compressor operation, main loop valve positions, and location of the piping rupture in the main coolant loop. A set of calculations was then performed for the corresponding range of core flows, 0 to 15,000 lb/hr, for the first hour after scram.[3] The oxidation rate used was the Hanford recommended rate of twice the experimental rate

observed for unirradiated block graphite, with the sleeve rate one-half the rate for the block.

Core temperature profiles, illustrated by the sleeve profiles in Fig. 7.2, were then determined for no cooling for 30 sec and 10 min after scram and for an envelope 50°F (28°C) higher than any calculated temperatures at 1/2 and 1 hr after scram. [The arbitrary 50°F (28°C) increase at the 1300°F (704°C) level results in an oxidation rate increase of about a factor of 2.] Maximum graphite temperatures during the first hour after scram varied from 1085 to 1350°F (575 to 732°C) in calculations to determine required air flows. These calculations also included consideration of annulus flows up to 15% of total flow to allow for accidental increased annulus flow. Core flows required at 30 sec, 1/2 hr, and 1 hr after scram were 30,000, 50,000, and 60,000 lb/hr, respectively, with up to 15% annulus flow and the initial temperature profiles shown in Fig. 7.2 (ref. 4).

A series of calculations was then performed to indicate the effect of increased initial temperatures compared with those used in the foregoing analyses. Common conditions assumed were 6% flow to the annulus, a normal oxidation rate of twice the Hanford experimental rate of Fig. 7.1 for a 50-kcal/mole activation energy and a 0.6 reaction rate order. Arbitrary temperature increases over the entire core were applied to the 10-min and 1-hr temperature profiles of Fig. 7.2. Figure 7.3 shows the required core air flow increases from 25,000 to 90,000 lb/hr for maximum sleeve temperatures increased from 1175 to 1375°F (635 to 745°C) at 10 min after scram. Similarly 90,000 lb/hr is required to control a maximum sleeve temperature of 1400°F (760°C) [50°F (28°C) added to curve 1 of Fig. 7.2] at 1 hr after scram.

Increased Oxidation Rate. The effect of increased oxidation rates of four and eight times the rate for unirradiated graphite was examined for various temperature conditions at 10 min and 1 hr after scram. A 0.6 reaction rate order and an annulus flow of 10% of the normal flow,

---

[4]J. O. Kolb, Graphite Oxidation in the Event of the Maximum Credible Accident, pp. 32–39, GCRP Semiann. Progr. Rept. Sept. 30, 1963, USAEC Report ORNL-3523, Oak Ridge National Laboratory.

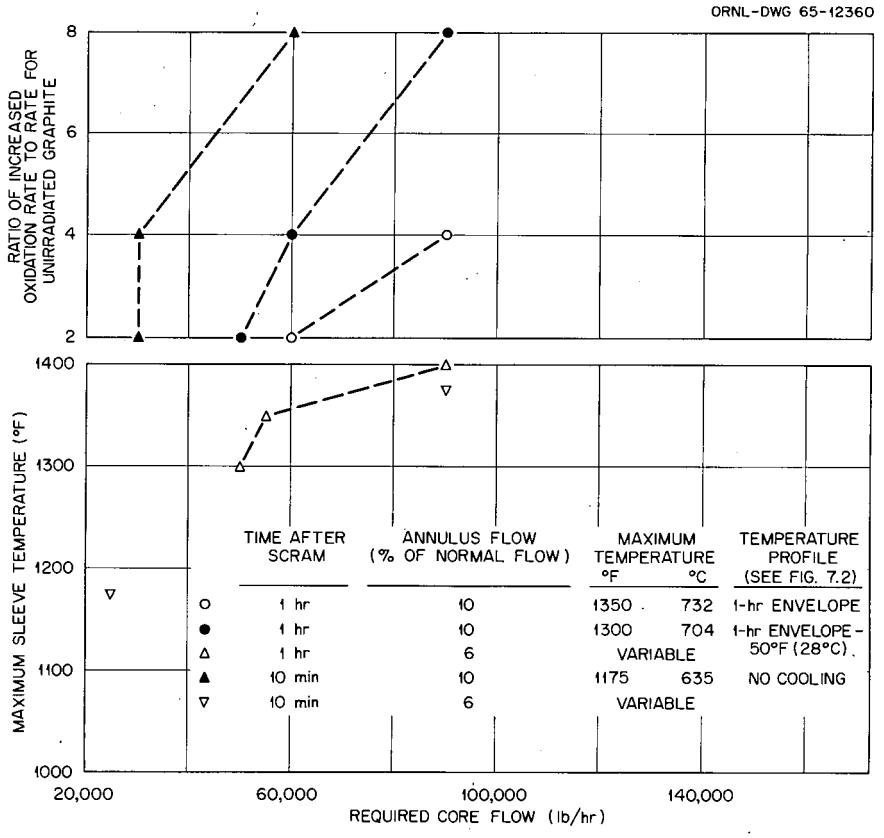

Fig. 7.3. Core Flow Required to Control Increased Temperatures and Oxidation Rates.

which allows for the most pessimistic annulus flow situation, were assumed for these calculations. Figure 7.3 shows the core air flow required to control initial temperatures up to 1350°F (732°C) for curve 1 of Fig. 7.2. For the "1-hr-envelope" initial temperature condition, the required core air flow exceeds 120,000 lb/hr with an oxidation rate increased by a factor of 8. Since the air flow available from one main coolant compressor at 100% speed may not exceed 120,000 lb/hr, the required flow value was outside the achievable range and was not determined.

The calculational results summarized in Fig. 7.3 demonstrate that required air flows become more sensitive to initial temperature with increased oxidation rate conditions. A single main compressor operating at 100% speed will provide sufficient air flow (80,000 lb/hr minimum) to cool all core channels except those with abnormally high graphite temperatures of approximately 1375°F (745°C) or 75°F (42°C) hotter than the

maximum estimated temperature at 1 hr after scram. The same core flow initiated 10 min or 1 hr after scram can control oxidation at rates up to eight and four times the Hanford experimental oxidation rate, respectively.

Oxidation Depth. The effective oxidation depth behavior for EGCR graphite has been determined by Hanford experiments, as previously described.[3] Based on the work of Robinson[5] with PGA graphite, the oxidation depth at a given temperature and oxidation rate was found to increase linearly with increased oxidation in air. This increasing oxidation depth results from the unblocking of closed pores within the graphite as oxidation occurs. Hence, decreased resistance to diffusive flow of oxygen into the graphite occurs in the pore-diffusion-controlled range of oxidation, above approximately 800°F (427°C), just as bulk oxidation rates increase during the first 5% burnoff for oxidation controlled by the chemical reaction rate at low temperatures, below approximately 800°F (427°C).[6]

A depth parameter, A, which increases from an initial value for exposure to oxidizing contaminants in the helium coolant, was evaluated from the first set of calculations described above for oxidizing conditions during the first 1/2 and 1 hr after scram. Table 7.4 summarizes the values of A determined for these situations and also Robinson's conservative value for PGA graphite.

The value of A increased from the initial value of 0.005 to the 0.010 and 0.015 values only in the highest temperature (middle) region of a maximum power channel. At the top and bottom of the channel, the value of A, and hence the oxidation depth, was overestimated with the 0.010 and 0.015 values, respectively, in calculations for 1/2 and 1 hr after scram.

The effect of an increased oxidation depth factor was evaluated by considering the Robinson A value in calculations to determine the

---

[5]P. J. Robinson, The Effects of Diffusional Control of Oxidation of Graphite on the Highest Safe Temperature in Air, UKAEA Report 143(RD/W), 1959.

[6]P. T. Walker et al., Gas Reactions of Carbon, Advances in Catalysis, XI: 133–221, Academic Press, 1959.

Table 7.4. Oxidation Depth Factors Used in EGCR Calculations

A, Depth Factor ($cm/hr^{1/2}$)	Oxidizing Conditions
0.0023	Unoxidized EGCR graphite
0.005	EGCR graphite oxidized to approximately 1% burnoff during 20-year moderator exposure to coolant
0.010	Maximum oxidation during first 1/2 hr after depressurization accident
0.015	Maximum oxidation during first hour after depressurization accident
0.033	Robinson value for oxidized PGA graphite[a]

[a]See Ref. 5.

required air flow 1 hr after scram. Calculation conditions used were 10% annulus flow, 0.6 reaction rate order, and a 50-kcal/mole activation-energy oxidation rate equal to twice the Hanford experimental rate. The initial sleeve temperatures were the conservative envelope of curve 1 of Fig. 7.2. For these conditions and an initial depth factor of 0.015, the required core air flow was determined to be 60,000 lb/hr, as in Fig. 7.3. For the Robinson value of A, a core flow of 90,000 lb/hr was found to be required to control graphite temperatures. Therefore more than doubling the initial value of A increased the required core air flow by only about 50% for the conservative conditions of these calculations.

8. COMPONENT DEVELOPMENT AND TESTING

H. W. Savage J. H. Coobs

Compressor Shaft Seals

E. R. Taylor F. H. Neill

The operation of the shaft seals of the EGCR main blowers and the vessel cooling compressors during the vendor's acceptance testing indicated operating limitations and other peculiarities that required additional investigation. Two serious problems were spillover of the seal buffering water into the bearing lubrication system when the shaft was stationary and spillover of the seal buffering water into the reactor primary coolant system when the shaft was rotating and the reactor system was either depressurized or at subatmospheric pressure. The first difficulty occurred only in the vessel cooling compressor; it did not exist in the main blowers.

The EGCR seal water system as originally designed supplied a pressure ranging from 5 to 10 psi across the atmospheric seal during normal plant operation. When operating at 10 psi, adequate buffering water flowed across the atmospheric seal element for all shaft speeds; however, at lower pressures the flow was reduced sufficiently (<0.5 gpm) that it was considered unsafe to operate the seal. Flows across the atmospheric seal as a function of shaft speed for three differential pressures are shown in Fig. 8.1. In the original vessel cooling compressor seal design, buffering water spilled over into the bearing lubrication system at a differential pressure of from 2 1/2 to 3 1/2 psi across the atmospheric seal with the shaft stationary. Since it was desired to have a 10-psi differential pressure for plant operation, it was not possible to start the compressor without spilling an unknown quantity of water into the lubrication system.

To prevent the spillover, a slinger ring was designed to fit on the compressor shaft outboard of the atmospheric seal. Tests with the slinger ring showed that the pressure differential across the atmospheric seal could be increased to 26 psi, that is, 2.6 times the operating pressure

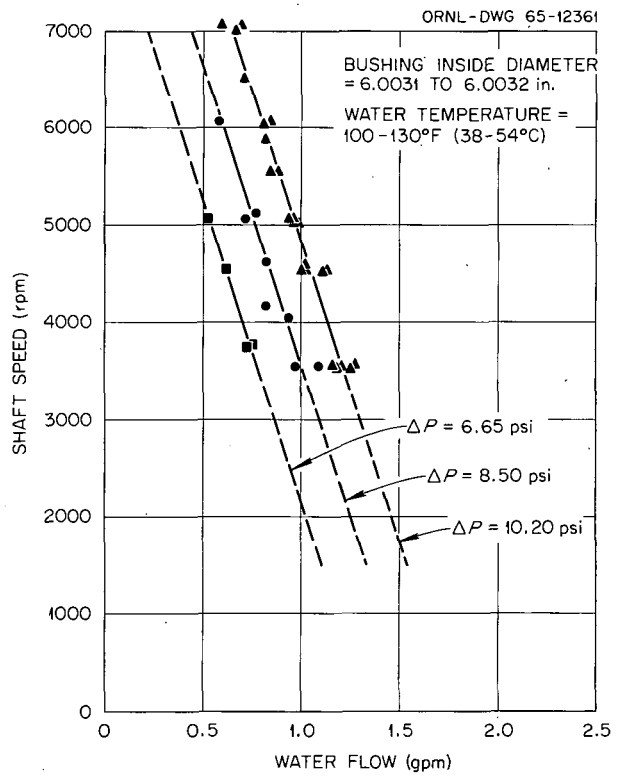

Fig. 8.1. Operating Characteristics of Atmospheric Seal Element on EGCR Vessel Cooling Compressors and Main Coolant Blowers.

differential of the system, without spillover with the shaft stationary. Added system reliability was achieved by installing a water leg in the drain-line secondary seal so that there would be a constant 10-psi pressure across the atmospheric seal element. With the shaft rotating, the rate of spillover was approximately one drop every 5 sec. To prevent this leakage, a "visco"-type seal was designed to replace one of the labyrinth seals of the original design. With the addition of the slinger ring, the visco seal, and the water leg in the seal water system, the spillover of the seal buffering water into the bearing lubrication system was eliminated without making any major changes to the compressors or the seal water system.

The second major problem, spillover of the seal buffering water into the reactor primary coolant system, was associated with the inability of the primary seal element labyrinth to prevent the counterflow of water

without an outward flow of gas. The primary seal element with the integral labyrinth presently installed in the EGCR compressors and blowers was tested in the seal test facility to determine the inadequacy inherent in the design.[1] Depressurization tests (with the shaft rotating) showed that a large quantity of the seal buffering water would enter the reactor when the coolant system pressure was 0 psig. The quantity of water that spilled through the labyrinth was too great to accept as a reasonable flow or spillover rate. During the test it would have been impossible to attempt any subatmospheric operation.

Since the EGCR compressors and blowers had already been fabricated and installed in the plant, the changes or modifications that could be made to the seal were limited to the primary seal element rather than to the seal cavity in the machinery. The approach used involved redesigning the labyrinth to establish a pumping action that would prevent seal water from flowing across this area into the reactor. A visco-type seal was designed that occupies the same space and has the same radial clearance to the shaft as the existing labyrinth. The new seal has a special square thread with 16 thread starts and 1/4 thread per inch. Results of tests with this seal, as presented in Fig. 8.2, show that no leakage of the seal buffering water will occur over the maximum range of subatmospheric pressures predicted for the EGCR blower suction-side seals.[1] It should be noted in Fig. 8.2 that the spillover point was not obtained for speeds above 5000 rpm because of the thrust-bearing reverse-load limitation of the test facility. Points A and B were obtained, however, which show that the visco-type seal can be operated as an integral part of the primary bushing at the maximum speed without any spillover or leakage of the seal buffering water into the reactor coolant system.

---

[1]J. T. Lence, Pressure Drop in the Primary Coolant System at or Near Atmospheric Conditions, Tennessee Valley Authority, EGCR Project Report 65-30 EAS, Rev. 1, dated April 9, 1965, Rev. 2, dated July 16, 1965.

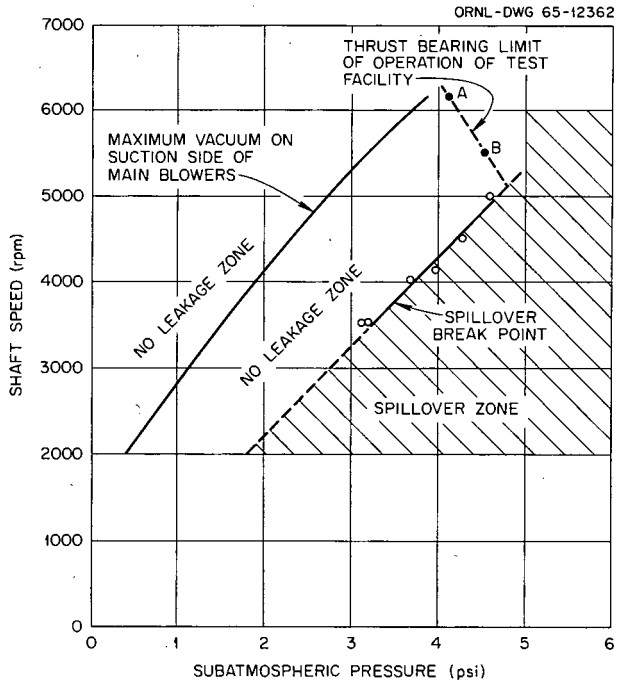

Fig. 8.2. Subatmospheric Operating Characteristics of Primary Seal Element on EGCR Vessel Cooling Compressors and Main Coolant Blowers with Integral Visco-Type Seals.

Control-Rod Drive Test

W. F. Ferguson F. H. Neill

An endurance test was run on the first production-model control-rod drive (General Electric Serial No. 2). Throughout testing the coolant gas pressure, inlet temperature, flow through the mechanism, and purity were controlled to simulate reactor conditions. Table 8.1 shows the desired operating level for each parameter; highest, lowest, and average values for each parameter; and other significant data pertaining to environmental conditions during testing.

The test was performed in accordance with requirements specified by ORNL and approved by the EGCR design team.[2] The test program required that the mechanism be operated through 130 full insertion-withdrawal

[2]G. C. Robinson, Jr., and G. D. Whitman, EGCR Control Rod and Drive Endurance Test, Rev. 2, Feb. 16, 1965, unpublished data.

Table 8.1. Summary of Environmental Conditions During Testing of Control-Rod Drive

	Desired Operating Level	Actual Operating Level[a]		
		High	Low	Average
Coolant gas components, vol %				
Helium		99.930	99.162	99.674
H_2O	0.0200	0.0369	0.0090	0.0211
O_2	Low as practical	0.0030	0.0001	0.0018
Coolant gas inlet temperature, °F (°C)	125 (52)	130.0 (54)	110.0 (43)	126.3 (52)
Coolant gas flow, lb/hr	125	129.6	123.6	125.7
Coolant gas pressure, psig	290	297.5	265.5	289.2
Core bottom temperature, °F (°C)	525 (274)			550 (288)
Core midplane temperature, °F (°C)	700 (371)			680 (360)
Core top, °F (°C)	800 (427)			785 (418)

[a]Data presented are highest, lowest, and average for the entire test period.

cycles, 2000 insertion-withdrawal cycles over 4 in. of rod travel, and 1400 scram cycles. During the course of testing, the drive mechanism was in a helium environment for 84 days. The drive motor was operated for 1018 hr in helium and 4 hr in air, for a total operating time of 1022 hr. A summary of test operations performed is given in Table 8.2.

The performance of the mechanism was entirely satisfactory and in all cases met or exceeded the specified design requirements.[3,4] A comparison of design requirements with test performance is presented in Table 8.3. A report[5] describing the endurance test and presenting pertinent test data was published.

[3]Allis-Chalmers Manufacturing Co., Experimental Gas-Cooled Reactor, Control Rod Drive Mechanism, Specification RD-2, April 26, 1961.

[4]Allis-Chalmers Manufacturing Co., Experimental Gas-Cooled Reactor, Control Rod Drive Mechanism Prototype and Acceptance Test, Specification RD-6, Feb. 27, 1961.

[5]W. F. Ferguson, EGCR Control-Rod-Drive Endurance Test, USAEC Report ORNL-TM-1197, Oak Ridge National Laboratory, September 1965.

Table 8.2. Summary of Test Operations of Control-Rod Drive

Test	Number of Tests	
	Completed During Shakedown	Completed Under Test Conditions
4-in. insertion-withdrawals	18	2014
Full insertion-withdrawals	1	130
Slack cable switch	6	4
Scrams		
Low elevation	188	1025
12-in. elevation		50
36-in. elevation		50
72-in. elevation		50
108-in. elevation		50
144-in. elevation		50
170-in. elevation		153

Table 8.3. Comparison of Design Requirements with Test Data[a] for Control-Rod Drive

Parameter	Design Requirement	Test Performance
Scram clutch response time, msec	<100	37–40
Scram time to 6 ft above crash stop, sec	1 1/2	<1
Scram time to 1 ft above crash stop, sec	8 1/2	<4
Total scram time, sec	23 1/2	<8 1/2
Rod deceleration, g	4 (max)	2.83–3.09
Control-rod speed		
Insertion, normal operation, in./min	1.8 (min)	2.14–2.16
Withdrawal, normal operation, in./min	1.8 (min)	2.14–2.16

[a]Scram data shown for rod fully withdrawn.

Charge-Machine Cylinder-Seal Development

R. E. Helms F. H. Neill

A test program is under way for developing a dynamic seal for the actuating cylinders in the EGCR charge machine. Dynamic seals are

required on the piston and the rod gland of each cylinder. Static seals are required on the cylinder end caps. The purpose of this program is to develop a dynamic seal that will complete 50 cycles with grade-A-purity helium at a pressure of 100 psia as the actuating fluid. A cycle consists of 64 single piston strokes at room temperature, heating of the seal at 350°F (177°C) for 4 hr, and then 22 single strokes of the piston while at 350°F (177°C). The assembly is then cooled to room temperature before starting the next cycle. Helium leakage from the cylinder is not to exceed a standard volume of gas consumed to perform the full stroke operations during each cycle. In addition, the seal material is required to have radiation-damage resistance equal to or better than that of Viton B.

Successful performance of a dynamic seal is dependent upon the surface finish of the mating parts with the seal, the seal geometry, the lubricity of the actuating fluid, the lubricity of the mating surfaces with the seal, the ability of the seal material to withstand radiation, and the compression set and relaxation properties of the material.

Two experimental facilities similar to the one shown in Fig. 8.3 were built to dynamically test a 3-in. Thompkins-Johnson cylinder and a 3-in. Tog-Loc cylinder. These cylinders are typical of the two designed for use in the EGCR charge machine. The Thompkins-Johnson cylinder is a simple stroke-operation actuator, while the Tog-Loc actuator has the characteristic that it can stroke and lock the shaft at both ends. Elastomeric materials are being considered for the seal. Both the 3-in. Thompkins-Johnson cylinder (Fig. 8.4) and the 3-in. Tog-Loc were redesigned to use carbon-wool-impregnated Viton B O-rings on the piston and the rod gland.

The results of the first series of tests are listed in Table 8.4. A nonelastomeric polymer material, SP-1, was used for test 4, and the seals for the piston and the rod were machined in V-ring configuration, as shown in Fig. 8.5. The results of this test are also given in Table 8.4. Based on the tests that have been completed in dry helium at 350°F (177°C), the two most important design parameters that must be considered are the lubricity of the seal mating surfaces and the compression set and

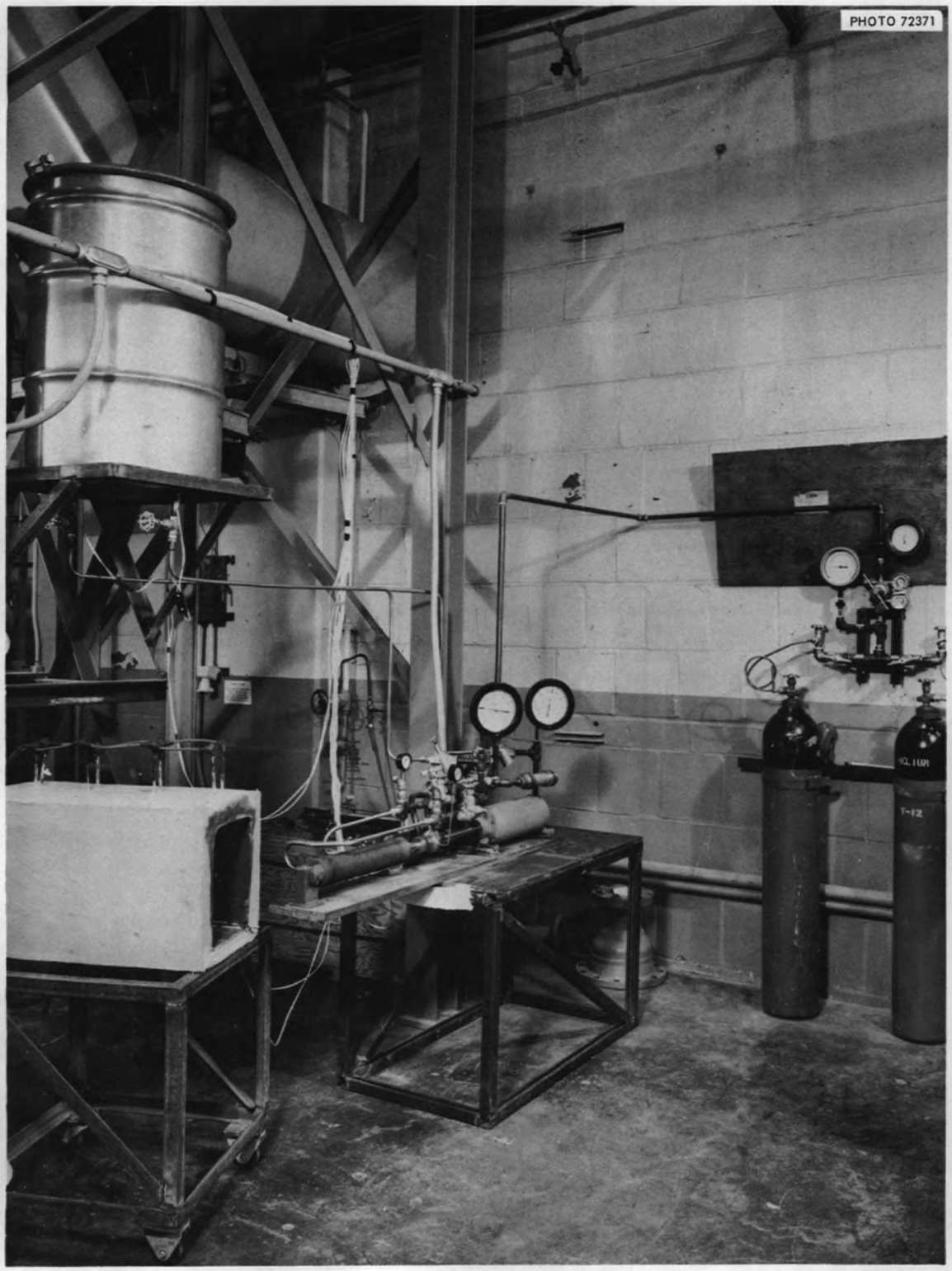

Fig. 8.3. Test Facility for Development of Cylinder Seal for EGCR Charge Machine.

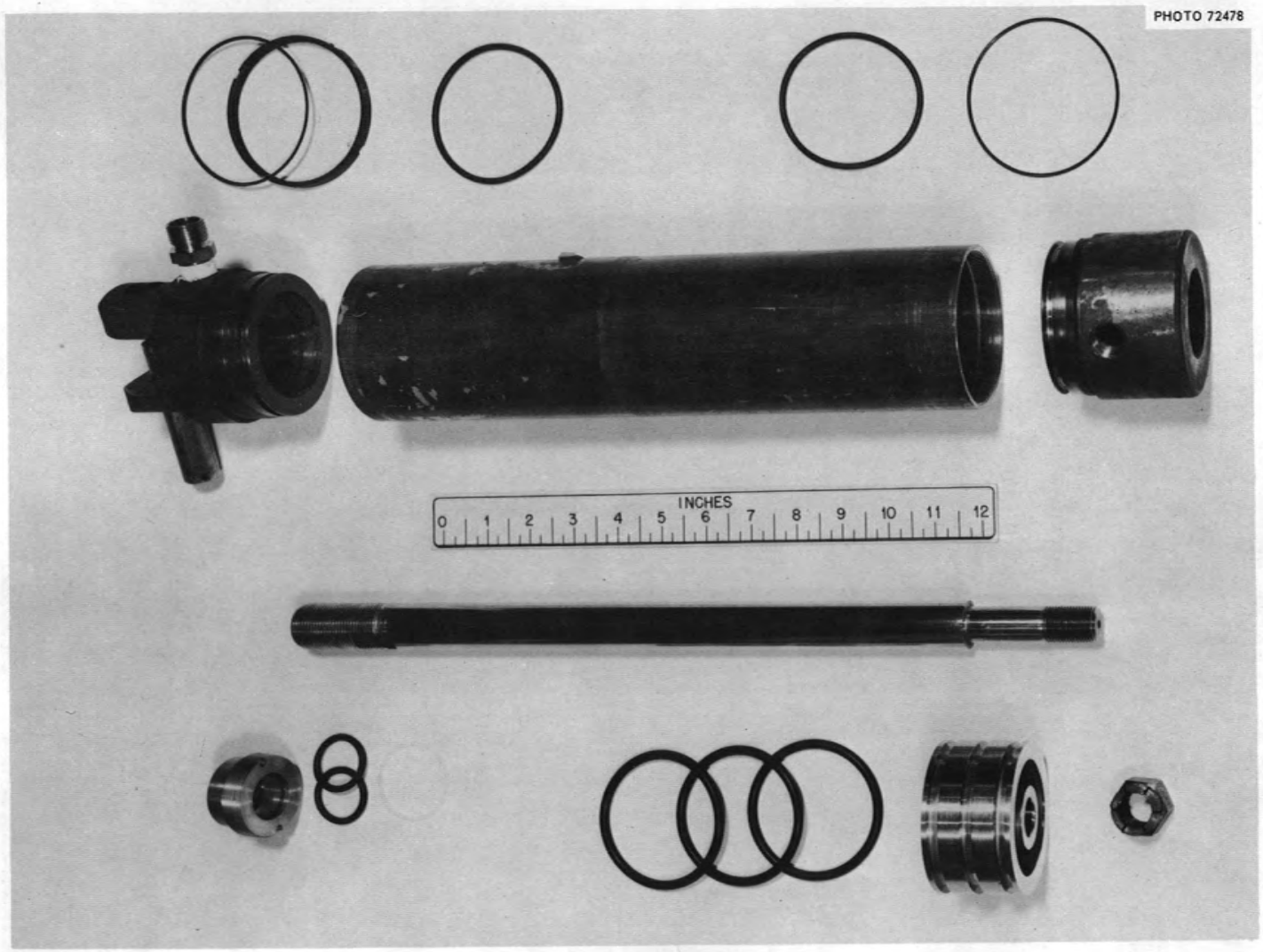

Fig. 8.4. Three-Inch Thompkins-Johnson Cylinder with Carbon-Wool-Impregnated Viton B O-Ring Piston and Rod Seals.

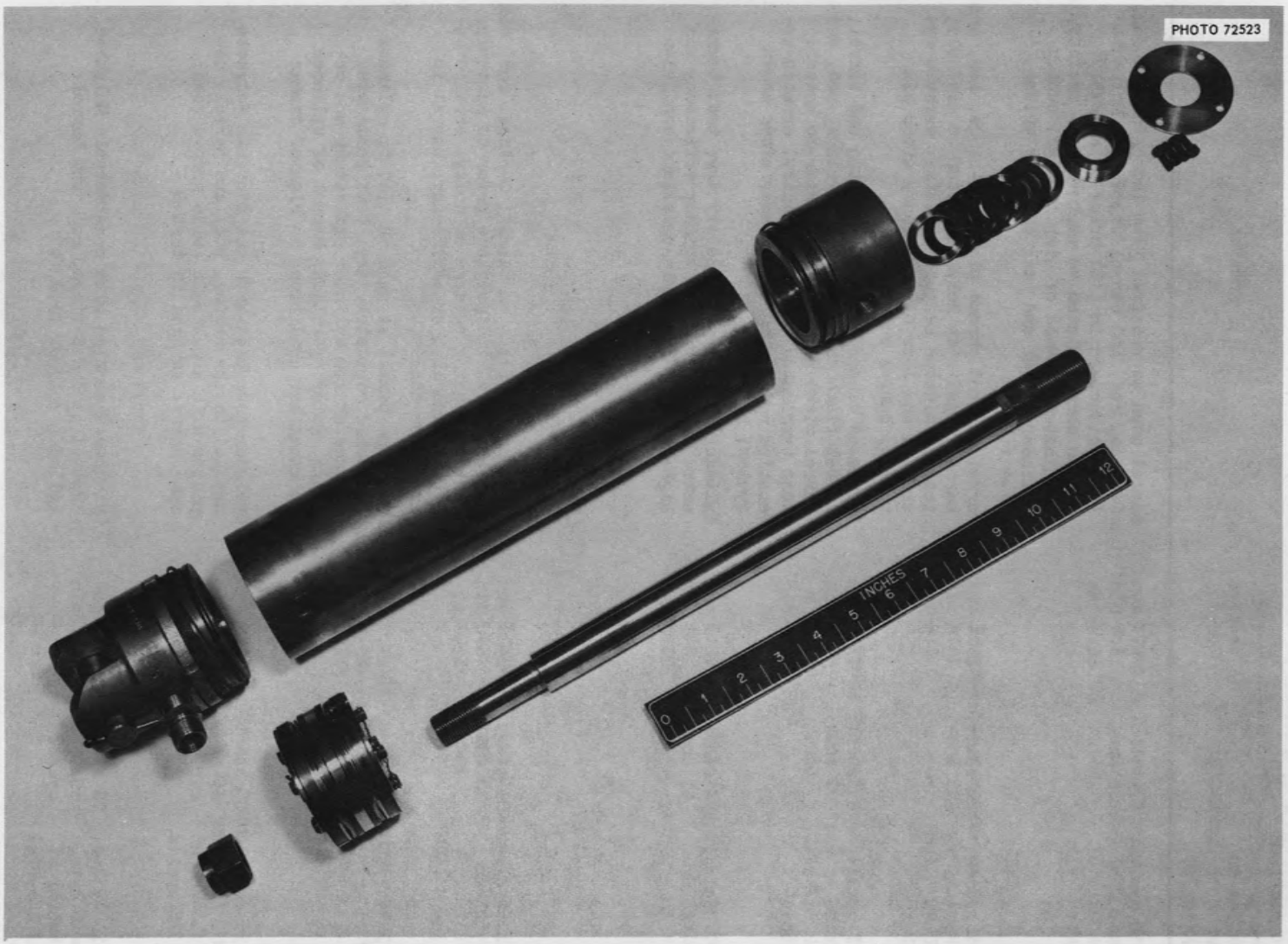

Fig. 8.5. Three-Inch Thompkins-Johnson Cylinder with SP-1 Polymer V-Ring Seals.

Table 8.4. Results of Development Tests on Seals for EGCR Charge Machine Cylinder

Test No.	Test Specimen	Seal Description				Seal Surface Finish (μin.)	Cycles and Exposure Time at 350°F (177°C)	Maximum Cylinder Efficiency (%)	Cold Leakage (ft^3)	Remarks
		Rings	Material	Diametral Squeeze (%)	Width (in.)					
1	3-in.-diam Thompkins-Johnson cylinder with ORNL seal	One O-ring on piston One O-ring on rod	Viton B, carbon-wool impregnated	6.4 on piston 12.6 on rod	0.282 on piston 0.140 on rod	4 to 6 on barrel 10 to 12 on rod	50 cycles, >200 hr	87 start, 83 end	178.5 max 18.5 min 66.31 av	Barrel used as received from Thompkins-Johnson; O-rings, rod, and barrel wiped with Molykote (MoS_2 dispersed in oil) prior to assembly; piston chrome plated to improve seal surface; terminated because of high leakage; scored cylinder barrel and rod; cylinder volume, 17.4 ft^3
2	3-in.-diam Thompkins-Johnson cylinder with ORNL seal	Three O-rings on piston Two O-rings on rod	Viton B, carbon-wool impregnated	9.9 on piston 13.04 on rod	0.220 on piston 0.140 on rod	2 to 3 on barrel 1 to 2 on rod	6 cycles, >24 hr	80 start, 73 end	15.4 max 10.4 min 11.8 av	Barrel and rod chrome plated; O-rings, rod, and barrel wiped with Molykote prior to assembly; test terminated because of noisy, erratic operation and loss of efficiency after six cycles; barrel scored
3	3-in.-diam Thompkins-Johnson cylinder with ORNL seal	Three O-rings on piston Two O-rings on rod	Viton B, carbon-wool impregnated	10.1 on piston 13.0 on rod	0.220 on piston 0.140 on rod	2 on barrel 1 to 2 on rod (same rod as in test 2)	7 cycles, >28 hr	87 start, 79 end	13.1 max 8.3 min 10.2 av	Increased clearance between piston and barrel; barrel flash chrome plated; O-rings, rod, and barrel wiped with Molykote prior to assembly; test terminated because of noisy, erratic operation and loss of efficiency after seven cycles; barrel scored
4	3-in.-diam Thompkins-Johnson cylinder with Republic Aviation seal	Two sets of three V-rings back to back on piston One set of three V-rings on rod	SP-1 polymer	Not available	0.125	4 to 6 on barrel 10 to 12 on rod	7 cycles, >28 hr	78 start, 65 end	70.5 max 8.5 min 28.0 av	Cylinder assembled completely dry; test terminated because of low cylinder efficiency and high leakage; barrel in excellent condition
5	3-in.-diam Thompkins-Johnson cylinder with ORNL seal	Three O-rings on piston Two O-rings on rod	Viton B, carbon-wool impregnated	10.1 on piston 13.0 on rod	0.220 on piston 0.140 on rod	1 1/2 to 2 on barrel 1 to 2 on rod (same rod as in test 3)	25 cycles, 100 hr	84 start, 83 end	14.9 max 6.0 min 10.8 av	Flash chrome plate on barrel; O-rings, rod, and barrel wiped with Molykote prior to assembly; test terminated because of noisy, erratic operation and loss of efficiency; barrel in excellent condition
6	3-in.-diam Thompkins-Johnson cylinder with ORNL seal	Three O-rings on pistron Two O-rings on rod	Viton B, carbon-wool impregnated	10.1 on piston 13.0 on rod	0.220 on piston 0.140 on rod	1 1/2 to 2 on barrel 1 to 2 on rod (same barrel and rod as in test 5)	2 cycles, 16 hr	58 start, 46 end	13.9 max 13.4 min 13.6 av	Used same barrel as used in test 5; cylinder assembled completely dry; test terminated because of low cylinder efficiency and erratic, noisy operation; barrel of cylinder in excellent condition; no sign of damage
7	3-in.-diam Thompkins-Johnson cylinder with ORNL seal	Three O-rings on piston Two O-rings on rod	Viton B, carbon-wool impregnated	7.67 on piston 13.0 on rod	0.285 on piston 0.140 on rod	1 1/2 to 2 on barrel 1 to 2 on rod (same barrel and rod as in test 6)	36 cycles to date, 144 hr at 36 cycles	88 start, 88 at 36 cycles	14.9 max 6.4 min 12.3 av for 26 cycles	Cylinder assembled with considerable Molykote applied to the O-ring, rod, and barrel; new piston with a 0.285-in.-wide groove used; same barrel as used in test 6
8	3-in.-diam Tog-Loc cylinder with ORNL seal	Three O-rings on first piston Three O-rings on second piston Two O-rings on rod		10.8 on first piston 6.2 on second piston 8.4 on rod	0.220 on first piston 0.140 on second piston 0.140 on rod	4 on second piston	14 cycles to date, 56 hr at 14 cycles	78 start, 66 at 14 cycles	22.0 max 14.1 min	Cylinder assembled with considerable Molykote applied to the O-rings, rod, and barrel; cylinder volume, 15.9 ft^3

stress relaxation properties of the material, which are functions of time and temperature exposure.

Experimental Studies of Steam-Graphite Reactions

R. E. Helms F. H. Neill

Rates of graphite reaction and hydrogen generation resulting from the exposure of EGCR core graphite to superheated steam were previously reported.[6–8] These reaction rates can be correlated, within the range of the experimental data, with a modified Arrhenius-type equation that describes the reaction rate as a function of temperature and burnoff. This equation is of the following form:

$$K = Ae^{-\Delta E/RT} = B^m e^n \, e^{-\Delta E/RT} , \qquad (1)$$

where

$A = B^m e^n$ = frequency factor,

ΔE = activation energy, cal/g·mole,

R = gas constant, 1.987 cal/°K/g·mole,

T = absolute temperature, °K,

K = reaction rate, grams of carbon per hour per square centimeter or standard cubic centimeter of hydrogen per hour per square centimeter,

B = burnoff, %,

and m and n are exponents determined from experimental data.

For EGCR fuel-element graphite (Speer 901-RYL), the experimental data for the graphite reaction rate as a function of temperature and burnoff

---

[6]R. E. Helms, R. E. MacPherson, and F. H. Neill, Experimental Studies of Steam-Graphite Reactions, p. 15, GCRP Semiann. Progr. Rept. Mar. 31, 1964, USAEC Report ORNL-3619, Oak Ridge National Laboratory.

[7]R. E. Helms and F. H. Neill, Experimental Studies of Steam-Graphite Reactions, pp. 264–271, GCRP Semiann. Progr. Rept. Sept. 30, 1964, USAEC Report ORNL-3731, Oak Ridge National Laboratory.

[8]R. E. Helms and F. H. Neill, Experimental Studies of Steam-Graphite Reactions, pp. 244–247, GCRP Semiann. Progr. Rept. Mar. 31, 1965, USAEC Report ORNL-3807, Oak Ridge National Laboratory.

can be described by

$$K\ (g/hr \cdot cm^2) = e^{25.996}\ B^{0.346}\ e^{-55,200/RT}\ , \qquad (2)$$

and the hydrogen production rate data as a function of temperature and burnoff can be described by

$$K\ (scc/hr \cdot cm^2) = e^{25.306}\ B^{0.323}\ e^{-63,600/RT}\ . \qquad (3)$$

For EGCR moderator graphite (National Carbon Co.), the experimental data for the graphite reaction rate as a function of temperature and burnoff can be described by

$$K\ (g/hr \cdot cm^2) = e^{25.378}\ B^{0.150}\ e^{-52,200/RT}\ , \qquad (4)$$

and the hydrogen production rate data as a function of temperature can be described by

$$K\ (scc\ H_2/hr \cdot cm^2) = e^{24.541}\ B^{0.209}\ e^{-48,300/RT}\ . \qquad (5)$$

Special Fuel Assemblies for Flux Mapping

R. M. Evans E. A. Franco-Ferreira

We assisted the EGCR operating group of TVA in the design and preparation of special fuel assemblies to be used for flux mapping the EGCR. Standard core-1 components were used to provide assemblies that can be readily dismantled and reassembled. The components for ten such special fuel assemblies were modified in accordance with the specifications.

Standard 0.707-in.-OD, 0.323-in.-ID, 0.740-in.-long UO_2 pellets were sliced by ultrasonic machining to provide half-length and assorted wafer-length pellets for adjusting the fuel column to the specified length. In addition, 50 half-length pellets were drilled ultrasonically to provide 13 axial 0.025-in.-diam holes to support copper flux-monitor wires. A special technique was developed for simultaneously drilling these 13 holes

to reasonably close tolerances on a consistent basis with a multipronged tool. Two views of a typical drilled pellet are shown in Fig. 8.6.

We also prepared 0.3-in.-diam extruded rods of Al–13 wt % U alloy containing highly enriched uranium. These rods were provided in various lengths to facilitate positioning of copper flux-monitor washers. The rods and flux-monitor washers will be loaded into the central holes of the fuel pellets.

PHOTO 81756

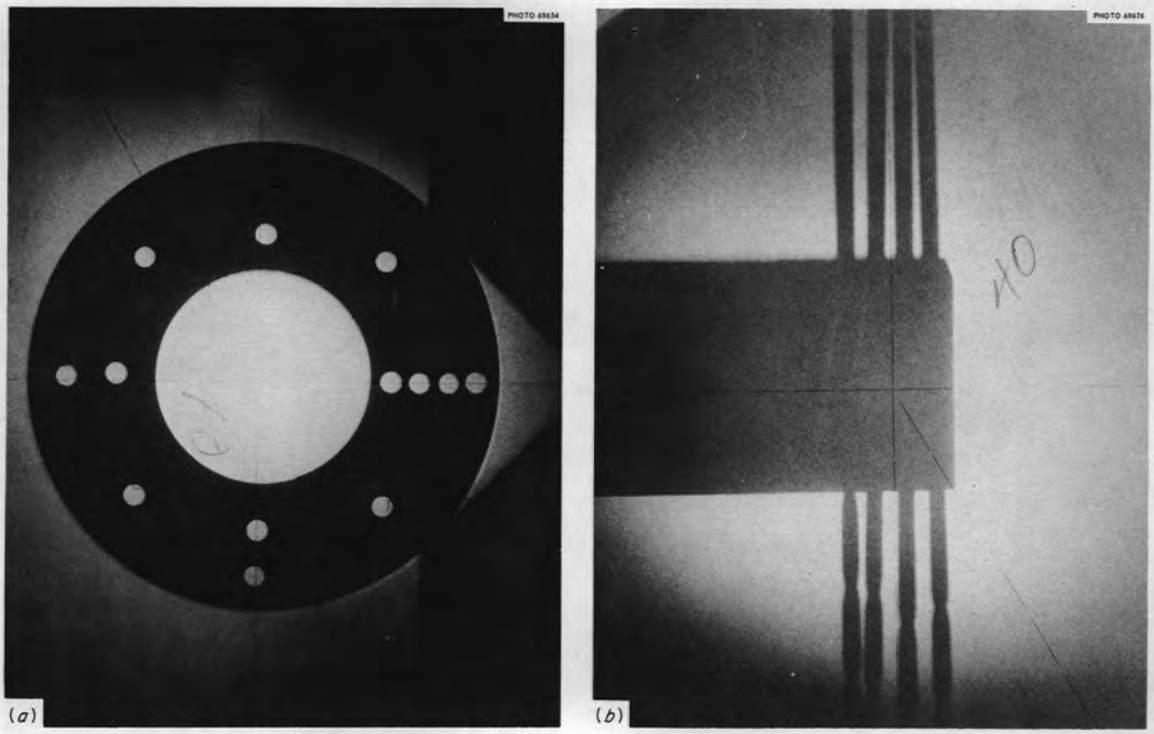

Fig. 8.6. Two Views of a Half-Length EGCR-Type UO_2 Fuel Pellet. (a) End view, as seen on the inspection profilometer, showing the positions of the axial holes for copper flux-monitoring wires. (b) Side view of the same pellet with drill bits positioned in the holes to indicate axial runout.

Analysis of Failure of 42-in. Bellows Between EGCR Containment Shell and Experimenter's Cell

G. M. Tolson T. M. Kegley

An investigation was carried out to determine the cause of the failure of the 42-in.-diam, 0.039-in.-thick, type 304 stainless steel bellows

that connects experimenter's cell 6 to the EGCR containment shell and to ascertain whether such a condition might recur. The failure consisted of several leaks at the bottom of the bellows, as shown in Fig. 8.7. The bellows in cell 5 shows signs of similar attack, but it has not failed. It was learned that the bellows were installed and concrete was poured around them about two years prior to the failure. Construction work, such as installing some of the experimental loop piping within the bellows, then continued. During this work the bellows was fouled with a large amount of debris that was removed before the failure was discovered.

One of the areas of failure was removed, and scrapings were taken from around other pitted areas. These samples were evaluated by metallography, x-ray diffraction, chemical analysis, and microprobe analysis. As may be seen in Fig. 8.8, the failure was the result of the pitting

Fig. 8.7. Photo Taken Inside 42-in. Bellows That Failed Due to Pitting Attack. Arrows point to areas of attack.

Fig. 8.8. Polished Section Through 42-in. Bellows That Failed Due to Pitting Attack. Note that the inner surface was severely corroded.

type of attack that is most often caused by chloride ions. The analyses showed the presence of chlorine and calcium, and it was learned that $CaCl_2$ may have been used as an antifreeze additive to the concrete poured around these bellows. The failure cannot be definitely attributed to $CaCl_2$, however, since other materials containing chloride ions could be responsible. Although the attack seemed to come from the inside of the sample examined, if $CaCl_2$ is responsible, any further attack could initiate on the outer surface.

9. IRRADIATION TESTING OF COMPONENTS AND MATERIALS

H. C. McCurdy O. Sisman
J. H. Coobs M. S. Wechsler

EGCR Prototype Fuel Tests

Irradiation of Capsules 03A-6 and 04-8 in ORR Poolside Facility (V. A. DeCarlo, F. R. McQuilkin)

Irradiation capsules 03A-6 and 04-8 contain prototype-diameter specimens of EGCR fuel and cladding supplied by the fuel-element vendor. The final irradiation data for capsule 03A-6, which was removed from the ORR poolside facility March 6, 1965,[1] are given in Table 9.1. Irradiation of capsule 04-8 is continuing, and as of September 15, 1965 it had accumulated an estimated burnup of 6140 Mwd/MT of UO_2. A description of this capsule was given previously.[2] The capsule temperatures listed in Table 9.2, which were read September 15, 1965, are typical of the temperatures indicated by the six cladding surface thermocouples.

Postirradiation Examination of EGCR Prototype Fuel (M. F. Osborne, E. L. Long, Jr., J. G. Morgan, H. E. Robertson)

All EGCR prototype fuel capsules have been examined, except capsule 04-8, which is still under irradiation in the ORR. Irradiation data for the four capsules (03A-6, E-3, E-11, and E-12R) examined in detail during this reporting period are summarized in Table 9.3. Some of the metallographic studies of these four capsules have not been completed. Six capsules (E-1R, E-2, E-4R, E-5, E-5R, and E-10) that had previously been inspected visually[3] were submitted for independent fission-product studies.

---

[1]V. A. DeCarlo and F. R. McQuilkin, Capsule Irradiations in ORR Poolside Facility, pp. 143–144, GCRP Semiann. Progr. Rept. Mar. 31, 1965, USAEC Report ORNL-3807, Oak Ridge National Laboratory.

[2]V. A. DeCarlo, F. R. McQuilkin, and R. L. Senn, Fueled-Capsule Irradiations in ORR Poolside Facility, p. 275, GCRP Semiann. Progr. Rept. Sept. 30, 1964, USAEC Report ORNL-3731, Oak Ridge National Laboratory.

[3]J. G. Morgan et al., Examination of ORR- and ETR-Irradiated Fuel Elements, pp. 280–282, GCRP Semiann. Progr. Rept. Sept. 30, 1964, USAEC Report ORNL-3731, Oak Ridge National Laboratory.

Table 9.1. Summary of Operating Data for EGCR Prototype Fuel in ORR Poolside Capsule 03A-6

Origin of fuel specimen	Westinghouse
Fuel identification	3008
Type of capsule	UO_2 pellets in type 304 stainless steel
Irradiation starting date	11-28-62
Irradiation ending date	3-7-65
Irradiation time normalized to operation at 30 Mw, days	681.7
Calculated effective thermal flux,[a] neutrons/cm^2·sec	1.39×10^{13}
Fuel density, % of theoretical	95.44
Fuel enrichment, % ^{235}U	2.46
Fuel oxygen-to-uranium ratio	2.001
Average linear power, Btu/hr·ft	31,350
Total heat flux, Btu/hr·ft^2	159,740
Burnup (calculated)	
Total, Mwd/MT of UO_2 of fueled specimen	9885
Rate, Mw/MT of UO_2 of fueled specimen (at full power)	14.5
Cladding outer surface temperature, °F (°C)	
Design, maximum of six thermocouples	1300 (704)
Highest reading for entire test	1330 (721)
Lowest[b] reading for entire test	983 (528)
Average reading for entire test	1166 (630)
Cladding external pressure, psig	300

[a]Based on ^{60}Co in the stainless steel dosimeter located outside the cladding and corrected for self-shielding factor of fuel (0.715).

[b]By definition, "lowest" in this case is the lowest temperature indicated by any of the six thermocouples while one of them is indicating 1300°F (704°C) or higher. This definition provides for indication of the spread in temperature readings registered by the six thermocouples.

Table 9.2. Cladding Temperatures in Capsule 04-8

Cladding Thermocouple Location	Temperature Element Designation	Temperature[a]	
		°F	°C
At 1st (top) pellet, back[b]	TE-406	1400	760
At 3rd pellet, front[b]	TE-403	1418	770
At 5th pellet, front	TE-404	1470	799
At 5th pellet, back	TE-401	1560	849
At 7th pellet, front	TE-405	1494	812
At 8th pellet (bottom), back	TE-402	1372	744

[a]Temperatures as read September 15, 1965.

[b]Back denotes side away from reactor; front denotes side facing reactor.

Table 9.3. Irradiation Data for EGCR Prototype Fuel Capsules

Capsule	Pellet Type	Design Cladding Temperature		Irradiation Period	Average Neutron Flux[a] (neutrons/cm^2·sec)
		°F	°C		
					$\times 10^{13}$
03A-6	Hollow	1300 av	704	11-28-62 to 3-7-65	1.94
E-3	Solid	1600 max	871	12-12-59 to 10-25-63	3.37
E-5R	Hollow	1600 max	871	12-7-60 to 7-8-64	3.38
E-11	Hollow, BeO central rod	1300 av	704	6-4-60 to 7-8-64	2.59
E-12R	Hollow	1600 max	871	10-14-61 to 7-8-64	4.38

[a]Determined from stainless steel flux monitors.

The NaK vessels from capsules E-5R, E-11, and E-12R were examined for nitride formation in the exterior regions.

Most of these capsules showed no unusual features by visual inspection. The cladding of capsule E-12R (Fig. 9.1) had distinct circumferential ridges at many pellet interfaces and was generally roughened, but no fractures were seen. Several other capsules had visible, but less extensive, cladding deformation. Only capsule E-3 was obviously damaged. Two large cladding fractures (Fig. 9.2) were found near the mid-length of the capsule; the larger fracture was approximately 1 in. long by 1/8 in. wide. The stainless steel-sheathed cladding thermocouples and the foil thermocouple bands were welded to the cladding and to the inner surface of the NaK vessel in numerous places. These welds and the appearance of the cladding near the fractures indicated that the capsule had exceeded the design temperature (Table 9.3). The absence of fission-product radioactivity in samples of the NaK from the other capsules indicated that none of these capsules had cladding failures.

For the four capsules examined in detail, only one gamma scan showed an unusual distribution of radioactivity. A smooth radioactivity gradient along the length of capsule E-12R indicated that the neutron flux had been about 30% greater at the bottom end of the capsule than at the top end. This effect is illustrated in Figs. 9.3 and 9.4, which show the

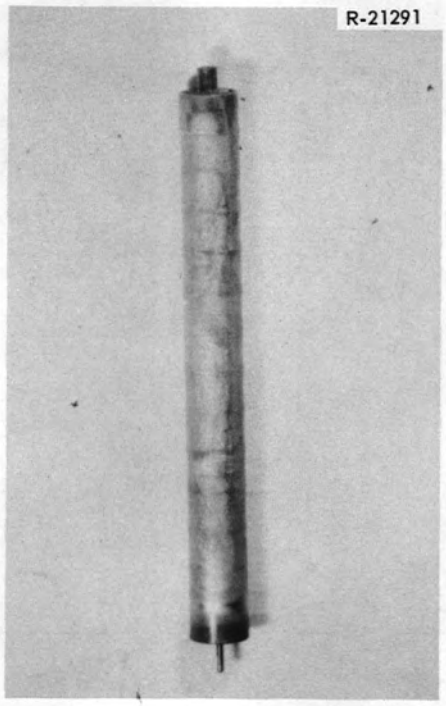

Fig. 9.1. EGCR Prototype Fuel Capsule E-12R Showing Extensive Cladding Deformation. Cladding did not fail. 0.35×

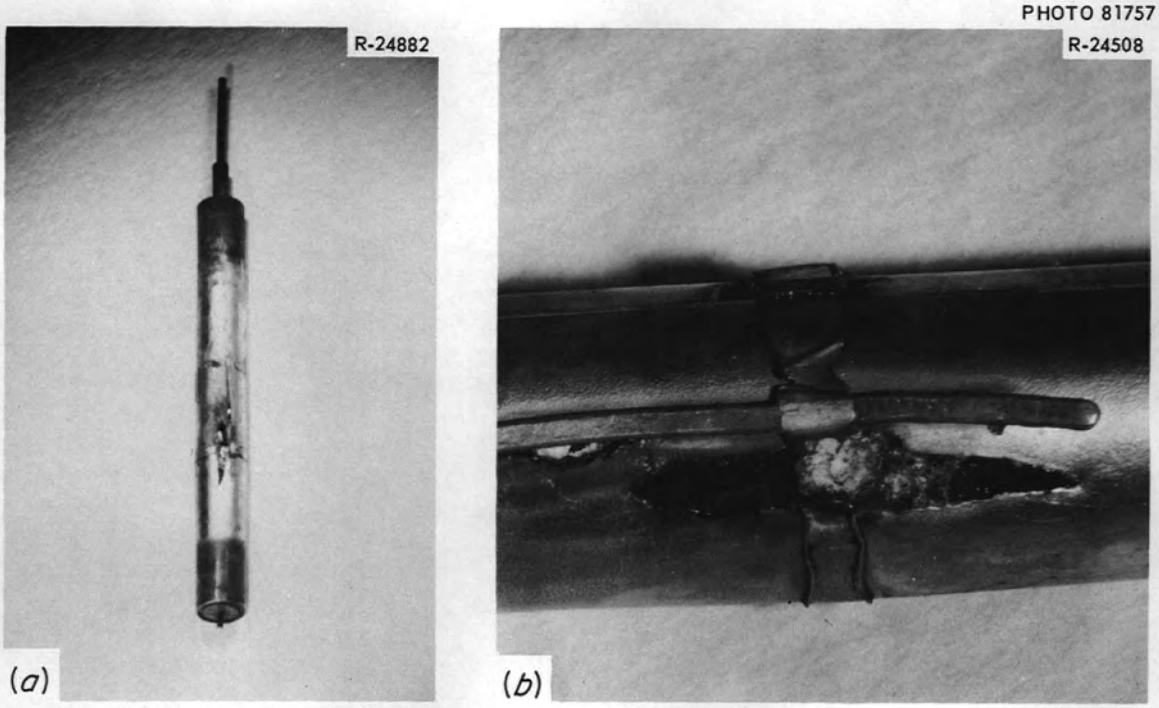

Fig. 9.2. EGCR Prototype Fuel Capsule E-3 Showing Cladding Failure. (a) Overall view of the capsule. 0.3× (b) Fracture region showing thermocouples and foil that were welded to the cladding. 2.2×

ORNL-DWG 65-12363

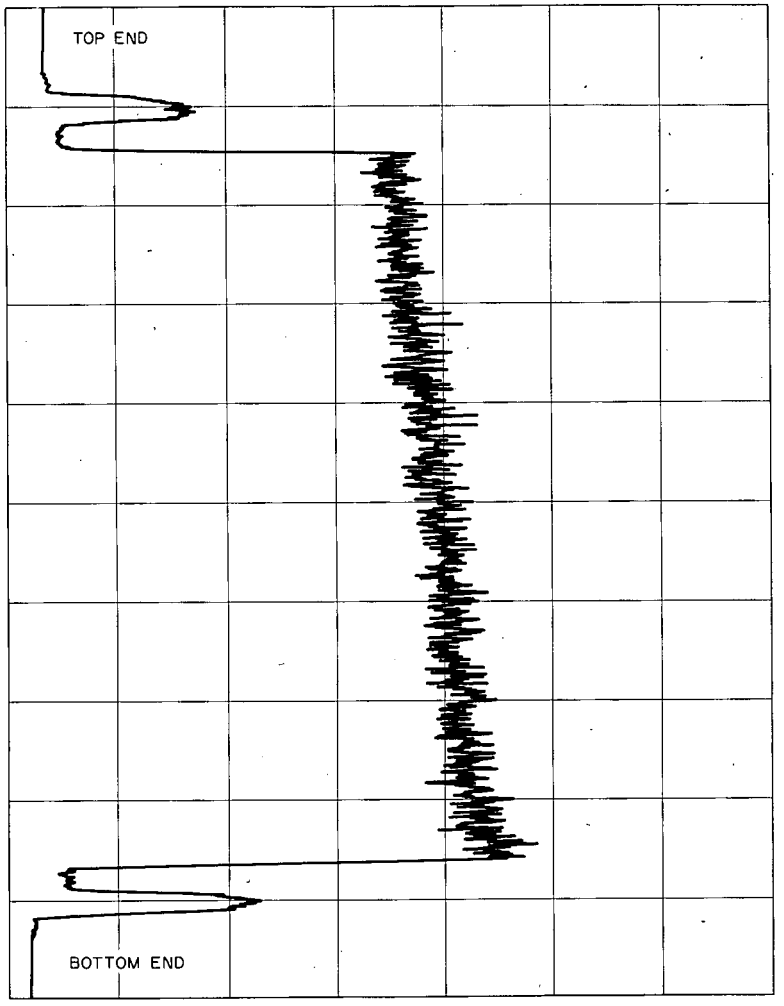

Fig. 9.3. Gamma Scan of EGCR Prototype Fuel Capsule E-12R. Note the axial radioactivity gradient, which indicates approximately 30% higher burnup at the bottom end than at the top end of the capsule.

ORNL-DWG 65-12364

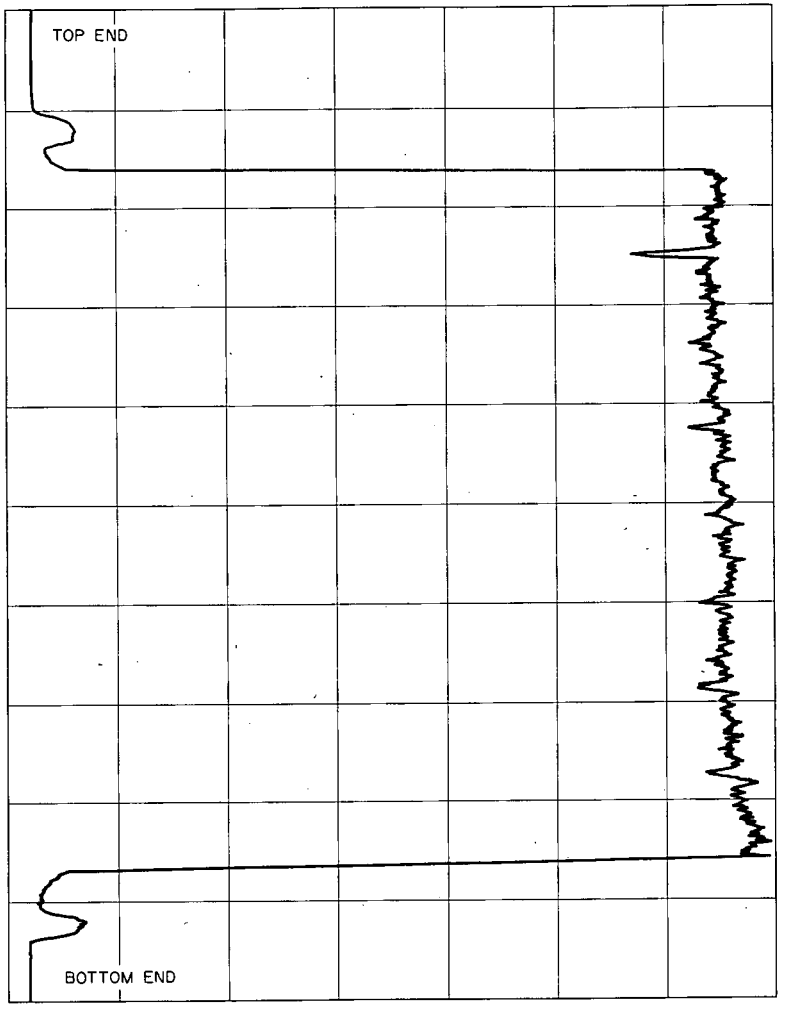

Fig. 9.4. Gamma Scan of EGCR Prototype Fuel Capsule 03A-6. This radioactivity distribution is typical of EGCR prototype fuel capsules; note the small space between the top two fuel pellets.

gamma scans for capsules E-12R and 03A-6; the scan shown in Fig. 9.4 is typical for these capsules.

Except for capsule E-3, which was severely swollen, no unusual dimensional changes were found, as indicated in Table 9.4. The cladding of capsules 03A-6 and E-11, which appeared to have operated under less stringent conditions than the other two capsules, had collapsed against the fuel. The diameter increases shown for capsule E-12R were caused by the extensive ridges and wrinkles of the cladding. The average diameter of capsule E-3 in the vicinity of the cladding fractures had increased as much as 0.063 in. Only capsule E-3 had a significant change in length — an increase of about 0.1 in.

The fission gas was collected from capsule 03A-6. Mass spectrometric analysis showed that the gas was more than 96% helium (fill gas) and 1.01% krypton and xenon (fission gas), and gamma spectrometric analysis indicated that about 0.08% of the ^{85}Kr formed was released from the fuel. Radiochemical analysis of a fuel sample for ^{144}Ce indicated a burnup of 11,200 Mwd/MT of UO_2, compared with a value of 10,000 Mwd/MT of UO_2 based on flux-monitor data.

Table 9.4. Diameter Changes of Irradiated EGCR Prototype Fuel Capsules

Position (in. from bottom end)	Change in Average Diameter[a] (mils)			
	Capsule 03A-6	Capsule E-3	Capsule E-11	Capsule E-12R
0				
0.5	-0.5	+0.1	-0.6	-4.1
1.0	+0.8	+0.5	-4.4	+0.3
1.5	-0.7	+15.5	-3.8	-0.6
2.0	-3.5	+33.5	+6.8	+1.6
2.5	-5.8	+62.9	+7.7	+1.0
3.0	-4.5	+40.5	-3.7	+6.8
3.5	-3.9	+39.1	-2.1	+6.7
4.0	-7.0	+25.7	-4.3	+4.9
4.5	-6.5	+24.9	-4.8	+5.8
5.0	-4.8	+24.4	-3.9	+5.1
5.5	-2.8	+17.7	-3.0	+8.6
6.0	-1.1	+1.8	-0.4	+7.2
6.5	0	-3.9	+0.6	+5.6

[a]Diameters were measured at 0 and 90°.

The macroscopic appearance of the UO_2 in the central area of each capsule was normal, except for capsule E-3. As was expected because of the extreme operating conditions for this capsule, there were structural changes in the UO_2. Circumferential fractures had formed in the solid pellets at a radius of about 0.25 in.; the UO_2 inside this circle showed columnar grains, but no central void was evident. The results of metallographic examination, which will be reported later, should show in detail the structural changes of the fuel and cladding of all four capsules.

The type 304 stainless steel NaK tubes from ETR-irradiated capsules E-5R, E-11, and E-12R were examined for the presence and extent of nitriding. [Nitrogen was used as a heat transfer gas, and the NaK tubes operated at a temperature conducive to nitriding (~1000°F, 538°C), so some nitriding was expected.] Severe nitriding of the NaK tube from capsule 02A-6, which was irradiated under similar conditions, was found and reported previously.[4]

As for NaK tubes from previous prototype fuel experiments, the exterior surfaces were darkened in the areas adjacent to the fuel capsules. This is shown in Fig. 9.5. Diameter measurements indicated consistent

---

[4]J. G. Morgan et al., Examination of Irradiated Capsules, pp. 33–42, GCRP Semiann. Progr. Rept. Mar. 31, 1964, USAEC Report ORNL-3619, Oak Ridge National Laboratory.

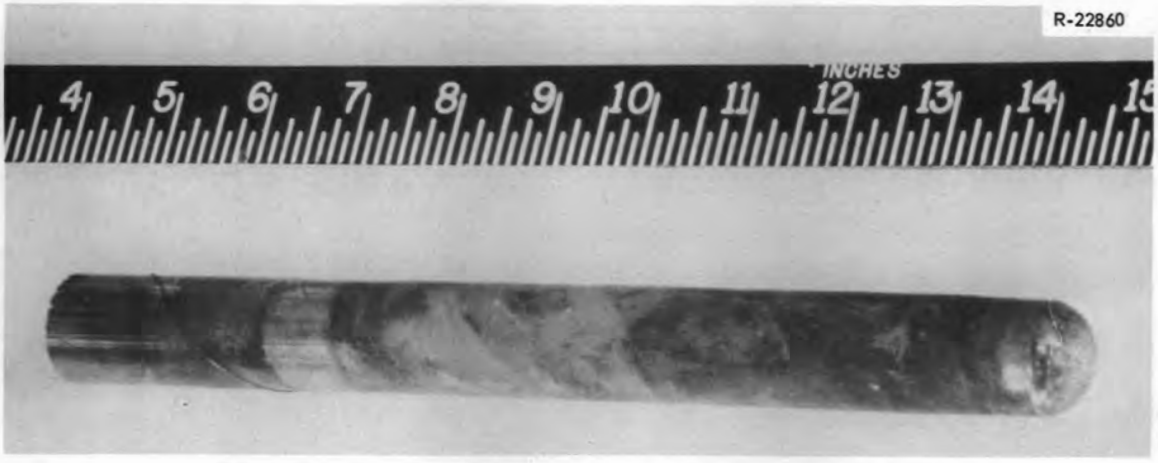

Fig. 9.5. Typical NaK Tube from an ETR-Irradiated EGCR Prototype Fuel Capsule. Note area of discoloration that shows the location of the fuel capsule inside.

increases, with up to a maximum of 0.042 in. at one location. The increases in the average diameters are listed in Table 9.5. Metallographic examination verified that the expected nitride reaction occurred and that the reaction product extended in from the exterior surfaces of the NaK vessels to depths generally consistent with the observed dimensional changes.

Table 9.5. Diameter Data for NaK Tubes from EGCR Prototype Fuel Capsules

Measurement Position (in. from bottom end)	Average Diameter Increases[a] (in.)		
	Capsule E-5R	Capsule E-11	Capsule E-12R
0	0.007	0.002	0.004
1	0.006	0.002	0.023
3	0.014	0.002	0.031
5	0.020	0.008	0.020
7	0.001	0.011	0.003
9	0.001	0.003	0.001

[a]Since the preirradiation measurements were made on a "go-no-go" basis and the actual measurements were not recorded, these increases are based on an initial diameter of 0.980 in.

Pressure-Vessel Surveillance Program

R. G. Berggren T. N. Jones
W. J. Stelzman M. S. Wechsler

Preparations for insertion of surveillance specimens in the EGCR pressure vessel are nearing completion.[5] Trial loading of a completed surveillance string into the removal cask indicated the necessity of minor modifications to the removal cask and to the pressure-cap linkages of the surveillance strings. Parts for these modifications are now on

[5]R. G. Berggren, W. J. Stelzman, and M. S. Wechsler, Pressure-Vessel Surveillance Program, pp. 282–289, GCRP Semiann. Progr. Rept. Sept. 30, 1964, USAEC Report ORNL-3731, Oak Ridge National Laboratory.

hand and modifications are in progress. Several of the surveillance-string cables were damaged during cleaning operations and replacement cables are on order. Final insertion and removal tests will be conducted after physics tests on the EGCR are completed. Control specimens for the surveillance program were sealed in inert atmosphere containers for storage.

Fast Fracture Analysis of the EGCR Pressure Vessel

A fast fracture analysis was conducted on the EGCR pressure vessel design and a report published.[6] Although the results of experimental stress analysis studies[7,8] demonstrated the structural adequacy of the EGCR pressure vessel, a fast fracture analysis was thought advisable in the unlikely event that major flaws either were not detected by nondestructive inspection or developed during operation of the vessel.

Since the EGCR pressure vessel will be operated at temperatures above those at which brittle fracture can occur, and stress levels when the vessel is cold will be below those at which brittle fracture can occur, the possibility of fast ductile failure rather than brittle failure of the vessel was studied. Increases in the nil-ductility transition temperature during operation of the vessel will be monitored by the periodic testing of surveillance specimens. The analysis of fast ductile fracture of the EGCR pressure vessel was based on the maximum flaw size that might occur prior to penetration of the vessel and detectable leakage. It was demonstrated that none of the postulated flaws could initiate fast ductile failure of the EGCR pressure vessel.

---

[6]R. G. Berggren, Fast Fracture Analysis of EGCR Pressure Vessel, USAEC Report ORNL-TM-1169, Oak Ridge National Laboratory, June 21, 1965.

[7]B. L. Greenstreet et al., Experimental Stress Analysis of EGCR Pressure Vessel, USAEC Report ORNL-3157, Oak Ridge National Laboratory, Nov. 14, 1961.

[8]J. E. Smith, C. C. Wilson, and W. J. Swinson, Photoelastic Analysis of EGCR Pressure Vessel, USAEC Report ORNL-3690, Oak Ridge National Laboratory, February 1965.

Accelerated Irradiations

Tensile tests of specimens irradiated in the ORR[9] at elevated temperatures are in progress. The Charpy impact testing machine was modified for improved specimen handling and test temperature control, recalibrated, and is being installed in the hot cell. Impact testing of EGCR steels irradiated in the ORR[9] at elevated temperatures will begin as soon as installation is completed. These tensile and impact tests will include the study of annealing behavior of the irradiated EGCR steels.

Graphite Surveillance Program

W. S. Ernst, Jr.

Specimens for use in a graphite surveillance program were obtained, and preirradiation measurements are in progress. The top spiders, support rods, and graphite sleeves are on hand. Assembly of the units will begin when the melt wires and flux-monitor wires are received. Dummy assemblies are ready for shipment to the EGCR when required.

---

[9]R. G. Berggren et al., Pressure-Vessel Surveillance Program, p. 263, GCRP Semiann. Progr. Rept. Mar. 31, 1965, USAEC Report ORNL-3807, Oak Ridge National Laboratory.

Previous reports in this series are:

ORNL-2500	Part 1–4, issued April 1, 1958
ORNL-2505	Issued June 19, 1958
ORNL-2510	Issued September 18, 1958
ORNL-2676	Period Ending December 31, 1958
ORNL-2767	Period Ending June 30, 1959
ORNL-2835	Period Ending September 30, 1959
ORNL-2888	Period Ending December 31, 1959
ORNL-2929	Period Ending March 31, 1960
ORNL-2964	Period Ending June 30, 1960
ORNL-3015	Period Ending September 30, 1960
ORNL-3049	Period Ending December 31, 1960
ORNL-3102	Period Ending March 31, 1961
ORNL-3166	Period Ending June 30, 1961
ORNL-3210	Period Ending September 30, 1961
ORNL-3254	Period Ending December 31, 1961
ORNL-3302	Period Ending March 31, 1962
ORNL-3372	Period Ending September 30, 1962
ORNL-3445	Period Ending March 31, 1963
ORNL-3523	Period Ending September 30, 1963
ORNL-3619	Period Ending March 31, 1964
ORNL-3731	Period Ending September 30, 1964
ORNL-3807	Period Ending March 31, 1965

ORNL-3885

UC-80 — Reactor Technology
TID-4500 (47th ed.)

Internal Distribution

1. G. M. Adamson
2. S. E. Beall
3. M. Bender
4. R. G. Berggren
5. D. S. Billington
6. E. P. Blizard
7. E. G. Bohlmann
8. C. J. Borkowski
9. G. E. Boyd
10. R. B. Briggs
11. R. S. Carlsmith
12. C. E. Center (K-25)
13. J. H. Coobs
14. W. B. Cottrell
15. J. A. Cox
16. F. L. Culler
17. J. H. DeVan
18. D. A. Douglas
19. I. T. Dudley
20. D. M. Eissenberg
21. R. B. Evans
22. R. M. Evans
23. D. E. Ferguson
24. L. M. Ferris
25. J. L. Fowler
26. A. P. Fraas
27. J. H. Frye, Jr.
28. W. R. Gall
29. R. J. Gray
30. W. R. Grimes
31. W. O. Harms
32. M. R. Hill
33. H. W. Hoffman
34. A. Hollaender
35. A. S. Householder
36. W. H. Jordan
37. P. R. Kasten
38. C. P. Keim
39. M. T. Kelley
40. E. M. King
41. J. A. Lane
42. C. E. Larson (K-25)
43. R. S. Livingston
44. H. G. MacPherson
45. R. E. MacPherson
46. R. W. McClung
47. H. C. McCurdy
48. F. R. McQuilkin
49. A. B. Meservey
50. H. J. Metz
51. J. G. Morgan
52. K. Z. Morgan
53. F. H. Neill
54. M. L. Nelson
55. R. C. Olson
56. L. G. Overholser
57. P. Patriarca
58. A. M. Perry
59. D. Phillips
60. C. A. Preskitt
61. M. E. Ramsey
62. M. W. Rosenthal
63. G. Samuels

64-65. A. W. Savolainen

66. J. L. Scott
67. O. Sisman
68. E. D. Shipley
69. M. J. Skinner
70. G. M. Slaughter
71. A. H. Snell
72. I. Spiewak
73. E. H. Taylor

74-80. D. B. Trauger

81. C. S. Walker
82. G. M. Watson
83. M. S. Wechsler
84. A. M. Weinberg
85. J. R. Weir
86. J. C. White

87-107. G. D. Whitman

108. F. J. Witt
109. Gale Young
110. J. Zasler

111-112. Y-12 Document Reference Section

113-115. Central Research Library

116-171. Laboratory Records Department

172. Laboratory Records Department, ORNL, R.C.

External Distribution

173. R. J. Ball, AEC, San Francisco Operations Office (GA)
174. R. A. Charpie, UCC Research Administration, New York, N.Y.
175-176. D. F. Cope, Reactor Division, AEC, ORO
177-178. R. W. Coyle, Vallecitos Atomic Laboratory
179. W. P. Eatherly, UCC, Lawrenceburg, Tenn.
180. H. L. Falkenberry, Tennessee Valley Authority
181. M. Janes, National Carbon Research Laboratories, Cleveland, Ohio
182. T. Jarvis, Ford Instrument Co.
183. James R. Johnson, Minnesota Mining and Manufacturing Company, Saint Paul, Minn.
184. R. F. Kirkpatrick, AEC, Gas Cooled Project Branch, Division of Reactor Development and Technology
185. C. W. Kuhlman, United Nuclear Corp.
186-187. H. Lichtenburger, General Nuclear Engineering Corp.
188. J. P. McGee, Bureau of Mines, Appalachian Experiment Station
189. R. W. McNamee, UCC Research Administration, New York, N.Y.
190. J. L. Mershon, AEC, Reactor Vessels Branch, Division of Reactor Development and Technology
191. R. G. Oehl, AEC, Gas Cooled Project Branch, Division of Reactor Development and Technology
192. R. E. Pahler, AEC, Gas Cooled Project Branch, Division of Reactor Development and Technology
193. J. B. Radcliffe, San Francisco Operations Office
194. H. B. Rahner, Savannah River Operations Office
195. Donald Stewart, AEC, Washington
196. J. A. Swartout, UCC, New York, N.Y.
197. S. A. Szawlewicz, AEC, Research and Development Branch, Division of Reactor Development and Technology
198. Philip L. Walker, Pennsylvania State University
199-200. W. L. Webb, East Central Nuclear Group, Inc.
201. D. J. Wille, AEC, Systems Engineering Branch, Division of Reactor Development and Technology
202. C. E. Winters, UCC, Cleveland, Ohio
203. J. H. Wright, Westinghouse Atomic Power Division
204-211. General Atomic Library (Att.: E. Creutz, R. B. Duffield (3 copies), D. V. Ragone, C. Rickard, M. T. Simnad, L. R. Zumwalt)
212. Division of Research and Development, AEC, ORO
213-547. Given distribution as shown in TID-4500 (47th ed.) under Reactor Technology category (75 copies — CFSTI)